An element-free Galerkin method for crack propagation in brittle materials

Document Version:
Publisher's PDF, also known as Version of Record (includes final page, issue and volume numbers)

Please check the document version of this publication:

An Element-free Galerkin Method for Crack Propagation in Brittle Materials

Dries Hegen
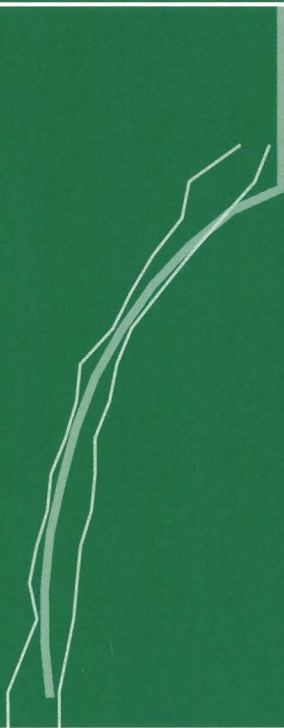
An Element-free Galerkin Method for Crack Propagation in Brittle Materials

On the cover: Comparison between experimental results and crack path obtained by simulation
of quasi-static crack propagation with combination of element-free Galerkin method and finite
element method for a single-edge notched beam under shear loading.

An Element-free Galerkin Method for Crack Propagation in Brittle Materials

PROEFSCHRIFT

ter verkrijging van de graad van doctor aan de Technische Universiteit Eindhoven, op gezag van de Rector Magnificus, prof.dr. M. Rem, voor een commissie aangewezen door het College van Dekanen in het openbaar te verdedigen op donderdag 6 maart 1997 om 16.00 uur

door

Dries Hegen

geboren te Exloo

Dit proefschrift is goedgekeurd door de promotoren:

prof.dr.ir. F.P.T. Baaijens
prof.dr.ir. R. de Borst

en de copromotor:

dr.ir. P.J.G. Schreurs

Aan mijn ouders:

Lucas Hegen

en

Trijntje Pepping

Samenvatting

Voor het simuleren van scheurpropagatie in brosse materialen wordt vaak de eindige elementen methode toegepast. Deze methode gebruikt een opdeling van het materiaaldomein in zogenaamde elementen. Relevante grootheden in het domein, zoals verplaatsingen en spanningen, worden benaderd per element. Een opdeling in elementen wordt gegeven door een verzameling van knooppunten die onderling verbonden zijn om de elementen te vormen. Omdat scheurpropagatie de uitbreiding van scheuroppervlakken inhoudt, dient tijdens simulaties de elementenopdeling en dus de zogenaamde connectiviteit van knooppunten, voortdurend te worden aangepast. Dit aanpassen van de elementenopdeling staat bekend als "remeshen" en kan het simuleren van scheurpropagatie behoorlijk gecompliceerd en tijdrovend maken.

De elementvrije Galerkin methode is een methode die ook knooppunten gebruikt, maar waarbij het gebruik van een connectiviteit afwezig is. Verplaatsingen en spanningen in het materiaaldomein worden benaderd met behulp van een techniek genaamd "moving least squares approximation", die vrij is van een connectiviteit. Deze techniek vereist, naast de informatie betreffende de knooppunten, een verzameling van gewichtsfuncties en een verzameling van basisfuncties. Omdat de uitbreiding van scheuroppervlakken kan worden weergegeven zonder het wijzigen van een connectiviteit van knooppunten, is het mogelijk scheurpropagatie te simuleren zonder de noodzaak tot "remeshen". Het doel van het onderzoek gepresenteerd in dit proefschrift is de formulering van een numeriek model, gebaseerd op de elementvrije Galerkin methode, dat geschikt is voor het simuleren van scheurpropagatie in brosse materialen.

Het numerieke model veronderstelt lineair elastisch materiaalgedrag en gebruikt criteria voor scheurgroei en de richting van scheurgroei in brosse materialen. Deze criteria komen voort uit de breukmechanica en worden uitgedrukt in spanningsintensiteitsfactoren. Met behulp van de elementvrije Galerkin methode worden benaderende waardes berekend voor de verplaatsingen en de spanningen in een materiaaldomein waarin een scheur aanwezig is. Daarvoor dienen de onbekende verplaatsingen van de knooppunten te worden verkregen. Hiervoor wordt een numeriek integratie schema gebruikt dat is gebaseerd op een onderliggende configuratie van integratiecellen. Deze configuratie kan onafhankelijk van de knooppuntsverdeling gekozen worden en hoeft niet te worden aangepast tijdens simulaties van scheurpropagatie. Het schema houdt rekening met de dichtheid van de knooppuntsverdeling, met de spanningssingulariteiten en met de discontinuïteiten van grootheden over de scheur. Voor de benaderingstechniek gebaseerd op "moving least squares approximation" worden verschillende modellen voor de discontinuïteit in het materiaaldomein ten gevolge van de aanwezigheid van een scheur onderzocht. Dit resulteert in een nieuw zogenaamd wig-model toegepast op de gewichtsfuncties en in het gebruik van speciale basisfuncties voor de representatie van spanningssingulariteiten. Uit de berekende verplaatsingen en spanningen in het materiaaldomein worden de spanningsintensiteitsfactoren bepaald, die vervolgens worden toegepast in de breukcriteria.

Een nadeel van de elementvrije Galerkin methode is de benodigde rekeninspanning. Voor een reductie daarvan zijn drie combinaties van deze methode met de eindige elementen methode onderzocht, zodat het uitbreiden van scheuroppervlakken nog steeds kan worden weergegeven zonder de noodzaak tot "remeshen". De effectiviteit van de ontwikkelde numerieke modellen wordt gedemonstreerd aan de hand van enkele typische twee-dimensionale breukmechanische

problemen. De resultaten voor statische problemen tonen aan dat de spanningsintensiteitsfactoren nauwkeurig berekend kunnen worden. Voor het probleem van quasi-statische scheurpropagatie in een balk met een enkelzijdige snede belast onder afschuifcondities, zijn scheurpaden verkregen die goed overeenkomen met experimentele resultaten uit de literatuur. Dit toont, tesamen met andere numerieke resultaten, dat het simuleren van quasi-statische scheurpropagatie resulteert in betrouwbare scheurpaden. De verschillen tussen de resultaten verkregen met de elementvrije Galerkin methode en die verkregen met een combinatie van deze methode met de eindige elementen methode, zijn relatief klein.

Er wordt geconcludeerd dat de elementvrije Galerkin methode een doeltreffende numerieke methode is voor elastostatische problemen. Door het nieuw ontwikkelde wig-model is de methode ook toepasbaar op scheurproblemen. Combinaties van de methode met de eindige elementen methode zijn mogelijk, zodat een reductie van rekentijd verkregen kan worden. Ondanks de rekeninspanning, blijken de geformuleerde numerieke modellen uitermate geschikt voor het simuleren van scheurpropagatie.

Summary

For the simulation of crack propagation in brittle materials, the finite element method is often applied. This method uses a division of the material domain into so-called elements. Relevant quantities in the domain, such as displacements and stresses, are approximated per element. A division into elements is given by a set of nodal points which are mutually connected to form the elements. Since crack propagation concerns the growth of crack surfaces, the element division, and therefore the connectivity of nodal points, has to be adapted continuously during simulation. This adaptation of the element mesh is known as remeshing and can make simulation of crack propagation rather complicated and time-consuming.

The element-free Galerkin method is a method which also uses nodal points, but where the use of a connectivity is absent. Displacements and stresses in the material domain are approximated by means of a connectivity-free technique known as moving least squares approximation. This technique requires, besides the nodal data, a set of weight functions and a set of basis functions. Since the growth of crack surfaces can be reflected without changing a connectivity of nodes, it is possible to simulate crack propagation without remeshing. The aim of the research presented in this thesis is the formulation of a numerical model based on the element-free Galerkin method, which is convenient for the simulation of crack propagation in brittle materials.

The numerical model assumes linear elastic material behaviour and uses criteria for crack growth and the direction of crack growth in brittle materials. These criteria arise from the field of fracture mechanics, and are expressed in terms of stress intensity factors. By means of the element-free Galerkin method, approximate values for the displacements and the stresses are calculated in a material domain containing a crack. To this end, the unknown displacements of the nodal points have to be obtained. Therefore, a numerical integration scheme is used, based on a background configuration of integration cells. This configuration can be chosen independently of the distribution of nodal points and does not have to be adapted during simulation of crack propagation. The scheme accounts for the density of the nodal distribution, for the stress singularities, and for the discontinuities of quantities over the crack. Concerning the moving least squares technique, several models are considered to account for the discontinuity in the material domain due to the presence of a crack. This results in a new so-called wedge model which is applied to the weight functions, and the use of special basis functions for the representation of stress singularities. From the calculated displacements and stresses in the material domain, the stress intensity factors are determined, which are subsequently applied in the fracture criteria.

A drawback of the element-free Galerkin method is its computational effort. For a reduction of computing time, three combinations of this method with the finite element method are investigated such that the growth of crack surfaces can still be reflected without remeshing. The effectiveness of the developed numerical models is demonstrated in several typical fracture mechanics problems in two dimensions. Results for static problems reveal that accurate stress intensity factors are computed. For the problem of quasi-static crack propagation in a single-edge notched beam loaded under shear conditions, crack paths are obtained which are in good agreement with experimental results reported in the literature. This shows, together with other numerical results, that simulation of quasi-static crack propagation results in reliable

crack paths. The differences between the results obtained by the element-free Galerkin method and those obtained by a combination of this method with the finite element method are only minor.

It is concluded that the element-free Galerkin method is an effective numerical method for elasto-static problems. Due to the new developed wedge model, the method is also applicable to problems involving cracks. Combinations of the method with the finite element method are possible, such that a reduction of computing time can be obtained. Despite the computational effort, the formulated numerical models appear to be very useful for the simulation of crack propagation.

Contents

Chapter 1

Introduction

This thesis deals with the simulation of crack propagation in brittle materials. A widely used numerical method for solving such mechanical problems is the finite element method. In the past decades, many applications of this method to crack propagation problems have been reported. The method is based on a division of the material into subdomains, so-called finite elements. Such a division is given by a set of nodal points which are connected in a certain way to form the elements. Since crack propagation concerns the growth of an internal free boundary, changing the element division for the material domain and, therefore, changing the connectivity of the nodes is necessary to simulate this crack propagation. The adaptation of the element mesh, which is also known as remeshing, can make the simulation of crack propagation by the finite element method rather complicated and time-consuming.

A few years ago, a numerical method known as the element-free Galerkin method has been introduced, which has many similarities with the finite element method. The element-free Galerkin method, however, is free from any connectivity of nodal points and it is because of this feature that the terminology "element-free" is used. Hence, the method is attractive for the simulation of crack propagation, since the formation of new crack surfaces can be reflected without changing any connectivity of nodes. Up to now, several applications of the method to crack propagation problems have been reported. However, some problems are still unsolved. Therefore, in this thesis a study of the method and its application to the simulation of quasi-static crack propagation in brittle materials is presented.

1.1 Numerical analysis of failure

Two different methodologies for failure of materials can be distinguished, namely, fracture mechanics and continuum damage mechanics. In fracture mechanics, a crack is assumed to be present in the material. Such a crack introduces a discontinuity in the material and, in the case of linearly elastic material behaviour, the stresses become infinite at the crack tip. This singularity in the stresses is proportional to the inverse square root of the distance to the crack tip. This relationship is illustrated in Figure 1.1 and can be expressed in the simplified form

$$\sigma = \frac{K}{\sqrt{2\pi r}},$$

(1.1)
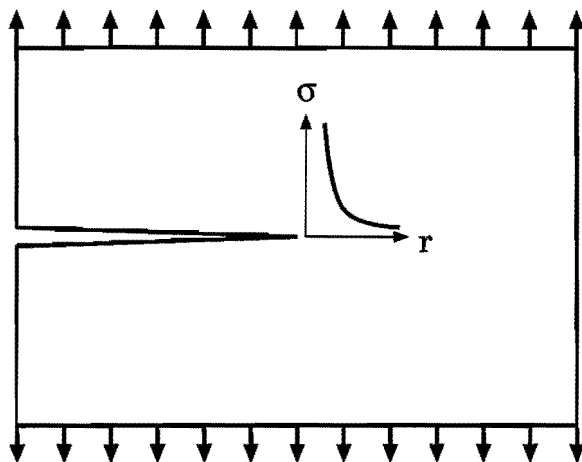
Figure 1.1: *Singularity in stresses.*

where σ represents the stress, r is the distance to the crack tip, and K is a normalizing factor known as the stress intensity factor. This factor is related to the geometry of the material, the applied forces, and the boundary conditions.

Equation (1.1) shows that the yield stress will be exceeded at positions sufficiently close to the crack tip, resulting in plastic deformation of the material. For brittle fracture there is only a small zone of plastic deformation near the crack tip (small-scale yielding, see Rice [60]). In this case, plasticity in the vicinity of the crack tip is neglected and equation (1.1) is assumed to be valid in a close neighbourhood of the crack tip. For ductile fracture this plastic material behaviour is essential and cannot be neglected.

In order to predict the behaviour of cracked material, criteria for crack growth and for the direction of crack growth have to be postulated, see Broek [13], Cherepanov [17] or Kanninen and Popelar [37]. A common criterion for brittle materials states that crack growth occurs when the stress intensity factor reaches a critical value. This value is a material constant and is known as the fracture toughness. When K is below the critical value, the crack remains stationary. The field of fracture mechanics is considered in more detail in the next chapter.

Continuum damage mechanics does not assume a discontinuity in the material. Defects such as microcracks and the growth of these defects are accounted for in a continuous, smeared way by means of so-called damage variables. These variables can be seen as internal variables representing the state of the material. A part of the material containing defects is therefore represented by a small zone with high values for the damage variables, resulting in a degradation of the material properties, see Figure 1.2. Such an approach generally works well for materials where the damage is smeared out over larger areas, such as in the case of ductile material behaviour. It is believed, however, that one can also obtain reliable results for brittle material behaviour. Reduction of the material stiffness is often characterized by a constitutive stress-strain relation of the form

$$\sigma = E_d \epsilon, \tag{1.2}$$
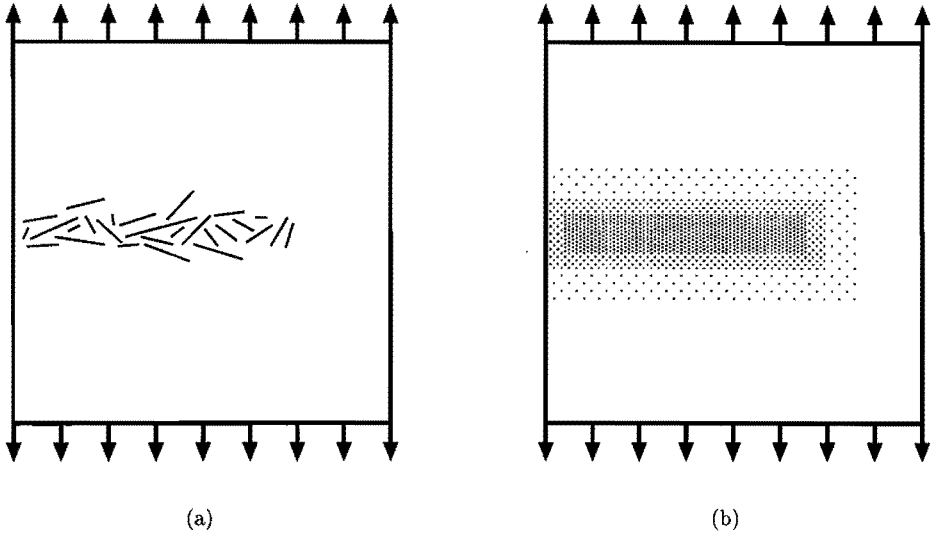
Figure 1.2: (a) *Microcracks modelled by* (b) *degradation of material properties in the dark-shaded areas.*

where σ and ϵ are the stress and the strain, respectively, and $E_d = (1 - \mathcal{D})E$, with E the Young's modulus of the original undamaged material. The parameter $\mathcal{D}$ is a damage variable.

In continuum damage mechanics, no criteria for the direction of crack growth have to be postulated as is the case in fracture mechanics. However, a criterion is necessary to specify the evolution of the damage variable $\mathcal{D}$. An increase of $\mathcal{D}$ is mostly given by a so-called evolution law in terms of the stresses, the strains, and the actual damage. For example, one can take the equation for creep damage

$$\dot{\mathcal{D}} = \eta \sigma^{\eta_1} (1 - \mathcal{D})^{\eta_2}, \tag{1.3}$$

as suggested by Chaboche [15]. The constants η, η_1 and η_2 in (1.3) are material dependent and have to be determined experimentally.

The constitutive relation (1.2) can be generalized to two and three dimensions. For materials exhibiting anisotropic damage behaviour it is necessary to introduce additional damage variables, which means that $\mathcal{D}$ is extended to a damage vector, e.g. see Murakami [55]. With the equations (1.2) and (1.3) the mathematical formulation of a problem in continuum damage mechanics is complete. However, the interpretation and the choice of the damage variables $\mathcal{D}$, the constitutive equations, and the evolution of $\mathcal{D}$ may change with the type of problem. For a complete description of the field of continuum damage mechanics, we refer to Chaboche [14, 15] and Lemaitre [46].

In the past decades, the finite element method has shown to be a powerful and efficient numerical method for solving mechanical problems involving non-linear constitutive material behaviour and/or large deformations, see Hughes [33], Johnson [36] or Zienkiewicz [75]. This method is

(a)   (b)
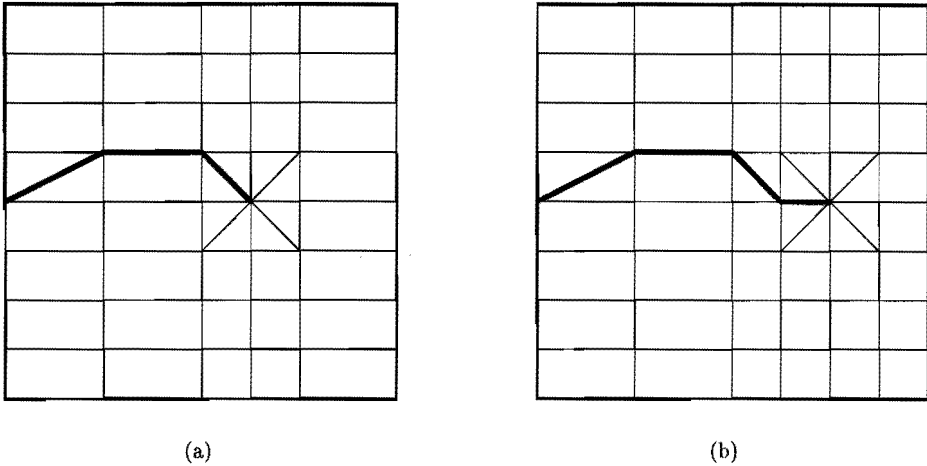
Figure 1.3: *Remeshing: Finite element division* (a) *before and* (b) *after crack propagation step. Crack path is indicated by a thick solid line.*

based on a weak form of the governing equations, in which the displacements are mostly taken piecewise linear or piecewise quadratic. Therefore, the material is divided into subdomains, so-called finite elements, see Figure 1.3. This division is given by the connection of a set of nodal points. The displacements are interpolated linearly or quadratically within an element, which leads to a sparse system of linear equations for the unknown displacements of the nodes. A result of the interpolation of the displacements is that the stresses are constant or linear in the element. For the application of the finite element method to the field of fracture mechanics, however, special crack-tip elements have to be used to describe the singular stresses (1.1) in a correct way, see Barsoum [3] or Stern and Becker [66, 67]. In [3] the singular stress behaviour is obtained by moving mid-side nodes of a quadratic element to a quarter-point position. This behaviour is obtained in [66, 67] by interpolation of the displacements with the help of special shape functions based on the square root function.

The field of fracture mechanics has been studied extensively in the past decades, which has resulted in a wide range of application and a high degree of accuracy of the developed approaches. However, when the finite element method is applied to fracture mechanics in order to simulate crack propagation, a main drawback is encountered. To reflect the formation of new crack surfaces, the mesh of elements has to be adapted after each crack propagation step. This remeshing of the element division is illustrated in Figure 1.3. In addition, the crack-tip elements have to be shifted to the new position of the crack tip and quantities such as strains and stresses, which are generally discontinuous over element boundaries, have to be projected from the old to the new element division. For complicated crack paths, this process of continuous remeshing, including projection of quantities and new assembly, concerns a large number of elements and can therefore be very time-consuming.

Application of the finite element method to the field of continuum damage mechanics does not suffer from remeshing problems, since no physical crack is assumed to exist in the material.
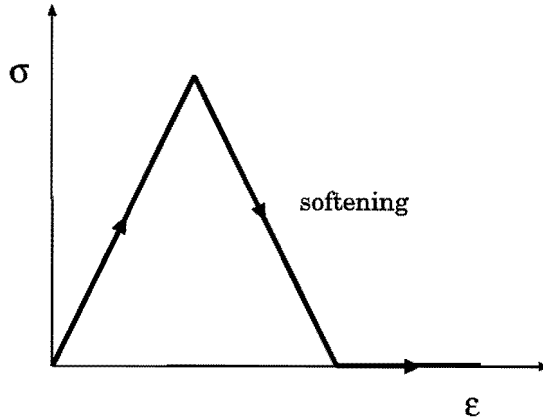
Figure 1.4: *Softening behaviour.*

Other problems, however, may occur. The evolution of the damage, e.g. see (1.3), can be chosen more or less arbitrary as long as the global material response is acceptable. Severe material degradation, as in the case of brittle fracture, can lead to softening behaviour. This means that the stress decreases with increasing strain, see Figure 1.4. As a result, the mathematical formulation of the problem becomes ill-posed. Application of the finite element method then results in irrelevant solutions and often shows a mesh dependency of the solution concerning both the width and the orientation of the elements, see Lasry and Belytschko [45] or Sluys [65, Ch. 3]. In general, a refinement of the element division leads to higher values of the damage in a region of smaller width. Furthermore, a change in the orientation of the finite element division mostly leads to a different direction of the damaged region. In many situations, damage is concentrated on very small parts of the material, which has the consequence that this localized deformation cannot be captured easily without a very fine element division.

For the above problems in the application of the finite element method to fracture mechanics and to continuum damage mechanics, a large number of solutions has been suggested in the literature. Only a few of these solutions are summarized here. In order to capture localized deformation in a correct way, Belytschko, Fish and Engelmann [4], Fish and Belytschko [24], and Hegen [29], consider finite element techniques where the strains can become discontinuous over a zone in an element. In [45] and [65, Chs. 4-7], the ill-posedness of the formulation is avoided by addition of higher-order terms in the governing equations. Xu and Needleman [74] circumvent the problem of remeshing in the case of fracture mechanics problems by restricting the direction of crack propagation to be along element boundaries. In Horsten and Van Vroonhoven [32] and Van Vroonhoven [72, Ch. 8], a hybrid fracture/damage approach is introduced. By a convenient combination of concepts of fracture mechanics and continuum damage mechanics, problems of remeshing are diminished. Furthermore, mesh dependency of the solution is absent in this approach.

In the past two decades, a new numerical method has been developed for application to fracture mechanics in order to simulate crack propagation: the boundary element method, see Brebbia and Dominguez [12] or Chen and Zhou [16]. The method is attractive, since, in contrast to the

finite element method, only the boundary of the material and the crack surfaces are discretized. Therefore, a significant part of the remeshing associated with the finite element method is avoided. In the boundary element method, the governing equations are transformed into boundary integral equations. To this end, a so-called fundamental solution (Green's function) of the problem equations has to be available. Hence, the method is limited to the class of isotropic, linearly elastic materials. The boundary integral equations are solved by means of an element division of the boundary and of the crack surfaces. In contrast to the finite element method, this leads to a non-sparse system of equations for the unknown displacements of the nodes. In the case of application of the boundary element method to fracture mechanics, substantial difficulties need to be overcome. In order to avoid the system of equations to be ill-conditioned, special techniques are necessary to formulate the equations concerning the crack surfaces. Furthermore, as in the finite element method, special elements have to be used near the crack tip. For more details and examples of the application of the boundary element method to fracture mechanics, we refer to the work of Mi [52].

1.2   Element-free analysis of fracture

Recently, a new numerical method known as the element-free Galerkin method has been developed for solving mechanical problems. The method approximates displacements by using a set of nodal points. However, a connectivity of nodal points is not used which explains the terminology "element-free". Because of this, the method is very attractive for application to fracture mechanics problems, since the formation of new crack surfaces can be reflected without remeshing, or equivalently, without changing any connectivity of nodal points. It is only necessary to place some nodal points around the newly created crack surfaces as is shown in Figure 1.5. Since the displacements in the element-free Galerkin method are generally continuously differentiable, the strains and the stresses are continuous. Hence, in the case of crack propagation problems, projection of strains and stresses from the old to the new discretization for the method is straightforward.

Similar to the finite element method, the element-free Galerkin method uses a weak form of the governing equations. Continuously differentiable representations for the displacements are used, which are obtained with the help of a technique known as moving least squares approximation, see Lancaster and Šalkauskas [43, 44]. For this technique, a set of nodal points and some nodal data have to be specified, as well as a set of so-called basis functions. The displacements are then given by a linear combination of the basis functions, which coefficients vary from point to point and are found by solving a set of linear equations. As for the finite element method, this approach leads to a sparse system of linear equations for the unknown displacements of the nodes. The discrete equations are obtained by means of numerical integration with the help of a background configuration of so-called integration cells.

The first work on the element-free Galerkin method has been presented by Nayroles, Touzot and Villon [56]. Their method is named "diffuse elements", since it is presented as a generalization of the finite element method. The current form of the element-free Galerkin method, however, is first described by Belytschko et al. [7, 48]. In their papers the ideas presented in [56] are worked out to a more general form. Furthermore, it is recognized in [7, 48] that the method can
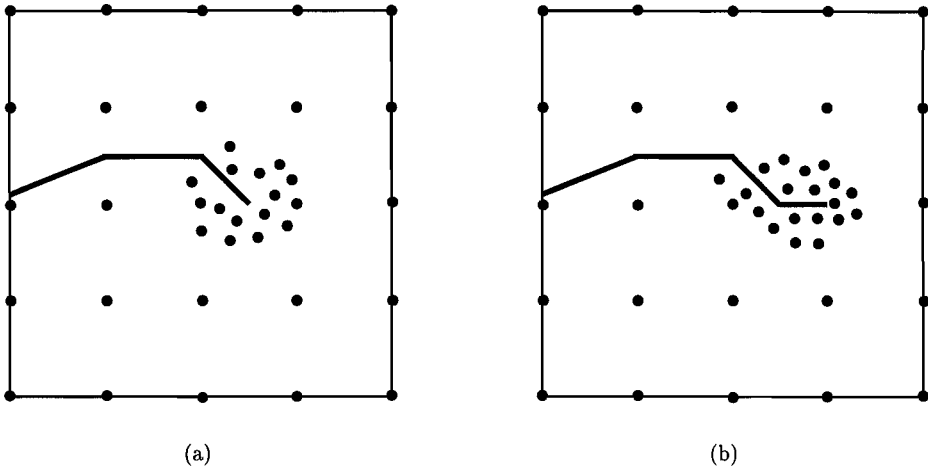
Figure 1.5: *Element-free set-up* (a) *before and* (b) *after crack propagation step. Crack path is indicated by a thick solid line.*

be an effective means for solving problems in fracture mechanics. A large amount of work on the application of the element-free Galerkin method to static and dynamic fracture problems has already been presented, see Belytschko et al. [5]-[11], [25], [48], [49] and [58]. Due to the fact that firstly the displacements are continuously differentiable and secondly the method is able to represent the specified set of basis functions exactly, the method is also attractive for application to other areas than fracture mechanics. For instance, Krysl and Belytschko [41, 42] describe analyses of thin plates by using the element-free Galerkin method.

Despite the work on the application of the element-free Galerkin method to fracture mechanics so far, there are still problems associated with the method. One of the main problems is that the application of moving least squares approximation near a crack is not straightforward and can lead to inaccurate approximations of displacements and stresses near the crack tip. In addition, special basis functions have to be used for the approximation technique in order to describe the singular stresses (1.1) correctly. A second problem concerns numerical integration. The background configuration of integration cells is chosen independently of the nodal points. Nevertheless, it has to account in a certain way for the density of the nodes in the neighbourhood of each cell, in order to obtain a certain degree of accuracy. Furthermore, there is the problem of integration of discontinuous quantities, when a part of a crack is in the interior of an integration cell.

In addition to the problems mentioned above, the method shows some drawbacks concerning computational effort. Moving least squares approximation requires that at each point under consideration a linear set of equations has to be solved to obtain the displacements. This causes the element-free Galerkin method to be computationally expensive in comparison with the finite element method. Moreover, the displacements are not piecewise linear or piecewise quadratic, which implies that numerical integration requires a large amount of integration points.

Several solutions to the above problems have already been proposed in [5]-[11], [25], [48], [49]

and [58]. A reduction of the computational costs of the method is obtained by coupling the method with the finite element method. An efficient scheme for numerical integration has been proposed based on a background configuration of integration cells. This scheme, however, does not account for the integration of discontinuous quantities within a cell. Furthermore, the scheme only partially accounts for the density of the nodal points, since the order of integration depends on the number of nodes in a cell. Several attempts have been made to apply the moving least squares technique near a crack path in a correct way. These efforts, however, lead to shape functions which are discontinuous in the material or to nodal points on one crack surface affecting the displacements on the opposite surface. Special basis functions obtained from the asymptotic expressions for the displacements are used in the moving least squares technique, in order to describe the singular stresses (1.1) correctly.

The main goal of the research presented in this thesis is the development of the element-free Galerkin method to a robust and accurate method for application to fracture mechanics problems. We shall restrict ourselves to the simulation of 2D quasi-static crack propagation in brittle materials. A secondary goal of the research concerns the development of a combination of the element-free Galerkin method with the finite element method, such that a reduction of computational costs can be obtained.

For the development of the element-free Galerkin method, solutions are presented to the problems mentioned above. Concerning moving least squares approximation, several ways are considered to apply this technique near a crack. For a correct representation of the singular stresses (1.1), the set of basis functions is extended with an extra basis function which behaves like the square root function near the crack tip. A numerical integration scheme based on a background configuration of integration cells is used. To account for the presence of a crack, cells can be divided into subcells matching the crack, such that quantities which are discontinuous over the crack are integrated correctly. Numerical integration within a cell is based on the number of nodes which contribute to the displacements in the cell and on the size of the cell. This yields that a change in the number of cells leads to small changes in the solution. Furthermore, in the case of the use of a basis function which behaves like the square root function near the crack tip, the scheme automatically accounts for efficient and accurate integration of the singular derivatives of the function. Three different ways for combining the element-free Galerkin method and the finite element method are studied. It turns out that a combination by means of interface elements, see Belytschko, Organ, Krongauz [10], has to be preferred.

Some characteristics and the performance of the developed methods are investigated by application of the methods to several typical fracture mechanics problems. These problems concern both static problems and crack propagation problems. The results of the applications show that the element-free Galerkin method and a combination of the method with the finite element method are effective means for numerical analysis of crack propagation.

1.3 Overview of the thesis

The thesis is organized as follows. Chapter 2 deals with fracture mechanics and the finite element method. The basic equations are given for linearly elastic material behaviour, which is

followed by a review of concepts of fracture mechanics. Stress intensity factors are introduced and criteria are considered for crack growth and the direction of crack growth in brittle materials. The chapter ends with a short presentation of the finite element method and its application to fracture mechanics problems.

Chapter 3 studies approximation techniques which are free from a connectivity of nodal points. The main part of the chapter is devoted to moving least squares approximation. First, the theory of this technique is described. Next, several ways are considered for the application of the moving least squares technique near a crack path. This leads to the use of the so-called wedge model for the description of the crack, and to the addition of special functions to the set of basis functions for the description of the singular stresses. Finally, other approximation techniques are reviewed for application in an element-free numerical solution method.

Next, in Chapter 4, the description of the element-free Galerkin method can be found. The discrete equations obtained by means of application of moving least squares approximation are given. This is followed by the numerical integration scheme for computation of the discrete equations. The determination of integration points for a cell, the integration of discontinuous quantities within a cell, and the integration near a crack tip in the case of the use of special basis functions are considered in detail. Essential features, such as the performance and the convergence of the method, are studied for several two-dimensional elasto-static problems. The chapter ends with a description of the computation of fracture mechanics parameters from fracture analyses.

Three possible ways to combine the element-free Galerkin method with the finite element method are considered in Chapter 5. First, a description is given of the three combinations, which is followed by a comparison of these combinations for two-dimensional elasto-static problems. As in Chapter 4 for the element-free Galerkin method, the convergence aspects of the combinations are studied.

In Chapter 6 results of the applications to fracture mechanics problems are given for both the element-free Galerkin method and a combination of the method with the finite element method. The ability of the numerical models to compute accurate stress intensity factors is studied. Moreover, the models are applied to the simulation of brittle crack propagation in two dimensions. Conclusions about the results and a comparison of the two approaches are presented at the end of the chapter.

The thesis ends with a chapter serving as a concluding discussion. A review is given of the methods and the applications to fracture mechanics problems. Furthermore, conclusions and open ends of the presented study, and recommendations for further research can be found in this chapter.

Chapter 2

Fracture mechanics and finite element method

This chapter deals with the field of study known as fracture mechanics, which concerns failure of materials. Furthermore, the finite element method and its application to failure problems is considered. The chapter starts with the introduction of the basic equations for the deformation of linearly elastic media. This is followed by the main concepts of fracture mechanics. The chapter ends with a description of the finite element method and the use of the method in fracture mechanics problems.

2.1 Deformation of linearly elastic media

In this section the problem of deformation of linearly elastic media is considered. The general problem for a three-dimensional, homogeneous, isotropic, medium is given. This is followed by two common situations in which the dimension of the problem is reduced by one. Finally, weak formulations of the problem of deformation are introduced.

2.1.1 Equations of linear elasticity

Consider the deformation of a homogeneous, isotropic, linearly elastic medium $\mathcal{B}$ under applied forces and prescribed displacements. In general, such a problem concerns 21 quantities: components u_i of the displacement vector $\mathbf{u}$, entries ϵ_{ij} of the symmetric Green Lagrange strain tensor ϵ, and entries σ_{ij} of the symmetric Cauchy stress tensor σ with indices $i, j = 1, 2, 3$. These quantities are taken with respect to a fixed orthonormal basis $\{\mathbf{e}_1, \mathbf{e}_2, \mathbf{e}_3\}$ of three-dimensional space and depend on the three spatial coordinates x_1, x_2, x_3 and on the time t. Small strains ϵ_{ij} and small rotations are assumed. Hence, for x_1, x_2 and x_3 one can take the Cartesian coordinates in the undeformed configuration Ω of the elastic medium $\mathcal{B}$.

The material behaviour of the elastic medium is characterized by two material constants, namely Young's modulus of elasticity E and Poisson's contraction ratio ν. Another frequently used material constant is the shear modulus $G = E/2(1+\nu)$. The density of the material is given by ρ. Let the medium be subject to volume forces f_i^* in Ω and subject to prescribed tractions p_i^*

and prescribed displacements u_i^* on the boundary $\partial\Omega$, $i = 1, 2, 3$. The problem of deformation of the elastic medium is described by kinematic relations, constitutive equations, equations of motion and a set of boundary conditions. This dynamic problem is given by:

Determine displacements u_i, strains ϵ_{ij}, and stresses σ_{ij}, $i, j = 1, 2, 3$, as sufficiently smooth functions of the spatial coordinates x_1, x_2, x_3 and the time t, such that the following equations are satisfied:

$$\epsilon_{ij} = \frac{1}{2}\left(u_{i,j} + u_{j,i}\right), \tag{2.1}$$

$$\sigma_{ij} = \frac{E}{1+\nu}\left(\epsilon_{ij} + \frac{\nu}{1-2\nu}\epsilon_{kk}\delta_{ij}\right), \tag{2.2}$$

$$\sigma_{ij,j} + f_i^* = \rho\ddot{u}_i, \tag{2.3}$$

in the domain Ω, $i, j = 1, 2, 3$, as well as the boundary conditions

$$\sigma_{ij}n_j = p_i^* \text{ on } \Gamma_{p_i}, \tag{2.4}$$

$$u_i = u_i^* \text{ on } \Gamma_{u_i}, \tag{2.5}$$

on the boundary $\partial\Omega = \Gamma_{p_i} \cup \Gamma_{u_i}$ with Γ_{p_i} and Γ_{u_i} disjoint, $i = 1, 2, 3$.

Differentiation with respect to the coordinate x_j is denoted by $_{,j}$ and a superposed dot is used for differentiation with respect to the time t. The entries of the outward unit normal on the boundary $\partial\Omega$ are given by n_i, $i = 1, 2, 3$, and δ_{ij} is Kronecker's symbol ($\delta_{ij} = 1$ when $i = j$, $\delta_{ij} = 0$ when $i \neq j$). In equations (2.2)-(2.4) and in the remaining part of the thesis, the Einstein convention of summation over repeated indices is employed.

For the static problem, the right-hand side of the equations of motion (2.3) is set equal to zero, yielding the equilibrium equations. For the dynamic problem, additional initial conditions for the displacements u_i and their time derivatives $\dot{u}_i$ have to be given.

The material behaviour of a homogeneous, isotropic, linearly elastic medium is expressed by the constitutive equations (2.2), which are known as Hooke's law. These equations are a special case of the constitutive equations for a (non-isotropic) linearly elastic medium

$$\sigma_{ij} = \chi_{ijkl}\,\epsilon_{kl}, \quad i, j = 1, 2, 3, \tag{2.6}$$

where the fourth-order tensor χ is positive definite and left, right and fully symmetric. When the medium is not homogeneous, the tensor χ depends on the position **x**.

2.1.2   Planar problems

There are two common situations in which the dimension of the problem of deformation of an elastic medium can be reduced by one. These two situations are known as plane strain and plane stress.

A situation of plane strain is characterized by the fact that the displacement and the strains in the x_3-direction are zero, i.e., $u_3 = 0$ and $\epsilon_{i3} = 0$, $i = 1, 2, 3$. Hence, the deformation only

takes place in the (x_1, x_2)-plane and this deformation is independent of the coordinate x_3. For instance, a situation of plane strain can be assumed for a medium for which displacement in the x_3-direction is not possible. Because of (2.2), the zero strains imply that the shear stresses σ_{13} and σ_{23} are zero, while the normal stress σ_{33} is given by

$$\sigma_{33} = \nu(\sigma_{11} + \sigma_{22}). \tag{2.7}$$

The problem of deformation in the case of plane strain is also given by equations (2.1)-(2.5). All the quantities, however, are independent of the coordinate x_3, while the indices are restricted to $1, 2$. Since the deformation is independent of x_3 and only takes place in the (x_1, x_2)-plane, the undeformed configuration Ω of the medium can be taken as two-dimensional.

The situation of plane stress is characterized by zero stresses in the x_3-direction, i.e. $\sigma_{i3} = 0$, $i = 1, 2, 3$. For example, a situation of plane stress can be assumed for a medium which is thin in the x_3-direction compared to its dimensions in the (x_1, x_2)-plane, subject to in-plane volume forces, i.e. $f_3^* = 0$. In practice, for such a medium the stresses in the x_3-direction only vanish after averaging over the thickness. As a consequence, the deformation is then independent of the coordinate x_3. This situation is often referred to as generalized plane stress. When $\sigma_{i3} = 0$, $i = 1, 2, 3$, the constitutive equations (2.2) yield that the shear strains ϵ_{13} and ϵ_{23} are zero, while ϵ_{33} is given by

$$\epsilon_{33} = -\frac{\nu}{1-\nu}(\epsilon_{11} + \epsilon_{22}). \tag{2.8}$$

The problem of deformation of an elastic medium in a situation of plane stress is given by (2.1)-(2.5), where all the quantities are independent of the coordinate x_3, the indices are restricted to $1, 2$ and Ω can be taken as two-dimensional. Because of (2.8), equation (2.2) has to be replaced by

$$\sigma_{ij} = \frac{E}{1+\nu}\left(\epsilon_{ij} + \frac{\nu}{1-\nu}\epsilon_{kk}\delta_{ij}\right), \tag{2.9}$$

where $i, j = 1, 2$ and k sums only over $1, 2$.

There is a correspondence between the problems of plane strain and plane stress. A problem of plane stress with $E = E_1/(1-\nu_1^2)$ and $\nu = \nu_1/(1-\nu_1)$ is equivalent to a problem of plane strain with Young's modulus E_1 and Poisson's ratio ν_1.

2.1.3 Weak forms of the problem of deformation

In general, the problem of deformation of an elastic medium, as given by the boundary value problem (2.1)-(2.5), cannot be solved exactly. Numerical methods are necessary to provide accurate approximations for the displacements, strains and stresses in the medium. The numerical methods discussed in this thesis use weak forms of the (strong) deformation problem (2.1)-(2.5). Some of these weak forms are given in this section. For a more detailed description, see Washizu [73, Chs. 1, 2].

For the introduction of weak forms of the deformation problem, we restrict ourselves to the static problem, i.e. $\rho\ddot{\mathbf{u}} = 0$. For simplicity of the presentation, it is assumed that $\Gamma_{u_i} = \Gamma_u$ and $\Gamma_{p_i} = \Gamma_p$, $i = 1, 2, 3$. Upon multiplication of the static version of (2.3) with a test displacement $\delta\mathbf{u}$ and integration over the undeformed configuration Ω, one obtains

$$\int_\Omega \delta u_i\, \sigma_{ij,j}\, d\Omega + \int_\Omega \delta u_i\, f_i^*\, d\Omega = 0, \tag{2.10}$$

where σ is related to $\mathbf{u}$ by means of (2.1) and (2.2). Note that (2.10) is valid for each test displacement $\delta\mathbf{u}$ for which the integrals in this equation exist. When $\delta\mathbf{u}$ is continuously differentiable on Ω and $\delta\mathbf{u} = \mathbf{0}$ on Γ_u, relation (2.10) can be rewritten. After partial integration of the first term in (2.10), one obtains with (2.4) and the integration theorem of Gauss

$$\int_\Omega \delta u_{(i,j)}\, \sigma_{ij}\, d\Omega - \int_\Omega \delta u_i\, f_i^*\, d\Omega - \int_{\Gamma_p} \delta u_i\, p_i^*\, d\Gamma = 0. \tag{2.11}$$

Here, $\delta u_{(i,j)}$ is the symmetric part of the gradient $\delta u_{i,j}$ and is given by

$$\delta u_{(i,j)} = \frac{1}{2}\left(\delta u_{i,j} + \delta u_{j,i}\right), \quad i, j = 1, 2, 3. \tag{2.12}$$

Equation (2.11) must be satisfied for all differentiable $\delta\mathbf{u}$ with $\delta\mathbf{u} = \mathbf{0}$ on Γ_u. For $\delta\mathbf{u}, \mathbf{u} \in (H^1(\Omega))^3$, however, expression (2.11) still has a meaning. Here, $H^1(\Omega)$ is the Sobolev space of order one. This space is defined by

$$H^1(\Omega) = \left\{ f \in L^2(\Omega) \,\middle|\, f_{,i} \in L^2(\Omega),\, i = 1, 2, 3 \right\}, \tag{2.13}$$

where $L^2(\Omega)$ is the set of square integrable functions, i.e.

$$L^2(\Omega) = \left\{ f \,\middle|\, \int_\Omega f(\mathbf{x})^2\, d\Omega < +\infty \right\}. \tag{2.14}$$

This space is also denoted by $H^0(\Omega)$. For more details about Sobolev spaces, see Ciarlet [18, Ch. 1]. As weak form of the deformation problem for a homogeneous, isotropic, linearly elastic medium we formulate:

Determine displacements $u_i \in H^1(\Omega)$, strains $\epsilon_{ij} \in H^0(\Omega)$, and stresses $\sigma_{ij} \in H^0(\Omega)$, $i, j = 1, 2, 3$, such that (2.1), (2.2) and (2.5) are satisfied, and (2.11) holds true for all $\delta u_i \in H^1(\Omega)$ with $\delta u_i = 0$ on Γ_u, $i = 1, 2, 3$.

From the derivation of (2.11), it is clear that the solution of the (strong) deformation problem (2.1)-(2.5) also satisfies this weak form. The weak form can be seen as a necessary condition for the solution of a minimization problem. Let the functional τ be defined for $u_i \in H^1(\Omega)$, $i = 1, 2, 3$, by

$$\tau(\mathbf{u}) = \frac{1}{2}\int_\Omega \sigma_{ij}\epsilon_{ij}\, d\Omega - \int_\Omega u_i f_i^*\, d\Omega - \int_{\Gamma_p} u_i p_i^*\, d\Gamma, \tag{2.15}$$

where ϵ and σ are related to $\mathbf{u}$ by (2.1) and (2.2). The functional τ is interpreted as the potential energy of the medium. The first term represents its internal elastic energy, while the second and third term represent the work of the external forces.

Among all displacements which satisfy the essential boundary conditions (2.5), τ is minimal for the solution $\mathbf{u}$ of the static deformation problem for the elastic medium, see Johnson [36, Chs. 1, 2]. As a consequence,

$$\frac{d}{d\varepsilon}\left[\tau(\mathbf{u} + \varepsilon\,\delta\mathbf{u})\right]_{\varepsilon=0} = 0 \tag{2.16}$$

for all test displacements $\delta u_i \in H^1(\Omega)$ with $\delta u_i = 0$ on Γ_u, $i = 1, 2, 3$. This yields equation (2.11).

In the above weak formulation, the solution $\mathbf{u}$ of the weak form (2.11) is sought in a subspace of $(H^1(\Omega))^3$. In the numerical techniques that are discussed in this thesis, the solution of this weak form is approximated by restricting $\mathbf{u}$ and $\delta\mathbf{u}$ to be in a finite dimensional subspace. For some of these finite dimensional subspaces, one cannot always fulfil the essential boundary conditions $\mathbf{u} = \mathbf{u}^*$ on Γ_u exactly. Therefore, weak forms have to be used where the essential boundary conditions are taken into account in a different way. For example, consider a weak form where the essential boundary conditions are accounted for by means of extra terms coming from a Lagrange multiplier formulation of these conditions (see also Belytschko, Lu and Gu [7]):

Determine displacements $u_i \in H^1(\Omega)$, strains $\epsilon_{ij} \in H^0(\Omega)$, stresses $\sigma_{ij} \in H^0(\Omega)$, and Lagrange multipliers $\lambda_i \in H^0(\Gamma_u)$, $i, j = 1, 2, 3$, such that (2.1), (2.2) are valid, and such that

$$\int_\Omega \delta u_{(i,j)}\,\sigma_{ij}\,d\Omega - \int_\Omega \delta u_i\, f_i^*\,d\Omega - \int_{\Gamma_p} \delta u_i\, p_i^*\,d\Gamma$$
$$- \int_{\Gamma_u} \delta\lambda_i\,(u_i - u_i^*)\,d\Gamma - \int_{\Gamma_u} \delta u_i\,\lambda_i\,d\Gamma = 0 \tag{2.17}$$

for all $\delta u_i \in H^1(\Omega)$ and $\delta\lambda_i \in H^0(\Gamma_u)$, $i = 1, 2, 3$.

When Γ_u only consists of a set of discrete points $\{\mathbf{z}_a\}$, one has to replace $\boldsymbol{\lambda}$ by a finite set of Lagrange multipliers $\{\boldsymbol{\lambda}^a\}$. Moreover, the two integrals in (2.17) concerning $\delta\lambda_i$ and λ_i then have to be replaced by finite sums over the discrete points $\mathbf{z}_a$, see Hegen [30].

There are more weak forms of the deformation problem for an elastic medium where the essential boundary conditions $\mathbf{u} = \mathbf{u}^*$ on Γ_u are accounted for by means of extra terms as in a Lagrange multiplier formulation. For example, a weak form where the Lagrange multiplier $\boldsymbol{\lambda}$ is replaced by its physical meaning, the traction $\mathbf{t} = \sigma\mathbf{n}$ along Γ_u. Or, for example, a weak form where the essential boundary conditions are accounted for by means of a penalty term. For more details, see [30] and Lu, Belytschko and Gu [48].

2.2 Concepts of fracture mechanics

In this section the field of study is considered which concerns failure of materials and which is known as fracture mechanics. In fracture mechanics attention is focused on cracked material.

<table>
<tr><td>Mode I</td><td>Mode II</td><td>Mode III</td></tr>
<tr><td>opening mode</td><td>sliding mode</td><td>tearing mode</td></tr>
</table>
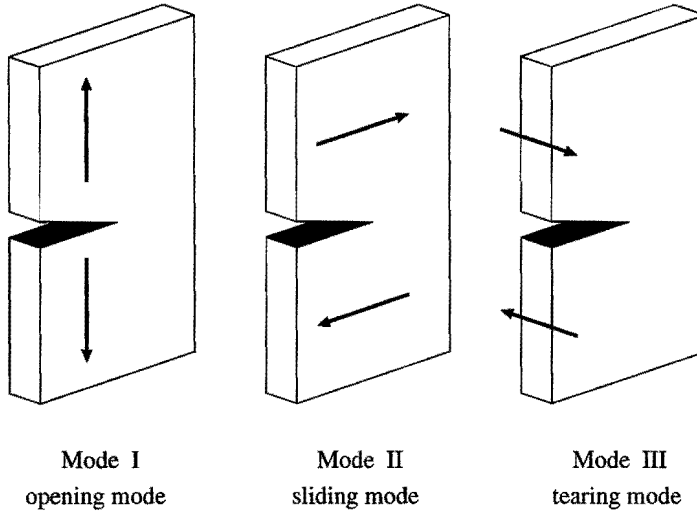
Figure 2.1: *Three fundamental modes for the loading of material with a crack.*

For the description of the behaviour of such material in a loading situation, criteria are necessary for crack growth and for the direction and speed of crack growth. Some of these criteria are considered.

2.2.1   Mechanics of crack growth

A crack is an internal boundary of the material, which makes the material discontinuous. For a crack one distinguishes between the crack flanks and the crack front. The crack flanks are the surfaces which make up this internal boundary. These flanks are connected by a line which is called the crack front. In two dimensions the crack flanks are lines and the crack front consists of a single point. In that case, one also speaks of the crack tip.

On the basis of energy dissipation, two types of fracture are distinguished: brittle fracture and ductile fracture, see Broek [13, Chs. 1, 2]. Ductile fracture is characterized by high energy dissipation due to plastic deformation and slip in the neighbourhood of the crack tip. This high energy dissipation is absent in brittle fracture. For this type of fracture, almost all the dissipated energy is due to the formation of new crack surfaces.

In this thesis we restrict ourselves to brittle materials and, therefore, only brittle fracture is considered. Fracture for brittle material behaviour is characterized by the occurrence of only a small area of plastic deformation around the crack tip (small-scale yielding, see Rice [60]). This is in contrast with ductile fracture, where mostly large areas of plasticity are observed. Therefore, homogeneous, isotropic, linearly elastic material behaviour is assumed for brittle materials and plasticity in the vicinity of the crack tip is neglected.

We distinguish between three fundamental modes for the loading of cracked material. These three modes differ in the orientation of the applied loads with respect to the crack flanks, see Figure 2.1. In the mode I loading situation, also known as the opening mode, the material is

loaded by tensile forces perpendicular to the crack flanks, while in the mode II loading situation, also known as the sliding mode, the material is loaded by shear forces which are parallel to the crack flanks and perpendicular to the crack front. Shear forces parallel to the crack front result in the mode III loading situation, which is also known as the tearing mode. A general situation of loading of cracked material consists of a superposition of these three fundamental modes. Since in this study one is only concerned with planar problems, problems with a mode III loading component will not be considered.

2.2.2 Planar deformation near a crack tip

Consider linearly elastic material which contains a crack. The material is loaded under planar conditions. The static problem is considered, i.e. $\rho \ddot{u}_i = 0$, $i = 1, 2, 3$. It is assumed that volume forces f_i^* are absent. We focus on the near-tip solution. Therefore, it is assumed that the crack is a semi-infinite line. The coordinate system $\{\mathbf{e}_1, \mathbf{e}_2\}$ is chosen such that the crack tip is the origin and $\mathbf{e}_1$ is parallel to the crack flanks with $\{x_1 \leq 0, \, x_2 = 0\}$ corresponding with the crack.

When the crack flanks are taken to be stress-free and when (anti-) symmetry conditions are applied to the displacement field, expressions can be derived for the displacements and the stresses for both mode I and mode II loading situations. This is described in several text books, see for instance [13, Ch. 3], Cherepanov [17, Ch. 3] or Kanninen and Popelar [37, Ch. 3]. Summation of these two solutions results in the solution for the displacements and the stresses for a mixed-mode planar loading situation. The stresses have the form

$$\sigma_{ij}(r, \theta) = \frac{K_I}{\sqrt{2\pi r}} f_{ij}^I(\theta) + \frac{K_{II}}{\sqrt{2\pi r}} f_{ij}^{II}(\theta) + \sigma_{ij}^0 + O(\sqrt{r}), \tag{2.18}$$

for $r \to 0$ and $i, j = 1, 2$. In equation (2.18), r and θ are the local polar coordinates such that $x_1 = r \cos \theta$ and $x_2 = r \sin \theta$, $r > 0$, $-\pi \leq \theta \leq \pi$, and σ_{ij}^0, $i, j = 1, 2$, are finite stresses at the crack tip. Since the crack surfaces are taken to be stress-free, the stresses σ_{12}^0 and σ_{22}^0 vanish, i.e. $\sigma_{12}^0 = \sigma_{22}^0 = 0$. Stress intensity factors K_I and K_{II} are introduced as normalizing constants for the symmetric and anti-symmetric parts of the stress field. These factors are the fracture parameters for the corresponding modes I and II. They are expressed in units $Nm^{-3/2}$ and are defined by

$$K_I = \lim_{r \to 0} \sqrt{2\pi r} \, \sigma_{22}(r, 0), \tag{2.19}$$

$$K_{II} = \lim_{r \to 0} \sqrt{2\pi r} \, \sigma_{12}(r, 0). \tag{2.20}$$

The dependence of the stresses on the polar angle θ is given by the functions f_{ij}^I and f_{ij}^{II}, $i, j = 1, 2$. Expressions for these functions are given in Appendix A.

The corresponding displacement field which is discontinuous over the crack, is given by

$$u_i = u_i^0 + \frac{K_I}{2G} \sqrt{\frac{r}{2\pi}} \, u_i^I(\theta) + \frac{K_{II}}{2G} \sqrt{\frac{r}{2\pi}} \, u_i^{II}(\theta) + O(r), \tag{2.21}$$

where u_i^0 are the displacements of the crack tip, $i = 1, 2$. The angular variation of the displacements in (2.21) is given by the functions u_i^I and u_i^{II}, $i = 1, 2$. These functions can also be found in Appendix A.

2.2.3 Fracture criteria

In this thesis we restrict ourselves to the growth of pre-existing cracks. It is assumed that crack initiation has occurred so that at least one crack is present in the material. The deformation of the cracked material is governed by the equations for the deformation of a linearly elastic material under planar conditions, e.g. see (2.1), (2.3)-(2.5) and (2.9). These equations, however, are not sufficient for the analysis of cracks. Fracture criteria for crack growth and for the crack growth direction have to be postulated, see [13, Ch. 1] or [17, Ch. 1].

Two different types of fracture criteria are distinguished: local and global criteria. Local criteria are based on the stress field in the neighbourhood of the crack tip. Global criteria are criteria based on an energy balance. For both types of fracture criteria, we discuss a fracture criterion for a mixed-mode loading situation. This fracture criterion can then be used to decide whether an existing crack will extend, and if so, in which direction.

First, consider a pure mode I loading situation. As follows from (2.18), the singular stresses in the neighbourhood of a crack tip are solely determined by the stress intensity factor K_I. It is postulated that crack growth will occur when K_I reaches the critical stress intensity factor K_{I_C}, i.e., when

$$K_I = K_{I_C}. \tag{2.22}$$

The factor K_{I_C} is a material parameter, the so-called mode I fracture toughness, and has to be determined experimentally. The direction of crack growth for this situation is trivial and is perpendicular on the direction of loading.

Next, consider a crack which is a semi-infinite line. Let the crack be loaded by a combination of modes I and II. It is assumed that $K_I > 0$. The critical stress and the direction of crack growth have to be determined. We discuss a criterion based on the maximum circumferential tensile stress, see [13, Ch. 14], [17, Ch. 4] or Erdogan and Sih [22]. When the stresses (2.18) are transformed into the local polar coordinate system (r, θ) around the crack tip, the circumferential tensile stress $\sigma_{\theta\theta}$ is given by

$$\begin{aligned}\sigma_{\theta\theta}(r, \theta) &= \sigma_{11}(r, \theta)\sin^2\theta + \sigma_{22}(r, \theta)\cos^2\theta - 2\sigma_{12}(r, \theta)\sin\theta\cos\theta \\ &= \frac{1}{\sqrt{2\pi r}}\left(K_I\cos^3(\tfrac{1}{2}\theta) - 3K_{II}\cos^2(\tfrac{1}{2}\theta)\sin(\tfrac{1}{2}\theta)\right).\end{aligned} \tag{2.23}$$

It is postulated that crack growth occurs in the direction θ_p where the circumferential stress is maximal and where it reaches the critical stress for a mode I loading situation, that is when

$$\frac{\partial\sigma_{\theta\theta}(r, \theta_p)}{\partial\theta} = 0, \tag{2.24}$$
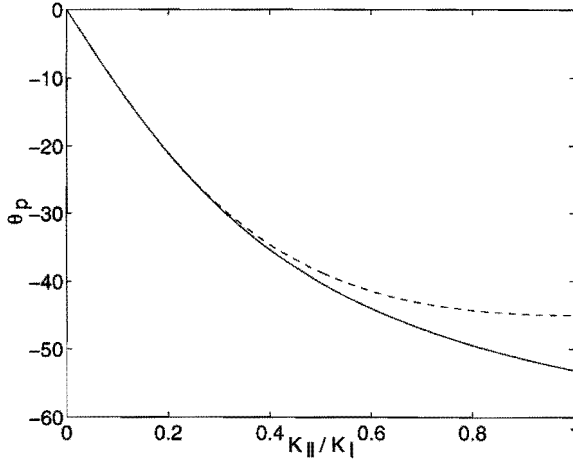
Figure 2.2: *Crack propagation angle θ_p in degrees for maximum circumferential stress criterion (——) and for the* **J***-vector (- - -).*

$$\frac{\partial^2 \sigma_{\theta\theta}(r, \theta_p)}{\partial \theta^2} \quad < \quad 0, \tag{2.25}$$

$$\sigma_{\theta\theta}(r, \theta_p) \quad = \quad \frac{K_{I_C}}{\sqrt{2\pi r}}. \tag{2.26}$$

The solution of the first two equations for θ_p is given by

$$\theta_p = 2 \arctan \left(\frac{K_I - \sqrt{K_I^2 + 8K_{II}^2}}{4K_{II}} \right). \tag{2.27}$$

Substitution of (2.27) into (2.26) results in the criterion for crack growth

$$\frac{4\sqrt{2} \, K_{II}^3 \left(K_I + 3\sqrt{K_I^2 + 8K_{II}^2} \right)}{\left(K_I^2 + 12K_{II}^2 - K_I\sqrt{K_I^2 + 8K_{II}^2} \right)^{3/2}} = K_{I_C}. \tag{2.28}$$

The propagation angle θ_p given in (2.27) is depicted for $0 \leq K_{II}/K_I \leq 1$ in Figure 2.2. In the case of a loading situation which is dominated by mode I, i.e. $|K_{II}|/K_I << 1$, (2.27) and (2.28) can be approximated by the first two terms of a Taylor expansion in K_{II}/K_I. These expansions are given by

$$\theta_p = -2\frac{K_{II}}{K_I} + \frac{14}{3}\frac{K_{II}^3}{K_I^3} + O\left(\frac{K_{II}^5}{K_I^5}\right), \tag{2.29}$$

$$K_I \left(1 + \frac{3}{2}\frac{K_{II}^2}{K_I^2} + O\left(\frac{K_{II}^4}{K_I^4}\right) \right) = K_{I_C}. \tag{2.30}$$
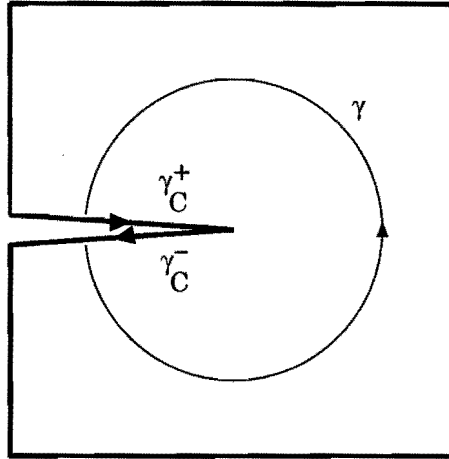
Figure 2.3: *Curves for J-integral.*

Another criterion for crack growth in a mixed-mode loading situation is the global criterion based on the amount of energy stored in the material and available for the creation of new crack surfaces. This amount is represented by a vector **J** which components have unit Jm^{-2}. The vector **J** is obtained by a so-called J-integral, see [60],

$$J_k = \int_{\gamma+\gamma_C^+ +\gamma_C^-} (W_e n_k - \sigma_{ij} n_j u_{i,k}) \, d\gamma, \quad k = 1, 2. \tag{2.31}$$

In (2.31), γ is a curve around the crack tip with begin and end points on the crack surfaces, and γ_C^- and γ_C^+ are two curves with the begin and end points of γ as their begin points and the crack tip as their end point, see Figure 2.3. The outward unit normal on these curves is denoted by **n** and W_e is the elastic energy density

$$W_e = \frac{1}{2}\sigma_{ij}\epsilon_{ij}. \tag{2.32}$$

Because of the integration theorem of Gauss and (2.1)-(2.3) and (2.9), one has for linearly elastic material behaviour in absence of volume forces that

$$\oint (W_e n_k - \sigma_{ij} n_j u_{i,k}) \, d\gamma = 0, \quad k = 1, 2, \tag{2.33}$$

when no singularity is inside the contour of integration. This means that (2.31) is independent of the choice of the curve γ.

In the local coordinate system with the crack tip as origin, the first component of the vector **J** equals the well-known energy release rate $\mathcal{G}$, see [37, Chs. 1, 3]. Since the components of **J** have the dimension of energy per unit of surface, **J** can be regarded as the energy flux per unit length into the crack tip, see [17, Ch. 5], or as the crack extension force per unit length, see

[13, Ch. 5]. Therefore, it is postulated that crack growth takes place when the stored energy per unit of surface reaches the critical energy release rate $\mathcal{G}_C$, i.e.

$$|\mathbf{J}| = \mathcal{G}_C. \tag{2.34}$$

The critical energy release rate $\mathcal{G}_C$ is a material parameter.

The components of $\mathbf{J}$ are related to the stress intensity factors K_I and K_{II} in the case of brittle fracture. Substitution of the expressions (2.18), (2.21) into (2.31), together with an integration curve γ close to the crack tip, yields that the components of $\mathbf{J}$ in the local coordinate system are given by, see [13, Ch. 5] or [60],

$$J_1 = \frac{(\kappa + 1)}{8G} \left(K_I^2 + K_{II}^2 \right), \tag{2.35}$$

$$J_2 = -\frac{(\kappa + 1)}{4G} K_I K_{II}, \tag{2.36}$$

where $\kappa = 3 - 4\nu$ in case of plane strain and $\kappa = (3 - \nu)/(1 + \nu)$ in case of plane stress. Substitution of (2.35), (2.36) into (2.34) results in

$$\frac{(\kappa + 1)}{8G} \left(K_I^4 + 6K_I^2 K_{II}^2 + K_{II}^4 \right)^{1/2} = \mathcal{G}_C. \tag{2.37}$$

When the critical stress intensity factor for a pure mode I loading situation is substituted into (2.37), a correspondence between $\mathcal{G}_C$ and K_{I_C} is obtained, i.e.

$$\frac{(\kappa + 1)}{8G} K_{I_C}^2 = \mathcal{G}_C. \tag{2.38}$$

In absence of volume forces, the vector $\mathbf{J}$ can be seen as the negative gradient of the potential energy per unit length of the material with respect to the direction of crack growth, see [37, Ch. 3]. Hence, the release of energy due to crack extension is maximal in the direction of $\mathbf{J}$. Therefore, the direction of $\mathbf{J}$ is taken as the direction of crack growth. Together with (2.35) and (2.36), this means that the angle θ_p of crack propagation is given by

$$\theta_p = \arctan \left(\frac{-2K_I K_{II}}{K_I^2 + K_{II}^2} \right). \tag{2.39}$$

For small values of $|K_{II}|/K_I$, the criterion (2.39) returns small propagation angles as is expected. However, in the case of mode II dominated problems, i.e. $|K_{II}|/K_I > 1$, the criterion is not suitable. This is seen, for instance, from the fact that (2.39) is symmetric in the stress intensity factors. Hence, for a pure mode II loading situation the same propagation angle is obtained as for a pure mode I loading situation.

In Figure 2.2, the propagation angle (2.39) is depicted for $0 \le K_{II}/K_I \le 1$. It is seen that for small values of K_{II}/K_I the difference between the propagation angles (2.27) and (2.39) is small. This can be deduced from the fact that the leading terms of the Taylor expansions of (2.37) and

(2.39) in terms of K_{II}/K_I are exactly the same as those for the maximum circumferential stress criterion, see (2.29), (2.30). Therefore, it is concluded that the fracture criteria (2.37), (2.39) and (2.27), (2.28) are equivalent for fracture problems dominated by mode I, i.e. $|K_{II}|/K_I \ll 1$. For fracture problems dominated by mode II, i.e. $|K_{II}|/K_I > 1$, the criteria (2.37), (2.39) are not suitable and (2.27), (2.28) have to be used.

2.3   Finite element method

In the previous section aspects of fracture mechanics have been introduced. Criteria have been presented for crack growth and for the direction of crack growth. To apply these criteria, the values of the fracture mechanics parameters, such as the stress intensity factors and the J-vector, have to be determined. They are computed from the displacements, strains and stresses in the neighbourhood of the crack tip. These quantities can be found from the problem of planar deformation of a linearly elastic medium, e.g. see (2.1), (2.3)-(2.5) and (2.9). In general, this problem cannot be solved exactly. Numerical methods are necessary to provide approximate solutions.

The finite element method, in short FE-method, is a numerical method for the solution of a boundary value problem, like (2.1), (2.3)-(2.5) and (2.9). Hence, this method can provide approximate values for displacements, strains and stresses in a material. The method uses a weak form of the deformation problem. With the help of a division of the material into a number of subdomains, so-called elements, then approximate values are obtained.

In this section the main concepts of the FE-method are presented. For a more thorough description of the method, the reader is referred to Hughes [33], [36] or Zienkiewicz [75]. The section ends with some aspects and problems of the application of the FE-method to fracture mechanics.

2.3.1   Approximation by means of FE-shape functions

Consider a domain Ω in two-dimensional space, which is divided into a number of elements Ω_e, $e = 1, \ldots, N$, see Figure 2.4. For these elements one often takes triangles or quadrilaterals. This division is such that

$$\Omega = \bigcup_{e=1}^{N} \Omega_e. \tag{2.40}$$

Two elements can only have parts of their boundaries in common. To be more specific, when two elements have a part of a side in common, they have the entire side in common. Furthermore, a set of nodal points $\{\mathbf{x}_a\}_{a=1,\ldots,n}$ is chosen such that the vertices of the elements are among the nodal points, see Figure 2.4. Interior points or boundary points of elements may also be among the nodal points. Hence, the division of Ω into elements is fully described by the specification of the nodal points of each element. Such a specification of nodes for the element division is called the connectivity of the nodal points.
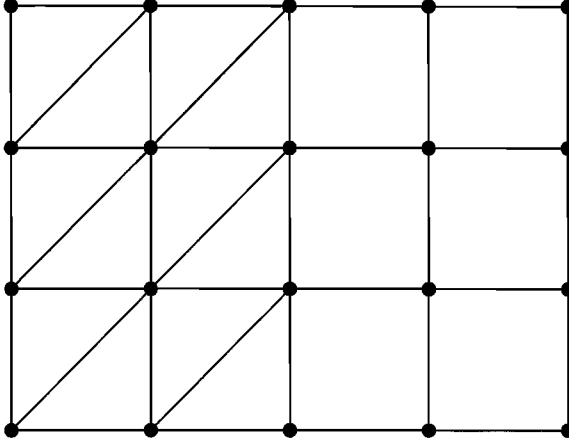
Figure 2.4: *Element division and nodal points for Ω.*

With the help of the connectivity of the nodal points, a global shape function $\phi_a(\mathbf{x})$ is defined for each nodal point $\mathbf{x}_a$. These shape functions satisfy the selectivity property

$$\phi_a(\mathbf{x}_b) = \delta_{ab}, \quad a, b = 1, \ldots, n. \tag{2.41}$$

Each shape function ϕ_a has a compact support, since ϕ_a is non-zero only in the elements surrounding $\mathbf{x}_a$. Furthermore, ϕ_a is zero on the sides of the elements on which the nodal point $\mathbf{x}_a$ is not positioned. Hence, when $\mathbf{x}_a \notin \partial\Omega$, ϕ_a vanishes on the boundary $\partial\Omega$.

An approximation u^h for a function u on Ω is then given by

$$u^h(\mathbf{x}) = \sum_{a=1}^{n} u_a \phi_a(\mathbf{x}), \tag{2.42}$$

where $u_a = u(\mathbf{x}_a)$. Due to (2.41), u^h interpolates u in the nodal points. Moreover, the values of u on the boundary $\partial\Omega$ are fully determined by those u_a for which $\mathbf{x}_a \in \partial\Omega$.

The way in which the shape functions are obtained for a FE-division is now described for a two-dimensional domain Ω. For $\mathbf{x} \in \Omega_e$ and $\mathbf{x}_a \notin \Omega_e$, we have $\phi_a(\mathbf{x}) = 0$. When $\mathbf{x}_a \in \Omega_e$ the value of $\phi_a(\mathbf{x})$ is determined in the following way.

For each group of elements Ω_e of the same type (triangle or quadrilateral) which contain the same number of nodal points, a standard element Ω_s is considered. For a quadrilateral for instance, this standard element is a square. The Cartesian coordinates in Ω_s are denoted by ξ_1 and ξ_2. Each nodal point $\mathbf{x}_a \in \Omega_e$ corresponds with a local node $\boldsymbol{\xi}_b \in \Omega_s$. Local shape functions $\varphi_b(\boldsymbol{\xi})$ correspond with the local nodes. These functions are polynomials such that the selectivity property (2.41) with respect to the local nodes holds true and such that φ_b vanishes on the sides of Ω_s on which $\boldsymbol{\xi}_b$ is not positioned. An isoparametric mapping from the standard element Ω_s onto the element Ω_e is then given by

$$\mathbf{x}(\boldsymbol{\xi}) = \sum_b \mathbf{x}_{a(b)} \varphi_b(\boldsymbol{\xi}), \tag{2.43}$$
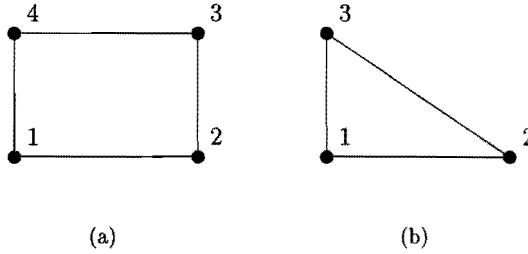
Figure 2.5: (a) *Quadrilateral element,* (b) *triangular element.*

where $\boldsymbol{\xi} \in \Omega_s$, the index b sums over the local nodes and $\mathbf{x}_{a(b)}$ is the nodal point which corresponds with the local nodal point $\boldsymbol{\xi}_b$. Note that $\mathbf{x}(\boldsymbol{\xi}_b) = \mathbf{x}_{a(b)}$.

With the help of the isoparametric mapping (2.43) the global shape functions on Ω_e are given by

$$\phi_{a(b)}(\mathbf{x}) = \varphi_b(\boldsymbol{\xi}), \qquad (2.44)$$

with $\boldsymbol{\xi}$ such that $\mathbf{x} = \mathbf{x}(\boldsymbol{\xi})$.

In order to have a correct definition of ϕ_a by means of (2.44), the isoparametric mapping (2.43) has to be bijective. Therefore, the element Ω_e may not be distorted too much from its original shape, the standard element Ω_s.

The definition of the FE-shape functions by means of (2.43) and (2.44) is called isoparametric, since the same set of local shape functions is used in both equations. There exist more general (non-isoparametric) FE-shape functions, where different sets of local shape functions are used for (2.43) and (2.44), see [33].

As an example of isoparametric shape functions, consider the four-node quadrilateral element depicted in Figure 2.5a. The standard element is $\Omega_s = \{(\xi_1, \xi_2) \mid -1 \leq \xi_1 \leq 1, -1 \leq \xi_2 \leq 1\}$ with the vertices as the local nodes. The local shape functions φ_b are bi-linear in the coordinates ξ_i,

$$\varphi_1(\boldsymbol{\xi}) = (1 - \xi_1)(1 - \xi_2)/4, \qquad \varphi_2(\boldsymbol{\xi}) = (1 + \xi_1)(1 - \xi_2)/4, \qquad (2.45)$$

$$\varphi_3(\boldsymbol{\xi}) = (1 + \xi_1)(1 + \xi_2)/4, \qquad \varphi_4(\boldsymbol{\xi}) = (1 - \xi_1)(1 + \xi_2)/4. \qquad (2.46)$$

The isoparametric mapping (2.43) for this quadrilateral is bijective only when the quadrilateral contains no angles larger than π. The global shape functions ϕ_a can then represent a linear function on Ω_e exactly and these shape functions are bi-linear in the coordinates x_i only when the quadrilateral is a rectangle. For more details, see [33, Ch. 3] or [75, Ch. 7].

In Figure 2.5b, a three-node triangular element is depicted. The standard element for this type of element is $\Omega_s = \{(\xi_1, \xi_2) \mid 0 \leq \xi_1 \leq 1, 0 \leq \xi_2 \leq 1, \xi_1 + \xi_2 \leq 1\}$ with the vertices as the local nodes. The local shape functions φ_b are linear in ξ_i,

$$\varphi_1(\boldsymbol{\xi}) = 1 - \xi_1 - \xi_2, \qquad \varphi_2(\boldsymbol{\xi}) = \xi_1, \qquad \varphi_3(\boldsymbol{\xi}) = \xi_2. \qquad (2.47)$$

The isoparametric mapping (2.43) is then linear and bijective. The global shape functions ϕ_a are then also linear in the spatial coordinates x_i and vanish on the side opposite to the node $\mathbf{x}_a$.

For the isoparametric mapping (2.43) restricted to a side of the standard element, the non-zero terms correspond with the nodal points on this side. Because of the symmetry in the local shape functions, the global shape functions are then continuous across element boundaries. In general, the derivatives of the global shape functions are not continuous across element boundaries.

Due to definition (2.44) the global derivatives of the shape functions $\phi_{a(b)}$ are related to the local derivatives of φ_b by means of the Jacobi matrix of the isoparametric mapping (2.43), i.e.

$$\frac{\partial \phi_{a(b)}(\mathbf{x})}{\partial \mathbf{x}} = \frac{\partial \varphi_b(\boldsymbol{\xi})}{\partial \boldsymbol{\xi}} \left(\frac{\partial \mathbf{x}}{\partial \boldsymbol{\xi}} \right)^{-1}. \tag{2.48}$$

This yields that the global derivatives of the shape functions become singular when the Jacobian of the isoparametric mapping (2.43) is singular. Later it will be shown that with this feature one can capture a $1/\sqrt{r}$-singularity with the global shape functions.

2.3.2   Discrete equations

Consider a planar problem of deformation of an elastic medium, e.g. see (2.1), (2.3)-(2.5) and (2.9). With the help of a division into finite elements of the domain Ω, one can obtain approximate solutions for the displacements, strains and stresses in the medium. Therefore, one uses the weak form (2.11) of the deformation problem and one sets

$$\mathbf{u}(\mathbf{x}) = \sum_{a=1}^{n} \mathbf{d}_a \phi_a(\mathbf{x}). \tag{2.49}$$

The nodal displacements $\mathbf{d}_a$ are obtained according to a Galerkin approach. The test displacements $\delta\mathbf{u}$ in (2.11) are restricted to be of the same form as $\mathbf{u}$. This leads to a linear system for the nodal displacements of the form

$$K\mathbf{d} = \mathbf{f}, \tag{2.50}$$

where the vector $\mathbf{d}$ consists of the nodal displacement vectors $\mathbf{d}_a$, i.e.

$$\mathbf{d}^T = \begin{bmatrix} \mathbf{d}_1^T & \cdots & \mathbf{d}_n^T \end{bmatrix}. \tag{2.51}$$

The stiffness matrix K and the right-hand side vector $\mathbf{f}$ are built from the 2×2 nodal submatrices K_{ab} and the 2×1 nodal subvectors $\mathbf{f}_a$, respectively, which are given by

$$K_{ab} = \int_{\Omega} B_a^T D B_b \, d\Omega, \quad a, b = 1, \dots, n, \tag{2.52}$$

$$\mathbf{f}_a = \int_{\Omega} \phi_a \mathbf{f}^* \, d\Omega + \int_{\Gamma_p} \phi_a \mathbf{p}^* \, d\Gamma, \quad a = 1, \dots, n. \tag{2.53}$$

It is emphasized that the submatrices K_{ab} and the subvectors $\mathbf{f}_a$ are nodal contributions and not element contributions to K and $\mathbf{f}$, respectively. However, in practice these submatrices and subvectors are determined for each element as is described in the sequel of this section. The matrix B_a consists of the derivatives of the shape functions ϕ_a,

$$B_a = \begin{bmatrix} \phi_{a,1} & 0 \\ 0 & \phi_{a,2} \\ \phi_{a,2} & \phi_{a,1} \end{bmatrix}, \quad a = 1, \ldots, n, \tag{2.54}$$

and the 3×3 matrix D represents the constitutive law of the elastic material. For instance, for a situation of plane stress, the matrix D is given by

$$D = \frac{E}{1 - \nu^2} \begin{bmatrix} 1 & \nu & 0 \\ \nu & 1 & 0 \\ 0 & 0 & \frac{1-\nu}{2} \end{bmatrix}. \tag{2.55}$$

The submatrix K_{ab} is non-zero only when ϕ_a and ϕ_b are non-zero on a common part, i.e., when $\mathbf{x}_a$ and $\mathbf{x}_b$ both belong to a common element Ω_e.

In order to meet the essential boundary conditions $\mathbf{u} = \mathbf{u}^*$ on Γ_u, the nodal displacements $\mathbf{d}_a$ for $\mathbf{x}_a \in \Gamma_u$ are set equal to $\mathbf{u}^*(\mathbf{x}_a)$ and the corresponding equations in (2.50) are skipped. With the solution $\mathbf{d}$ of (2.50), equation (2.49) then results in approximations for the displacements in the material. Taking derivatives of (2.49) and using the constitutive equations, e.g. (2.9), results in approximate values for the strains and stresses. Since FE-shape functions have mostly discontinuous derivatives across element boundaries, the stresses and strains obtained from (2.49) are normally not continuous in the domain.

2.3.3   Numerical integration

To obtain the stiffness matrix K and the right-hand side vector $\mathbf{f}$, integrals over the domain Ω and the boundary Γ_p have to be calculated. In general, the exact values for these integrals cannot be found. Numerical integration is necessary to obtain the entries for K and $\mathbf{f}$. The shape functions are given per element Ω_e by means of a transformation of local (polynomial) shape functions given on a standard element Ω_s. Furthermore, the derivatives of the shape functions are generally discontinuous across element boundaries. Therefore, numerical integration is performed for each element. For instance, the contribution of Ω_e to (2.52) is computed by means of

$$\int_{\Omega_e} B_a^T(\mathbf{x}) D B_b(\mathbf{x}) \, d\Omega = \int_{\Omega_s} B_a^T(\mathbf{x}(\boldsymbol{\xi})) D B_b(\mathbf{x}(\boldsymbol{\xi})) \left| \frac{\partial \mathbf{x}}{\partial \boldsymbol{\xi}} \right| d\Omega. \tag{2.56}$$

The integral over the standard element Ω_s is then evaluated by means of a particular numerical integration rule. In most cases, Gaussian quadrature is taken as integration rule, see Atkinson [2, Ch. 5]. In general, numerical integration does not lead to the exact element contribution. However, by taking an integration rule of a specific order which depends on the order of interpolation in the standard element, sufficiently accurate element contributions can be obtained.
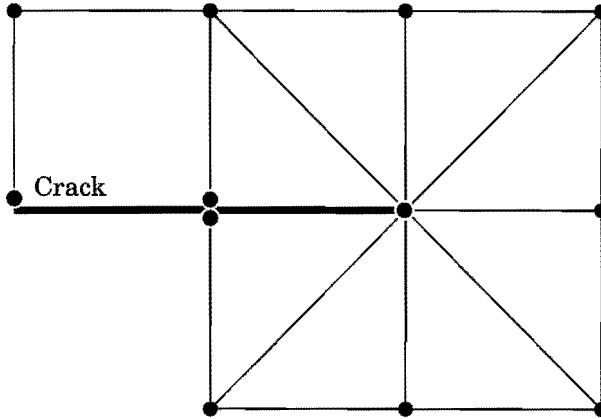
Figure 2.6: *Part of FE-discretization near crack tip.*

Summation of all the element contributions (2.56) leads to the nodal submatrix matrix K_{ab}. In the same way the domain integral for the nodal right-hand side subvectors $\mathbf{f}_a$ are obtained. The boundary integrals for $\mathbf{f}_a$ are obtained by summation of the contributions of the non-empty intersections of Γ_p with the element boundaries.

A schematic set-up of a FE-analysis for a (cracked) material domain is given in Appendix B.

2.3.4 Finite element method in fracture mechanics

By means of FE-analysis of cracked material, fracture mechanics parameters can be obtained. These parameters can then be used in fracture criteria, such as (2.27) and (2.28). Some aspects and problems of the application of the FE-method for fracture mechanics are now considered.

A crack in the material can be easily modelled by means of the connectivity of nodal points. Consider a part of a FE-discretization near a crack tip as depicted in Figure 2.6. On both crack surfaces nodal points are present, but these nodal points are not connected by means of an element. Hence, the FE-shape functions are discontinuous over the crack. Since the displacements are also discontinuous over the crack, see (2.21), the shape functions can be used in the representation (2.49) of the displacements.

It has been shown in (2.21), that the displacements near the crack tip behave like $\sqrt{r}$ with r being the distance to the crack tip. To obtain an accurate approximation of the displacements by means of a FE-discretization, special crack tip elements are used near the crack tip, see Barsoum [3], Lim, Johnston and Choi [47], Stern [66], and Stern and Becker [67]. These elements provide shape functions which embody the $1/\sqrt{r}$-singularity of the stresses in their derivatives. A short description of the isoparametric finite elements presented in [3] now follows.

Consider the triangular element Ω_e depicted in Figure 2.7. This collapsed quadrilateral element is given by eight nodal points $\mathbf{x}_1, \ldots, \mathbf{x}_8$. The nodes $\mathbf{x}_1$, $\mathbf{x}_4$ and $\mathbf{x}_8$ coincide with the crack tip and the nodes $\mathbf{x}_5$ and $\mathbf{x}_7$ are on one fourth of the element sides on which the crack tip is positioned. As standard element Ω_s the eight-node serendipity square is taken with bi-quadratic local shape
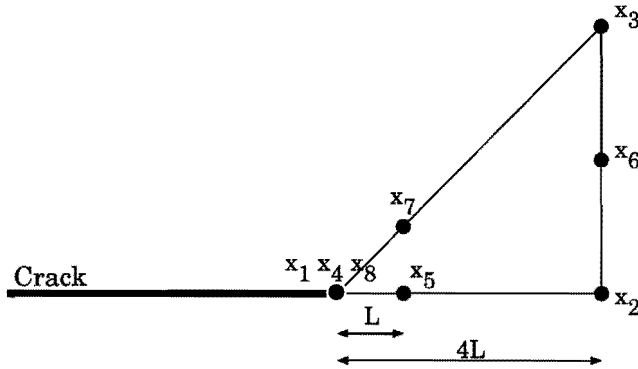
Figure 2.7: *Crack-tip element of Barsoum.*

functions, see [33, Ch. 3] or [75, Ch. 7]. Due to the coincidence of the nodes x_1, x_4 and x_8 and the special choices for the quarter point nodes x_5 and x_7, the Jacobian of the isoparametric mapping (2.43) is singular on the side of Ω_s which corresponds with the crack tip. This yields with (2.48) singular derivatives of the global shape functions in the crack tip. The singularity equals $1/\sqrt{r}$ along the two element sides on which the crack tip is positioned.

From a FE-analysis of cracked material, fracture mechanics parameters can be obtained in several ways. When crack-tip elements are used, the computed strains and stresses reveal a $1/\sqrt{r}$-like singularity. With the help of the expressions (2.18) and (2.21) values for the stress intensity factors can then be found from the computed displacements and stresses. Due to the finite representation of the displacements in the neighbourhood of the crack tip, the angular variation in displacements and stresses cannot be represented exactly. Therefore, the use of (2.18) and (2.21) does not necessarily have to lead to very accurate values for K_I and K_{II}.

The stress intensity factors can also be obtained from the vector $\mathbf{J}$ with the help of (2.35) and (2.36). The vector $\mathbf{J}$, given by (2.31), can be obtained by means of contour integration. For the computation of $\mathbf{J}$ in the case of a FE-analysis, one should account for the discontinuities in the strains and stresses across element boundaries. Furthermore, due to the finite representation of the displacements close to the crack tip, a correction for the crack surface integrals in (2.31) has to be used as introduced by Eischen [20]. This correction is considered in more detail in Section 4.4.

The vector $\mathbf{J}$ for a FE-analysis can also be obtained by the method of crack extension, see Ishikawa [35] and Parks [59]. Crack extension can be easily modelled in the FE-method by a shift of only some nodes near the crack tip, resulting in a small change in the stiffness matrix K. From this shift the potential energy of the material for a slightly longer crack can be obtained without a complete FE-analysis for the material. Since $\mathbf{J}$ can be regarded as the negative gradient of the potential energy per unit length of the material with respect to the direction of crack growth, see [37, Ch. 3], $\mathbf{J}$ can be obtained by using the values of the potential energy for several crack extensions. Contour integration is thus avoided for the computation of $\mathbf{J}$.

With the computed fracture parameters, the direction of crack propagation can be determined. However, when the FE-method is used for the simulation of crack propagation, in successive

analysis steps, generally, the same mesh of finite elements cannot be used. After each propagation step local (and global) remeshing of the set of elements is necessary. Extra nodal points and a different connectivity have to be introduced to model the new crack surfaces, see Sumi [68]. Furthermore, when crack-tip elements are used, these elements have to be shifted to the new position of the crack tip, see Nishioka and Atluri [57]. This process of remeshing and new assembly of the stiffness matrix can be very time-consuming for complicated crack paths. Moreover, it is not always possible possible to generate an element-division for each crack path without distorted finite elements.

Recently, see Nayroles, Touzot and Villon [56], Belytschko, Gu and Lu [5], [7] and [48], a numerical technique has been introduced for application to fracture mechanics, which differs from the FE-method. A numerical method is used which provides shape functions without using any connectivity of nodal points. Hence, there are no remeshing problems in the case of crack propagation. In the remaining part of the thesis, this method is studied and applied to fracture mechanics problems in two dimensions.

Chapter 3

Connectivity-free approximation techniques

For an element-free numerical solution method for a boundary value problem, based on a weak formulation of the problem, one has to use an approximation technique which provides shape functions without the use of a connectivity of nodal points. In this chapter some of these techniques are considered. First, a technique known as moving least squares approximation, in short MLSA, is introduced. Since the approximation of quantities near a crack for MLSA is not straightforward, several ways of approximation near a crack are considered. The chapter concludes with an overview of other approximation techniques which are free from a connectivity of points. By a comparison of these techniques with MLSA, it is made clear why MLSA is preferred in the element-free numerical solution method which is described in Chapter 4.

3.1 Moving least squares approximation

Moving least squares approximation is a technique which provides an approximation of a function without the use of a connectivity of points. The technique uses a set of nodal points, a set of weight functions, and a set of basis functions. At every point of the domain, the approximant of a function is a linear combination of the basis functions. The coefficients for the basis functions in this linear combination differ from point to point and are computed with the help of the weight functions and the nodal values of the function under consideration. As a consequence, a system of equations has to be solved at every point of the domain in order to obtain the coefficients for the basis functions. Hence, this way of approximation is computationally expensive in comparison with approximation by finite elements, where the approximant is given per element. The MLSA-approximant is obtained, however, without the use of any connectivity of nodal points.

Moving least squares approximation is introduced for a two-dimensional domain Ω. It is easy to see that this introduction applies for any space dimension. It is shown that MLSA can be described in terms of shape functions. Some essential features of these shape functions are considered and examples of shape functions are given. A more detailed description of MLSA can be found in Lancaster and Šalkauskas [43], [44, Chs. 2, 9].

3.1.1   Approximation by means of MLSA-shape functions

Consider a domain Ω in two-dimensional space (e.g. the domain Ω for the problem of deformation of an elastic medium, see Section 2.1). To approximate a certain function $u(\mathbf{x})$ on Ω, a finite set $\{p_c(\mathbf{x})\}_{c=1,\ldots,m}$ of so-called basis functions is considered. This set can, for instance, be a finite subset of the set of monomials in the space coordinates $\{1, x_1, x_2, x_1^2, x_1 x_2, \ldots\}$.

The moving least squares approximant $u^h(\mathbf{x})$ of a function $u(\mathbf{x})$ on Ω is given for $\mathbf{x} \in \Omega$ by a linear combination of the basis functions $p_c(\mathbf{x})$ with coefficients $\mu_c(\mathbf{x})$, that is by

$$u^h(\mathbf{x}) = \mathbf{p}(\mathbf{x})^T \boldsymbol{\mu}(\mathbf{x}), \tag{3.1}$$

where

$$\mathbf{p}(\mathbf{x})^T = [p_1(\mathbf{x})\ p_2(\mathbf{x})\ \cdots\ p_m(\mathbf{x})], \tag{3.2}$$

$$\boldsymbol{\mu}(\mathbf{x})^T = [\mu_1(\mathbf{x})\ \mu_2(\mathbf{x})\ \cdots\ \mu_m(\mathbf{x})]. \tag{3.3}$$

In order to determine the vector $\boldsymbol{\mu}(\mathbf{x})$, a set of nodal points $\{\mathbf{x}_a\}_{a=1,\ldots,n}$ is chosen together with a set of weight functions $\{w_a(\mathbf{x})\}_{a=1,\ldots,n}$ defined on a neighbourhood of Ω such that $\mathbf{x}_a \in \Omega$, $0 \le w_a(\mathbf{x}) \le 1$ and $w_a(\mathbf{x}_a) > 0$, $a = 1, \ldots, n$. Here one can think of weight functions which have a compact support, i.e., which are only non-zero on a small bounded subset of Ω.

The entries of $\boldsymbol{\mu}(\mathbf{x})$ are obtained for each $\mathbf{x} \in \Omega$ by minimization with respect to $\boldsymbol{\mu}$ of the sum

$$S(\boldsymbol{\mu}) = \sum_{a=1}^{n} w_a(\mathbf{x}) \left(\mathbf{p}(\mathbf{x}_a)^T \boldsymbol{\mu}(\mathbf{x}) - u_a\right)^2. \tag{3.4}$$

Here, u_a is the value of u in $\mathbf{x}_a$, i.e. $u_a = u(\mathbf{x}_a)$, $a = 1, \ldots n$. If the weight functions w_a have compact support, the summation in (3.4) consists only of a few terms and the value of $u^h(\mathbf{x})$ is then fully determined by a few nodal values u_a.

From (3.4) it is seen that the entries of $\boldsymbol{\mu}(\mathbf{x})$ are determined by means of a weighted least squares procedure. Since the weights differ from point to point, one speaks of moving least squares approximation. Equation (3.4) can also be written as

$$S(\boldsymbol{\mu}) = \left(P^T \boldsymbol{\mu}(\mathbf{x}) - \mathbf{u}\right)^T W(\mathbf{x}) \left(P^T \boldsymbol{\mu}(\mathbf{x}) - \mathbf{u}\right), \tag{3.5}$$

where $\mathbf{u}$ is the vector with entries u_a, and $a = 1, \ldots n$ such that $w_a(\mathbf{x}) > 0$, and the entries of the matrices P and W are given by

$$P_{ca} = p_c(\mathbf{x}_a), \quad c = 1, \ldots, m, a \in \{i = 1, \ldots, n \mid w_i(\mathbf{x}) > 0\}, \tag{3.6}$$

$$W_{ab} = w_a(\mathbf{x})\delta_{ab}, \quad a, b \in \{i = 1, \ldots, n \mid w_i(\mathbf{x}) > 0\}. \tag{3.7}$$

The fact that $S(\boldsymbol{\mu})$ has to be stationary with respect to $\boldsymbol{\mu}(\mathbf{x})$ results in a set of linear equations for $\boldsymbol{\mu}(\mathbf{x})$,

$$PW(\mathbf{x})P^T \boldsymbol{\mu}(\mathbf{x}) = PW(\mathbf{x})\mathbf{u}. \tag{3.8}$$

For the sake of simplicity, the following short-hand notation is introduced

$$A(\mathbf{x}) = PW(\mathbf{x})P^T. \tag{3.9}$$

When the system of equations (3.8) has a unique solution $\boldsymbol{\mu}(\mathbf{x})$ for each $\mathbf{x} \in \Omega$, we will say that MLSA is well-defined for the domain Ω. This is the case if and only if the rank of the matrix P equals m, the number of basis functions p_c, see Hegen [29] or [43]. Hence, a necessary condition for MLSA to be well-defined for Ω is that at least m weight functions are non-zero in each $\mathbf{x} \in \Omega$. At the end of this section it is explained in which way MLSA can be made well-defined for Ω. For the remaining part of this section it is assumed that this is indeed the case. When MLSA is well-defined, a unique value $u^h(\mathbf{x})$ can be found for each $\mathbf{x} \in \Omega$ by means of (3.1). It is noticed that multiplication of all the weight functions by an arbitrary positive scalar does not change the approximant and its derivatives.

The approximant u^h can also be expressed with the help of shape functions. One can write

$$u^h(\mathbf{x}) = \sum_{a=1}^{n} u_a \phi_a(\mathbf{x}), \tag{3.10}$$

where the shape functions ϕ_a, $a = 1, \ldots, n$, are defined by

$$\phi_a(\mathbf{x}) = \begin{cases} \sum_{c=1}^{m} p_c(\mathbf{x}) \left[A^{-1}(\mathbf{x}) P W(\mathbf{x}) \right]_{ca}, & w_a(\mathbf{x}) > 0, \\ 0, & w_a(\mathbf{x}) = 0. \end{cases} \tag{3.11}$$

Examples of shape functions ϕ_a are shown later in this section. Equation (3.11) shows that $w_a(\mathbf{x}) = 0$ yields that $\phi_a(\mathbf{x}) = 0$. Hence, when w_a has compact support, ϕ_a also has compact support. Derivatives of the shape functions are obtained by differentiation of (3.11). The derivative of the inverse $A^{-1}(\mathbf{x})$ can be obtained easily by differentiation of the identity $A(\mathbf{x})A^{-1}(\mathbf{x}) = I$, I being the identity matrix.

The smoothness of the approximant u^h and the shape functions ϕ_a are related to the smoothness of both the basis functions and the weight functions. Let $C^k(\Omega)$ be the space of k times continuously differentiable functions on Ω. Then, when $w_a \in C^k(\Omega)$, $a = 1, \ldots, n$, $k \in \mathbb{N}$, and $p_c \in C^l(\Omega)$, $c = 1, \ldots, m$, $l \in \mathbb{N}$, one has that $u^h \in C^s(\Omega)$ and $\phi_a \in C^s(\Omega)$, $a = 1, \ldots, n$, where $s = \min(k, l)$. A proof of this is found in [29] and [43].

Replacing $u(\mathbf{x})$ by $p_c(\mathbf{x})$, or equivalently u_a by $p_c(\mathbf{x}_a)$, results in $u^h(\mathbf{x}) = p_c(\mathbf{x})$, i.e.

$$p_c(\mathbf{x}) = \sum_{a=1}^{n} p_c(\mathbf{x}_a) \phi_a(\mathbf{x}), \quad c = 1, \ldots, m. \tag{3.12}$$

Hence, the basis functions can be represented exactly by the shape functions. However, the shape functions are not a linear combination of the basis functions. For instance, when the basis functions are monomials in the space coordinates, the shape functions are not polynomial as is shown in the sequel. Let the set of basis functions $\{p_c\}_{c=1,\ldots,m}$ be replaced by the set of basis functions $\{q_c\}_{c=1,\ldots,m}$ consisting of linear combinations of p_c such that the same set of functions

is spanned by the two sets. Then, since (3.1) is linear in the basis functions, MLSA results for both sets of basis functions in the same approximant and the same set of shape functions.

A disadvantage of MLSA is that for each point under consideration a linear system must be solved to obtain the value of the approximant u^h and the shape functions ϕ_a. This is a burdensome task. In [48] matrix inversion is avoided by orthogonalization of the basis functions with respect to the weight functions. It is claimed that the computational cost of solving the system is then reduced. The computational cost of the orthogonalization procedure, however, are of the same order as the cost of matrix inversion. Orthogonalization of the basis functions is equivalent to solving the linear system (3.8) by means of the singular value decomposition of the matrix $A(\mathbf{x})$. Since the matrix $A(\mathbf{x})$ can become poorly conditioned in some cases, orthogonalization is preferred to matrix inversion.

In the orthogonalization procedure, a new basis $\{q_c\}_{c=1,\ldots,m}$ is obtained from the original basis $\{p_c\}_{c=1,\ldots,m}$ by a Gramm-Schmidt orthogonalization procedure. These basis functions q_c are linear combinations of the functions p_c, where the scalars depend on the coordinates of the point under consideration $\bar{\mathbf{x}}$. The basis $\{q_c\}_{c=1,\ldots,m}$ is given by

$$q_1(\mathbf{x}, \bar{\mathbf{x}}) = p_1(\mathbf{x}), \tag{3.13}$$

$$q_c(\mathbf{x}, \bar{\mathbf{x}}) = p_c(\mathbf{x}) - \sum_{d=1}^{c-1} \alpha_{cd}(\bar{\mathbf{x}}) q_d(\mathbf{x}, \bar{\mathbf{x}}), \quad c = 2, \ldots, m, \tag{3.14}$$

where

$$\alpha_{cd}(\bar{\mathbf{x}}) = \frac{\sum_{a=1}^{n} w_a(\bar{\mathbf{x}}) p_c(\mathbf{x}_a) q_d(\mathbf{x}_a, \bar{\mathbf{x}})}{\sum_{a=1}^{n} w_a(\bar{\mathbf{x}}) q_d(\mathbf{x}_a, \bar{\mathbf{x}})^2}, \quad c = 2, \ldots, m, \ d = 1, \ldots, c-1. \tag{3.15}$$

The basis functions q_c are orthogonal with respect to the weight functions,

$$\sum_{a=1}^{n} w_a(\bar{\mathbf{x}}) q_c(\mathbf{x}_a, \bar{\mathbf{x}}) q_d(\mathbf{x}_a, \bar{\mathbf{x}}) = 0, \quad c, d = 1, \ldots, m, \ c \neq d, \tag{3.16}$$

as can easily be verified. Hence, one speaks of orthogonal basis functions q_c. When the orthogonal basis is used for MLSA instead of the original basis, the matrix $A(\bar{\mathbf{x}})$ is diagonal and the coefficients $\mu_c(\bar{\mathbf{x}})$ can be found directly. They are given by

$$\mu_c(\bar{\mathbf{x}}) = \frac{\sum_{b=1}^{n} w_b(\bar{\mathbf{x}}) q_c(\mathbf{x}_b, \bar{\mathbf{x}}) u_b}{\sum_{b=1}^{n} w_b(\bar{\mathbf{x}}) q_c(\mathbf{x}_b, \bar{\mathbf{x}})^2}, \quad c = 1, \ldots, m. \tag{3.17}$$

Taking $u_b = \delta_{ab}$ yields that the shape functions ϕ_a, $a = 1, \ldots, n$, given in (3.11), can be written for $\bar{\mathbf{x}} = \mathbf{x}$ as

$$\phi_a(\mathbf{x}) = w_a(\mathbf{x}) \sum_{c=1}^{m} \frac{q_c(\mathbf{x}_a, \mathbf{x}) q_c(\mathbf{x}, \mathbf{x})}{\sum_{b=1}^{n} w_b(\mathbf{x}) q_c(\mathbf{x}_b, \mathbf{x})^2}, \quad a = 1, \ldots, n. \tag{3.18}$$

Note that this expression for the shape functions is also valid for indices a with $w_a(\mathbf{x}) = 0$. Derivatives of the shape functions can be obtained by taking derivatives of (3.18) and (3.13)-(3.15).

(a) (b)
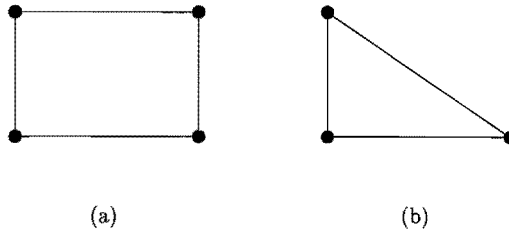
Figure 3.1: (a) *Rectangular set*, (b) *triangular set.*

From (3.18) it is clear that indeed $\phi_a \in C^s(\Omega)$, $s = \min(k, l)$, when $w_a \in C^k(\Omega)$, $a = 1, \ldots, n$, $k \in I\!N$, and $p_c \in C^l(\Omega)$, $c = 1, \ldots, m$, $l \in I\!N$. Furthermore, (3.18) shows that when the basis functions are monomials, the shape functions are not necessarily polynomial, and that the influence of the weight functions on the values of the shape functions is only relative.

In general, the shape functions ϕ_a do not have the selectivity property

$$\phi_a(\mathbf{x}_b) = \delta_{ab}, \quad a, b = 1, \ldots, n. \tag{3.19}$$

As a consequence, the constants u_a do not have to be the nodal values of u^h,

$$u^h(\mathbf{x}_a) \neq u_a, \quad a = 1, \ldots, n. \tag{3.20}$$

Moreover, in contrast with the finite element (in short FE) shape functions described in Section 2.3, the shape function ϕ_a corresponding to the nodal point $\mathbf{x}_a \notin \partial\Omega$ can be non-zero on the boundary of the domain.

There is a possibility to enforce property (3.19). For this purpose, one should take the constant function on Ω in the basis and one should use weight functions of the form

$$w_a(\mathbf{x}) = t_a(\mathbf{x})|\mathbf{x} - \mathbf{x}_a|^{-2\beta_a}, \quad \mathbf{x} \neq \mathbf{x}_a, \tag{3.21}$$

where $\beta_a \in I\!N$, $\beta_a > 0$, and $|\mathbf{x}|$ is the Euclidean norm of $\mathbf{x}$. The functions $t_a(\mathbf{x})$, $a = 1, \ldots, n$ are defined on a neighbourhood of Ω such that $0 \leq t_a(\mathbf{x}) \leq 1$ and $t_a(\mathbf{x}_a) > 0$, $a = 1, \ldots, n$. The weight functions (3.21) are singular in the nodal points. For such weight functions, MLSA still defines shape functions, which remain finite and which satisfy the smoothness property. Furthermore, the selectivity property (3.19) holds true. For more details the reader is referred to [29] and [43].

Other situations where the selectivity property (3.19) is satisfied, are situations where the shape functions coincide with shape functions originating from a finite element discretization. Consider four nodal points of a rectangular set of nodal points, see Figure 3.1a. Let the monomials 1, x_1, x_2 and $x_1 x_2$ form the set of basis functions and let the weight functions w_a for these four points be positive in the interior of the rectangle formed by these four points and
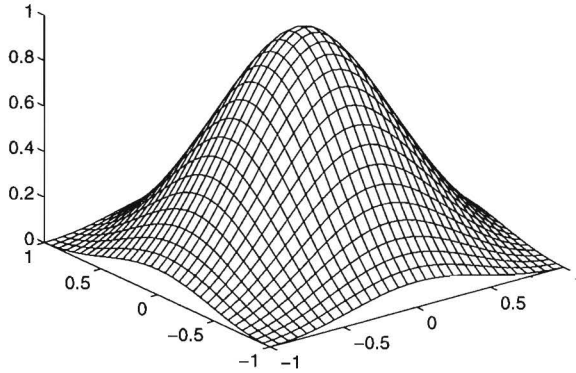
Figure 3.2: C^0-weight functions of Gaussian type.

be zero on the sides of the rectangle on which $\mathbf{x}_a$ is not positioned. When all the other weight functions are zero on this rectangle, MLSA results in bi-linear interpolation, as can be seen from (3.12). Hence, the shape functions ϕ_a are bi-linear on the rectangle and satisfy (3.19). These shape functions are equal to those of a finite element interpolation for such a rectangle, see (2.43)-(2.46).

When the four nodal points form a non-rectangular quadrilateral, the shape functions ϕ_a emerging from MLSA are still bi-linear. The finite element interpolation for such a quadrilateral via the isoparametric mapping (2.43), however, results in shape functions which are not bi-linear. In that case, the shape functions do not coincide with those emerging from MLSA.

Another situation where the shape functions satisfy (3.19) and coincide with the shape functions of a finite element interpolation, is depicted in Figure 3.1b. Assume for this triangular set that the monomials 1, x_1, x_2 form the set of basis functions. Let the weight functions w_a for these three points be positive in the interior of the triangle formed by these points and be zero on the side opposite to $\mathbf{x}_a$. When all the other weight functions are zero on this triangle, MLSA results in linear interpolation and the shape functions ϕ_a are linear on the triangle and satisfy (3.19). These shape functions are exactly the same shape functions which are used in a linear finite element interpolation for such a triangle, see (2.43), (2.44) and (2.47).

Hence, it is possible to obtain shape functions by MLSA which satisfy (3.19). In some situations these shape functions are identical to shape functions which are used in the finite element method.

3.1.2   Examples of shape functions

Some examples of shape functions obtained by moving least squares approximation are now presented. To this end, several types of weight functions are introduced first. The following weight functions with compact support are taken:
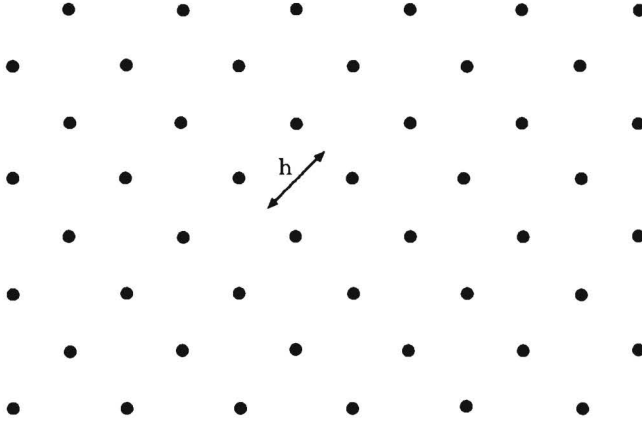
Figure 3.3: *Equidistant pattern of nodal points.*

- C^0-weight functions of Gaussian type with circular disk as support:

$$w_a(\mathbf{x}) = \begin{cases} \dfrac{\exp\left(-r_a^2/s_a^2\right)-\exp\left(-R_a^2/s_a^2\right)}{1-\exp\left(-R_a^2/s_a^2\right)}, & r_a \leq R_a, \\ 0, & r_a > R_a, \end{cases} \tag{3.22}$$

where $r_a = |\mathbf{x} - \mathbf{x}_a|$ is the distance between $\mathbf{x}$ and $\mathbf{x}_a$ and $R_a > 0$ is the radius of the support of w_a. The constants s_a control the relative weights.

- C^0-weight functions which are products of two one-dimensional versions of weight functions of Gaussian type.

- C^1-weight functions of polynomial type with circular disk as support:

$$w_a(\mathbf{x}) = \begin{cases} 1 - 6\dfrac{r_a^2}{R_a^2} + 8\dfrac{r_a^3}{R_a^3} - 3\dfrac{r_a^4}{R_a^4}, & r_a \leq R_a, \\ 0, & r_a > R_a, \end{cases} \tag{3.23}$$

where $r_a = |\mathbf{x} - \mathbf{x}_a|$ and $R_a > 0$.

- C^1-weight functions which are products of two one-dimensional weight functions of polynomial type.

- Weight functions of singular type:

$$w_a(\mathbf{x}) = t_a(\mathbf{x})r_a^{-2}, \tag{3.24}$$

where $r_a = |\mathbf{x} - \mathbf{x}_a|$ and $t_a(\mathbf{x})$ is one of the previous weight functions.

The C^0-weight functions are differentiable except on the boundary of their supports. In a numerical implementation the derivatives on this boundary are set equal to zero. The discontinuity in the derivatives for the Gaussian weight functions can be neglected when s_a is chosen
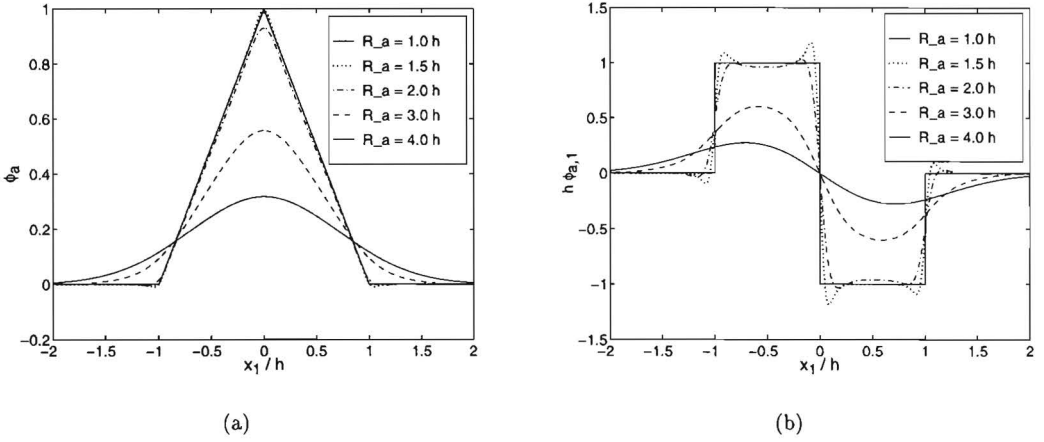
Figure 3.4: *Cross section of* (a) *shape functions* ϕ_a *and* (b) *derivatives* $\phi_{a,1}$ *for square set of nodal points.*

such that $R_a/s_a \geq 4$. For an example of a weight function of Gaussian type, see Figure 3.2. The other types of weight functions, except those of singular type, have a similar form. Some examples of shape functions are now depicted. Consider a square set of nodal points, i.e., the nodes are vertices of a set of squares in the domain as in Figure 3.3. Let the coordinate system be such that the nodes are positioned along the lines $x_1 = \text{constant}$ and $x_2 = \text{constant}$. The set $\{1, x_1, x_2, x_1x_2\}$ of bi-linear functions is taken as set of basis functions and products of one-dimensional Gaussian weight functions are taken as weight functions with the scaling constant set equal to $s_a = R_a/4$. Let the grid size h of the nodal distribution be equal to the distance in the x_1-direction (and hence, also the distance in the x_2-direction) between the nodes. Different radii R_a for the supports of the weight functions are taken. Cross sections of the resulting shape functions ϕ_a and their derivative $\phi_{a,1}$ for a particular nodal point $\mathbf{x}_a$ are depicted in Figure 3.4.

This figure shows that the shape functions indeed coincide with the FE-shape functions when the supports of the weight functions are equal to the union of the surrounding squares. For relatively small supports, the shape functions are similar to these FE-shape functions and hence, the shape functions emerging from MLSA and their derivatives are locally strongly non-polynomial. From Figure 3.4 it is seen that the shape functions behave locally as high-order polynomials for relatively large radii R_a for the supports of the weight functions. The shape functions depicted in Figure 3.4 show that the selectivity property (3.19) does not hold true and that the shape functions are not piecewise polynomial.

Different radii R_a for the supports of the singular weight functions are also taken. Cross sections of the obtained shape functions ϕ_a and derivatives $\phi_{a,1}$ are depicted in Figure 3.5. This figure shows that the selectivity property (3.19) holds true. For both relatively small and relatively larger radii for the supports of this type of weight functions, the shape functions are similar to the FE-shape functions for such a set of nodes. Hence, the shape functions and their derivatives are strongly non-polynomial on small parts of the domain.
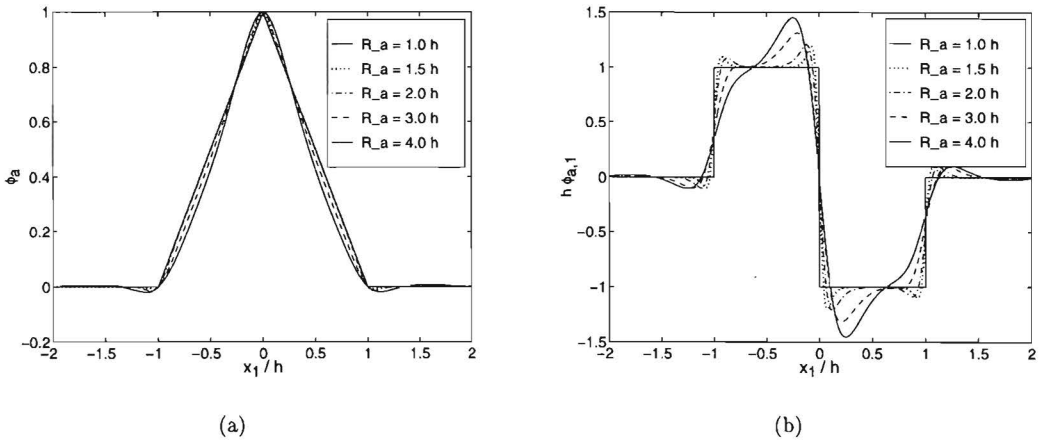
Figure 3.5: *Cross section of* (a) *shape functions* ϕ_a *and* (b) *derivatives* $\phi_{a,1}$ *for square set of nodal points, singular weight functions.*

From the previous examples it is concluded that the shape functions are locally strongly non-polynomial in the case of singular weight functions. This is also the case for non-singular weight functions with supports which are just large enough such that MLSA is well-defined. For non-singular weight functions with relatively large supports, the shape functions are locally high-order polynomials. In Chapter 4 the element-free Galerkin method is described which uses shape functions obtained by MLSA. In this method, numerical integrations are performed in a more or less arbitrary way. Therefore, for a good performance of the method, the shape functions should locally behave as high-order polynomials. Hence, non-singular weight functions are used with relatively large supports. Singular weight functions and non-singular weight functions with relatively small supports are not used.

3.1.3 Parameters for MLSA

This section ends with some considerations about the parameters of MLSA. A description is given of the distributions of nodal points, the weight functions, and the basis functions which are used for MLSA in the remaining part of the thesis. Moreover, it is explained in which way MLSA can be made well-defined.

Nodal points $\mathbf{x}_a$, $a = 1, \ldots, n$, are mostly placed equidistant in two (mutually orthogonal) directions, see Figure 3.3. Extra patterns of nodes are added to such a distribution on parts of the domain where more accuracy is required. Such a nodal distribution has the advantage that it can be generated easily. Furthermore, such a distribution is more convenient for the definition of weight functions, in order to accomplish that moving least squares approximation is well-defined for the domain.

As set of basis functions, a subset of the set of monomials in the space coordinates is mostly considered. In the case of fracture mechanics problems, however, a special non-polynomial

function is added to the basis. This is described in the next section. The non-singular weight functions (3.22), (3.23) are considered. For the weight functions of Gaussian type, the scalar s_a is set equal to $s_a = R_a/4$, $a = 1, \ldots, n$. Since these weight functions have a circular disk as support, there are no directions introduced in the shape functions obtained by moving least squares approximation.

When nodal points $\mathbf{x}_a$, $a = 1, \ldots, n$, and basis functions $p_c(\mathbf{x})$, $c = 1, \ldots, m$, are given, the radii R_a, $a = 1, \ldots, n$, of the supports of the weight functions should be chosen such that MLSA is well-defined for each point $\mathbf{x}$ of the domain Ω. For a general distribution of nodal points, this cannot be verified. Therefore, one can hardly find a way to determine radii R_a such that MLSA is well-defined for Ω and such that these radii are not too large in comparison with the dimensions of the domain Ω.

For distributions of nodes which are equidistant in two directions, however, it is possible to guarantee that MLSA is well-defined for Ω. It is assumed that one can think of the domain Ω divided into a set of quadrilaterals with the nodal points as vertices. Such a division is not unique and in some cases (e.g. a superposition of an arbitrary set of nodes on a part of Ω upon an equidistant pattern) it can be hardly determined. These quadrilaterals have more or less the same size. Only on parts of the domain where the nodal distribution has been refined, these quadrilaterals have a smaller size.

If one can guarantee that MLSA is well-defined for each quadrilateral, MLSA is well-defined for the entire domain. Therefore, under the assumption that each nodal point $\mathbf{x}_a$ is a vertex of a set of quadrilaterals which cover its entire neighbourhood in the domain Ω, a local mesh size h_a is determined for the quadrilaterals surrounding $\mathbf{x}_a$, $a = 1, \ldots, n$. With the help of this mesh size h_a the radius R_a for the support of w_a is given a value, in order to achieve that MLSA is well-defined on the quadrilaterals surrounding $\mathbf{x}_a$.

Let $\mathbf{v}_1$ be the unit vector pointing from $\mathbf{x}_a$ in the direction of the node which is closest to $\mathbf{x}_a$, and let $\mathbf{v}_2$ be such that $\mathbf{v}_2 \perp \mathbf{v}_1$. The vectors $\mathbf{v}_1$ and $\mathbf{v}_2$ divide two-dimensional space into four quadrants Q_a^i, $i = 1, 2, 3, 4$, with $\mathbf{x}_a$ as the origin. For instance, we have

$$Q_a^1 = \left\{ \mathbf{x} \ \middle| \ \mathbf{v}_1^T(\mathbf{x} - \mathbf{x}_a) \geq 0, \ \mathbf{v}_2^T(\mathbf{x} - \mathbf{x}_a) \geq 0 \right\}. \tag{3.25}$$

The vector $\mathbf{v}_1$ does not have to be unique. In the case of nodal patterns which are (locally) equidistant in two mutually orthogonal directions such as in this thesis, this does not affect the following procedure to determine a value for h_a. In the case of a non-unique $\mathbf{v}_1$ for a more general nodal pattern, however, the procedure can explicitly depend on the choice for $\mathbf{v}_1$.

Let Q_a^i, $i = 5, 6, 7, 8$, be the four quadrants obtained after rotation of Q_a^i, $i = 1, 2, 3, 4$, over an angle $\pi/4$. For the eight quadrants Q_a^i, $i = 1, \ldots, 8$, a size h_a^i is determined in the following way. Let the set H_a^i be defined by

$$H_a^i = \left\{ |\mathbf{x}_b - \mathbf{x}_a| \ \middle| \ \mathbf{x}_b \in Q_a^i, \ \mathbf{x}_b \neq \mathbf{x}_a, \ b = 1, \ldots, n \right\}. \tag{3.26}$$

Then, when H_a^i contains more than two non-zero elements, h_a^i is set to the third non-zero value of H_a^i. Here, we think H_a^i to be sorted such that the elements are given in ascending order.
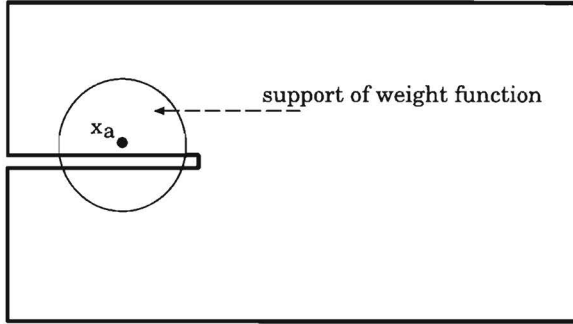
Figure 3.6: *Non-convex domain.*

When H_a^i is not empty and contains one or two non-zero elements, h_a^i is set to the maximal value of H_a^i. If H_a^i is empty, h_a^i is set equal to zero. The local mesh size h_a is now defined by

$$h_a = \sum_{i=1}^{8} \frac{h_a^i}{\sqrt{2} N_a},$$
(3.27)

where N_a is the number of non-empty sets H_a^i.

It is seen easily that, for a set of nodes which are vertices of a set of squares with length h, one obtains $h_a = h$ for all interior nodes. The above computation of h_a has been modified in such a way that this is also the case for boundary nodes.

The radii R_a of the supports of the weight functions are now set equal to a scalar multiple of h_a, i.e.

$$R_a = v h_a, \quad a = 1, \dots, n.$$
(3.28)

By setting $v > 0$ to a specific value one can guarantee for the assumed nodal distribution that, given the number of basis functions, enough weight functions are non-zero in each quadrilateral and hence, that moving least squares approximation is well-defined for Ω. To obtain shape functions from MLSA which behave locally as high-order polynomials, see Figure 3.4, in most cases v has a value which is much larger than the minimal value such that moving least squares approximation is well-defined.

3.2 Moving least squares approximation near a crack

In contrast with discretizations according to the finite element method, it is not straightforward for moving least squares approximation to have a correct discretization in the neighbourhood of a crack by means of the nodal points, the weight functions, and the basis functions. In cracked material, quantities such as displacements and stresses are discontinuous over a crack, see (2.18) and (2.21). Therefore, in the case of cracked material, special choices must be made for the parameters of MLSA in order to provide discontinuous approximations of such quantities.
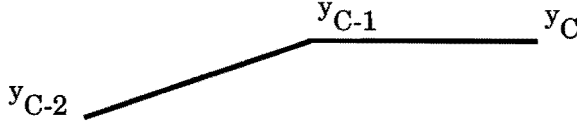
Figure 3.7: *Piecewise linear crack.*

A crack is an internal boundary which makes the domain under consideration non-convex. This is illustrated in Figure 3.6, where a non-convex domain is depicted with a nodal point $\mathbf{x}_a$. Such a non-convexity can result in a poor performance of MLSA for the domain. In order for MLSA to be well-defined for the domain, the radius of the circular support of the weight function w_a of the nodal point $\mathbf{x}_a$ can be so large that w_a is non-zero on the lower part of the domain. Hence, the shape function ϕ_a is non-zero on the lower part, which implies that the nodal point $\mathbf{x}_a$ influences the value of the MLSA-approximant on this part of the domain. Such a discretization for MLSA can lead to an inaccurate approximation, since in general the behaviour of quantities is totally different on the upper and lower part of the domain. In this section discretizations for MLSA are considered, which attempt to circumvent this problem in the case of domains containing a crack. Moreover, since the displacements in the vicinity of a crack tip show a $\sqrt{r}$-behaviour, special basis functions for MLSA are considered.

For the remaining part of this thesis it is assumed that a crack is a piecewise linear curve, represented by a set of points $\{\mathbf{y}_b\}_{b=1,\ldots,C}$, $C \geq 2$, such that the crack is made up of the line segments $[\mathbf{y}_b, \mathbf{y}_{b+1}]$, see Figure 3.7. The crack tip is represented by $\mathbf{y}_C$ which is an internal point of the material. The line segments $[\mathbf{y}_b, \mathbf{y}_{b+1}]$ are thought of as the union of two line segments $[\mathbf{y}_b, \mathbf{y}_{b+1}]_+$ and $[\mathbf{y}_b, \mathbf{y}_{b+1}]_-$ which represent the upper and lower crack surfaces, respectively. We restrict ourselves to cracks for which the crack path given by $\{\mathbf{y}_b\}_{b=1,\ldots,C}$ cannot have segments which are (almost) parallel and having opposite directions.

For the presentation of crack discretizations for MLSA, a function g_C is specified first, which specifies the position of a point relative to the crack. The crack and its extensions ahead and behind the crack, divide the material into two parts. Then, the function g_C is defined such that $g_C(\mathbf{x}) = \pm 1$ yields that $\mathbf{x}$ is positioned on the upper and lower part, respectively, while $g_C(\mathbf{x}) = 0$ implies that $\mathbf{x}$ is positioned on the extensions of the crack, see Figure 3.8. This is mathematically specified below.

Let $\mathbf{v}_1^b$ be the unit vector in the direction of $\mathbf{y}_{b+1} - \mathbf{y}_b$ and $\mathbf{v}_2^b$ be obtained after anti-clockwise rotation of $\mathbf{v}_1^b$ over an angle $\pi/2$, $b = 1, \ldots, C - 1$, and let the sets $V_0, \ldots, V_C$ be given by

$$
\begin{align}
V_C &= \left\{ \mathbf{x} \mid (\mathbf{x} - \mathbf{y}_C)^T \mathbf{v}_1^{C-1} \geq 0 \right\}, \tag{3.29} \\
V_b &= \left\{ \mathbf{x} \mid \mathbf{x} \notin \cup_{a=b+1}^{C} V_a, \ (\mathbf{x} - \mathbf{y}_b)^T \mathbf{v}_1^b \geq 0 \right\}, \quad b = 1, \ldots, C-1, \tag{3.30} \\
V_0 &= \left\{ \mathbf{x} \mid \mathbf{x} \notin \cup_{a=1}^{C} V_a \right\}. \tag{3.31}
\end{align}
$$

Note that the sets $V_0, \ldots, V_C$ are disjoint, see Figure 3.8. The function g_C is defined for $\mathbf{x} \in V_C$
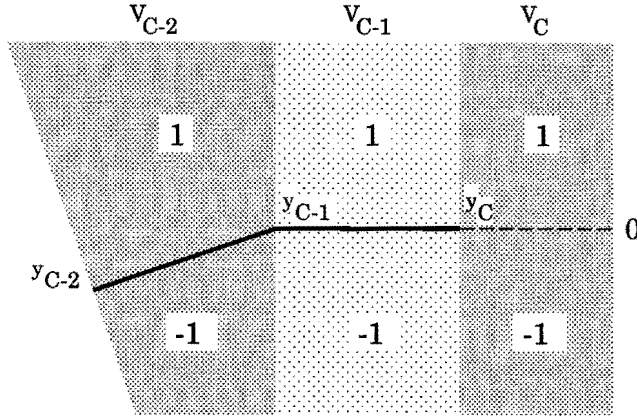
Figure 3.8: *Sets V_{C-2}, V_{C-1}, V_C and values of g_C.*

according to

$$g_C(\mathbf{x}) = \begin{cases} 1, & (\mathbf{x} - \mathbf{y}_C)^T \mathbf{v}_2^{C-1} > 0, \\ -1, & (\mathbf{x} - \mathbf{y}_C)^T \mathbf{v}_2^{C-1} < 0, \\ 0, & (\mathbf{x} - \mathbf{y}_C)^T \mathbf{v}_2^{C-1} = 0. \end{cases} \tag{3.32}$$

For $\mathbf{x} \in V_b$, $b = 1, \ldots, C - 1$, the function g_C is defined by

$$g_C(\mathbf{x}) = \begin{cases} 1, & (\mathbf{x} - \mathbf{y}_b)^T \mathbf{v}_2^b > 0 \text{ or } \mathbf{x} \in [\mathbf{y}_b, \mathbf{y}_{b+1}]_+, \\ -1, & (\mathbf{x} - \mathbf{y}_b)^T \mathbf{v}_2^b < 0 \text{ or } \mathbf{x} \in [\mathbf{y}_b, \mathbf{y}_{b+1}]_-. \end{cases} \tag{3.33}$$

And for $\mathbf{x} \in V_0$, the function g_C is defined by

$$g_C(\mathbf{x}) = \begin{cases} 1, & (\mathbf{x} - \mathbf{y}_1)^T \mathbf{v}_2^1 > 0, \\ -1, & (\mathbf{x} - \mathbf{y}_1)^T \mathbf{v}_2^1 < 0, \\ 0, & (\mathbf{x} - \mathbf{y}_1)^T \mathbf{v}_2^1 = 0. \end{cases} \tag{3.34}$$

Note that $g_C(\mathbf{y}_C) = 0$. The definition of g_C can be extended to smooth versions of the piecewise linear cracks considered in this thesis. However, such a definition is beyond the scope of the thesis.

In Section 3.1 moving least squares approximation has been considered. It has been described in which way shape functions are obtained and that the supports of these shape functions are equal to the supports of the weight functions, see (3.11) or (3.18). Moreover, it has been shown that the smoothness of the shape functions is related to the smoothness of the weight functions. When $\mathbf{x}$ is in the support of the shape function ϕ_a, or equivalently in the support of the weight function w_a, we say that the nodal point $\mathbf{x}_a$ has influence in $\mathbf{x}$.

For all crack discretizations for MLSA presented in this section, it is assumed that weight functions are initially defined without taking the crack into account. The weight functions are
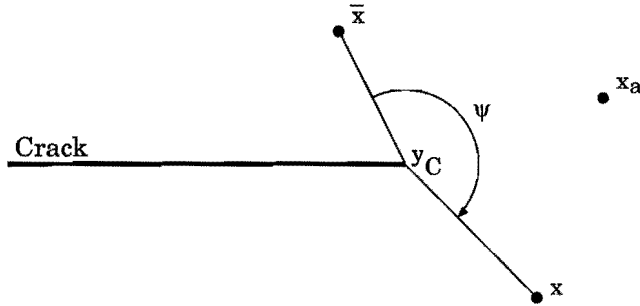
Figure 3.9: *Angle of influence.*

modified afterwards for the presence of a crack. These modified weight functions are used for MLSA on the cracked domain. Such a modification only considers a few nodal points and, for most cases, it is of the form

$$w_a^{\mathrm{new}}(\mathbf{x}) = d_a(\mathbf{x})w_a^{\mathrm{old}}(\mathbf{x}), \quad a = 1, \ldots, n. \tag{3.35}$$

The modification function $d_a(\mathbf{x})$ accounts for the crack in the material. For this function the following requirements are formulated:

[R1] Moving least squares approximation with the modified weight function w_a^{new} is well-defined for the entire domain.

[R2] The shape functions are able to represent quantities which are discontinuous over a crack.

[R3] Nodal points on one crack surface have no influence on the other crack surface.

[R4] The influence of nodal points near the crack tip may not extend over a polar angle which exceeds π.

The requirements R1 and R2 are obvious from the previous considerations. Requirement R3 states that when $\mathbf{x}_a$ is on one crack surface its shape function has to be zero on the other crack surface. Requirement R4, which can be seen as a generalization of R3, is illustrated in Figure 3.9. For the nodal point $\mathbf{x}_a$, the points $\mathbf{x}$ and $\bar{\mathbf{x}}$ in the support of w_a make an angle Ψ with respect to the crack tip $\mathbf{y}_C$. The maximum Ψ_a of these angles represents the angle over which the nodal point $\mathbf{x}_a$ has influence. This angle Ψ_a may not be too large, i.e. $\Psi_a \leq \pi$. The limit value in requirement R4 is a choice. One could also have taken a smaller value. However, since in this thesis nodal distributions are considered for which not many nodes are distributed in the angular direction around the crack tip, e.g. see Figure 3.15, this value may not be taken too small. Note that requirement R3 states that $\Psi_a < 2\pi$ for nodal points $\mathbf{x}_a$ on a crack surface. In the next sections it is seen whether the requirements R1-R4 can all be satisfied.

3.2.1   Discontinuous crack model of Belytschko

The first modification function to satisfy the requirements R1-R4 can be found in the paper of Belytschko et al. [7]. When nodal points, weight functions and basis functions have been
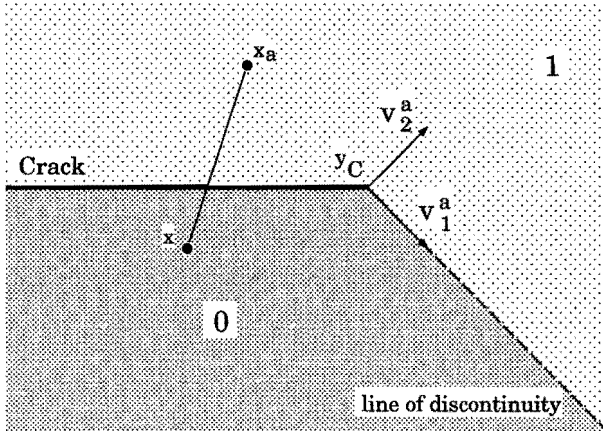
Figure 3.10: *Discontinuous crack model of Belytschko.*

chosen, nodal points $\mathbf{x}_a$ in the summation (3.4) are neglected if the line which connects $\mathbf{x}_a$ and the point under consideration $\mathbf{x}$, intersects the crack, see Figure 3.10.

This crack model can be put into the form (3.35). Let $\mathbf{v}_1^a$ be the unit vector in the direction of $\mathbf{y}_C - \mathbf{x}_a$ and let the vector $\mathbf{v}_2^a$ be obtained after anti-clockwise rotation over the angle $g_C(\mathbf{x}_a)\pi/2$. Then, for each nodal point $\mathbf{x}_a$, the modification function d_a is defined as

$$d_a(\mathbf{x}) = \begin{cases} 0, & g_C(\mathbf{x})g_C(\mathbf{x}_a) = -1, \ (\mathbf{x} - \mathbf{y}_C)^T\mathbf{v}_2^a < 0, \\ 1, & \text{otherwise.} \end{cases} \qquad (3.36)$$

When $g_C(\mathbf{x})g_C(\mathbf{x}_a) = -1$ the points $\mathbf{x}$ and $\mathbf{x}_a$ are positioned on different parts of the material and when $(\mathbf{x} - \mathbf{y}_C)^T\mathbf{v}_2^a < 0$ the line connecting $\mathbf{x}$ and $\mathbf{x}_a$ intersects the crack. In Figure 3.10, the values of d_a are depicted for a nodal point $\mathbf{x}_a$ for which $g_C(\mathbf{x}_a) = 1$.

The modification function d_a is discontinuous over the crack. Therefore, the modified weight function given by (3.35) is also discontinuous over the crack. Together with a continuous set of basis functions this results in shape functions which are discontinuous over the crack, see Section 3.1. Hence, requirement R2 is met. The shape functions for nodal points on a crack surface are zero on the opposite one, which means that requirement R3 is also met. From the definition (3.36) it follows that for nodal points $\mathbf{x}_a$ close to a crack surface, the angle of influence is approximately π. However, for nodal points ahead of the crack tip, the angle of influence can be about 2π. Therefore, requirement R4 is not met. Requirement R1 for MLSA can be guaranteed for this crack model by taking a sufficient number of nodal points in the neighbourhood of the crack tip or sufficiently large radii for the supports of the weight functions.

Hence, only requirement R4 is not met. This model, however, has another disadvantage. The modification function d_a is not only discontinuous over the crack, but also over a line in the interior of the material, see Figure 3.10. As a consequence, the shape functions are discontinuous in the interior of the material over several lines emanating from the crack tip. This makes the crack model not convenient for the approximation of quantities which are continuous in the material and discontinuous over a crack.
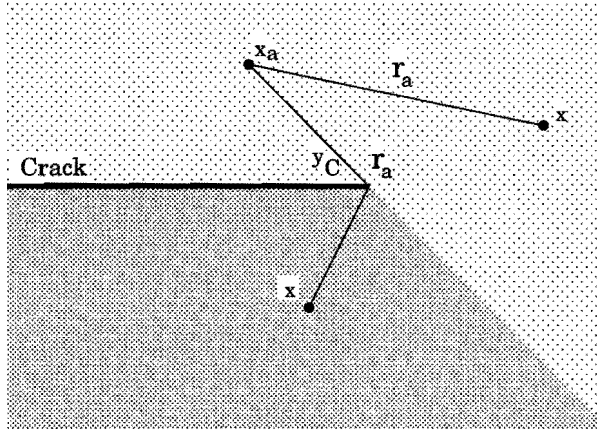
Figure 3.11: *Continuous crack model of Belytschko.*

3.2.2   Continuous crack model of Belytschko

Belytschko, Krongauz, Fleming, Organ and Liu [6] present an improvement of the previous crack model, which does not exactly fit in the form (3.35). In this model, discontinuities of the shape functions in the material are absent by a different manner of computation of the parameter r_a for the weight functions (3.22) and (3.23). The parameter r_a is given by, see also Figure 3.11,

$$r_a = \begin{cases} |\mathbf{x} - \mathbf{y}_C| + |\mathbf{x}_a - \mathbf{y}_C|, & g_C(\mathbf{x})g_C(\mathbf{x}_a) = -1, \ (\mathbf{x} - \mathbf{y}_C)^T \mathbf{v}_2^a < 0, \\ |\mathbf{x} - \mathbf{x}_a|, & \text{otherwise.} \end{cases} \tag{3.37}$$

Due to this improvement, the weight function is continuous over the line where the previous crack model failed to be continuous. However, the weight functions have discontinuous derivatives over this line with the consequence that the shape functions are continuous in the interior of the material but not continuously differentiable, see Section 3.1. The definition of r_a in (3.37) implies that for nodal points on one crack surface and close to the crack tip, the weight functions are non-zero on the other crack surface. Hence, the shape functions are also non-zero and this yields that the crack model violates requirements R3 and R4. It can be easily seen that requirement R2 is met, since r_a is discontinuous over the crack, which makes the weight and shape functions discontinuous over the crack.

Some other manners for the computation of r_a are presented in Organ, Fleming, Terry and Belytschko [58]. These manners are similar to (3.37) and violate also requirements R3 and R4. The problems of the crack model (3.37) were also recognized in [6], where it was remarked that application of the model in the element-free numerical solution method which is described in the next chapter, resulted in substantial oscillations in the stress fields near the crack tip.

The discontinuity in the modification function (3.36) can also be avoided by changing these functions in such a way that they are continuously differentiable in the material, e.g.
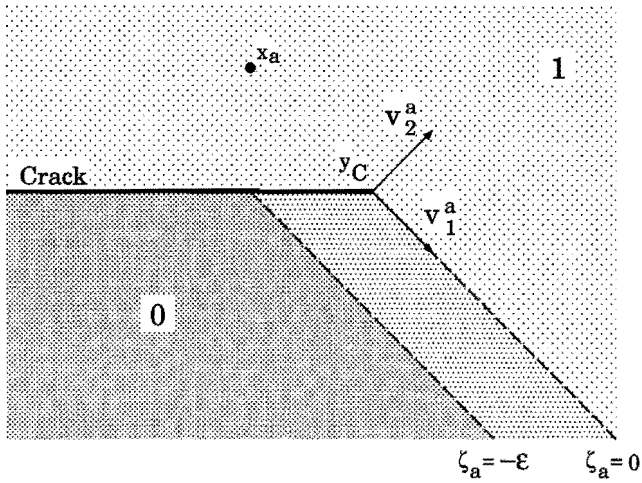
(a) Flat plot
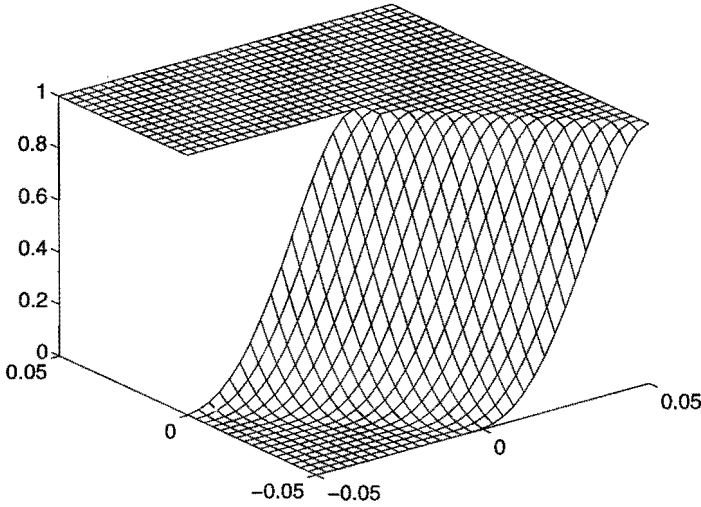
(b) Surface plot

Figure 3.12: *Continuous version of discontinuous crack model of Belytschko.*

$$
d_a(\mathbf{x}) = \begin{cases} 0, & g_C(\mathbf{x})g_C(\mathbf{x}_a) = -1, \ \zeta_a \leq -\varepsilon, \\ 1 - 6\frac{\zeta_a^2}{\varepsilon^2} + 8\frac{\zeta_a^3}{\varepsilon^3} - 3\frac{\zeta_a^4}{\varepsilon^4}, & g_C(\mathbf{x})g_C(\mathbf{x}_a) = -1, \ -\varepsilon < \zeta_a < 0, \\ 1, & \text{otherwise}, \end{cases} \tag{3.38}
$$

where $\zeta_a = (\mathbf{x} - \mathbf{y}_C)^T \mathbf{v}_2^a$ and ε is a positive constant.

In Figure 3.12, with the help of a flat and a surface plot, the values of d_a are depicted for a nodal point $\mathbf{x}_a$ for which $g_C(\mathbf{x}_a) = 1$. By means of $(3.38)^2$ the function d_a varies in the zone $-\varepsilon < \zeta_a < 0$ between 0 and 1 such that d_a is continuously differentiable. Hence, the weight functions and, therefore, the shape functions, are continuously differentiable in the material and discontinuous over the crack. However, for nodal points on a crack surface, the shape functions are continuous over the crack and, as for (3.37), requirements R3 and R4 are violated.

3.2.3   Continuous crack model

In Hegen [31] another crack model is suggested in order to meet the requirements R1-R4. Similar to (3.38) the following modification function d_a is introduced, see also Figure 3.13,

$$d_a(\mathbf{x}) = \begin{cases} 0, & g_C(\mathbf{x})g_C(\mathbf{x}_a) = -1,\ \zeta \leq -\varepsilon_a < 0, \\ 1 - 6\dfrac{\zeta^2}{\varepsilon_a^2} + 8\dfrac{\zeta^3}{\varepsilon_a^3} - 3\dfrac{\zeta^4}{\varepsilon_a^4}, & g_C(\mathbf{x})g_C(\mathbf{x}_a) = -1,\ -\varepsilon_a \leq \zeta < 0, \\ 1, & \text{otherwise}, \end{cases} \qquad (3.39)$$

where $\zeta = (\mathbf{x} - \mathbf{y}_C)^T \mathbf{v}_1^{C-1}$, ε_a is a non-negative constant and $\mathbf{v}_1^{C-1}$ is the unit vector used in the definition (3.29). It is suggested to take $\varepsilon_a = \max(R_a - |\mathbf{x}_a - \mathbf{y}_C|, 0)/4$, with R_a the radius of the support of the weight function w_a. In Figure 3.13, by means of a flat and a surface plot, the values of d_a are depicted for a nodal point $\mathbf{x}_a$ for which $g_C(\mathbf{x}_a) = 1$.

This modification function is continuously differentiable in the material and discontinuous over the crack. Hence, via the modified weight function (3.35) shape functions are discontinuous over the crack and requirement R2 is met. The requirements R3 and R4, however, are still violated. Nodal points on one crack surface have a non-zero shape function on the other crack surface. By taking a small value for ε_a one can try to isolate this inconvenience on a small part of the crack surface. Large gradients in the modification function and hence, in the shape functions are then the result.

3.2.4   Wedge model for crack

The previous crack models show that it is not possible to meet the requirements R1-R4. In fact, requirement R1 is in conflict with requirements R3 and R4. In order for MLSA to be well-defined in the crack tip $\mathbf{y}_C$, a certain number of weight functions should be non-zero in $\mathbf{y}_C$. Since the weight functions have to be continuous in the material (in order to have continuous shape functions), one cannot avoid that nodal points near the crack tip have a large angle of influence Ψ_a. Therefore, requirement R1 is weakened to:

[R1a] Moving least squares approximation with the modified weight function w_a^{new} is well-defined for the entire domain except for the crack tip.

Concerning the nodal distribution, it is assumed that one nodal point coincides with the crack tip. For simplicity, this nodal point is taken to be $\mathbf{x}_1$, i.e. $\mathbf{x}_1 = \mathbf{y}_C$. It is shown now that it
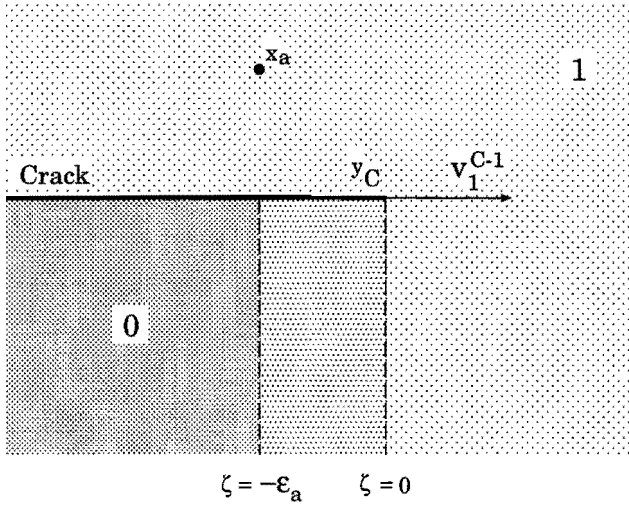
(a) Flat plot
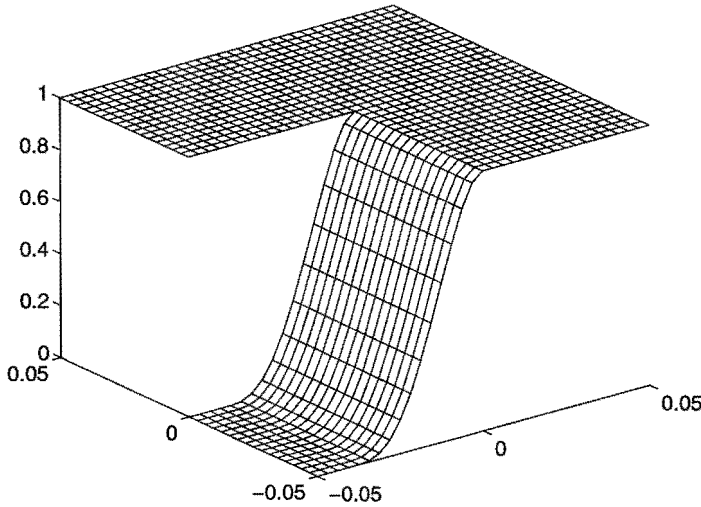
(b) Surface plot

Figure 3.13: *Continuous crack model.*

is possible to meet the requirements R1a-R4. Therefore, a modification function d_a is given, which is built from three functions d_a^1, d_a^2 and d^3. The function d_a^1 accounts for the requirements R1a-R4. Since these requirements consider only a small neighbourhood of the crack tip, the function is only used in this neighbourhood. On the remaining part the function d_a^2 is used which is continuously coupled with d_a^1 with the help of the function d^3.

For the definition of the functions, let θ be the polar angle of $\mathbf{x}$ with respect to the local coordinate system with $\mathbf{y}_C$ as origin, such that the lines $\theta = \pm\pi$ correspond with the crack faces. Let θ_a be the polar angle of the nodal point $\mathbf{x}_a$. The function d_a^1 is then given for $a > 1$ by

$$
d_a^1(\mathbf{x}) = \begin{cases} 0, & |\theta - \theta_a| \geq \omega/2, \\ \left(2(\frac{\zeta_a^1}{R_1})^2 - (\frac{\zeta_a^1}{R_1})^4\right)\left(2(\frac{\zeta_a^2}{R_1})^2 - (\frac{\zeta_a^2}{R_1})^4\right), & |\theta - \theta_a| < \omega/2. \end{cases} \tag{3.40}
$$

For $a = 1$, one sets $d_1^1(\mathbf{x}) = 1$. R_1 is the radius of the support of w_1, $\zeta_a^1 = \min(R_1, (\mathbf{x} - \mathbf{y}_C)^T \mathbf{v}_1^a)$, $\zeta_a^2 = \min(R_1, (\mathbf{x} - \mathbf{y}_C)^T \mathbf{v}_2^a)$ and

$$
\mathbf{v}_1^a = \begin{bmatrix} -\sin(\theta_a - \omega/2) & \cos(\theta_a - \omega/2) \end{bmatrix}^T, \tag{3.41}
$$

$$
\mathbf{v}_2^a = \begin{bmatrix} \sin(\theta_a + \omega/2) & -\cos(\theta_a + \omega/2) \end{bmatrix}^T. \tag{3.42}
$$

In the flat and surface plot given in Figure 3.14, the values of d_a^1 are depicted for a nodal point $\mathbf{x}_a$ for which $g_C(\mathbf{x}_a) = 1$. By means of $(3.40)^2$ the function d_a^1 varies in the wedge $\theta_a - \omega/2 < \theta < \theta_a + \omega/2$ between 0 and 1 such that d_a^1 is continuously differentiable. Since in the neighbourhood of a crack the nodal points are mostly distributed equidistant in two mutually orthogonal directions, see Figure 3.15, we suggest $\omega = 3\pi/4$ for the wedge angle in order for MLSA to be well-defined near the crack tip.

Let the function d_a^2 for $a > 1$ be given by

$$
d_a^2(\mathbf{x}) = \begin{cases} 0, & g_C(\mathbf{x}_a) = -1, \ \theta \geq \theta_a + \pi, \\ 0, & g_C(\mathbf{x}_a) = +1, \ \theta \leq \theta_a - \pi, \\ 1, & \text{otherwise}. \end{cases} \tag{3.43}
$$

For $a = 1$, one sets $d_a^2(\mathbf{x}) = 1$. The function d_a^2 is similar to the modification function (3.36) for the discontinuous crack model of Belytschko. Furthermore, let the function d^3 be defined by

$$
d^3(\mathbf{x}) = \begin{cases} 1, & r \leq R_1, \\ 2(2 - \frac{r}{R_1})^2 - (2 - \frac{r}{R_1})^4, & R_1 < r < 2R_1, \\ 0, & r \geq 2R_1, \end{cases} \tag{3.44}
$$

where $r = |\mathbf{x} - \mathbf{y}_C|$. Hence, the continuous differentiable function d^3 has value 1 near the crack and vanishes at a remote distance of the crack.

The function d_a^2 is discontinuous over a line in the material. However, by premultiplication with $1 - d^3$ this discontinuity is outside the support of the weight function w_a, since the radii R_a for the supports of the weight functions of the nodal points close to the crack tip, are near the radius R_1 of the support of w_1. The modification function d_a is now given by

$$
d_a(\mathbf{x}) = d^3(\mathbf{x})d_a^1(\mathbf{x}) + \left(1 - d^3(\mathbf{x})\right) d_a^2(\mathbf{x}). \tag{3.45}
$$
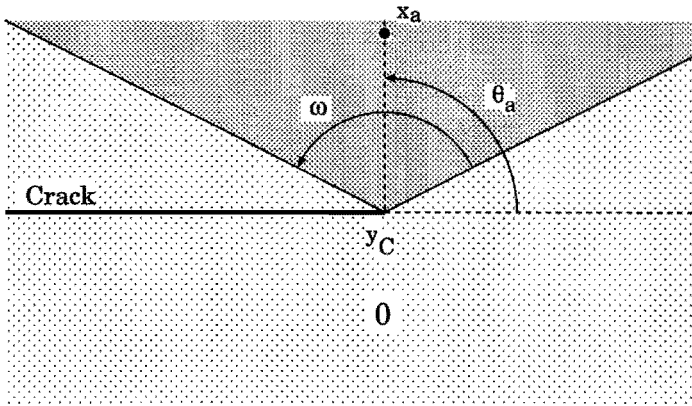
(a) Flat plot
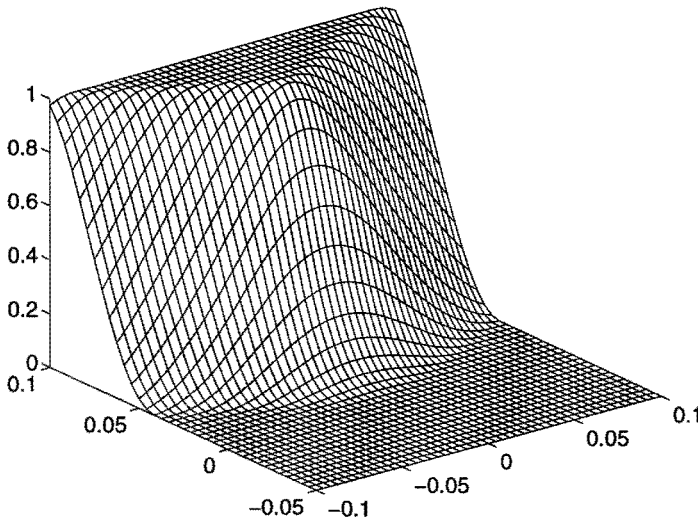
(b) Surface plot

Figure 3.14: *Wedge around* $\mathbf{x}_a$ *with* $\mathbf{y}_C$ *as vertex.*

Hence, d_a behaves like d_a^1 in the neighbourhood of the crack tip and like d_a^2 for most of the remaining part of the material. Note that $d_1(\mathbf{x}) = 1$ and that $d_a(\mathbf{y}_C) = 0$, $a > 1$.

It is seen easily from (3.45) and the definitions of d_a^1 and d_a^2 that requirement R3 is met. Because the wedge angle ω for d_a^1 is less than π and because of the definition of d_a^2, the angles of influence for the nodal points do not exceed π, which means that requirement R4 is valid. Requirement R2 is also met, because shape functions are discontinuous over the crack. By taking a sufficient amount of nodal points in the vicinity of the crack or sufficiently large radii

for the weight functions, MLSA is well-defined for the entire material, except for the crack tip $\mathbf{y}_C$. The discontinuity of d_a is exterior to the supports of the weight functions, which yields continuously differentiable modified weight functions (3.35). This yields that the shape functions are continuously differentiable, except for the crack tip $\mathbf{y}_C$.

For the crack tip $\mathbf{y}_C$, one has that $w_a(\mathbf{y}_C) > 0$ only for $a = 1$. Hence, MLSA is not well-defined for the crack tip. The matrix A given in (3.9) is singular. Nevertheless, a value can be obtained for the approximant u^h given by (3.1). Therefore, assume the constant function $p_1(\mathbf{x}) = 1$ is among the basis functions. Then by changing to the basis $\{p_1(\mathbf{x}), p_2(\mathbf{x}) - p_2(\mathbf{y}_C), \ldots, p_m(\mathbf{x}) - p_m(\mathbf{y}_C)\}$, MLSA is still well-defined for the domain, except for the crack tip. For $\mathbf{y}_C$ the approximant (3.1) equals

$$u^h(\mathbf{y}_C) = \mu_1(\mathbf{y}_C)p_1(\mathbf{y}_C) + \sum_{c=2}^{m} \mu_c(\mathbf{y}_C)(p_c(\mathbf{y}_C) - p_c(\mathbf{y}_C)) = \mu_1(\mathbf{y}_C). \tag{3.46}$$

The coefficients $\mu_c(\mathbf{y}_C)$, $c > 1$ do not have to be computed, while $\mu_1(\mathbf{y}_C)$ can be found from minimization of

$$S(\boldsymbol{\mu}) = w_1(\mathbf{y}_C)(\mu_1(\mathbf{y}_C) - u_1)^2. \tag{3.47}$$

Equation (3.46) shows that u^h can still be given a value and that u^h is continuous. The values for $\mu_c(\mathbf{y}_C)$ for $c > 1$ can not be found due to the singular matrix A, which yields that u^h is not differentiable for $\mathbf{y}_C$. The shape functions ϕ_b are special cases of u^h (take $u_a = \delta_{ab}$ in (3.10)) from which one can conclude that the shape functions for this model are continuously differentiable, except for the crack tip where they are only continuous. In the case of continuously differentiable basis functions, the derivatives of the shape functions and the derivatives of the approximant are bounded in the neighbourhood of the crack tip. A mathematical proof of this and of the previous statements can be found in Appendix C.

For the wedge model requirements R1a-R4 are all met. The displacements for cracked elastic material are also continuously differentiable except for the crack tip, see (2.21). Hence, one can conclude that among the presented crack models the wedge model is the most suitable crack model for the representation of displacements in cracked elastic material. Therefore, this model is used in the sequel for MLSA near a crack.

3.2.5   Nodal distributions and basis functions

In the previous subsections several modifications of weight functions for the presence of a crack have been presented. The other parameters for MLSA are now considered in the case of a crack.

In order to provide accurate approximations for a function in the vicinity of a crack tip and to guarantee that MLSA is well-defined, the following is done concerning the nodal distributions. It is accomplished by means of reflection that the nodes are locally symmetric with respect to the line segment $[\mathbf{y}_{C-1}, \mathbf{y}_C]$ of the crack, see Figure 3.15. Furthermore, the nodal distribution is refined by addition of extra patterns of nodes in the neighbourhood of the crack. These extra patterns are also locally symmetric with respect to $[\mathbf{y}_{C-1}, \mathbf{y}_C]$, see Figure 3.15. Hence,
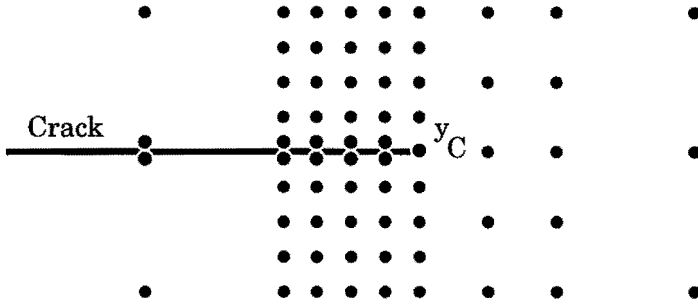
Figure 3.15: *Extra locally symmetric pattern of nodes near crack, more nodes just behind crack tip than ahead of crack tip.*

nodal points on the crack are double, i.e., for a nodal point $\mathbf{x}_a$ on one crack surface there is a corresponding nodal point $\mathbf{x}_b = \mathbf{x}_a$, $a \neq b$, on the other crack surface. The extra nodal patterns are also equidistant and the occurrence of double points which are not on the crack, is avoided.

In this section it has been concluded that the wedge model is the most suitable model for moving least squares approximation near a crack. Application of this model by means of (3.35), however, yields that near the crack surfaces just behind the crack tip $\mathbf{y}_C$ only a few nodes are involved in the sum (3.4). As described in Section 3.1 this can lead to shape functions which are locally strongly non-polynomial. To avoid this feature, more nodes are placed just behind the crack tip than ahead of the crack tip, see Figure 3.15. However, then one can still have that only a few nodes are involved in (3.4) for points close to the crack tip. Therefore, the radii of some nodes near the crack tip are taken larger. For the nodes $\mathbf{x}_a$ which are behind the crack tip, i.e., which are not in the set V_C, see (3.29), and for which

$$|\mathbf{x}_a - \mathbf{y}_C| \leq 1.75 R_1, \tag{3.48}$$

the radii of the supports of the weight functions w_a are changed to

$$R_a^{\text{new}} = 1.5 R_a^{\text{old}}. \tag{3.49}$$

For all the other nodal points, the radii R_a remain unchanged. In (3.48), R_1 is the radius of the support of w_1, which is the weight function for the nodal point $\mathbf{x}_1$ positioned at the crack tip. The parameters in (3.48) and (3.49) are just a choice. One can replace them by values which are smaller than or larger than 1.75 and 1.5, respectively.

It was shown in Section 2.2 that the displacements of a linearly elastic medium show a $\sqrt{r}$-behaviour (r being the distance to the crack tip) in the neighbourhood of a crack, see (2.21). In order to obtain an accurate approximation of the displacements near the crack tip, the function $\sqrt{r}$ is added to the set of basis functions as suggested in [31]. The shape functions then show a $\sqrt{r}$-behaviour in the neighbourhood of the crack tip, see Figure 3.16. Furthermore, these functions are not differentiable in the crack tip since the derivatives reveal a $1/\sqrt{r}$ singularity. On the remaining part of the material the shape functions are continuously differentiable.

Since the displacements of a linearly elastic medium only show a $\sqrt{r}$-behaviour in a small neighbourhood of the crack tip, it is not necessary to use the basis function $\sqrt{r}$ for the entire
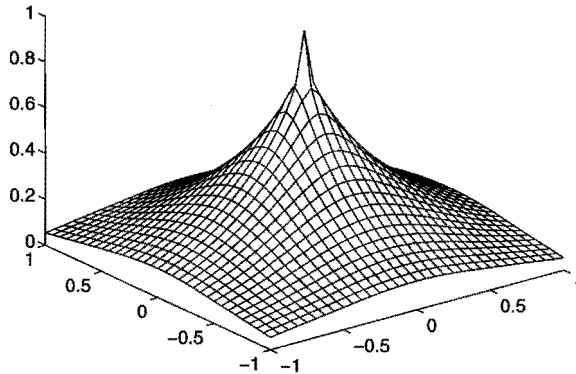
Figure 3.16: *Shape function with square root behaviour.*

material. The use of a local basis function which is only non-zero in a small neighbourhood of the crack tip and which behaves like $\sqrt{r}$ in this neighbourhood, looks convenient. However, the fact that such a basis function vanishes on a large part of the material, results in MLSA being not well-defined for that part. Taking such a function in the basis in the vicinity of the crack tip only, leads to discontinuous shape functions.

More promising is the use of a basis function which is the square root function combined with a monomial, i.e., a continuously differentiable function which equals $\sqrt{r}$ in a neighbourhood of $\mathbf{y}_C$ and which behaves like a monomial on most of the remaining material. The $\sqrt{r}$-behaviour near the crack tip can then be achieved and MLSA can then be made well-defined for the material. Therefore, in the sequel the following basis function p is used:

$$p(\mathbf{x}) = d^3(\mathbf{x})\sqrt{r} + (1 - d^3(\mathbf{x}))x_1 x_2, \tag{3.50}$$

where $\mathbf{x} \in \Omega$ and $r = |\mathbf{x} - \mathbf{y}_C|$ the distance to the crack tip. The function d^3 is given in (3.44). Hence, the basis function (3.50) behaves like $\sqrt{r}$ near the crack tip and like $x_1 x_2$ on most of the remaining material.

3.3   Other connectivity-free approximation techniques

Connectivity-free approximation techniques are often addressed in literature as techniques for scattered data interpolation or approximation. An overview and comparison of some classes of such techniques is found in the paper of Franke [26].

The first class of techniques discussed in [26] are inverse distance weighted methods. These methods have the drawback that generally low-order polynomials, especially linear functions, cannot be represented exactly. Moreover, approximants do not have to be differentiable at nodal points, see Gordon and Wixom [28]. In [43] and [44], these techniques are extended

to the concept of moving least squares approximation with singular weight functions. The latter technique can represent low-order polynomials exactly and reveals the selectivity property (3.19). As has been shown in Section 3.1, the use of singular weight functions yields shape functions which are locally strongly non-polynomial.

The second class of techniques discussed in [26] are blending methods based on a division of the domain into rectangles or triangles. In order to obtain approximations of quantities which can be discontinuous over a crack in the material, such a division has to match the crack and, therefore, these techniques are not connectivity-free. This is also the case for the third class of techniques discussed, which are techniques based on finite element divisions of the domain.

The other classes of techniques which are considered in [26], Foley's methods and global basis function type methods, respectively, all reveal the problem that low-order polynomials, especially linear functions, cannot be represented exactly. This however, did not stop researchers to apply a global basis function technique, the so-called multi-quadratic technique, in a numerical method, see Kansa [38, 39].

Another connectivity-free interpolation technique used in a numerical method, is the interpolation technique related to smoothed particle hydrodynamics, see Monaghan [53]. The approximant $u^h(\mathbf{x})$ of a function $u(\mathbf{x})$ on the domain Ω is given for $\mathbf{x} \in \Omega$ by the weighted integral

$$u^h(\mathbf{x}) = \int_\Omega w(\mathbf{x} - \mathbf{y})u(\mathbf{y}) \, d\Omega. \tag{3.51}$$

The weight function $w(\mathbf{x})$ is such that it approaches Dirac's delta function $\delta(\mathbf{x})$, i.e., w has a relatively small compact support which contains the origin $\mathbf{0}$ and

$$\int_\Omega w(\mathbf{x}) \, d\Omega = 1. \tag{3.52}$$

In general, the approximant (3.51) cannot represent linear functions exactly. Furthermore, since exact values for the integral in (3.51) cannot be determined, numerical integration is necessary to obtain accurate values for u^h. In [5] it is shown that when the finite sum (3.4) is replaced by an integral, this continuous counterpart of moving least squares approximation can be seen as equivalent to (3.51).

We conclude that other connectivity-free approximation techniques can hardly be found which provide shape functions with as nice properties as those for moving least squares approximation. These properties are:

- The shape functions have compact support.

- The shape functions are continuously differentiable in the interior of the problem domain and behave locally as high-order polynomials.

- Low-order polynomials can be represented exactly by the shape functions.

- Special shapes, like $\sqrt{r}$, can be added to the shape functions.

- In the case of the presence of a crack, shape functions can be obtained which are convenient for the representation of the linear elastic displacement field near a crack tip.

The main drawback of MLSA is its computational effort. For each point under consideration, a linear system has to be solved to obtain the values of the shape functions. This is in contrast with FE-shape functions which are obtained per element. Some modifications of MLSA have been proposed to reduce these computational costs, see Franke and Nielson [27] and [44]. These modifications concern the computation of the values of the vector μ for a set of discrete points only. With these values new modified vectors $\bar{\mu}$ are obtained for the entire domain in a relatively cheap way. In [44] this is done by a composition with spline methods and FE-methods with the consequence that a connectivity is introduced which prevents the technique from being connectivity-free. In [27] new vectors $\bar{\mu}$ are obtained for the entire domain by means of a weighted method in such a way that the resulting shape functions can represent linear functions exactly. However, for this latter approach the shape functions do have supports which are reasonably larger than the supports of the given weight functions. Hence, this technique is more non-local than MLSA.

From the considerations in this section we conclude that to come to an element-free numerical solution method for a boundary value problem we have to make use of the shape functions obtained by moving least squares approximation. This solution method is described in Chapter 4.

Chapter 4

Element-free Galerkin method

In this chapter an element-free numerical method known as the element-free Galerkin method, in short EFG-method, is presented for the solution of a boundary value problem. Firstly, the discrete equations are considered. Shape functions obtained by moving least squares approximation (MLSA) are used for the approximation of the displacements in linearly elastic material. Secondly, a description is given of the numerical integration to obtain the discrete equations. Convergence aspects of the EFG-method are investigated and the chapter ends with a description of the computation of fracture mechanics parameters from an EFG-analysis of a fracture mechanics problem.

The element-free Galerkin method has already been considered in [7], [48] and [56]. The method as introduced in this chapter, however, differs in some ways from the EFG-techniques described in these papers. In [56], where the method was given the name diffuse elements, a term in the derivatives of the MLSA-shape functions is neglected. Furthermore, to find the contribution of an integration point to the stiffness matrix, nodal points which have influence in the integration point are determined in a rather arbitrary way. In [7] and [48], the EFG-method is reported in its current form. In these papers, the derivatives of the MLSA-shape functions are obtained in a correct way. To find the contribution of an integration point to the stiffness matrix, nodal points which have influence in the integration point are determined correctly by using the weight functions. For numerical integration a scheme has been introduced by means of a division of the problem domain into integration cells.

In this chapter new concepts for the EFG-method are introduced. Integration points for an integration cell are chosen in a different way than described in [7] and [48], and the scheme for integration in a cell is adapted in the case of the presence of a crack. Furthermore, special basis functions and special integration cells near a crack tip are used. Stress intensity factors are obtained by means of contour integration with a correction for the crack-surface integrals.

4.1 Discrete equations

Consider a planar problem of deformation of an elastic medium, e.g. see (2.1), (2.3)-(2.5) and (2.9). It is assumed that a set of nodal points $\{x_a\}_{a=1,...,n}$, a set of weight functions $\{w_a(x)\}_{a=1,...,n}$ and a set of basis functions $\{p_c(x)\}_{c=1,...,m}$ are chosen such that moving least

squares approximation is well-defined for the undeformed configuration Ω of the elastic medium. As described in Section 3.1, MLSA results in shape functions $\phi_a(\mathbf{x})$, $a = 1, \ldots, n$. In a similar way as in the finite element method, these shape functions are used to obtain approximate solutions for the displacements, strains and stresses in the medium.

In general, the shape functions ϕ_a can be non-zero on the boundary of the domain, when $\mathbf{x}_a \notin \partial\Omega$. Therefore, the weak form (2.17) of the problem of deformation is used to account for the essential boundary conditions. Like in the finite element method, see (2.49), one sets

$$\mathbf{u}(\mathbf{x}) = \sum_{a=1}^{n} \mathbf{d}_a \phi_a(\mathbf{x}). \tag{4.1}$$

Since the shape functions generally fail to satisfy the selectivity property (3.19), the vector $\mathbf{d}_a$ does not have to contain the nodal values of $\mathbf{u}$, i.e., in general

$$\mathbf{u}(\mathbf{x}_a) \neq \mathbf{d}_a, \quad a = 1, \ldots, n. \tag{4.2}$$

For the Lagrange multiplier $\boldsymbol{\lambda}$ on Γ_u one sets

$$\boldsymbol{\lambda}(\mathbf{x}) = \sum_{b=1}^{k} \mathbf{l}_b \psi_b(\mathbf{x}), \tag{4.3}$$

where $\mathbf{x} \in \Gamma_u$ and $\{\psi_b(\mathbf{x})\}_{b=1,\ldots,k}$ is a set of shape functions on Γ_u. For this set of functions, the shape functions ϕ_a restricted to Γ_u are taken for those a with $\mathbf{x}_a \in \Gamma_u$, which yields that $k < n$. When according to a Galerkin approach the test displacements $\delta\mathbf{u}$ and the test Lagrange multipliers $\delta\boldsymbol{\lambda}$ in (2.17) are also taken of the form (4.1) and (4.3), respectively, one obtains the following linear system for $\mathbf{d}_a$ and $\mathbf{l}_b$,

$$\begin{bmatrix} K & L \\ L^T & 0 \end{bmatrix} \begin{bmatrix} \mathbf{d} \\ \mathbf{l} \end{bmatrix} = \begin{bmatrix} \mathbf{f} \\ \mathbf{r} \end{bmatrix}. \tag{4.4}$$

The matrix 0 contains only zeros and the vectors $\mathbf{d}$ and $\mathbf{l}$ contain the nodal vectors $\mathbf{d}_a$ and $\mathbf{l}_b$, respectively,

$$\mathbf{d}^T = \begin{bmatrix} \mathbf{d}_1^T & \cdots & \mathbf{d}_n^T \end{bmatrix}, \tag{4.5}$$

$$\mathbf{l}^T = \begin{bmatrix} \mathbf{l}_1^T & \cdots & \mathbf{l}_k^T \end{bmatrix}. \tag{4.6}$$

The stiffness matrix K and the matrix L for the Lagrange multipliers are built from 2×2 nodal submatrices K_{ab} and L_{ab}, respectively, and the right-hand side vectors $\mathbf{f}$ and $\mathbf{r}$ are built from 2×1 nodal subvectors $\mathbf{f}_a$ and $\mathbf{r}_b$. These submatrices and subvectors are given by

$$K_{ab} = \int_\Omega B_a^T D B_b \, d\Omega, \quad a, b = 1, \ldots, n, \tag{4.7}$$

$$L_{ab} = -\int_{\Gamma_u} \phi_a \psi_b I \, d\Gamma, \quad a = 1, \ldots, n, \ b = 1, \ldots, k, \tag{4.8}$$

$$\mathbf{f}_a = \int_\Omega \phi_a \mathbf{f}^* \, d\Omega + \int_{\Gamma_p} \phi_a \mathbf{p}^* \, d\Gamma, \quad a = 1, \ldots, n, \tag{4.9}$$

$$\mathbf{r}_b = -\int_{\Gamma_u} \psi_b \mathbf{u}^* \, d\Gamma, \quad b = 1, \ldots, k. \tag{4.10}$$

The matrix I is the 2×2 identity matrix while the matrix B_a is given by

$$
B_a = \begin{bmatrix} \phi_{a,1} & 0 \\ 0 & \phi_{a,2} \\ \phi_{a,2} & \phi_{a,1} \end{bmatrix}, \quad a = 1, \dots, n. \tag{4.11}
$$

The 3×3 matrix D represents the constitutive equations of the elastic material, e.g. see (2.55).

When the boundary Γ_u consists (in addition) of a set of discrete points, one obtains a similar linear system (4.4), see [30]. In (4.8) and (4.10), the integrals then have to be replaced by finite sums. Notice that K_{ab} is non-zero only when ϕ_a and ϕ_b are non-zero on a common part of Ω, i.e., when the intersection of the supports of ϕ_a and ϕ_b is not empty.

Solving the linear system (4.4) for $\mathbf{d}$ and $\mathbf{l}$ and using (4.1) results in approximations for the displacements. Taking derivatives of (4.1) and subsequently using the constitutive equations, e.g. (2.9), leads to approximate values for the strains and stresses in the material.

To arrive at the discrete equations in this section, a Galerkin approach is considered with shape functions which are obtained without using an element division. Therefore, the method is named element-free Galerkin method.

4.2 Numerical integration

To obtain the stiffness matrix K, the matrix L, and the right-hand side vectors $\mathbf{f}$ and $\mathbf{r}$ for the discrete equations (4.4) of the EFG-method, integrals over the domain Ω and the boundaries Γ_p and Γ_u have to be evaluated. The exact values for these integrals cannot be computed. Therefore, numerical integration is necessary to obtain approximate values. As in the FE-method, the domain and the boundary are partitioned into subdomains, so-called integration cells, and the integrations are performed numerically for each cell.

Since the shape functions in the EFG-method are quite general and not, contrary to the FE-method, obtained by a transformation of local (polynomial) functions, there is no optimal division of the domain and the solution depends on this division, see [30] or Krysl and Belytschko [42]. The pattern for numerical integration by the set of integrations cells, however, has to account for the local mesh size of the distribution of nodal points. Moreover, the pattern should be such that a small variation in the number of cells results in a small change in the solution. This is described in the present section. In order to obtain values for integrals of quantities which are discontinuous over a crack, it is shown in which way the configuration of integrations cells accounts for such a discontinuity. Furthermore, special integration cells near the crack tip are considered when a $\sqrt{r}$-like function is added to the basis.

4.2.1 Division into integration cells

For a numerical evaluation of the domain integral for the stiffness matrix K in (4.4), the domain Ω is divided into a number of integration cells Δ_e, $e = 1, \dots, N$, as proposed in [7], see Figure 4.1. For these cells we take triangles and quadrilaterals. The division is such that two
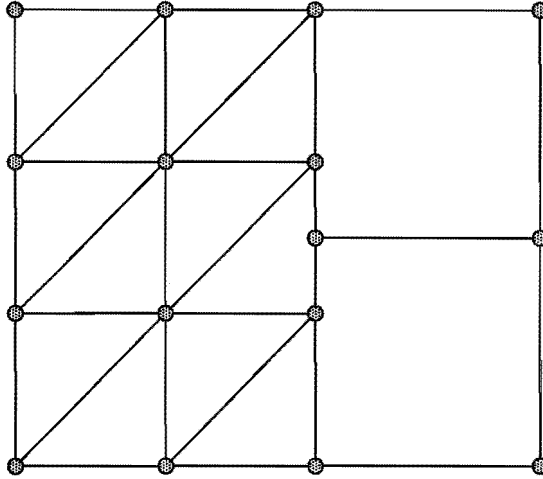
Figure 4.1: *Integration cells with definition points for Ω.*

integration cells can only have parts of their boundaries in common and such that

$$\Omega = \bigcup_{e=1}^{N} \Delta_e. \tag{4.12}$$

In contrast with a division of Ω into finite elements, as described in Section 2.3, it is not necessary for a division into integration cells that two integration cells having a part of a side in common, must have the entire side in common, see Figure 4.1.

Each integration cell Δ_e, $e = 1, \ldots, n$, is defined with the help of a number of so-called definition points $\mathbf{z}_\varrho^e$. Hence, the division of Ω into integration cells is fully described by the connectivity of the definition points $\mathbf{z}_\varrho^e$. This connectivity, however, is independent of the choice for the nodal distribution, the basis functions and the weight functions.

With the help of the connectivity of the definition points for the integration cells, the integral (4.7) is evaluated numerically for each integration cell in the following way. Similar as in the FE-method, for each group of integration cells Δ_e of the same type, a standard integration cell Δ_s is considered. The Cartesian coordinates in Δ_s are denoted by ξ_1 and ξ_2. Each definition point $\mathbf{z}_\varrho^e \in \Omega_e$ corresponds with a local definition point $\boldsymbol{\xi}_\varsigma \in \Delta_s$. Local shape functions $\varphi_\varsigma(\boldsymbol{\xi})$ correspond with the local definition points. These shape functions are polynomials such that the selectivity property (2.41) with respect to the local definition points holds true and such that φ_ς vanishes on the sides of Δ_s on which $\boldsymbol{\xi}_\varsigma$ is not positioned.

Let the following mapping from the standard cell Δ_s onto the cell Δ_e be defined with the help of the local shape functions:

$$\mathbf{x}(\boldsymbol{\xi}) = \sum_\varsigma \mathbf{z}_{\varrho(\varsigma)}^e \varphi_\varsigma(\boldsymbol{\xi}). \tag{4.13}$$

In equation (4.13), $\boldsymbol{\xi} \in \Delta_s$, the index ς sums over the local definition points, and $\mathbf{z}_{\varrho(\varsigma)}^e$ is the definition point which corresponds with the local definition point $\boldsymbol{\xi}_\varsigma$. Note the similarity with

the isoparametric mapping (2.43) in Section 2.3.

With the help of the mapping (4.13) the integral (4.7) over the integration cell Δ_e is obtained by

$$\int_{\Delta_e} B_a^T(\mathbf{x}) D B_b(\mathbf{x}) \, d\Delta = \int_{\Delta_s} B_a^T(\mathbf{x}(\boldsymbol{\xi})) D B_b(\mathbf{x}(\boldsymbol{\xi})) \left| \frac{\partial \mathbf{x}}{\partial \boldsymbol{\xi}} \right| d\Delta. \tag{4.14}$$

The integral over the standard integration cell Δ_s is then evaluated numerically by means of Gaussian quadrature, see [2, Ch. 5]. In the sequel it is described in which way the integration points for Gauss integration are determined for Δ_s.

Summation of all cell contributions (4.14) leads to the nodal submatrix K_{ab}. A similar procedure leads to the domain integral for the right-hand side subvectors $\mathbf{f}_a$. By means of divisions of the boundaries Γ_p and Γ_u into boundary integration cells, the boundary integrals in (4.8)-(4.10) are determined numerically.

In most situations, integration cells Δ_e are used which have the shape of a square and which are given with the help of four definition points. As a consequence, the Jacobian in (4.14) is constant. The sizes of the integration cells are taken of the same order as the maximum mesh size of the nodal distribution. The boundary integration cells are mostly taken to be the non-empty intersections of the volume integration cells with the boundaries Γ_p and Γ_u.

Since the shape functions for MLSA are locally high-order polynomials, see Section 3.1, high-order Gaussian quadrature is performed in Δ_s. In the sequel of this section it is described that triangular integration cells given by three definition points are used to match a crack. For a triangle we take the 13-point Gaussian quadrature formula given in Cowper [19], which has degree of precision 7. Equivalently for a quadrilateral (4,4)-point Gaussian quadrature is used, which has the same degree of precision. For a boundary integration cell 4-point Gaussian quadrature is taken.

The division of the domain into integration cells Δ_e is independent of the discretization for moving least squares approximation. However, in order to obtain accurate entries for the submatrices (4.7), (4.8) and subvectors (4.9), (4.10) for both coarse and fine MLSA-discretizations, the pattern for numerical integration has to account for the distribution of nodes. More accuracy is required near the boundary of the domain, near a crack and near the crack tip, since less nodal points are involved in the summation (3.4). As a result, the shape functions tend to be locally strongly non-polynomial as was shown in Section 3.1. The pattern for numerical integration accounts for the distribution of nodes in the following way.

For each integration cell Δ_e, the standard integration cell Δ_s is split into a number of subcells of the same size. Per subcell (4,4)-point or 13-point Gaussian quadrature is then performed to obtain the integral (4.14). The number of subcells depends on the distribution of the nodes near Δ_e and the size and position of this cell. For the integration cell Δ_e, the nodal points $\mathbf{x}_a$ are determined which are either in the cell or which have one of the vertices of the cell in the support of their weight function w_a. It is assumed that these nodal points contribute only to the cell contributions for K. The number of subcells is then based on the mean distance of these nodal points to the central point of Δ_e, the characteristic size of the integration cell Δ_e and on the number of nodal points in Δ_e. Furthermore, it is taken into account whether the
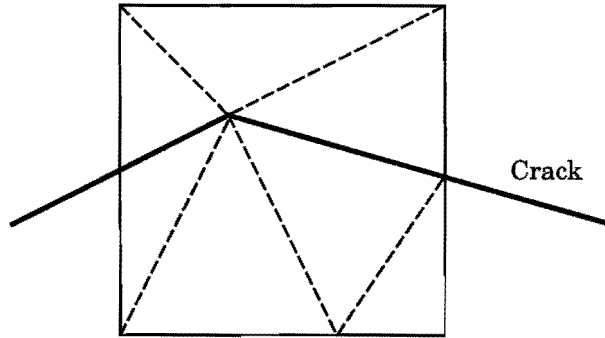
Figure 4.2: *Internal subdivision of integration cell.*

integration cell is near the boundary, near the crack or near the crack tip. This procedure to arrive at the number of subcells for quadrilateral, triangular and boundary integration cells is given in Appendix D. The procedure is designed in such a way that, when the subdivision is transformed to Δ_e by (4.13), approximately the same number of integration points is used for each quadrilateral made up of nodal points. Only near the boundary and near the crack the number of integration points is larger.

4.2.2   Cell configuration near a crack path

Shape functions are discontinuous over a crack, see Section 3.2. Hence, the configuration of integration cells has to determine accurately the integrals of quantities which are discontinuous over a crack. Gauss quadrature, however, assumes a certain degree of continuity of the quantities which have to be integrated, see [2]. It is therefore essential that integration is not performed in a cell which contains (a part of) a crack in its interior. Hence, the configuration of integration cells has to match the crack. However, the complex process of generating a set of cells for a domain with a crack has to be avoided, since otherwise the configuration of integration cells must be adapted after each crack increment (in a quasi-static analysis).

The configuration of integration cells can be chosen independently of the distribution of nodes for moving least squares approximation. Hence, one can easily account for a crack in the domain during the process of building up the matrices K_{ab}, L_{ab} and the vectors $\mathbf{f}_a$ and $\mathbf{r}_b$. A division of Ω into integration cells Δ_e is assumed where the presence of a crack is neglected. During the process of the numerical computation of submatrices and subvectors for each cell Δ_e, the presence of (a part of) a crack in the cell is checked. If a crack is not present, numerical integration is performed in the cell as described above. When (a part of) a crack is present in the cell, a subdivision of Δ_e into triangular subcells is generated, which matches the crack, see Figure 4.2. This subdivision into triangular subcells is obtained by using the program SEPMESH of the SEPRAN package [64]. The integrations are then performed for each triangular subcell as described above. Summation of the contributions of these subcells results in the contribution of Δ_e.

One should notice that when two neighbouring integration cells are subdivided because of the
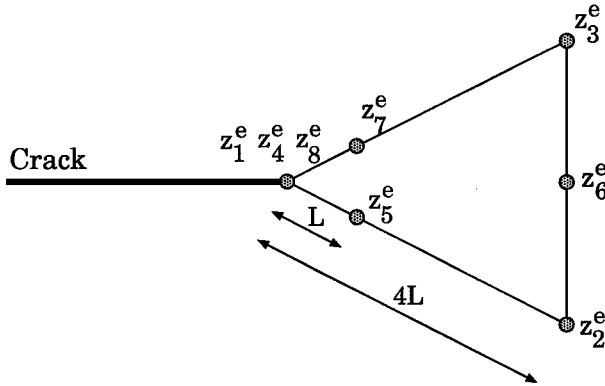
Figure 4.3: *Triangular integration cell with crack tip as vertex.*

presence of a crack in the cells, the subdivisions of the two cells are made independently of each other. In the case of simulation of crack propagation, the internal subdivisions into triangular integration cells can be used in the next computation steps. In one of the following steps, it is then possible that some of these triangular integration cells can be subdivided again.

4.2.3 Cell configuration near a crack tip

In the case of the use of a basis function with $\sqrt{r}$-behaviour for MLSA (with r being the distance to the crack tip), the shape functions ϕ_a contain a $\sqrt{r}$-component. This results in singular derivatives of the shape functions which behave like $1/\sqrt{r}$ near the crack tip. A special integration pattern is then necessary in the neighbourhood of the crack tip in order to obtain sufficiently accurate values for the domain integrals in (4.7). To this end, not only each integration cell containing a crack tip is subdivided into triangular subcells, but also each integration cell for which the crack tip is positioned on their boundaries. Hence, the crack tip is a vertex of a set of triangular integration cells, which matches the crack. While each triangular cell is defined with three definition points as the vertices of the cell, the triangular cells which surround the crack tip are defined by eight definition points $\mathbf{z}_1^e, \ldots, \mathbf{z}_8^e$, see Figure 4.3. These points are such that $\mathbf{z}_1^e = \mathbf{z}_4^e = \mathbf{z}_8^e = \mathbf{y}_C$, $\mathbf{z}_2^e$ and $\mathbf{z}_3^e$ represent the other two vertices, $\mathbf{z}_5^e = (3\mathbf{z}_1^e + \mathbf{z}_2^e)/4$, $\mathbf{z}_6^e = (\mathbf{z}_2^e + \mathbf{z}_3^e)/2$ and $\mathbf{z}_7^e = (3\mathbf{z}_1^e + \mathbf{z}_3^e)/4$. The square $\Delta_s = \{(\xi_1, \xi_2) \mid -1 \leq \xi_1 \leq 1, -1 \leq \xi_2 \leq 1\}$ with eight local definition points is taken as standard integration cell, similar to the crack-tip element of Barsoum [3] described in Section 2.3. The mapping (4.13) with bi-quadratic local shape functions on Δ_s then behaves like $\sqrt{r}$ along the cell sides for $\xi_1 \to -1$. Therefore, accurate values for the cell integrals over Δ_e are obtained with (4.14) when $\phi_a \sim \sqrt{r}$ in the neighbourhood of the crack tip.

In the case of simulation of quasi-static crack propagation, the triangular integration cells surrounding the crack tip can in most cases also be used in the following steps of the process. However, these cells are then defined with three definition points only. When the crack tip is at the vertex of a quadrilateral integration cell, the cell is split into triangular subcells, but in the following steps again the quadrilateral cell is used.

(a)   (b)
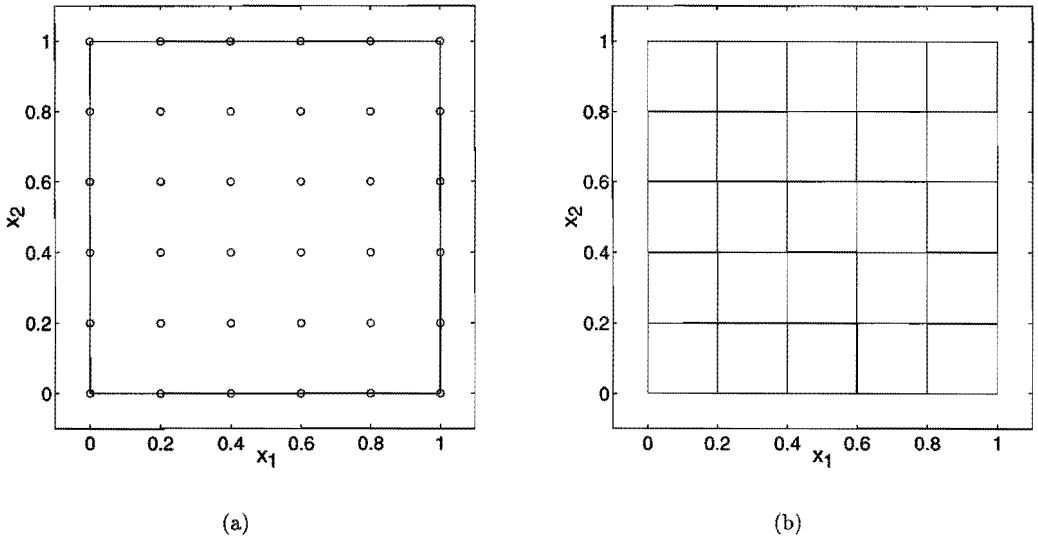
Figure 4.4: *Nodal distribution* (a) *and cell configuration* (b) *for patch tests.*

4.3   Convergence aspects of EFG-method

In this section the performance of the EFG-method in two-dimensional elasto-static problems is studied. Results of some patch tests are considered as well as convergence aspects of the method. In each example, all the quantities and material parameters are thought of as being non-dimensional. Homogeneous, isotropic, linearly elastic material behaviour is assumed and volume forces f_i^* are absent. The arbitrary material parameters are taken to be $E = 1$ and $\nu = 0.25$.

Some convergence studies for the EFG-method have already been reported, e.g. see the papers [7], [30] and [48]. In these papers, however, the integration points for an integration cell are chosen in a different way than in the scheme proposed in Section 4.2 and Appendix D.

The results reported in this section are obtained by means of an implementation of the EFG-method in the MATLAB programming environment [51]. A schematic set-up of an EFG-analysis for a (cracked) material domain is found in Appendix B. By a comparison of the different steps in this set-up with those in the set-up for the FE-method given in this appendix, the similarity between the two methods can be seen.

4.3.1   Patch tests

As described by Taylor, Simo, Zienkiewicz and Chan [69], satisfaction of several patch tests for a FE-formulation is a necessary and a sufficient condition for convergence of the formulation. In these patch tests the ability of the FE-formulation to represent linear elasto-static solutions on the problem domain is investigated. Two patch tests proposed in [69] are studied for the

EFG-parameters	$\|\mathbf{u}^h - \mathbf{u}\|_0/\|\mathbf{u}\|_0$	$\|\mathbf{u}^h - \mathbf{u}\|_1/\|\mathbf{u}\|_1$
Gaussian, $\upsilon = 2.0$, 36 nodes, 25 cells	$3.93 \cdot 10^{-5}$	$1.67 \cdot 10^{-4}$
Gaussian, $\upsilon = 2.5$, 36 nodes, 25 cells	$1.45 \cdot 10^{-4}$	$9.74 \cdot 10^{-4}$
Polynomial, $\upsilon = 2.0$, 36 nodes, 25 cells	$4.82 \cdot 10^{-4}$	$2.88 \cdot 10^{-3}$
Polynomial, $\upsilon = 2.5$, 36 nodes, 25 cells	$1.81 \cdot 10^{-3}$	$1.21 \cdot 10^{-2}$
Gaussian, $\upsilon = 2.0$, 121 nodes, 100 cells	$1.36 \cdot 10^{-5}$	$1.10 \cdot 10^{-4}$
Gaussian, $\upsilon = 2.5$, 121 nodes, 100 cells	$7.79 \cdot 10^{-5}$	$7.44 \cdot 10^{-4}$
Polynomial, $\upsilon = 2.0$, 121 nodes, 100 cells	$1.35 \cdot 10^{-4}$	$1.61 \cdot 10^{-3}$
Polynomial, $\upsilon = 2.5$, 121 nodes, 100 cells	$6.33 \cdot 10^{-4}$	$9.42 \cdot 10^{-3}$

Table 4.1: *EFG-results for problem of prescribed linear boundary displacements, linear basis.*

EFG-method.

Consider the patch shown in Figure 4.4a. This patch has length 1 in the x_1- and x_2-directions. An equidistant distribution of nodal points for MLSA is depicted in the figure. With a linear basis, the shape functions obtained by MLSA are able to represent linear displacements exactly, see (3.12). However, these linear displacements are generally not exactly obtained from an EFG-analysis because of errors introduced by numerical integration. This is due to the fact that the shape functions are not piecewise polynomial as has been shown in Section 3.1, which means that it is not possible to obtain sufficiently accurate values for the system (4.4) by numerical integration, which has also been remarked in [30] and [40].

Furthermore, shape functions for nodal points near the boundary of the domain are generally non-zero on this boundary. This implies that the imposition of the exact boundary displacements in the EFG-method is not possible. Therefore, additional errors are introduced due to the fact that the essential boundary conditions are not satisfied.

This can be seen from the following patch test. Let displacements be given according to the elasto-static solution of the problem of a uniform axial stress σ applied at the boundary $x_1 = 1$. In a situation of plane stress these displacements are given by

$$u_1 \;=\; \frac{\sigma}{E}x_1, \tag{4.15}$$

$$u_2 \;=\; -\nu\frac{\sigma}{E}x_2, \tag{4.16}$$

where $0 \leq x_1 \leq 1$, $0 \leq x_2 \leq 1$.

Let the displacements (4.15), (4.16) be imposed at all the boundary nodes. The set $\{1, x_1, x_2\}$ is taken as set of basis functions, 36 and 121 nodal points are used and the domain is divided into 25 and 100 integration cells Δ_e, see Figure 4.4b. Weight functions of Gaussian and polynomial type, see (3.22), (3.23), and two different values for the parameter υ are considered. The radii of the supports of the weight functions are proportional to the values of υ, see (3.28). Errors in the computed solutions are found in Table 4.1, where $\|\mathbf{u}\|_0$ is the norm of the Sobolev space $H^0(\Omega)$, i.e.

$$\|\mathbf{u}\|_0 = \left(\int_\Omega u_i u_i \, d\Omega \right)^{1/2}, \tag{4.17}$$

EFG-parameters	$\|\mathbf{u}^h - \mathbf{u}\|_0/\|\mathbf{u}\|_0$	$\|\mathbf{u}^h - \mathbf{u}\|_1/\|\mathbf{u}\|_1$
Gaussian, $\upsilon = 2.0$, 36 nodes, 25 cells	$4.86 \cdot 10^{-5}$	$2.40 \cdot 10^{-4}$
Gaussian, $\upsilon = 2.5$, 36 nodes, 25 cells	$2.18 \cdot 10^{-4}$	$1.44 \cdot 10^{-3}$
Gaussian, $\upsilon = 2.0$, 36 nodes, 64 cells	$2.60 \cdot 10^{-3}$	$8.86 \cdot 10^{-3}$
Gaussian, $\upsilon = 2.5$, 36 nodes, 64 cells	$1.92 \cdot 10^{-4}$	$6.40 \cdot 10^{-4}$
Polynomial, $\upsilon = 2.0$, 36 nodes, 25 cells	$1.67 \cdot 10^{-5}$	$9.55 \cdot 10^{-5}$
Polynomial, $\upsilon = 2.5$, 36 nodes, 25 cells	$2.71 \cdot 10^{-5}$	$2.40 \cdot 10^{-4}$
Polynomial, $\upsilon = 2.0$, 36 nodes, 64 cells	$2.49 \cdot 10^{-5}$	$1.10 \cdot 10^{-4}$
Polynomial, $\upsilon = 2.5$, 36 nodes, 64 cells	$8.87 \cdot 10^{-5}$	$3.46 \cdot 10^{-4}$

Table 4.2: *EFG-results for problem with constant uniaxial stress, linear basis.*

and $\|\mathbf{u}\|_1$ is the norm of the Sobolev space $H^1(\Omega)$, i.e.

$$\|\mathbf{u}\|_1 = \left(\int_\Omega u_i u_i + u_{i,j} u_{i,j} \, d\Omega \right)^{1/2} . \tag{4.18}$$

These errors are obtained numerically by means of the division of the domain Ω into integration cells Δ_e.

The results of Table 4.1 show that, unless the fact that the boundary displacements are satisfied exactly at the nodes, indeed the solution (4.15), (4.16) is not obtained exactly for both the weight functions of Gaussian type and those of polynomial type. It is also seen that an increase of the radii for the supports of the weight functions leads to an increase in the error, since more nodal points in the interior influence the solution on the boundary. In this example, the performance of the EFG-method for weight functions of Gaussian type is slightly better than the performance of the weight functions of polynomial type. This can be explained from the fact that due to the exponential type of the Gaussian weight functions, see (3.22), the shape functions in the case of these weight functions tend faster to zero near the boundary of their supports. Hence, interior points have less influence on the boundaries in comparison with weight functions of polynomial type.

Table 4.1 shows that when the pattern of nodes is refined together with a refinement of the cell configuration, the errors in the computed displacements decrease due to the fact that the essential boundary conditions are satisfied in more boundary nodes. Therefore, we conclude that this patch test for the exact representation of the linear solution (4.15), (4.16) is satisfied in the weak sense, that is, for $h_a \to 0$, where h_a is the local mesh size, see (3.27).

As a second patch test, consider the solution (4.15), (4.16). This time, the displacement u_1 is prescribed at the boundary $x_1 = 0$ and u_2 is prescribed at $x_2 = 0$ by means of the Lagrange multiplier formulation (4.4). The constant normal stress σ is prescribed at the boundary $x_1 = 1$ while the boundary $x_2 = 1$ is stress-free. For an EFG-analysis 36 nodal points are taken in the domain, see Figure 4.4a, and $\{1, x_1, x_2\}$ is taken as set of basis functions. Weight functions of Gaussian type and polynomial type, a division into 25 and 64 integration cells and two different values for the parameter υ are considered. Results are summarized in Table 4.2.

In Table 4.2, again errors are found in the solution due to numerical integration and due to

the fact that the essential boundary conditions are not satisfied. An increase in the radii for the weight functions (due to an increase of v) generally leads to an increase in the errors, because more nodes influence the displacements at the boundaries. It is seen, especially for the weight functions of polynomial type, that there is not much difference in the results for the two divisions into quadrilateral integration cells. This test has also been considered with divisions into triangular integration cells, which leads to similar results.

Table 4.2 shows that in this example the performance of the weight functions of polynomial type is better than the performance of the weight functions of Gaussian type. Furthermore, the results for weight functions of polynomial type are less sensitive to a variation in the number of cells than the weight functions of Gaussian type. This is explained from the fact that the shape functions for weight functions of Gaussian type show a more exponential behaviour in contrast with those for the weight functions of polynomial type, which show a more polynomial behaviour. Hence, the latter type results in a better performance of the scheme proposed for numerical integration. Therefore, in the numerical examples that are considered in this chapter and in the next chapters, weight functions of polynomial type are used.

As for the first patch test, refinement of the nodal distribution together with a refinement of the cell configuration will lead to a decrease in the error due to a better satisfaction of the essential boundary conditions, since more shape functions are involved in the representation (4.3) of the Lagrange multiplier. Hence, it is concluded that this patch test for the exact representation of the linear solution (4.15), (4.16) is also satisfied in the weak sense.

In the two patch tests for the EFG-method, the problem has been considered that essential boundary conditions along a continuous part of the boundary are not satisfied. It should be remarked that for an elasto-static problem where only three displacements are prescribed, in order to suppress the rigid-body motions, the essential boundary conditions are exactly satisfied when these conditions are imposed at the corresponding points of the domain.

The element-free Galerkin method and the finite element method differ only in the choice for the shape functions and the numerical integration to obtain the discrete equations. Therefore, it is expected that, as described in [69] for the FE-method, satisfaction of the two patch tests implies convergence of the EFG-method. This is shown in the next numerical example.

4.3.2 Shear force on a plate

Consider the patch $0 \leq x_1 \leq l$, $0 \leq x_2 \leq d$, where $l = d = 1$ are the dimensions of the patch, see Figure 4.4. At the right boundary $x_1 = 1$, a transverse shear force F is applied. When the shear stress on this boundary is distributed according to $\sigma_{12} = -6(F/d^3)x_2(x_2 - 1)$, the cubic solution of the elasto-static problem in a situation of plane strain is given by, see Timoshenko and Goodier [70, Ch. 3],

$$u_1 = -\frac{F}{Gd^3}\left[3(1-\nu)x_1(2l-x_1) + (2-\nu)x_2(x_2-d)\right]\left(x_2 - \frac{d}{2}\right), \tag{4.19}$$

$$u_2 = \frac{F}{Gd^3}\left[(1-\nu)(3l-x_1)x_1^2 + 3\nu(l-x_1)(x_2-\frac{d}{2})^2 + \frac{d^2}{4}(4+\nu)x_1\right], \tag{4.20}$$
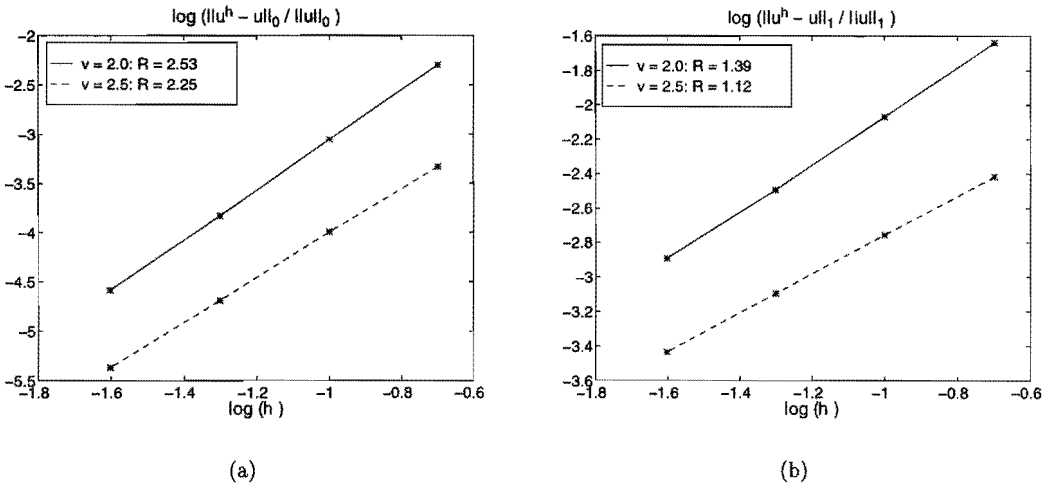
Figure 4.5: *EFG-errors and -convergence rates R for* (a) *H^0-norm and* (b) *H^1-norm, problem of shear force on a plate, linear basis.*

where $0 \leq x_1 \leq l$ and $0 \leq x_2 \leq d$.

The convergence of the EFG-method for this problem is studied. Equidistant patterns of 36, 121, 441 and 1681 nodal points together with a division of the domain into 25, 100, 400, and 1600 integration cells are taken, respectively. The linear set $\{1, x_1, x_2\}$ is taken as set of basis functions and weight functions of polynomial type are used with $\upsilon = 2.0$ and $\upsilon = 2.5$ in equation (3.28) for the radii of the supports. The displacements u_1 and u_2 are prescribed on the boundary $x_1 = 0$ and the shear stress σ_{12} is prescribed on $x_1 = 1$. The boundaries $x_2 = 0$ and $x_2 = 1$ are stress-free.

In Figure 4.5, the logarithms of the errors in the H^0- and H^1-norm, (4.17) and (4.18), are depicted versus the logarithm of the mesh parameter h. This parameter h is taken to be the distance between the neighbouring nodal points along lines $x_1 =$ constant. A linear correspondence is seen in the figure, which yields that the following estimate holds true for the errors in the Sobolev norms,

$$\|\mathbf{u}^h - \mathbf{u}\|_i \leq Mh^R \|\mathbf{u}\|_i, \quad i = 0, 1, \tag{4.21}$$

for positive constants M and R. Note that M and R may be different for $i = 0$ and $i = 1$. The constants R, so-called convergence rates, equal the slopes of the given lines. Their values are found in Figure 4.5

Figure 4.5 shows that the EFG-method converges and that the convergence rates R for the two values of υ exceed those for an equivalent FE-discretization, which are exactly 2 and 1 for the H^0- and H^1-norms, respectively, see [33, Ch. 4]. Similar convergence rates were obtained for this problem in the case of a division of the domain into triangular integration cells. Equivalent FE-discretizations should be understood as the use of element divisions which can represent linear displacements exactly, e.g. divisions into three-node triangles or four-node quadrilaterals.
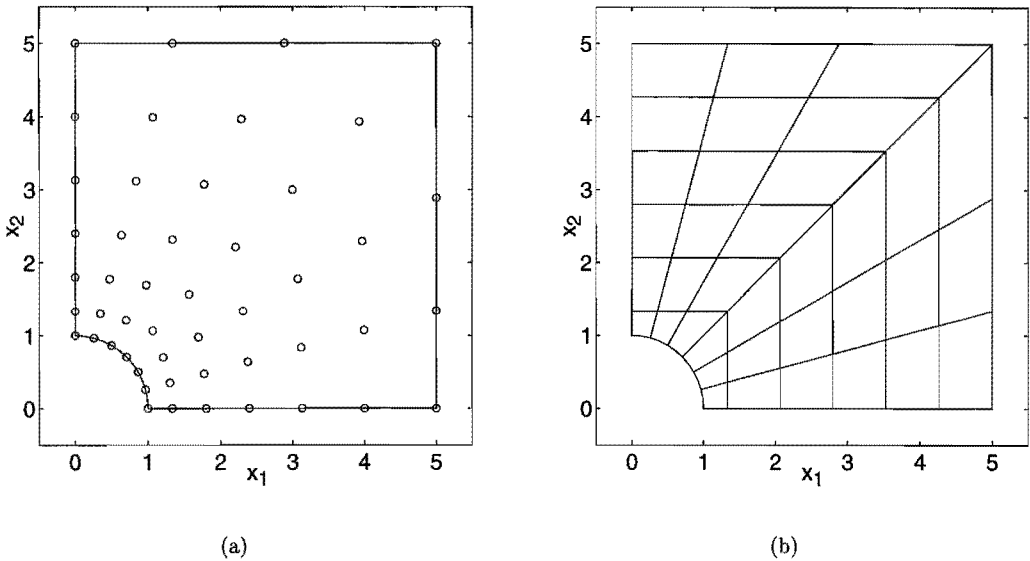
Figure 4.6: *Nodal distribution* (a) *and cell configuration* (b) *for problem of infinite plate with circular hole.*

The convergence rates for $v = 2$ are slightly larger than those for $v = 2.5$. In general, one expects higher convergence rates for an increase in v, since the shape functions then locally behave more as high-order polynomials, which make them more convenient for the representation of smooth and steep solutions. This is indeed the case as is seen in the next example.

4.3.3 Infinite plate with circular hole

We study the performance of the EFG-method for the problem of the plate with a circular hole. This problem has a non-polynomial solution and due to the circular boundary nodal patterns have to be used which are not equidistant in two mutually orthogonal directions.

Consider an infinite plate with a circular hole with radius a. Let a uniform axial tension σ in the x_1-direction be applied at infinity. The stresses in the plate for a situation of plane strain are then given by, see Atkin and Fox [1, Ch. 5],

$$\sigma_{11} = \sigma \left[1 - \frac{a^2}{r^2} \left(\frac{3}{2} \cos 2\theta + \cos 4\theta \right) + \frac{3a^4}{2r^4} \cos 4\theta \right], \tag{4.22}$$

$$\sigma_{12} = \sigma \left[-\frac{a^2}{r^2} \left(\frac{1}{2} \sin 2\theta + \sin 4\theta \right) + \frac{3a^4}{2r^4} \sin 4\theta \right], \tag{4.23}$$

$$\sigma_{22} = \sigma \left[-\frac{a^2}{r^2} \left(\frac{1}{2} \cos 2\theta - \cos 4\theta \right) - \frac{3a^4}{2r^4} \cos 4\theta \right], \tag{4.24}$$

where $r \geq a$ and $-\pi \leq \theta \leq \pi$ are polar coordinates. The corresponding displacements are

(a)   (b)
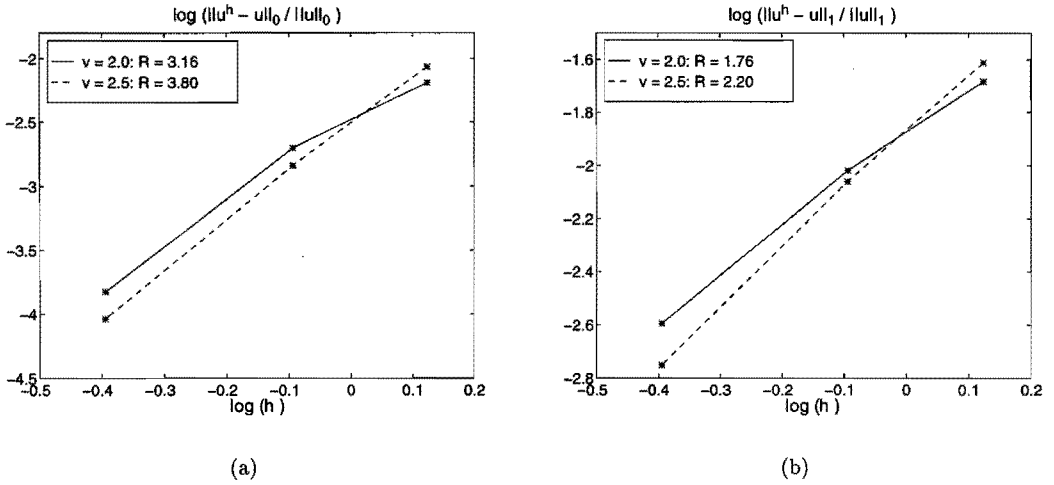
Figure 4.7: *EFG-errors and -convergence rates R for* (a) H^0-norm *and* (b) H^1-norm, *problem of infinite plate with circular hole, linear basis.*

given by

$$u_1 = \frac{\sigma}{2G}\left[(1-\nu)r\cos\theta + \frac{a^2}{r}\left(2(1-\nu)\cos\theta + \frac{1}{2}\cos 3\theta\right) - \frac{a^4}{2r^3}\cos 3\theta\right], \qquad (4.25)$$

$$u_2 = \frac{\sigma}{2G}\left[-\nu r\sin\theta - \frac{a^2}{r}\left((1-2\nu)\sin\theta - \frac{1}{2}\sin 3\theta\right) - \frac{a^4}{2r^3}\sin 3\theta\right]. \qquad (4.26)$$

Both the displacements and the stresses have relatively large gradients in the neighbourhood of the circular hole.

The part $0 \leq x_1 \leq 5$ and $0 \leq x_2 \leq 5$ of the upper right quadrant of the plate is considered, see Figure 4.6. On the boundaries $x_1 = 5$ and $x_2 = 5$ the applied tractions are prescribed according to (4.22)-(4.24). Displacements are prescribed according to $u_1 = 0$ on $x_1 = 0$ and $u_2 = 0$ on $x_2 = 0$. The circular boundary has radius $a = 1$ and is assumed traction-free. For EFG-analyses of the problem, the nodal points are spaced regularly in the θ-direction and irregularly in the r-direction, see Figure 4.6a, such that there are more points in the neighbourhood of the circular boundary in order to achieve accurate approximations of the steep displacements. The same number of points are taken in the r- and θ-directions. Weight functions of polynomial type are used with two different values for the parameter v for the determination of the radii of the weight functions. The set $\{1, x_1, x_2\}$ is taken as set of basis functions.

The problem domain is divided into integration cells Δ_e as depicted in Figure 4.6b. All integration cells are quadrilaterals defined with four definition points, except the cells next to the circular boundary which have five definition points to obtain a better approximation of this boundary. The same number of cells is taken in the r- and θ-directions.

The convergence of the EFG-method for this problem is investigated by means of EFG-analyses with 49, 121 and 441 nodal points together with a division into 36, 100 and 400 integration

(a)   (b)
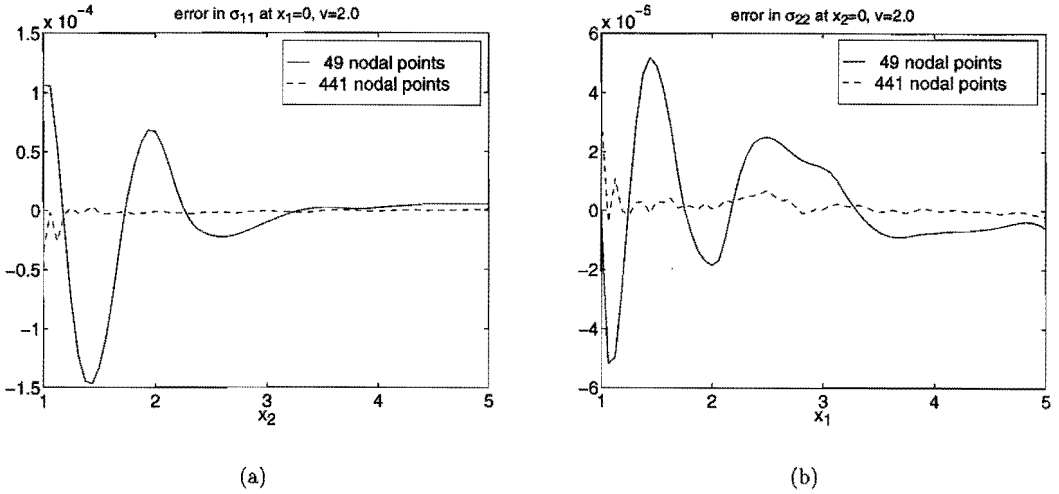
Figure 4.8: *EFG-errors in σ_{11} at $x_1 = 0$ (a) and in σ_{22} at $x_2 = 0$ (b), problem of infinite plate with circular hole, linear basis.*

cells, respectively. The local mesh size h_a, see (3.27), averaged over the nodal points $\mathbf{x}_a$ is taken as global mesh size h. In Figure 4.7, the logarithms of the errors are depicted versus the logarithm of h. Convergence rates R are also given in the figure. These rates are taken equal to the mean slope of the depicted lines.

The figure shows that the EFG-method converges for this problem, despite the non-convex domain and the approximation of it by integration cells. As in the previous example, the convergence rates exceed those for an equivalent FE-discretization, which are exactly 2 and 1 for the H^0- and H^1-norms, respectively. The convergence rates for $v = 2.5$ are higher than those for $v = 2.0$. This is due to the fact that the shape functions for $v = 2.5$ locally behave more as high-order polynomials than the ones for $v = 2.0$. Hence, the numerical integration scheme for the EFG-method performs better for these shape functions and an improved convergence of the representation of the displacements is obtained.

Convergence of the method is also seen from a comparison of the computed stresses with the solution (4.22)-(4.24). In Figure 4.8, the errors in the stresses σ_{11} and σ_{22} are depicted for $x_1 = 0$ and $x_2 = 0$, respectively. The value of σ in (4.22)-(4.24) was set to $1 \cdot 10^{-3}$. It is seen that for the distribution of 441 nodal points the stresses are in good agreement with the exact values.

The convergence of the EFG-method for this problem has also been studied with the quadratic set $\{1, x_1, x_2, x_1^2, x_1 x_2, x_2^2\}$ as set of basis functions. The same nodal distributions and divisions into integration cells are used as for the linear basis. Only larger values of v are considered, since more basis functions are involved. Logarithms of the errors and convergence rates for this approach are found in Figure 4.9.

It is seen again that the method converges and that the convergence rates exceed those for an equivalent FE-discretization, which are exactly 3 and 2, respectively for the H^0- and H^1-

(a)   (b)
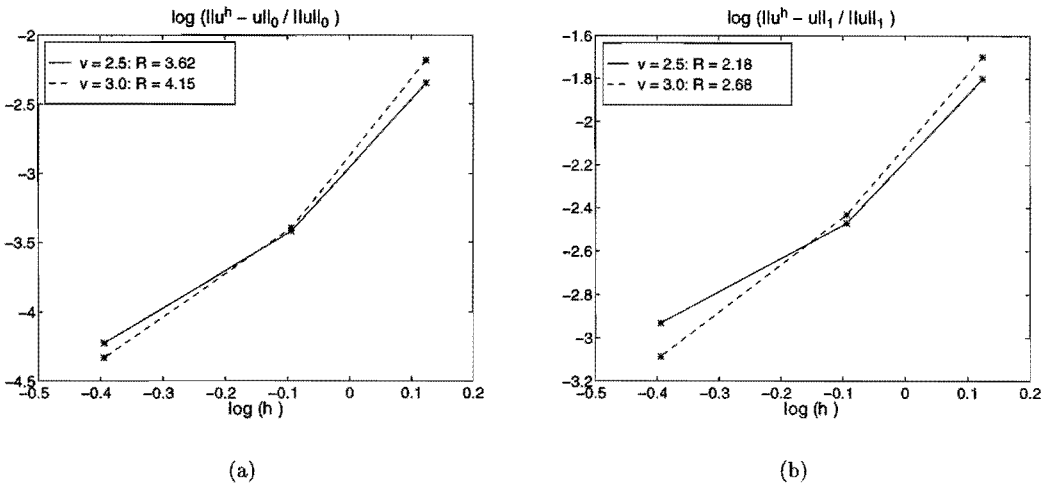
Figure 4.9: *EFG-errors and -convergence rates R for* (a) H^0*-norm and* (b) H^1*-norm, problem of infinite plate with circular hole, quadratic basis.*

norms, see [33, Ch. 4]. Equivalent FE-discretizations should be understood here as the use of element divisions which can represent linear and quadratic displacements exactly. For example, divisions into six-node triangles and/or nine-node quadrilaterals. The errors in Figure 4.9 are of the same order as the errors given in Figure 4.7 for the approach using the linear basis. As for the linear basis, an increase of v leads to an increase in the convergence rates. The convergence rates for $v = 3.0$ exceed those for the linear basis depicted in Figure 4.7. This is due to the fact that the shape functions for the quadratic basis can represent more low-order polynomials exactly than the ones for a linear basis. The rates for the quadratic basis do not exceed the ones for the linear basis in the case of $v = 2.5$. This can be explained from the fact that for the quadratic basis three extra basis function are involved. When the same radii of the weight functions are used for both sets of basis functions, the shape functions for the quadratic basis are locally more strongly non-polynomial than the ones for the linear basis. Hence, the numerical integration scheme for the EFG-method performs better for the linear basis resulting in lower convergence rates for the quadratic basis.

4.3.4   Conclusions and discussion

In this section the performance of the element-free Galerkin method has been studied. The numerical examples presented above lead to the following conclusions. The errors in the numerical solutions are attributed to errors due to numerical integration and to the fact that essential boundary conditions are not satisfied along continuous boundaries. However, patch tests for the exact representation of linear solutions are satisfied in the weak sense. From the reported results for the patch tests it was concluded that in the sequel weight functions of polynomial type are preferred to those of Gaussian type.

It has been shown that the EFG-method is a convergent method for elasto-static problems.

The convergence rates exceed those for equivalent finite element discretizations. Increase of the radii of the supports of the weight functions generally leads to an increase of the convergence rates. The same holds true for addition of higher order polynomials together with an increase in the radii.

Similar convergence rates have been reported in [7], [30] and [48]. In these papers, higher values for v were also used, which lead to higher convergence rates. In this thesis, however, we restrict ourselves to values for v which are relatively large with respect to the minimal value for MLSA to be well-defined. But v is not taken too large ($v \leq 3$), since an increase of v leads to a significant increase of the computational effort of the method. Furthermore, larger values for v result in linear systems (4.4), which are more non-sparse than those for smaller values.

From the examples it can also be concluded that the numerical integration scheme proposed in Section 4.2 and Appendix D, results in an accurate performance of the method for different sets of basis functions. Some variation of the number of cells and the type of cells resulted in similar convergence rates. Therefore, we conclude that in the case when the sizes of the integration cells are of the same order as the local mesh size of the nodal distribution, the performance of the EFG-method is almost independent of the division of the domain into integration cells.

4.4 Computation of fracture mechanics parameters

Consider an EFG-analysis of cracked material. Displacements, strains and stresses are determined as described Section 4.1. To use fracture criteria for crack growth, e.g. see (2.27) and (2.28), the stress intensity factors K_I and K_{II} have to be computed from these quantities. In this section several ways are described to determine the stress intensity factors.

In Section 2.2 the displacements and stresses near the crack tip were studied, see (2.18) and (2.21). In Section 3.2 it has been described how the $\sqrt{r}$-behaviour of these displacements and stresses can be captured in an EFG-analysis. Therefore, in the case of shape functions which behave like $\sqrt{r}$ near the crack tip, the stress intensity factors K_I and K_{II} can be determined with the help of (2.18), (2.21) and (A.1)-(A.10). For instance, K_I is computed from the displacements and stresses in the direction $\theta = 0$ ahead of the crack by means of

$$K_I = \lim_{r \to 0} \sqrt{2\pi r}\, \sigma_{22}(r, 0), \tag{4.27}$$

$$K_I = \lim_{r \to 0} \sqrt{2\pi r}\, \left(\sigma_{11}(r, 0) - \sigma_{11}^0\right), \tag{4.28}$$

$$K_I = \lim_{r \to 0} \frac{2G}{\kappa - 1} \sqrt{\frac{2\pi}{r}} \left(u_1(r, 0) - u_1^0\right), \tag{4.29}$$

and K_{II} is computed by means of

$$K_{II} = \lim_{r \to 0} \sqrt{2\pi r}\, \sigma_{12}(r, 0), \tag{4.30}$$

$$K_{II} = \lim_{r \to 0} \frac{2G}{1 - \kappa} \sqrt{\frac{2\pi}{r}} \left(u_2(r, 0) - u_2^0\right). \tag{4.31}$$

When $\sqrt{r}$ is left out of the basis for MLSA, the expressions (4.27)-(4.31) cannot be used. Moreover, as for an analysis by means of the FE-method, the displacements are represented by the finite sum (4.1). Hence, a finite number of shape functions represents the displacements near the crack tip. This implies that, despite the addition of $\sqrt{r}$ to the basis, an error is made in the representation of the angular variation in the displacements. Therefore, the use of expressions (4.27)-(4.31) for computation of the stress intensity factors does not have to result in sufficiently accurate values for K_I and K_{II}.

The stress intensity factors can also be found from the components of the $\mathbf{J}$-vector, see (2.35), (2.36). Under the assumption that $K_I \geq |K_{II}|$, these factors are given by

$$K_I \;=\; \frac{1}{2}\sqrt{\frac{8G}{\kappa+1}}\left(\sqrt{J_1-J_2}+\sqrt{J_1+J_2}\right), \tag{4.32}$$

$$K_{II} \;=\; \frac{1}{2}\sqrt{\frac{8G}{\kappa+1}}\left(\sqrt{J_1-J_2}-\sqrt{J_1+J_2}\right). \tag{4.33}$$

In (4.32) and (4.33), the components of $\mathbf{J}$ are taken with respect to the local coordinate system with the crack tip as origin. When $|J_2|/J_1 << 1$, equations (4.32), (4.33) can be approximated by Taylor expansions in J_2/J_1. These expansions are given by

$$K_I \;=\; \sqrt{\frac{8GJ_1}{\kappa+1}}\left(1-\frac{1}{8}\frac{J_2^2}{J_1^2}+O\left(\frac{J_2^4}{J_1^4}\right)\right), \tag{4.34}$$

$$K_{II} \;=\; \sqrt{\frac{8GJ_1}{\kappa+1}}\left(-\frac{1}{2}\frac{J_2}{J_1}+O\left(\frac{J_2^3}{J_1^3}\right)\right). \tag{4.35}$$

Hence, for $|J_2|/J_1 << 1$, J_2 has a greater influence on K_{II} than on K_I.

The $\mathbf{J}$-vector is determined by means of J-integration, see (2.31). In this equation the curve γ can be taken at a remote distance from the crack tip, while γ_C^+ and γ_C^- are curves along the (piecewise linear) crack surfaces from the begin and end points of γ to the crack tip. Due to the error in the representation of the displacements near the crack tip, the contribution of the integrals over γ_C^+ and γ_C^- can lead to inaccuracies in the components of $\mathbf{J}$. Taking into account that the crack surfaces are stress-free, the contributions are given by

$$\int_{\gamma_C^+ + \gamma_C^-} W_e n_k \, d\gamma = \int_{\gamma_C}\left(W_e^+ - W_e^-\right)n_k \, d\gamma, \quad k=1,2, \tag{4.36}$$

where $\gamma_C = \gamma_C^+$, $\mathbf{n}$ is the outward unit normal on γ_C^+ and W_e^+ and W_e^- are the elastic energy densities (2.32) on γ_C^+ and γ_C^-, respectively. With the help of (2.18) and (2.21) it can be shown that, see [20],

$$W_e^+ - W_e^- = -\frac{4(\kappa+1)\sigma_{11}^0 K_{II}}{E\sqrt{2\pi r}} + O(\sqrt{r}), \tag{4.37}$$

for $r \to 0$. Therefore, as suggested in [20], the contribution (4.36) to the components of $\mathbf{J}$ can be computed in an accurate way by leaving out a part of γ_C next to the crack tip as is described below.
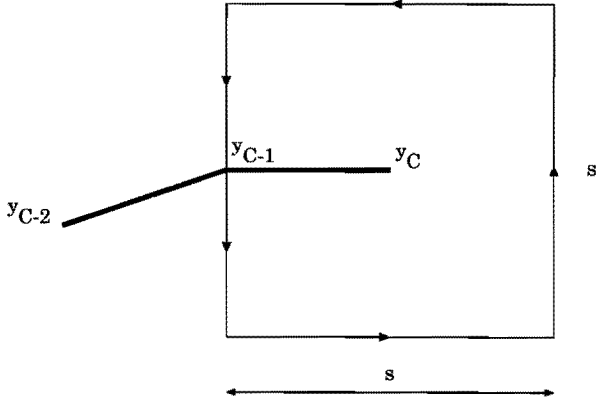
Figure 4.10: *Square curve for computation of* **J**.

Since a crack is represented as piecewise linear, γ_C consists of line segments. Consider (4.36) where γ_C is replaced by the curve γ_C^1, which is the curve γ_C without a small part with length ε_1 of the line segment next to the crack tip. With (4.37) this yields for $k = 1, 2$ that

$$\int_{\gamma_C^1} \left(W_e^+ - W_e^- \right) n_k \, d\gamma = \int_{\gamma_C} \left(W_e^+ - W_e^- \right) n_k \, d\gamma + \frac{8(\kappa + 1)\sigma_{11}^0 K_{II} n_k}{E\sqrt{2\pi}} \sqrt{\varepsilon_1}. \tag{4.38}$$

For γ_C^2, which is the curve γ_C without a small part with length $\varepsilon_2 \neq \varepsilon_1$ of the line segment next to the crack tip, the equation (4.38) holds true with ε_1 replaced by ε_2. By a convenient combination of (4.38) for γ_C^1 and γ_C^2, the value for (4.36) can be found. For this way of computation of the contribution (4.36) to the components of **J**, no integrations have to be performed over a part of γ_C next to the crack tip. Only the integrals for γ_C^1 and γ_C^2 have to be calculated. Hence, the problem of the inaccuracy of the representation of the displacements near the crack tip is circumvented.

In Section 2.3 a method for a FE-analysis was considered where the **J**-vector is obtained by means of crack extension, see [35] and [59]. Crack extension can also easily be modelled in the EFG-method by means of a shift of nodal points and leads to a small change in the stiffness matrix K. However, this change cannot be found as easily as in the FE-method. Many cells surrounding the crack tip have to be considered to determine the change in K. Therefore, the method of crack extension is not useful for application in the EFG-method.

As described by Moran and Shih in [54], the **J**-vector is determined in [48] by converting the integral in (2.31) over the curve γ into a domain integral over the domain enclosed by γ. However, then still integrations over the crack surfaces need to be performed. Furthermore, the enclosed domain contains the crack tip and, therefore, this domain integral is influenced by the inaccuracy in the representation of the angular variation in the displacements near the crack tip.

From the above considerations, it is concluded that J-integration by (2.31) and (4.38) is preferred to obtain the vector **J**. In the numerical examples shown in the sequel, a part of the last segment of the crack is taken for γ_C and a square curve perpendicular on the last crack segment

is taken for γ, see Figure 4.10. The size s of γ is taken larger than the length of the last crack segment. As for the computation of the boundary integrals in (4.8)-(4.10), the curves γ_C and γ are divided into integration cells to obtain the components of $\mathbf{J}$. The integrations in these cells are performed similar to the ones for the boundary integration cells described in Section 4.2. Furthermore, to compute the crack surface contributions (4.36) by means of (4.38), we take ε_1 and ε_2 equal to $0.75h_1$ and $1.5h_1$, h_1 being the local mesh size, see (3.27), of the nodal point in the crack tip.

In this chapter the essential features of the element-free Galerkin method have been introduced. The performance of the method was studied by means of application in two patch tests. Furthermore, convergence of the method has been shown for two different problems. In the last section of the chapter, the computation has been described of fracture mechanics parameters in the case of an EFG-analysis of a fracture mechanics problem. With the techniques given in this chapter and the study of moving least squares approximation given in Chapter 3 we are now able to apply the EFG-method to static fracture mechanics problems and to simulations of quasi-static crack propagation. First, however, combinations of the EFG-method and the FE-method are studied in the next chapter. In Chapter 6 then results are given of the application to fracture mechanics problems of the EFG-method and a combination of the method with the FE-method.

Chapter 5

Combinations of EFG-method and FE-method

As presented in Chapter 4, the element-free Galerkin (EFG) method makes use of shape functions obtained by moving least squares approximation (MLSA). In Chapter 3 it has been remarked that this connectivity-free approximation technique is computationally expensive, relative to approximation by means of finite elements. Application of the EFG-method is therefore expensive in comparison with application of the finite element (FE) method, which has been described in Chapter 2.

The computational effort can be diminished when the EFG-method is used only on the parts of the domain where application of this method is necessary. Here, one has to think of the neighbourhood of a crack. For the remaining part of the domain the FE-method can be used. For such an approach, however, the two parts have to be coupled in a certain way. In this chapter, three possible combinations of the EFG-method and the FE-method are studied.

5.1 Combination by means of element-free coupling

In Section 3.1 it has been shown that several FE-shape functions can also emerge from moving least squares approximation. As a consequence, some FE-discretizations can be regarded as an approach by the EFG-method. This leads to the first way to combine the EFG-method and the FE-method. The combination can be regarded as an overall EFG-approach, which yields that problems of coupling both methods are absent. This combination of EFG and FE has already been reported by the author in [30] and is illustrated below.

Let a division of the problem domain into finite elements Ω_e, $e = 1, \ldots, N$, be given by the connectivity of the nodal points $\mathbf{x}_a$, $a = 1, \ldots, n$. As described in Section 3.1, let weight functions and basis functions be chosen such that MLSA with the nodes $\mathbf{x}_a$ results in shape functions $\phi_a(\mathbf{x})$, $a = 1 \ldots, n$, which coincide with the shape functions for the element division. When the domain is divided into integration cells Δ_e such that $\Delta_e = \Omega_e$, $e = 1, \ldots, N$, and the numerical integration per integration cell is such that it is equivalent to the integrations performed for the corresponding element, application of the EFG-method is identical to application of the FE-method.
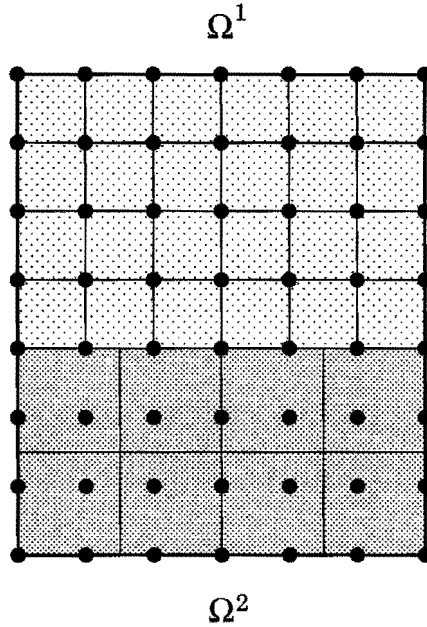
Figure 5.1: *Nodal points and integration cells for EFG-method on $\Omega = \Omega^1 \cup \Omega^2$ resulting in FE-discretization on Ω^1.*

The above considerations lead to a straightforward way to apply the EFG-method and the FE-method together on a single domain. This is illustrated in Figure 5.1, where the domain $\Omega = \Omega^1 \cup \Omega^2$ is depicted together with a set of nodal points. According to Section 3.1, the EFG-method for the upper part Ω^1 will be identical to a FE-discretization by means of four-node rectangular elements, if

- the set of basis functions is $\{1, x_1, x_2, x_1 x_2\}$,

- the nodal points in Ω^1 have weight functions with supports equal to the union of the surrounding rectangles with the nodal points as vertices,

- the nodal points in Ω^2 have weight functions which vanish on Ω^1,

- the nodal points on the internal boundary between Ω^1 and Ω^2 have weight functions such that the intersections of the supports of these weight functions with Ω^1 are equal to the surrounding rectangles with the nodal points as vertices,

- the integration cells for Ω^1 coincide with the rectangles with the nodal points as vertices and numerical integration for these cells is equivalent to numerical integration for a four-node rectangular element.

For Ω^2 a general EFG-approach can be used. Of course, the weight functions should be chosen such that MLSA is well-defined for Ω^2. Furthermore, a division of Ω^2 into integration cells can be made independent of the nodal pattern, see Figure 5.1. Since this example can be

regarded as an overall EFG-approach for Ω, the FE-method on Ω^1 and the EFG-method on Ω^2 are automatically coupled.

When the nodal points for Ω^1 are vertices of non-rectangular quadrilaterals, such a combination of EFG and FE is not possible. This is due to the fact that FE-shape functions and MLSA-shape functions do not coincide for such a distribution, see Section 3.1. For a nodal distribution in Ω^1 coming from a division into triangular elements, however, this element-free coupling of the methods is always possible.

When Γ_u is part of the boundary of the FE-domain Ω^1, the essential boundary conditions can be satisfied exactly. In that situation, these conditions can be prescribed at the nodes and the problem that the conditions are not satisfied, as for a general EFG-approach, is circumvented. When a part of Γ_u is in the boundary of the EFG-domain, the essential boundary conditions for this part are accounted for by means of a Lagrange multiplier description, see (4.4).

5.2   Combination by means of Lagrange multiplier

The second possibility to combine the EFG-method and the FE-method is to divide the problem domain into a subdomain for EFG and a subdomain for FE. These two subdomains are then coupled by means of a Lagrange multiplier. Such a combination has already been reported by the author in [30] and is described below.

Let the problem domain Ω be divided into two subdomains Ω^1 and Ω^2, i.e. $\Omega = \Omega^1 \cup \Omega^2$, see Figure 5.1. The boundaries of these subdomains are denoted by Γ_1 and Γ_2, respectively. For a combination of a FE-approach for Ω^1 and an EFG-approach for Ω^2, one should account for a coupling of the two subdomains over the common boundary $\Gamma_1 \cap \Gamma_2$. To this end, we consider an extension of the weak form (2.17) of the deformation problem for an elastic medium. In this extension, Ω^1 and Ω^2 are coupled over $\Gamma_1 \cap \Gamma_2$ by means of a Lagrange multiplier:

Determine displacements $u_i^1 \in H^1(\Omega^1)$ and $u_i^2 \in H^1(\Omega^2)$, strains $\epsilon_{ij}^1 \in H^0(\Omega^1)$ and $\epsilon_{ij}^2 \in H^0(\Omega^2)$, stresses $\sigma_{ij}^1 \in H^0(\Omega^1)$ and $\sigma_{ij}^2 \in H^0(\Omega^2)$, and Lagrange multipliers $\lambda_i \in H^0(\Gamma_1 \cap \Gamma_2)$, $\lambda_i^1 \in H^0(\Gamma_u \cap \Gamma_1)$ and $\lambda_i^2 \in H^0(\Gamma_u \cap \Gamma_2)$, $i,j = 1,2,3$, such that (2.1), (2.2) are valid on both Ω^1 and Ω^2, and such that

$$
\begin{aligned}
&\int_{\Omega^1} \delta u_{(i,j)}^1 \, \sigma_{ij}^1 \, d\Omega \;-\; \int_{\Omega^1} \delta u_i^1 f_i^* \, d\Omega \;-\; \int_{\Gamma_p \cap \Gamma_1} \delta u_i^1 p_i^* \, d\Gamma \\
&\quad -\int_{\Gamma_u \cap \Gamma_1} \delta \lambda_i^1 \left(u_i^1 - u_i^* \right) d\Gamma - \int_{\Gamma_u \cap \Gamma_1} \delta u_i^1 \lambda_i^1 \, d\Gamma - \int_{\Gamma_1 \cap \Gamma_2} \delta u_i^1 \lambda_i \, d\Gamma \\
&\quad +\int_{\Omega^2} \delta u_{(i,j)}^2 \, \sigma_{ij}^2 \, d\Omega - \int_{\Omega^2} \delta u_i^2 f_i^* \, d\Omega - \int_{\Gamma_p \cap \Gamma_2} \delta u_i^2 p_i^* \, d\Gamma \qquad (5.1) \\
&\quad -\int_{\Gamma_u \cap \Gamma_2} \delta \lambda_i^2 \left(u_i^2 - u_i^* \right) d\Gamma - \int_{\Gamma_u \cap \Gamma_2} \delta u_i^2 \lambda_i^2 \, d\Gamma + \int_{\Gamma_1 \cap \Gamma_2} \delta u_i^2 \lambda_i \, d\Gamma \\
&\quad -\int_{\Gamma_1 \cap \Gamma_2} \delta \lambda_i \left(u_i^1 - u_i^2 \right) d\Gamma = 0
\end{aligned}
$$

for all $\delta u_i^1 \in H^1(\Omega^1)$, $\delta u_i^2 \in H^1(\Omega^2)$, $\delta \lambda_i \in H^0(\Gamma_1 \cap \Gamma_2)$, $\delta \lambda_i^1 \in H^0(\Gamma_u \cap \Gamma_1)$ and $\delta \lambda_i^2 \in H^0(\Gamma_u \cap \Gamma_2)$, $i = 1,2,3$.

In the weak form (5.1), the Lagrange multiplier $\boldsymbol{\lambda}^1$ accounts for the essential boundary conditions on $\Gamma_u \cap \Gamma_1$, $\boldsymbol{\lambda}^2$ accounts for these conditions on $\Gamma_u \cap \Gamma_2$ and $\boldsymbol{\lambda}$ accounts for the conditions $\mathbf{u}^1 = \mathbf{u}^2$ on $\Gamma_1 \cap \Gamma_2$.

In order to derive discrete equations, a division into finite elements is assumed for Ω^1, given by the connectivity of nodal points $\mathbf{x}_a^1$, $a = 1, \ldots, n_1$. As described in Section 2.3, this leads to FE-shape functions $\phi_a^1(\mathbf{x})$, $a = 1, \ldots, n_1$. Nodal points $\mathbf{x}_a^2$, $a = 1, \ldots, n_2$, weight functions and basis functions are chosen such that moving least squares approximation is well-defined for Ω^2. As described in Section 3.1, this leads to MLSA-shape functions $\phi_a^2(\mathbf{x})$, $a = 1, \ldots, n_2$.

With these two sets of shape functions, the displacements on Ω^1 and Ω^2 in (5.1) are taken of the form

$$\mathbf{u}^1(\mathbf{x}) \;=\; \sum_{a=1}^{n_1} \mathbf{d}_a^1 \phi_a^1(\mathbf{x}), \quad \mathbf{x} \in \Omega^1, \tag{5.2}$$

$$\mathbf{u}^2(\mathbf{x}) \;=\; \sum_{a=1}^{n_2} \mathbf{d}_a^2 \phi_a^2(\mathbf{x}), \quad \mathbf{x} \in \Omega^2. \tag{5.3}$$

The Lagrange multipliers in (5.1) are taken of the form

$$\boldsymbol{\lambda}(\mathbf{x}) \;=\; \sum_{b=1}^{k} \mathbf{l}_b \psi_b(\mathbf{x}), \quad \mathbf{x} \in \Gamma_1 \cap \Gamma_2, \tag{5.4}$$

$$\boldsymbol{\lambda}^1(\mathbf{x}) \;=\; \sum_{b=1}^{k_1} \mathbf{l}_b^1 \psi_b^1(\mathbf{x}), \quad \mathbf{x} \in \Gamma_u \cap \Gamma_1, \tag{5.5}$$

$$\boldsymbol{\lambda}^2(\mathbf{x}) \;=\; \sum_{b=1}^{k_2} \mathbf{l}_b^2 \psi_b^2(\mathbf{x}), \quad \mathbf{x} \in \Gamma_u \cap \Gamma_2, \tag{5.6}$$

where $\{\psi_b(\mathbf{x})\}_{b=1,\ldots,k}$, $\{\psi_b^1(\mathbf{x})\}_{b=1,\ldots,k_1}$ and $\{\psi_b^2(\mathbf{x})\}_{b=1,\ldots,k_2}$ are sets of shape functions on the boundaries $\Gamma_1 \cap \Gamma_2$, $\Gamma_u \cap \Gamma_1$ and $\Gamma_u \cap \Gamma_2$, respectively.

For the sets $\{\psi_b^1\}$ and $\{\psi_b^2\}$, the shape functions ϕ_a^1 and ϕ_a^2 are taken for those indices for which $\mathbf{x}_a^1$ or $\mathbf{x}_a^2$ is positioned on $\Gamma_u \cap \Gamma_1$ or on $\Gamma_u \cap \Gamma_2$, respectively. For the set $\{\psi_b\}$ on the common boundary, the shape functions ϕ_a^1 are taken for those indices for which $\mathbf{x}_a^1$ is on $\Gamma_1 \cap \Gamma_2$.

When according to a Galerkin approach the test displacements $\delta\mathbf{u}^1$ and $\delta\mathbf{u}^2$ and the test Lagrange multipliers $\delta\boldsymbol{\lambda}$, $\delta\boldsymbol{\lambda}^1$ and $\delta\boldsymbol{\lambda}^2$ are taken of the same form as (5.2)-(5.6), one obtains a linear system for the coefficient vectors in (5.2)-(5.6), which is similar to (4.4). This system is of the form

$$\begin{bmatrix} K_1 & 0 & L_1 & 0 & H_1 \\ 0 & K_2 & 0 & L_2 & H_2 \\ L_1^T & 0 & 0 & 0 & 0 \\ 0 & L_2^T & 0 & 0 & 0 \\ H_1^T & H_2^T & 0 & 0 & 0 \end{bmatrix} \begin{bmatrix} \mathbf{d}^1 \\ \mathbf{d}^2 \\ \mathbf{l}^1 \\ \mathbf{l}^2 \\ \mathbf{l} \end{bmatrix} = \begin{bmatrix} \mathbf{f}^1 \\ \mathbf{f}^2 \\ \mathbf{r}^1 \\ \mathbf{r}^2 \\ \mathbf{0} \end{bmatrix}. \tag{5.7}$$

The matrix 0 and the vector $\mathbf{0}$ contain only zeros. The submatrices K_1, K_2, L_1, L_2, and the vectors $\mathbf{d}^1$, $\mathbf{d}^2$, $\mathbf{l}^1$, $\mathbf{l}^2$, $\mathbf{l}$, $\mathbf{f}^1$, $\mathbf{f}^2$, $\mathbf{r}^1$, $\mathbf{r}^2$ are given by expressions similar to (4.5)-(4.10). The submatrices H_1 and H_2 emerge from the integrals over $\Gamma_1 \cap \Gamma_2$ in (5.1).

Since the shape functions $\phi_a^1(\mathbf{x})$ are zero on $\Gamma_u \cap \Gamma_1$ for nodal points $\mathbf{x}_a^1$ which are not positioned on this boundary, the essential boundary conditions for Ω^1 can also be imposed directly at the boundary nodes, instead of using the Lagrange multiplier description in (5.1). This is the common procedure in FE-analyses and leads also to a system of the form (5.7).

In order to obtain the linear system (5.7), numerical integration is performed as described in Section 2.3 and Section 4.2. For integration over the common boundary $\Gamma_1 \cap \Gamma_2$, this boundary is split into integration cells and integrations are performed similar to the boundary integrations described in Section 4.2. In order to provide restrictions of FE-shape functions for the representation of the Lagrange multiplier on $\Gamma_1 \cap \Gamma_2$, see (5.4), we take the non-empty intersections of the boundaries of the elements in Ω^1 with $\Gamma_1 \cap \Gamma_2$ as the division of this internal boundary.

Solving the linear system (5.7) for $\mathbf{d}^1$, $\mathbf{d}^2$, $\mathbf{l}^1$, $\mathbf{l}^2$ and $\mathbf{l}$ and using (5.2) and (5.3), results in approximations for the displacements on Ω. Taking derivatives of (5.2) and (5.3) and subsequently using the constitutive equations, e.g. (2.9), leads to approximate values for the strains and the stresses. Note that due to the coupling of Ω^1 and Ω^2, strains and stresses are generally discontinuous across the internal boundary $\Gamma_1 \cap \Gamma_2$.

5.3 Combination by means of interface elements

The third possible way to combine the EFG-method and the FE-method has been presented by Belytschko, Organ and Krongauz [10]. A band of special elements, so-called interface elements, is introduced between the EFG- and FE-domains to enforce continuity of the displacements over this band. A description of this approach is given in this section.

Let the problem domain be divided into the subdomains Ω^1, Ω^2 and Ω^i, i.e. $\Omega = \Omega^1 \cup \Omega^2 \cup \Omega^i$. The subdomain Ω^i is the interface of finite width between the other two subdomains. The subdomains Ω^1 and Ω^2 are disjoint, while Ω^1 and Ω^i, and Ω^2 and Ω^i have only parts of their boundaries in common, see Figure 5.2.

For a combination of the EFG-method and the FE-method, a division of $\Omega^1 \cup \Omega^i$ into finite elements Ω_e is assumed and nodal points, weight functions and basis functions are chosen such that MLSA is well-defined for the subdomain $\Omega^2 \cup \Omega^i$. The division of $\Omega^1 \cup \Omega^i$ into elements is such that the interface Ω^i is made up by a subset of the elements, see Figure 5.2. Let the set $\{\mathbf{x}_a\}_{a=1,\dots,n}$ of nodal points for Ω be given such that $\mathbf{x}_a$ is in $\Omega^1 \cup \Omega^i$ and nodal point of an element Ω_e, or such that $\mathbf{x}_a$ is in $\Omega^2 \cup \Omega^i$ and nodal point for MLSA. When $\mathbf{x}_a$ is in Ω^i, the nodal point may be both nodal point of a finite element and nodal point for moving least squares approximation.

Two sets of shape functions $\{\phi_a^1(\mathbf{x})\}_{a=1,\dots,n}$ and $\{\phi_a^2(\mathbf{x})\}_{a=1,\dots,n}$ are considered for the nodal points. If $\mathbf{x}_a$ is nodal point of an element, $\phi_a^1(\mathbf{x})$ is the FE-shape function on $\Omega^1 \cup \Omega^i$ for $\mathbf{x}_a$. If this is not the case, $\phi_a^1(\mathbf{x})$ vanishes. If $\mathbf{x}_a$ is a nodal point for moving least squares approximation, $\phi_a^2(\mathbf{x})$ is the MLSA-shape function on $\Omega^2 \cup \Omega^i$. If this is not the case, $\phi_a^2(\mathbf{x})$ vanishes. From these two sets of shape functions, a new set of continuous shape functions $\{\phi_a(\mathbf{x})\}_{a=1,\dots,n}$ on Ω will be defined in such a way that these functions coincide with the FE-shape functions ϕ_a^1 on Ω^1 and with the MLSA-shape functions ϕ_a^2 on Ω^2. For the definition of

$$\Omega^1$$

$$\Omega^2$$
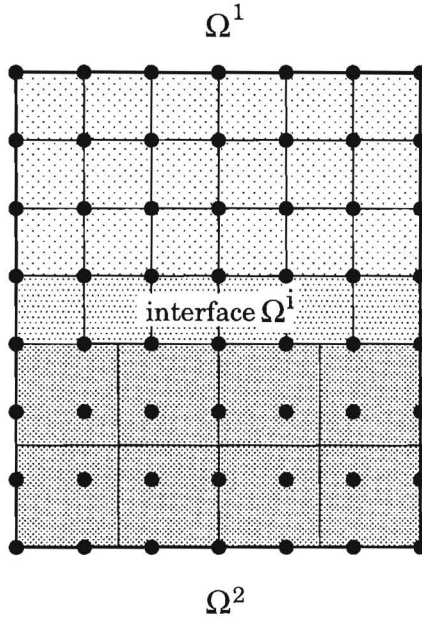
Figure 5.2: *Finite elements, nodal points and integration cells for combination of EFG and FE by means of interface elements.*

the functions ϕ_a an interface function $t(\mathbf{x})$ on Ω is defined. This function is given by

$$t(\mathbf{x}) = \begin{cases} \sum_{\mathbf{x}_a \in \Omega^1} \phi_a^1(\mathbf{x}), & \mathbf{x} \in \Omega^1 \cup \Omega^i, \\ 0, & \mathbf{x} \notin \Omega^1 \cup \Omega^i. \end{cases} \tag{5.8}$$

In (5.8) there is only summation over those a for which the nodal point $\mathbf{x}_a$ is in Ω^1. Since the FE-shape functions ϕ_a^1 are continuous and can represent constant functions exactly, the interface function is continuous, $t(\mathbf{x}) = 1$ for $\mathbf{x} \in \Omega^1$ and we have $t(\mathbf{x}) = 0$ for $\mathbf{x} \in \Omega^2$ and $0 \leq t(\mathbf{x}) \leq 1$ for $\mathbf{x} \in \Omega^i$. The interface function t, however, is not differentiable across the boundaries of the interface Ω^i.

With the help of the interface function $t(\mathbf{x})$, the shape functions $\phi_a(\mathbf{x})$, $a = 1, \ldots, n$, on Ω are defined by

$$\phi_a(\mathbf{x}) = t(\mathbf{x})\phi_a^1(\mathbf{x}) + (1 - t(\mathbf{x}))\,\phi_a^2(\mathbf{x}), \tag{5.9}$$

where $\mathbf{x} \in \Omega$ and $a = 1, \ldots, n$.

From (5.9) and the features of the interface function, it is seen that the shape functions ϕ_a are continuous on Ω, and that $\phi(\mathbf{x}) = \phi_a^1(\mathbf{x})$ for $\mathbf{x} \in \Omega^1$ and $\phi(\mathbf{x}) = \phi_a^2(\mathbf{x})$ for $\mathbf{x} \in \Omega^2$. The shape functions are differentiable on Ω except for the element boundaries in $\Omega^1 \cup \Omega^i$.

It is seen easily that when the FE-shape functions and the MLSA-shape functions can both represent polynomials up to a certain degree exactly, the same holds true for the shape functions

defined by (5.9). For example, consider the four-node quadrilateral elements for $\Omega^1 \cup \Omega^i$ and the nodes for MLSA on $\Omega^2 \cup \Omega^i$ depicted in Figure 5.2. On quadrilateral elements linear functions can be represented exactly. Hence, when the linear basis $\{1, x_1, x_2\}$ is used for MLSA, linear functions can be represented exactly on $\Omega^2 \cup \Omega^i$ because of (3.12), and the same holds true on Ω for the shape functions (5.9).

The set of shape functions $\{\phi_a\}_{a=1,\dots,n}$ for this combination of the EFG-method and the FE-method is used for representation of the displacements, see (2.49) or (4.1). This representation is then applied in a Galerkin formulation for the weak form (2.11) or (2.17), depending on whether the essential boundary conditions can be imposed exactly. The combination leads to a similar linear system as (2.50) or (4.4). Numerical integration in $\Omega^1 \cup \Omega^i$ is performed for each element, while in Ω^2 numerical integration is performed by means of a division into integration cells Δ_e, see Figure 5.2. A prescribed number of integration points is used for the elements in Ω^1 and the integration points for the elements in Ω^i are determined in the same way as for an integration cell Δ_e, see Section 4.2.

When Γ_u is part of the boundary of the FE-domain Ω^1, the essential boundary conditions can be satisfied exactly. This was recognized by Krongauz and Belytschko [40]. In this paper they use a band of interface elements along Γ_u to impose the essential boundary conditions. By means of this approach they circumvent the problem, discussed for the EFG-method in Section 4.3, that essential boundary conditions are not satisfied along a continuous part of the boundary.

5.4 Convergence aspects of EFG-FE combinations

In the first three sections of this chapter, different ways to combine the EFG-method and the FE-method have been described. By means of the problems studied for the EFG-method in Section 4.3, we focus on the performance of the combinations. In each example, all the quantities and material parameters are thought of as being non-dimensional. Homogeneous, isotropic, linearly elastic material behaviour is assumed with the material parameters taken equal to $E = 1$ and $\nu = 0.25$. Volume forces f_i^* are absent. As a result of the convergence study in Section 4.3, in each example weight functions of polynomial type (3.23) are used on the EFG-part of the domain.

Some convergence studies for these ways to combine the EFG-method and the FE-method have already been reported, see [10] and [30]. In these papers, however, the EFG-method is applied with integration points for an integration cell chosen in a different way than in the scheme proposed in Section 4.2 and Appendix D.

The results reported in this section are obtained by means of implementations of the combinations of the EFG-method and the FE-method in the MATLAB programming environment [51]. A short description of an analysis by means of a combination of both methods is found in Appendix B.

(a)   (b)
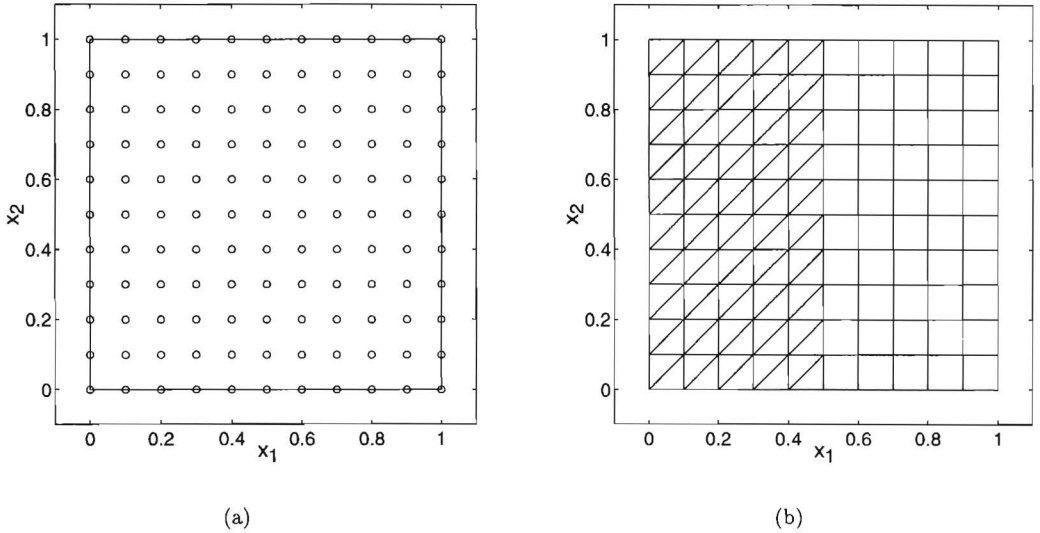
Figure 5.3: *Nodal distribution* (a) *and element/cell configuration* (b) *for patch tests by means of combinations of EFG and FE.*

5.4.1   Patch tests

The two patch tests considered in Section 4.3 are studied for the three combinations of the element-free Galerkin method and the finite element method. We start with the square plate depicted in Figure 5.3, with the linear displacements (4.15), (4.16) for the plane stress problem of a uniform axial stress σ applied at $x_1 = 1$, prescribed at the boundaries. The FE-method is applied on the left half $x_1 \leq 0.5$ and the EFG-method on the right half. As FE-discretization 100 and 400 three-node triangular elements are taken and for the EFG-method the linear basis $\{1, x_1, x_2\}$ is considered together with 66 and 232 nodal points. Hence, a total number of 121 and 441 nodes is used, see Figure 5.3a.

The linear displacements (4.15), (4.16) are imposed at all the boundary nodes. These displacements can be represented exactly by the FE-shape functions and the MLSA-shape functions. On the EFG-part two different values are considered for v to determine the radii of the supports of the weight functions. These radii are proportional to the value of v, see (3.28). Furthermore, for numerical integration purposes the EFG-part of the domain is divided into 50 and 200 quadrilateral integration cells, respectively, see Figure 5.3b.

For the combination of the EFG-method and the FE-method by means of element-free coupling, products of one-dimensional weight functions are used for the nodal points on the line $x_1 = 0.5$. The radii of the supports of these weight functions are given values such that MLSA on the right part results in shape functions which coincide with the FE-shape functions on $x_1 = 0.5$. The weight functions for the other nodal points in the EFG-part of the domain are modified such that these are zero on the FE-part. When the domains are connected by means of a Lagrange multiplier, the nodes on $x_1 = 0.5$ are double, i.e., there is a set of nodes on $x_1 = 0.5$

EFG+FE-parameters	$\|\mathbf{u}^h - \mathbf{u}\|_0 / \|\mathbf{u}\|_0$	$\|\mathbf{u}^h - \mathbf{u}\|_1 / \|\mathbf{u}\|_1$
Element-free, $v = 2.0$, 121 nodes, 150 elements/cells	$6.54 \cdot 10^{-4}$	$8.09 \cdot 10^{-3}$
Element-free, $v = 2.5$, 121 nodes, 150 elements/cells	$9.41 \cdot 10^{-4}$	$1.29 \cdot 10^{-2}$
Element-free, $v = 2.0$, 441 nodes, 600 elements/cells	$2.54 \cdot 10^{-4}$	$6.09 \cdot 10^{-3}$
Element-free, $v = 2.5$, 441 nodes, 600 elements/cells	$3.36 \cdot 10^{-4}$	$9.16 \cdot 10^{-3}$
Lagrange, $v = 2.0$, 132 nodes, 150 elements/cells	$9.75 \cdot 10^{-5}$	$1.13 \cdot 10^{-3}$
Lagrange, $v = 2.5$, 132 nodes, 150 elements/cells	$4.46 \cdot 10^{-4}$	$6.61 \cdot 10^{-3}$
Lagrange, $v = 2.0$, 462 nodes, 600 elements/cells	$2.49 \cdot 10^{-5}$	$5.69 \cdot 10^{-4}$
Lagrange, $v = 2.5$, 462 nodes, 600 elements/cells	$1.09 \cdot 10^{-4}$	$3.21 \cdot 10^{-3}$
Interface, $v = 2.0$, 121 nodes, 150 elements/cells	$9.99 \cdot 10^{-5}$	$1.14 \cdot 10^{-3}$
Interface, $v = 2.5$, 121 nodes, 150 elements/cells	$4.50 \cdot 10^{-4}$	$6.65 \cdot 10^{-3}$
Interface, $v = 2.0$, 441 nodes, 600 elements/cells	$2.53 \cdot 10^{-5}$	$5.71 \cdot 10^{-4}$
Interface, $v = 2.5$, 441 nodes, 600 elements/cells	$1.09 \cdot 10^{-4}$	$3.20 \cdot 10^{-3}$

Table 5.1: *EFG+FE-results for problem of prescribed linear boundary displacements, linear basis.*

for the FE-discretization on the left half of the domain and another set for the EFG-method on the right half. For the combination by means of interface elements, the triangular elements in the band next to $x_1 = 0.5$ are replaced by triangular interface elements.

The results for the three combinations are shown in Table 5.1. In this table, $\|\mathbf{u}^h - \mathbf{u}\|_0$ and $\|\mathbf{u}^h - \mathbf{u}\|_1$ are the errors in the H^0- and H^1-norms, see (4.17) and (4.18). These errors are obtained by means of numerical integration over the elements and over the integration cells.

The results in Table 5.1 show that the linear solution (4.15), (4.16) is not obtained exactly by the combinations, unless the fact that the boundary displacements are satisfied exactly at the nodes. Errors are introduced due to the fact that the essential boundary conditions on the EFG-part of the domain are not satisfied and due to errors because of numerical integration in this domain. These problems were also reported in Section 4.3. From the table it is seen that for all three combinations the errors increase when the value of v increases. This can be explained from the fact that for a higher value of v the sizes of the supports of the MLSA-shape functions are larger, such that more nodes influence the displacements on the EFG-boundary.

Table 5.1 also shows that a refinement of the element distribution together with a refinement of the nodal distribution for the EFG-method leads to a decrease in the errors for all three combinations. This can be explained from the fact that for such a refinement the boundary conditions are satisfied at more nodes of the EFG-boundary. Therefore, one can conclude that this patch test for the exact representation of the linear solution is satisfied in the weak sense, that is, for $h_a \rightarrow 0$, where h_a is the local mesh size, see (3.27).

Nearly all errors in the table are of the same order. The combinations by means of a Lagrange multiplier and by means of interface elements result in almost equal errors. The performance of these two combinations for this problem is slightly better than the performance of the combination by means of element-free coupling.

In Figure 5.4, the relative error in σ_{11} is depicted for the combination by means of element-free
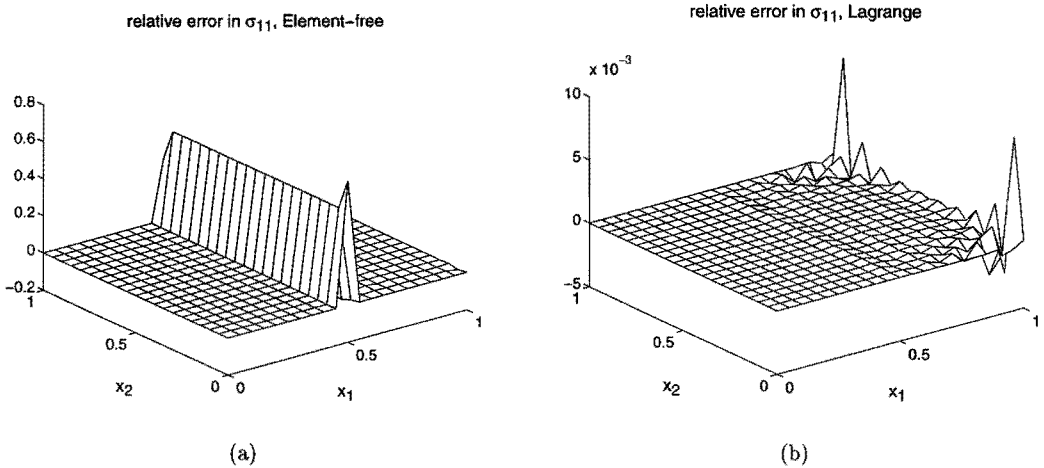
Figure 5.4: *Relative error in σ_{11} for element-free coupling* (a) *and Lagrange multiplier* (b), *problem of prescribed linear boundary displacements, linear basis.*

coupling and for the combination by means of a Lagrange multiplier in the case of $v = 2.0$ and a nodal distribution of 441 and 462 nodal points, respectively. The error for the combination by means of interface elements is similar to the one depicted in Figure 5.4b. It is seen that the error in Figure 5.4b is small and that there is hardly a discontinuity in σ_{11} over the common boundary of EFG-part and FE-part.

From Figure 5.4a, a large error at $x_1 = 0.5$ is seen for the combination by means of element-free coupling. Hence, as in [30], one might conclude that this way to combine the two methods is not correct. However, a close look at this error shows that it is only due to the fact that MLSA is not well-defined on $x_1 = 0.5$. On this internal boundary the only nodes for MLSA involved in the summation (3.4) are the nodes on this boundary, which yields that the matrix P in (3.8) does not have maximal rank. As we have seen before for the wedge model in Section 3.2, this does not prevent MLSA to define a unique value for the shape functions on the internal boundary. However, the derivative of the shape functions with respect to the x_1-coordinate and, therefore, the stresses cannot be determined at $x_1 = 0.5$. The stresses at $x_1 = 0.5$ depicted in Figure 5.4a are found by performing MLSA without the basis function x_1. For $x_1 > 0.5$, MLSA is well-defined and the derivatives and stresses can be determined. It was found that for $x_1 > 0.5$ the error in σ_{11} is of the same order as for the combination by means of a Lagrange multiplier. Hence, we conclude that the combination of EFG and FE by means of element-free coupling is a correct way to combine the methods.

The second patch test concerns the square plate with applied traction and displacements prescribed at the boundaries. The domain is divided into a part for the EFG-method and a part for the FE-method in a similar way as in the previous patch test. Again the solution (4.15), (4.16) is considered. Displacement u_1 is prescribed at the boundary $x_1 = 0$ by means of imposition at the nodes. At the boundary $x_2 = 0$ displacement u_2 is prescribed by imposition at the nodes on the FE-part ($x_1 \leq 0.5$) of this boundary and by means of a Lagrange multiplier description

EFG+FE-parameters	$\|\mathbf{u}^h - \mathbf{u}\|_0/\|\mathbf{u}\|_0$	$\|\mathbf{u}^h - \mathbf{u}\|_1/\|\mathbf{u}\|_1$
Element-free, $\upsilon = 2.0$, 121 nodes, 150 elements/cells	$6.84 \cdot 10^{-4}$	$8.10 \cdot 10^{-3}$
Element-free, $\upsilon = 2.5$, 121 nodes, 150 elements/cells	$8.86 \cdot 10^{-4}$	$1.14 \cdot 10^{-2}$
Lagrange, $\upsilon = 2.0$, 132 nodes, 150 elements/cells	$7.23 \cdot 10^{-5}$	$7.56 \cdot 10^{-4}$
Lagrange, $\upsilon = 2.5$, 132 nodes, 150 elements/cells	$1.68 \cdot 10^{-5}$	$2.41 \cdot 10^{-4}$
Interface, $\upsilon = 2.0$, 121 nodes, 150 elements/cells	$2.35 \cdot 10^{-5}$	$1.20 \cdot 10^{-4}$
Interface, $\upsilon = 2.5$, 121 nodes, 150 elements/cells	$1.47 \cdot 10^{-5}$	$1.57 \cdot 10^{-4}$

Table 5.2: *EFG+FE-results for problem with constant uniaxial stress, linear basis.*

for the EFG-part ($x_1 \geq 0.5$) of the boundary. The constant normal stress σ is prescribed at the boundary $x_1 = 1$, while the boundary $x_2 = 1$ is stress-free.

For an analysis by means of combinations of EFG and FE, the FE-part is divided into 100 three-node triangular elements. For the EFG-part the linear basis $\{1, x_1, x_2\}$ is taken. A total number of 121 nodes is used, see Figure 5.3a. Two different values for υ are used and for numerical integration the EFG-part of the domain is divided into 50 quadrilateral integration cells, see Figure 5.3b. The results for the three combinations are shown in Table 5.2. The errors found in the solution are due to numerical integration and due to the fact that the essential boundary conditions at the boundary of the EFG-part of the domain are not satisfied exactly. An increase of υ does not lead to an increase in the errors for the second and third way for combining EFG- and FE-methods. This can be explained by the fact that a significant part of the essential boundary conditions are prescribed on the boundary of the FE-part of the domain, which means that these conditions are not satisfied exactly only on a small part of the boundary.

The errors for the combination by means of a Lagrange multiplier and by means of interface elements are of the same order. The errors for the combination by means of element-free coupling are significantly higher. For the latter combination, the weight functions for MLSA have to vanish on the FE-part of the domain. Hence, almost all the weight functions are small near the internal boundary between the FE-part and the EFG-part, resulting in highly non-polynomial shape functions near this boundary for the EFG-method, see Section 3.1. Therefore, numerical integration of these shape functions leads to a less accurate performance of this combination of the EFG-method and FE-method. Since these problems are absent in the other two ways for combining EFG-method and FE-method, the combination by means of element-free coupling is not considered in the next examples.

As for the first patch test, refinement of the element mesh and the nodal distribution together with a refinement of the pattern for numerical integration, will lead to a decrease in the errors. Since more shape functions are involved in the representation (4.3) of the Lagrange multiplier, the error in the representation of the boundary displacements decreases. Hence, it is concluded that this patch test for the exact representation of the linear solution (4.15), (4.16) is satisfied in the weak sense.

As for the EFG-method in Section 4.3, one expects that satisfaction of the two patch tests implies convergence of the combinations of the element-free Galerkin method and finite element
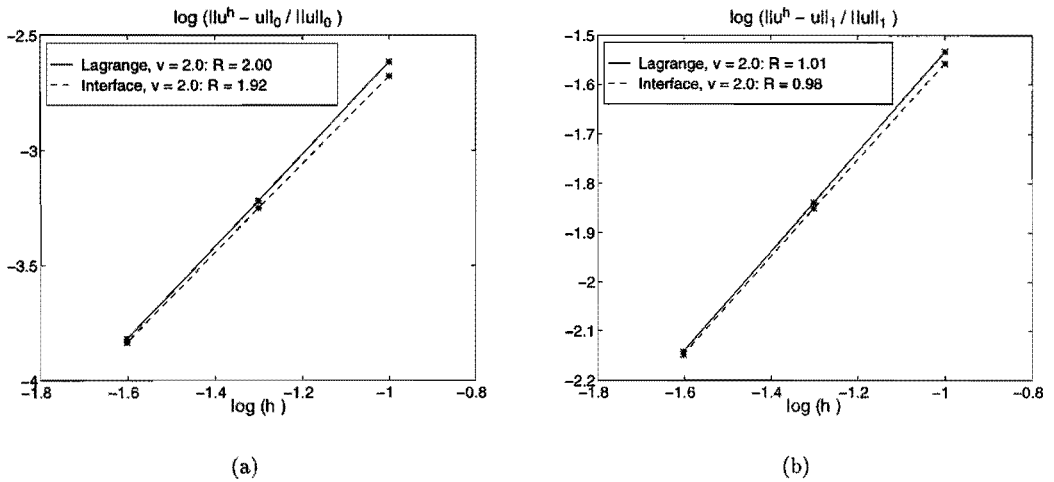
Figure 5.5: *EFG+FE-errors and -convergence rates R for* (a) H^0*-norm and* (b) H^1*-norm, problem of shear force on a plate, linear basis.*

method. This is shown in the next two examples where we focus on combinations by means of a Lagrange multiplier and by means of interface elements.

5.4.2   Shear force on a plate

Consider the square plate depicted in Figure 5.3. Let a transverse shear force F be applied at the boundary $x_1 = 1$. When the shear stress on this boundary is distributed according $\sigma_{12} = -6(F/d^3)x_2(x_2 - 1)$, where $d = 1$ is the length of the plate in the x_2-direction, the displacements in the situation of plane strain are given by (4.19) and (4.20). The convergence of the combinations of the EFG-method and the FE-method by means of a Lagrange multiplier and by means of interface elements is studied for this problem. The displacements (4.19), (4.20) are prescribed on the boundary $x_1 = 0$ and the shear stress σ_{12} is prescribed on the boundary $x_1 = 1$. The boundaries $x_2 = 0$ and $x_2 = 1$ are taken stress-free.

On the left half of the plate ($x_1 \leq 0.5$) the FE-method is applied and on the right half ($x_1 \geq 0.5$) the EFG-method. As FE-discretization divisions into 50, 200 and 800 four-node quadrilateral elements are used. For the EFG-method on the right half, the linear basis $\{1, x_1, x_2\}$ is taken together with nodal distributions with local mesh sizes identical to the mesh sizes of the element discretizations. This leads to a total number of 121, 441 and 1681 nodes, respectively. The displacements (4.19) and (4.20) are prescribed at the (finite element) nodes on the boundary $x_1 = 0$.

On the EFG-part of the domain, two different values are considered for v in equation (3.28) for the sizes of the supports of the weight functions. For numerical integration purposes the EFG-part of the domain is divided into 100, 400 and 1600 triangular integration cells, respectively, leading to a total number of 150, 600 and 2400 elements/cells. For the combination by means

of interface elements, the band of elements next to $x_1 = 0.5$ is replaced by interface elements and for the combination by means of a Lagrange multiplier the nodes on $x_1 = 0.5$ are double.

In Figure 5.5, the logarithms of the errors in the H^0- and H^1-norm, see (4.17) and (4.18), are depicted versus the logarithm of the mesh parameter h. The mesh parameter h is taken to be the distance in the x_1-direction between neighbouring nodes. To obtain accurate values for the errors in the Sobolev-norms by means of the division into elements and integration cells, (4,4)-point Gaussian quadrature is used in the elements. A linear correspondence is seen in the figure, which yields that the error estimates (4.21) hold true. The convergence rates R in these estimates are equal to the slopes of the given lines. The values for R are also given in Figure 5.5. In the figure only the rates for $v = 2.0$ are depicted, since for the value $v = 2.5$ almost equal errors and hence, equal convergence rates were found. Similar convergence rates have been found for both $v = 2.0$ and $v = 2.5$ when rectangular integration cells are used in the EFG-part of the domain instead of triangular integration cells.

Figure 5.5 shows that the combinations of the EFG-method and the FE-method converge. The convergence rates are approximately equal to those for a FE-discretization of the entire patch into four-node quadrilateral elements. The convergence rates for such FE-analyses are exactly equal to 2 and 1 in the H^0- and H^1-norms, respectively, see [33, Ch. 4]. In Section 4.3, it has been shown that the convergence rates for a pure EFG-approach for this problem are higher than the ones for the combined approaches. As a result, it is concluded that the convergence of the combinations of the EFG-method and the FE-method is dominated by the FE-discretizations. In the next example it is shown that the convergence for the combinations can even be slower than the convergence for the FE-discretizations.

5.4.3 Infinite plate with circular hole

The performance of the combinations of the EFG-method and the FE-method by means of a Lagrange multiplier and by means of interface elements is studied for the problem of a plate with a circular hole discussed in Section 4.3. As in this section, the part $0 \leq x_1 \leq 5$ and $0 \leq x_2 \leq 5$ of the upper right quadrant of the plate is considered, see Figure 5.6. On the part $0 \leq x_1 \leq 3$ and $0 \leq x_2 \leq 3$, the EFG-method is applied and on the remaining part the FE-method. As FE-discretization, divisions into 20, 64 and 132 four-node quadrilateral elements are used, see Figure 5.6b. For the EFG-method the linear basis $\{1, x_1, x_2\}$ is taken. In the EFG-part of the domain, the nodal points are spaced regularly in the θ-direction and irregularly in the r-direction, see Figure 5.6a, in order to achieve accurate approximations of the steep displacements and the stress concentrations near the circular boundary, see (4.22)-(4.26). The total number of nodes which are used, is 105, 241 and 433, respectively.

On the boundaries $x_1 = 5$ and $x_2 = 5$, the tractions are prescribed according to the stresses (4.22)-(4.24), which are proportional to σ. The circular boundary has radius $a = 1$ and is assumed traction-free. Displacements are prescribed on the boundary of the patch according to the solution (4.25), (4.26). On the boundary $x_1 = 0$, we set $u_1 = 0$ while on $x_2 = 0$, we set $u_2 = 0$. On the FE-parts of these boundaries the displacements are prescribed at the nodes, while on the EFG-parts of these boundaries the displacements are accounted for by means of a Lagrange multiplier description, see (2.17). The EFG-part of the domain is divided into 64,
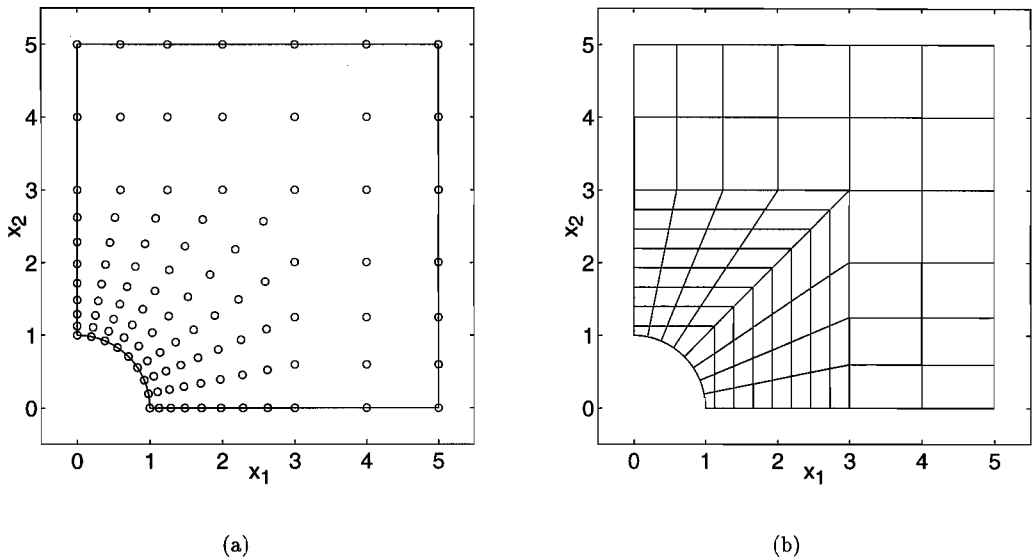
Figure 5.6: *Nodal distribution* (a) *and element/cell configuration* (b) *for combination of EFG and FE, problem of infinite plate with circular hole.*

144 and 256 integration cells, see Figure 5.6b. These integration cells are quadrilaterals with four definition points. The cells next to the circular boundary are given with the help of the connectivity of five definition points to achieve a better approximation of this boundary. The same number of cells is taken in the r- and θ-directions. For the EFG-method, two different values for v are used and thus two different sizes for the supports of the weight functions, see (3.28). For the combination by means of interface elements, the elements next to the internal boundary between EFG- and FE-parts are replaced by interface elements. For the combination by means of a Lagrange multiplier, the nodes on this internal boundary are double.

In Figure 5.7, the logarithms of the errors are depicted versus the logarithm of h. Convergence rates R are also given in the figure. These rates are taken equal to the mean slope of the depicted lines. The local mesh size h_a, see (3.27), averaged over the nodal points $\mathbf{x}_a$ is taken as global mesh size h. To this end, h_a is also computed for the nodes of the FE-discretization. For an accurate computation of the errors in the Sobolev-norms by means of the division into elements and integration cells, (4,4)-point Gaussian quadrature is used in the elements to obtain these errors. In the figure, we see that the combinations converge for this problem, despite the non-convex domain and the approximation of it by the integration cells, and the coupling of EFG-method and FE-method over a piecewise linear internal boundary. In the figure it is also seen that only in the case of a combination by means of a Lagrange multiplier and $v = 2.0$ the convergence rates exceed those for a FE-discretization of the entire domain into four-node elements. The convergence rates for such FE-analyses are exactly equal to 2 and 1 for the H^0- and H^1-norms, respectively, see [33, Ch. 4]. For the other three situations, the convergence rates are smaller than the rates for the FE-discretization. In Section 4.3 it has been shown that the convergence rates of a pure EFG-approach for this problem are higher than the values for

Figure 5.7: *EFG+FE-errors and -convergence rates R for* (a) *H^0-norm and* (b) *H^1-norm, problem of infinite plate with circular hole, linear basis.*

the FE-approach. As a result, we conclude that the combinations of the EFG-method and the FE-method can lead to convergence rates which are smaller than the convergence rates for the FE-discretizations.

From Figure 5.7 it is also seen that a higher value for v leads to an increase in the errors and a decrease in the convergence rates for the combination by means of a Lagrange multiplier. This is due to the fact that a higher value for v results in larger sizes for the supports of the weight functions, see (3.28). Therefore, more nodal points in the EFG-part of the domain influence the displacements on the internal boundary between the EFG-part and the FE-part of the domain. This yields that it is more difficult to have continuity of displacements across this boundary. It is seen that for the combination by means of interface elements the errors are smaller than those for the combination by means of a Lagrange multiplier. However, the convergence rates for the latter one are a little higher. Furthermore, a higher value for v in the case of interface elements does not lead to an increase in the errors, since the errors for both values of v are almost the same.

Convergence of the combination by means of a Lagrange multiplier is also seen from a comparison of the computed stresses with the solution (4.22)-(4.24). In Figure 5.8, the errors in σ_{11} and σ_{22} are given for $x_1 = 0$ and $x_2 = 0$, respectively. A decrease in the errors is observed for an increase in the number of nodal points. The value of σ in the applied tractions was set to $1 \cdot 10^{-3}$. In the figure discontinuities in the stresses are seen at the internal boundary between the EFG-part and the FE-part of the domain, i.e., at $x_2 = 3$ and $x_1 = 3$, respectively. This is due to the fact that the combination by means of a Lagrange multiplier accounts only for a weak formulation of the continuity of the displacements across this boundary. For the combination by means of interface elements, discontinuities in the stresses along the boundaries of the interface elements are also observed. However, for this combination, no discontinuities are obtained in the displacements over the internal boundary between the EFG- and FE-parts.

(a)   (b)
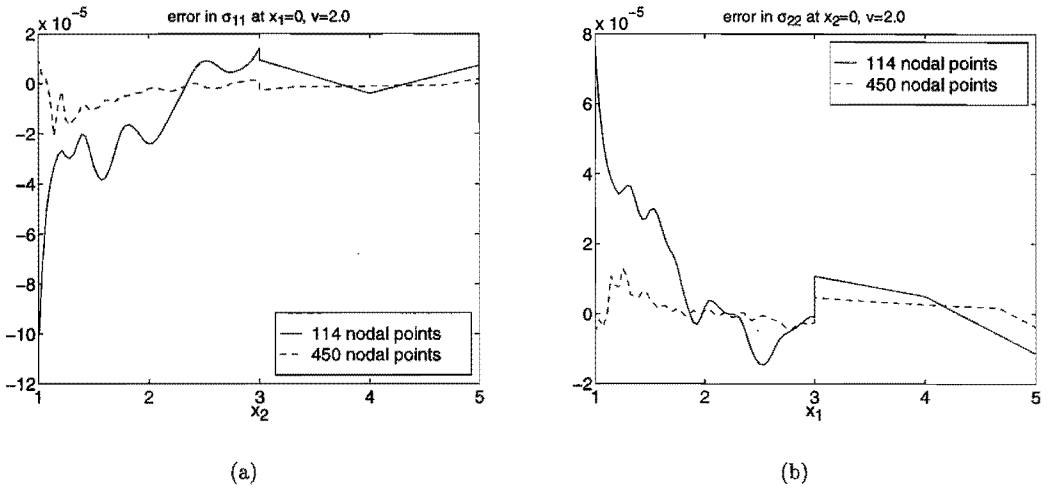
Figure 5.8: *Errors in σ_{11} at $x_1 = 0$ (a) and in σ_{22} at $x_2 = 0$ (b), combination of EFG and FE by means of Lagrange multiplier, problem of infinite plate with circular hole, linear basis.*

It should be remarked that in Figure 5.8 the stresses on the FE-part of the boundary have been averaged.

The convergence of the combinations for this problem has also been studied for an approach using a quadratic basis. The FE-part of the domain is divided into 5, 16 and 33 nine-node quadrilateral elements, respectively. For the EFG-method on the part for which $0 \leq x_1 \leq 3$ and $0 \leq x_2 \leq 3$, the quadratic set $\{1, x_1, x_2, x_1^2, x_1 x_2, x_2^2\}$ of basis functions is used together with the same distributions of nodes and the same configuration of integration cells as for the approach using a linear basis. The two values for v are taken which have also been used for the quadratic EFG-approach for this problem reported in Section 4.3. Convergence rates for the combinations are given in Figure 5.9. It is seen that the combinations converge for this problem. The convergence rates are smaller than the rates for a FE-discretization of the entire domain into nine-node quadrilateral elements. The convergence rates for such FE-analyses are exactly equal to 3 and 2 for the H^0- and H^1-norms, respectively, see [33, Ch. 4].

The errors for the combination by means of a Lagrange multiplier are of the same order as those given in Figure 5.7 for the approach using the linear basis. Similar to that linear approach, an increase in v leads in Figure 5.9 to an increase in the errors. For this way to combine the EFG-method and the FE-method, it is also seen that the convergence rates for $v = 2.5$ are smaller than the ones for $v = 3.0$ and smaller than the ones for $v = 2.5$ given in Figure 5.7. This is explained by the same considerations as those given in Section 4.3 for the approach using the quadratic basis. In comparison with an approach using a linear basis, three extra basis function are involved. Hence, when the same radii of the weight functions are used for both sets of basis functions, the shape functions for the quadratic basis are locally more non-polynomial than the ones for the linear basis. The numerical integration scheme for the EFG-method performs therefore better for the linear basis, resulting in higher convergence rates. For $v = 3.0$ and a quadratic basis, the shape functions are locally more polynomial than the ones for $v = 2.5$.
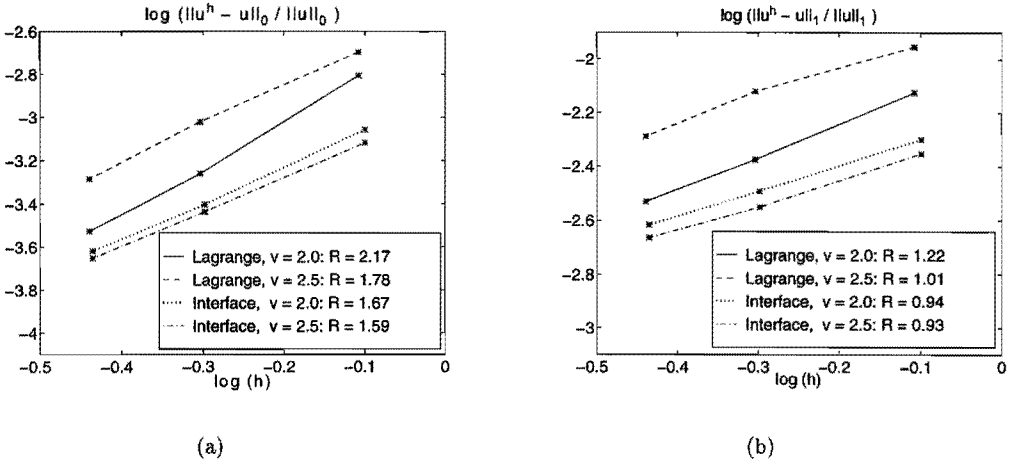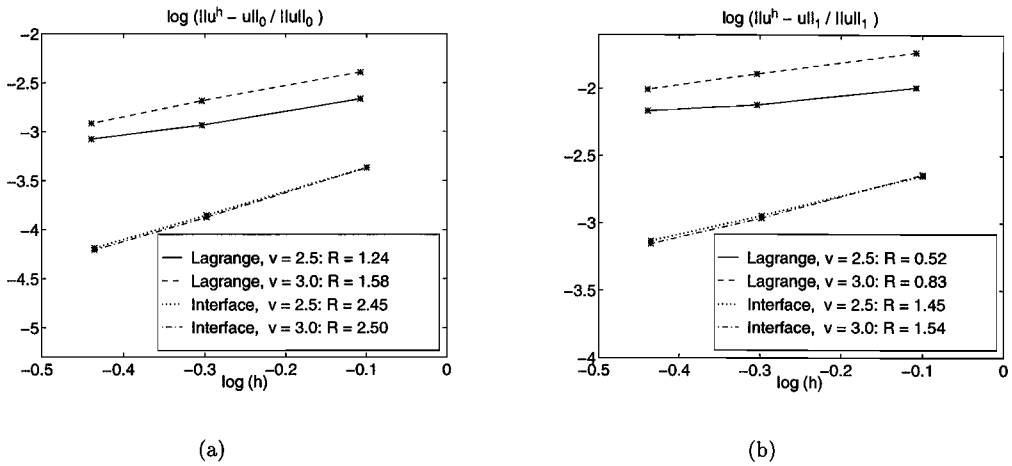
Figure 5.9: *EFG+FE-errors and -convergence rates R for* (a) H^0*-norm and* (b) H^1*-norm, problem of infinite plate with circular hole, quadratic basis.*

This results in higher convergence rates, despite the fact that more nodal points influence the displacements at the internal boundary between the EFG- and FE-parts of the domain. In contrast with the application of a pure EFG-approach for this problem reported in Section 4.3, the use of a quadratic basis for the combination by means of a Lagrange multiplier, does not lead to higher convergence rates than when a linear basis is used.

It is seen from Figure 5.9 that, for the approach using the quadratic basis, the combination by means of interface elements performs better than the combination by means of a Lagrange multiplier. The errors are smaller and the convergence rates for the interface elements exceed those for the Lagrange multiplier. For interface elements, the errors in the computed displacements and stresses are for both values of v almost the same. Hence, a higher value of v does not lead to an increase in these errors, as for a Lagrange multiplier. Furthermore, it is seen that the convergence rates for interface elements with a quadratic basis exceed the ones given in Figure 5.7 for the linear basis, as for a pure EFG-approach.

5.4.4 Conclusions and discussion

In this section three different ways of combining the element-free Galerkin method and the finite element method have been discussed: element-free coupling, combination by means of a Lagrange multiplier and combination by means of interface elements. The examples presented above lead to the following conclusions. The errors in the numerical solutions can be attributed to various reasons, namely due to numerical integration, due to the fact that essential boundary conditions are not exactly satisfied along continuous boundaries, and due to the coupling of EFG-part and FE-part of the domain. Patch tests for the exact representation of linear solutions show that the three ways of combining EFG-method and FE-method all perform well. These patch tests are satisfied in the weak sense by the combinations. From the results for the

patch tests it is concluded that the combination by means of a Lagrange multiplier and the combination by means of interface elements is preferred to an element-free coupling of the methods. This conclusion is because the latter one results in shape functions for the EFG-method which are locally strongly non-polynomial near the FE-part of the domain.

It has been shown that the combinations by means of a Lagrange multiplier and by means of interface elements converge for elasto-static problems. Furthermore, it has been shown that, despite the high convergence rates for pure EFG-analyses reported in Section 4.3, the convergence rates of the combined approaches do not exceed the rates for the applied FE-discretizations.

From the examples it has been seen that the combination by means of interface elements, especially in the case of an approach by quadratic basis functions, performs better than the combination by means of a Lagrange multiplier. For the latter case, larger errors are obtained when larger values are used for the radii of the supports of the weight functions. For this way of combining the EFG-method and the FE-method, the continuity across the internal boundary between the EFG-part and the FE-part of the domain is only accounted for by means of a weak formulation of the continuity conditions. This in contrast with the combination by means of interface elements, where the displacements are continuous across the internal boundary. For this way of combining the EFG-method and the FE-method, an increase in the radii does not lead to an increase in the errors.

Similar convergence rates for interface elements for the problem of a shear force on a plate have also been reported in [10]. In [30] the convergence of the combination by means of a Lagrange multiplier has been studied for the problem of a shear force on a plate and the problem of an infinite plate with a circular hole. In this paper the rates obtained for such a combination for the first problem are similar, as in this section, to the rates for the FE-discretization. For the problem of a circular hole, however, the paper reports convergence rates which exceed the obtained rates in this section. The explanation for this comes from the fact that in [30] the Sobolev-norms are computed with low-order Gaussian quadrature in the elements, yielding that a significant part of the convergence is due to the numerical computation of these norms.

In the next chapter the EFG-method and the combination of the EFG-method and the FE-method by means of interface elements, are applied to fracture mechanics. Results are reported for both static and quasi-static problems.

Chapter 6

Simulation of crack propagation

In Chapter 4 and Chapter 5, the element-free Galerkin (EFG) method and combinations of this method with the finite element (FE) method have been considered. This chapter studies the application of the EFG-method and the application of a combination of the EFG- and FE-methods to fracture mechanics problems. Results are given of analyses of static problems, where stress intensity factors are determined, and of simulations of quasi-static crack propagation where crack paths are computed.

Application of the EFG-method to fracture mechanics problems has already been reported in the literature. In [7] and [48], stress intensity factors are computed for the problem of an edge crack in a mode I loading situation. The crack is taken into account by symmetry considerations and by the use of the discontinuous crack model of Belytschko presented in Chapter 3. Results of the use of this model can also be found in [5], [8]-[11] and [49]. In [5] and Belytschko, Lu and Gu [8], results of simulations of quasi-static crack propagation are reported. In Belytschko, Lu, Gu and Tabbara [9], Belytschko and Tabbara [11] and Lu, Belytschko and Tabbara [49], the EFG-method is applied to dynamic fracture problems. In [10] the discontinuous crack model of Belytschko is used in a coupled EFG- and FE-approach for dynamic fracture problems. The EFG-method and the FE-method in this paper are coupled by means of the interface elements described in Chapter 5. In [6] the continuous crack model of Belytschko presented in Chapter 3 is applied to static fracture problems. In [5]-[11], [48] and [49], polynomial basis functions are used for the representation of the displacements and the stresses near the crack tip and the configurations of integration cells are not adapted for the presence of a crack.

Recently, in Fleming, Chu, Moran and Belytschko [25] and in [58], results have been reported of static and quasi-static fracture analyses where, as in this chapter, special basis functions are used for accurate representations of displacements and stresses near the crack tip. In [25] and [58], a polynomial basis is extended with four extra basis functions taken from the near-tip displacements (2.21). This has the consequence that large radii have to be used for the weight functions of the nodes, yielding shape functions with relatively large supports and making the approach more non-local than an approach with fewer basis functions. In [25] a second approach is described, where a polynomial basis is used and the asymptotic expressions (2.21) for the displacements are added directly to the set of shape functions. Since these asymptotic expressions are global functions, this results in a global approach. Both approaches described in [25], however, are used locally near a crack tip and are coupled with an EFG-approach for

the remaining part of the material, which uses only a polynomial basis. Two ways of coupling are considered. The first one uses the way of coupling which is also applied in the combination of the EFG-method and the FE-method by means of interface elements given in Chapter 5. The second way of coupling simply changes the basis at a remote distance of the crack tip, which results in discontinuous shape functions. In [25] and [58], the continuous crack model of Belytschko given in Chapter 3 is applied and the configuration of cells is not adapted for the presence of a crack.

The results in this chapter are obtained in a different way than those given in [5]-[11], [25], [48], [49] and [58]. As described in Chapter 3, the wedge model is applied for an EFG-analysis on (a part of) the domain, together with the addition of only one special basis function, in order to compute accurate displacements and stresses near the crack tip and to keep the approach as local as possible. During numerical integration by means of the configuration of integration cells, the presence of a crack is accounted for by dividing integration cells into subcells. Integration points for an integration cell are chosen on the basis of the nodal distribution and the size of the cell. This has been described in Chapter 4.

In this chapter results are given of analyses of both static and quasi-static problems. Three problems are considered, namely the problem of an edge crack in a mode I loading situation, the problem of an edge crack in a mixed-mode loading situation and the problem of a single-edge notched beam under shear loading. The static problems concern geometries with stationary (non-propagating) cracks. Stress intensity factors are computed and compared with exact values. The use of special basis functions in the EFG-method and the dependence of this method on the configuration of integration cells are investigated. The quasi-static problems concern geometries with (slowly) propagating cracks. The analyses are quasi-static, since dynamic effects such as wave propagation are not taken into account. Step lengths for crack propagation and local mesh sizes for the nodal distribution are studied for an accurate performance of the EFG-method. The calculated crack paths are compared with results reported in the literature.

In Chapter 5, different combinations of the element-free Galerkin method and the finite element method have been studied. The combination by means of interface elements turned out to be the combination with the best performance. This combination is also applied to the above-mentioned problems. In all applications of the combination, the nodal distributions and cell configurations are taken similar to those used for the EFG-method in these problems.

The reported results in this chapter are obtained by means of implementations of the EFG-method and the combination of this method with the finite element method, in the MATLAB programming environment [51]. Schematic set-ups of analyses for a cracked material domain by the EFG-method and by the combination of EFG- and FE-methods, are found in Appendix B. In each fracture example presented in this chapter, all the quantities and material parameters are thought of as being non-dimensional. Homogeneous, isotropic, linearly elastic material behaviour in a situation of plane strain is assumed with the material parameters taken equal to $E = 1$ and $\nu = 0.25$. Volume forces f_i^* are absent. Furthermore, weight functions of polynomial type (3.23) are used.

Each of the first three sections of this chapter deals with one of the above mentioned fracture mechanics problems. The chapter ends with a section in which a discussion and conclusions are found concerning the reported results.
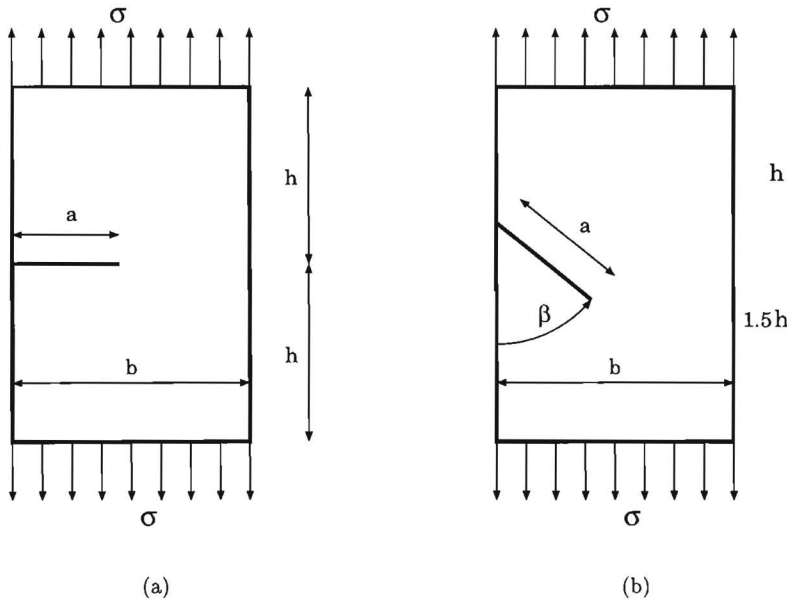
Figure 6.1: *Edge crack in* (a) *mode I and* (b) *mixed-mode loading situation.*

6.1 Edge crack in mode I loading situation

In this section we study the the problem of an edge crack in a mode I loading situation, see Figure 6.1a. In analyses of the problem the influences of the number of nodal points, the cell configuration, the set of basis functions, and the combination of the EFG- and FE-methods are investigated. Therefore, one fixed geometry is chosen: the dimensions of the cracked material domain in Figure 6.1a are set equal to $b = h = 1$ and the crack length is taken as $a = 0.3b$.

6.1.1 Results for EFG-method

For EFG-analyses of the problem, two different nodal distributions are considered. The first one consists of a global equidistant distribution of 66 nodes for the domain, see Figure 6.2a, together with an extra set of 209 nodes near the crack, see Figure 6.2b. In the figure it is seen that, as described in Section 3.2, more extra nodes are placed just behind the crack tip than ahead of the crack tip. The second nodal distribution consists of 231 global nodes together with 233 nodes near the crack. For this nodal distribution, the local mesh sizes for the nodes are approximately 50% of those for the first distribution.

The following sets of basis functions are used: the linear basis $\{1, x_1, x_2\}$, the linear basis extended with $\sqrt{r}$, i.e. $\{1, x_1, x_2, \sqrt{r}\}$, with r being the distance to the crack tip, and the basis $\{1, x_1, x_2, p(\mathbf{x})\}$, where the function $p(\mathbf{x})$ is defined by (3.50) and behaves like $\sqrt{r}$ near the crack tip and like the monomial $x_1 x_2$ on most of the remaining part of the domain. The sizes
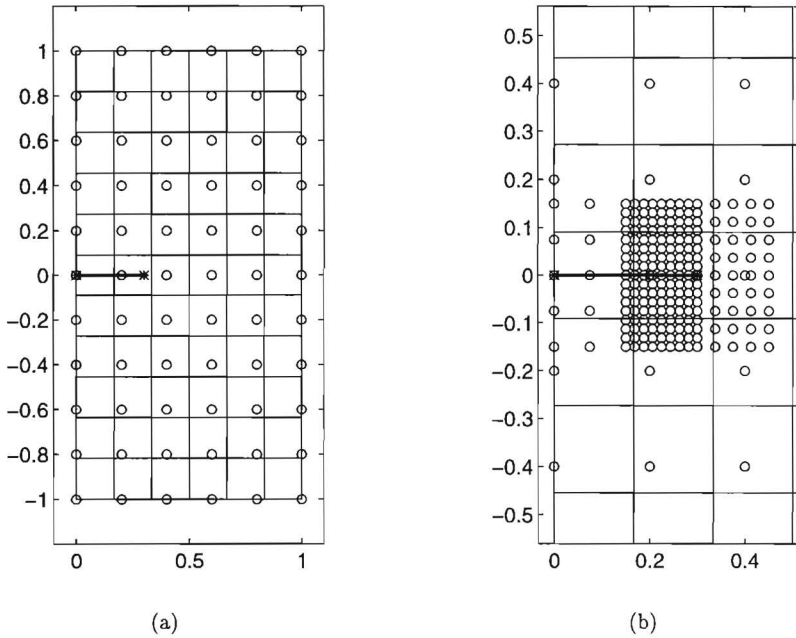
Figure 6.2: *Crack, integration cells and global distribution* (a), *and extra local distribution* (b) *of nodal points for EFG-analysis of edge crack in mode I loading situation.*

of the supports of the weight functions are given by equation (3.28). The parameter v in this equation is set equal to $v = 2.0$ when the basis consists of three basis functions, and to $v = 2.5$ in the case of four basis functions.

For the distribution of 275 nodes, the domain is divided into 50 or 66 rectangular integration cells. The latter one is depicted in Figure 6.2. In the case of 50 integration cells, the crack is at the boundary of several rectangular cells, while for 66 integration cells the crack is in the interior of several cells such that in an EFG-analysis these cells are subdivided into triangular integration cells, see Section 4.2. For the distribution of 464 nodes, the domain is divided into 200 or 231 rectangular integration cells. The constant normal stress σ is prescribed at the horizontal boundaries, while the vertical boundaries are taken stress-free. The rigid body motions are suppressed by setting three displacements at the boundary equal to zero.

Stress intensity factors are computed from the components of the J-vector, see (4.32), (4.33). This vector is obtained from an EFG-analysis by J-integration. As described in Section 4.4, a square curve surrounding the crack tip is used in the computation of the J-integral, see Figure 4.10. Furthermore, as considered in Section 4.4, a correction is used to avoid integrations near the crack tip. To investigate the path-independence of the values for $\mathbf{J}$ and therefore for K_I and K_{II}, the vector is computed for 10 different curves γ. These curves start on the lower crack surface at a distance $0.125a$ from the crack tip and the sizes s of the contours range from $0.2a$ to $0.8a$.

Results obtained by EFG-analyses with the given nodal distributions, the different sets of basis

EFG-parameters		K_I^h/K_I	SD_I
$\{1, x_1, x_2\}$,	$v = 2.0$, 275 nodes, 50 cells	0.962	$2.33 \cdot 10^{-2}$
$\{1, x_1, x_2\}$,	$v = 2.0$, 275 nodes, 66 cells	0.967	$2.37 \cdot 10^{-2}$
$\{1, x_1, x_2, \sqrt{r}\}$,	$v = 2.5$, 275 nodes, 50 cells	0.997	$1.15 \cdot 10^{-2}$
$\{1, x_1, x_2, \sqrt{r}\}$,	$v = 2.5$, 275 nodes, 66 cells	0.996	$1.13 \cdot 10^{-2}$
$\{1, x_1, x_2, p(\mathbf{x})\}$,	$v = 2.5$, 275 nodes, 50 cells	0.892	$2.97 \cdot 10^{-1}$
$\{1, x_1, x_2, p(\mathbf{x})\}$,	$v = 2.5$, 275 nodes, 66 cells	1.303	$4.45 \cdot 10^{-1}$
$\{1, x_1, x_2\}$,	$v = 2.0$, 464 nodes, 200 cells	0.986	$1.36 \cdot 10^{-2}$
$\{1, x_1, x_2\}$,	$v = 2.0$, 464 nodes, 231 cells	0.988	$1.14 \cdot 10^{-2}$
$\{1, x_1, x_2, \sqrt{r}\}$,	$v = 2.5$, 464 nodes, 200 cells	1.002	$7.30 \cdot 10^{-3}$
$\{1, x_1, x_2, \sqrt{r}\}$,	$v = 2.5$, 464 nodes, 231 cells	1.001	$6.24 \cdot 10^{-3}$
$\{1, x_1, x_2, p(\mathbf{x})\}$,	$v = 2.5$, 464 nodes, 200 cells	1.229	$1.17 \cdot 10^{-1}$
$\{1, x_1, x_2, p(\mathbf{x})\}$,	$v = 2.5$, 464 nodes, 231 cells	1.231	$1.18 \cdot 10^{-1}$

Table 6.1: *Mean values and standard deviations of K_I^h/K_I for EFG-analyses of edge crack in mode I loading situation.*

functions, the different values for v and the given cell configurations are reported in Table 6.1. In the first column, the mean values of K_I^h/K_I are given, where K_I^h is the computed mode I stress intensity factor for the contours γ and $K_I = 1.65\sigma\sqrt{\pi a}$ is the exact value for this factor given in Rooke and Cartwright [61, Ch. 1]. In the second column, the standard deviations SD_I of the set of values K_I^h/K_I are given. Mode II stress intensity factors K_{II}^h are also computed. Since these factors are always orders of magnitude smaller than K_I^h, they are not given.

From the results in Table 6.1 it is concluded that taking $\sqrt{r}$ in the basis results in more accurate stress intensity factors than in the case of a linear basis. For a basis with $\sqrt{r}$, the mean values of K_I^h are within 0.4% of the exact value with a standard deviation of about 1%, while the errors in K_I^h for a linear basis are several percents. For contours γ which start at the lower crack surface at a larger distance from the crack tip, smaller errors in K_I^h are observed for the linear basis. It should be noticed that, due to the symmetry of the problem, the integrations over the crack surfaces in the computation of $\mathbf{J}$ have (almost) no influence on the values of K_I^h, see (2.31) and (4.34).

In contrast to the addition of $\sqrt{r}$ to the basis, the addition of the function $p(\mathbf{x})$ does not result in more accurate values for the mode I stress intensity factor. Although this function behaves like $\sqrt{r}$ near the crack tip, the values for K_I^h are even worse than the results obtained with the linear basis. A good explanation for this phenomenon is not evident. Variations in the size of the region near the crack tip over which p behaves like $\sqrt{r}$ and in the size of the zone where the function is continuously coupled with the monomial $x_1 x_2$, show no improvement in the results. The poor performance of the basis with the function p might be due to the coupling of $\sqrt{r}$ and $x_1 x_2$. Using 275 nodes, parts of the contours of γ pass through the zone over which these functions are coupled and a large variation in the results is observed. In the sequel the function p will not be used in EFG-analyses.

From Table 6.1 it is also seen that refinement of the nodal distribution results in more accurate values for K_I^h. Furthermore, the results are not sensitive to variations in the configurations of

<div align="center">(a)   (b)   (c)</div>
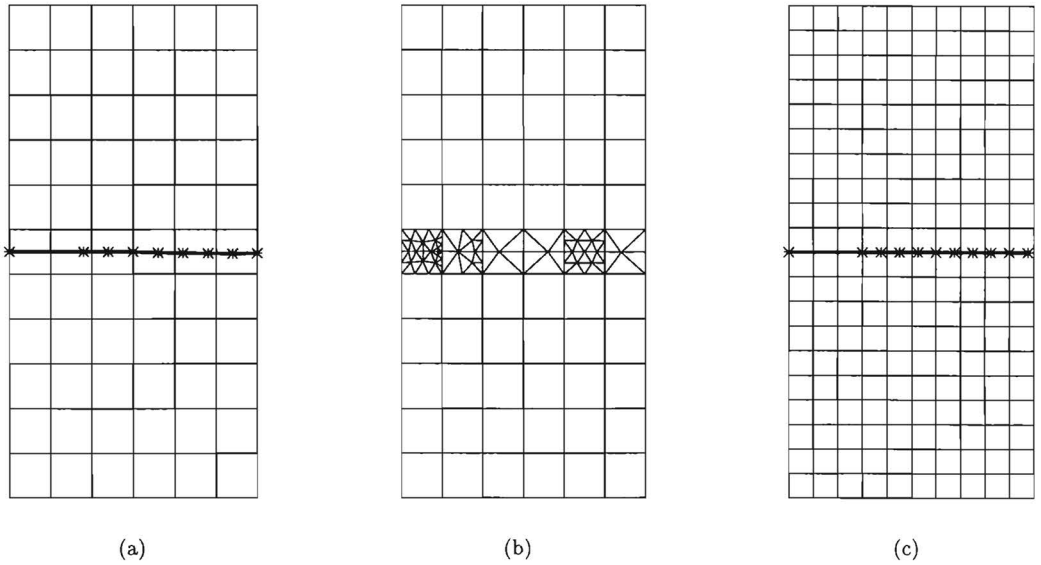
Figure 6.3: Results of simulation of quasi-static crack propagation by EFG-method for edge crack in mode I loading situation: (a) Crack path and initial cell configuration, and (b) final cell configuration for initial distribution of 275 nodal points, and (c) crack path and initial cell configuration for initial distribution of 464 nodal points. The cracks are indicated by thick solid lines and the subsequent positions of the crack tip are indicated by *.

integration cells. Two different types of configurations have been used: one with the crack at the boundary of several cells and another with the crack in the interior of cells resulting in internal subdivisions of some cells, e.g. see Figure 6.3b. The results for both types of configurations do not differ very much. Only, in the case of 275 nodes and the use of the function $p(\mathbf{x})$, a large difference in the stress intensity factors is observed. This is explained from the fact that the function p leads to a bad performance of the method as is indicated above.

Application of the EFG-method to the problem of quasi-static crack propagation for this mode I loading situation is also considered. The nodal distributions of 275 nodes and 464 nodes are used in the initial step of simulation of crack propagation. For these initial nodal distributions, the basis $\{1, x_1, x_2, \sqrt{r}\}$ is used together with $v = 2.5$ in equation (3.28) for the radii of the supports of the weight functions. For the simulation with the initial nodal distribution of 275 nodes, the division into 66 rectangular integration cells is used. And for the simulation with the initial nodal distribution of 475 nodes, the division of the domain into 200 rectangular cells is taken.

In each simulation step, an EFG-analysis for the domain containing the piecewise linear crack $\{\mathbf{y}_b\}_{b=1,...,C}$ is performed. The stress intensity factors K_I^h and K_{II}^h are computed from the **J**-vector. This vector is obtained by J-integration with a correction for the crack-surface integrals, see Section 4.4. To this end, a square curve γ is used, see Figure 4.10, starting at the point $\mathbf{y}_{C-1}$ and for which the size is set equal to $s = 3|\mathbf{y}_C - \mathbf{y}_{C-1}|$. The stress intensity factors are

substituted into equation (2.27), to determine the propagation angle θ_p. The crack is then extended with the line segment $[\mathbf{y}_C, \mathbf{y}_{C+1}]$, where the new crack tip $\mathbf{y}_{C+1}$ is obtained from

$$\mathbf{y}_{C+1} = \mathbf{y}_C + \Delta a\, \mathbf{e}. \tag{6.1}$$

The unit vector $\mathbf{e}$ is given by

$$\mathbf{e}^T = [\cos(\theta_p + \theta_{C-1}) \quad \sin(\theta_p + \theta_{C-1})], \tag{6.2}$$

where θ_{C-1} is the angle of the direction of the line segment $[\mathbf{y}_{C-1}, \mathbf{y}_C]$. For the simulation with initial distribution of 275 nodes, we take $\Delta a = 0.1b$ and for the one with initial distribution of 464 nodes, we take $\Delta a = 0.075b$. Next, a new EFG-analysis is performed with the extended crack path $\{\mathbf{y}\}_{b=1,...C+1}$.

In the process of simulation, the configuration of integration cells is kept fixed. This configuration can only be changed during an EFG-analysis due to subdivisions of some cells. Furthermore, a large part of the nodal distribution is kept fixed. Only, extra sets of nodes are placed around the new crack path. Of course, the dense pattern of nodes around the last crack segment, see Figure 6.2b, is moved to the new crack segment. Hence, the number of nodal points increases. For example, in the last step of the simulation which starts with 275 nodes, 348 nodes are used, while in the last step of the simulation which starts with 464 nodes, 562 nodes are used. The crack paths, however, are obtained in an element-free way, since during simulation no remeshing of a connectivity of nodal points takes place.

Simulation results are depicted in Figure 6.3. For the simulation with an initial distribution of 275 nodes, the computed crack path and the initial and final cell configurations are given in Figure 6.3a and 6.3b. Figure 6.3b shows that the cell at the left of the middle row of cells is also subdivided. This is due to the fact that the initial crack is given by two parallel line segments, in order to provide extra patterns of nodes near the crack path. From the depicted final cell configuration, it is seen that the internal subdivisions of the rectangular integration cells into triangular integration cells match the crack path. For the simulation with initial distribution of 464 nodes, the computed crack path and the initial cell configuration are found in Figure 6.3c. From the figure it is seen that symmetry is preserved for the simulations. The computed crack paths are within a vertical distance of $0.007h$ from the line of symmetry of the domain.

As described in Section 3.2, the nodal distributions in these simulations are locally symmetric with respect to the last crack segment. Furthermore, the cell configurations are symmetric with respect to the line of symmetry of the domain. From the computed crack paths we can therefore conclude that the symmetry of the problem is preserved by the algorithms to determine integration points for the cells, see Appendix D, and by the algorithms for the internal subdivisions of cells due to the presence of a crack in a cell or due to the presence of the crack tip at the boundary of a cell. Simulations with non-symmetric cell configurations have also been performed, which again resulted in crack paths close to the line of symmetry.
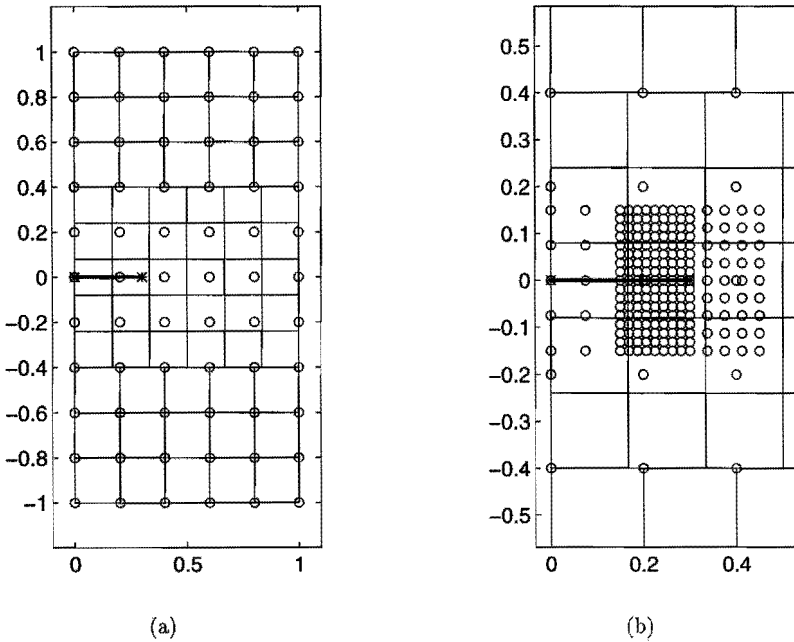
Figure 6.4: *Crack, elements, integration cells and global distribution* (a), *and extra local distribution* (b) *of nodal points for EFG+FE-analysis of edge crack in mode I loading situation.*

6.1.2   Results for combination of EFG-method and FE-method

Next, we consider analyses of the problem by means of the combination of the element-free Galerkin method and the finite element method with the help of interface elements. The same nodal distributions, consisting of 275 and 464 nodes, respectively, are taken as in the pure EFG-analyses of the problem. However, for the nodal distribution of 275 nodes, three rows of nodes on the bottom and the top of the plate are regarded as coming from a FE-discretization by means of four-node quadrilateral elements, see Figure 6.4. These elements are coupled with the EFG-part of the domain with the help of four-node quadrilateral interface elements. Hence, the EFG-method is applied on only 40% of the domain. This part of the domain contains the crack. In the case of the distribution of 464 nodes, six rows of nodes on the bottom and on the top of the plate are regarded as coming from a FE-discretization by means of four-node quadrilateral elements. Also in this case, pure EFG is performed on only 40% of the domain.

For the distribution of 275 nodes, the EFG-part is divided into 20 or 30 rectangular integration cells leading to a total number of 50 and 60 elements/cells, respectively. The latter one is given in Figure 6.4. For the situation of 30 integration cells, the crack is in the interior of some cells which are subdivided into triangular integration cells in the analysis by the combination of EFG and FE. For the distribution of 464 nodes, the EFG-part of the domain is divided into 80 or 99 rectangular integration cells leading to a total number of 200 and 219 elements/cells, respectively.

EFG+FE-parameters	K_I^h/K_I	SD_I
$\{1, x_1, x_2, \sqrt{r}\}$, $\upsilon = 2.5$, 275 nodes, 50 elements/cells	0.995	$1.19 \cdot 10^{-2}$
$\{1, x_1, x_2, \sqrt{r}\}$, $\upsilon = 2.5$, 275 nodes, 60 elements/cells	0.997	$1.85 \cdot 10^{-2}$
$\{1, x_1, x_2, \sqrt{r}\}$, $\upsilon = 2.5$, 464 nodes, 200 elements/cells	1.004	$9.55 \cdot 10^{-3}$
$\{1, x_1, x_2, \sqrt{r}\}$, $\upsilon = 2.5$, 464 nodes, 219 elements/cells	1.003	$1.05 \cdot 10^{-2}$

Table 6.2: *Mean values and standard deviations of K_I^h/K_I for EFG+FE-analyses of edge crack in mode I loading situation.*

In the analyses, the set of basis functions $\{1, x_1, x_2, \sqrt{r}\}$ is used together with $\upsilon = 2.5$ in equation (3.28) for the radii of the supports of the weight functions. Furthermore, stress intensity factors are obtained with the help of the same curves γ which are used in the EFG-analyses for the problem. Hence, the curves are completely in the EFG-part of the domain, such that one does not have to account for discontinuities in the strains and the stresses in the computation of **J**. In Table 6.2, results are reported for different analyses. Mean values and standard deviations are given for the set of values K_I^h/K_I. For each analysis, the mode II stress intensity factors are several orders of magnitude smaller than K_I^h and are therefore not given. From the table, it is seen that accurate stress intensity factors are obtained with the help of the combination. The mean values of K_I^h are within 0.5% of the exact value with a standard deviation of about 1%. The results are similar to those obtained with the same basis in a pure EFG-analysis, reported in Table 6.1. Furthermore, it is seen that the results are not very sensitive to variations in the cell configurations for the EFG-part of the domain.

Analyses of the problem of quasi-static crack propagation for this mode I loading situation are also performed with the help of the combination. To this end, the nodal distributions of 275 and 464 nodes are used in the initial step of simulation by means of the combination of the EFG- and FE-methods. When 275 nodes are used in the initial step of a simulation, the EFG-part is divided into 30 rectangular integration cells, and when 464 nodes are used this part is divided into 99 rectangular integration cells. In the simulation process, new crack segments are determined in the same way as for the simulations for this problem with the help of the EFG-method, see (6.1), (6.2). The same curves γ are used for the determination of the stress intensity factors after each step of the process. Hence, γ is entirely positioned in the EFG-part of the domain. For the initial step this is accomplished by taking a smaller size for γ and shifting its starting point towards the crack tip.

During simulation the configuration of elements/cells is kept fixed. Only, some integration cells can be subdivided during an analysis. Furthermore, the FE-nodes and the global EFG-nodes are fixed. Only, extra sets of nodes for EFG are placed around the new crack path. The dense pattern of nodes around the last crack segment, see Figure 6.4b, moves with the crack tip. Hence, the number of nodal points increases. In the last step of the simulation which started with 275 nodes, 343 nodes were used, while for the one which started with 464 nodes, 562 nodes were used in the last step. Although a connectivity is used for the definition of the FE-discretization, the crack paths are computed without changing any connectivity of nodal points and, therefore, one can say that the paths are obtained in an element-free way.

Computed crack paths are shown in Figure 6.5. The initial and the final configurations of

(a) (b) (c)

Figure 6.5: *Results of simulation of quasi-static crack propagation by combination of EFG- and FE-methods for edge crack in mode I loading situation:* (a) *Crack path and initial element/cell configuration, and* (b) *final element/cell configuration for initial distribution of* 275 *nodal points, and* (c) *crack path and initial element/cell configuration for initial distribution of* 464 *nodal points. The cracks are indicated by thick solid lines and the subsequent positions of the crack tip are indicated by* ∗.

elements/cells and the obtained crack path for the simulation with the initial distribution of 275 nodal points are given in Figure 6.5a and 6.5b. The final configuration shows that some cells in the EFG-part of the domain are subdivided due to the presence of crack segments in these cells. It is seen that the internal subdivisions of some cells are not completely symmetric with respect to the crack. For the simulation with initial distribution of 464 nodal points, the crack path and the initial configuration of elements/cells are depicted in Figure 6.5c.

As for the EFG-approach for this problem, symmetry is preserved. The computed crack paths are within a vertical distance of $0.001h$ from the line of symmetry. In the simulations nodal patterns and element/cell configurations are almost (locally) symmetric with respect to this line. From the computed crack paths it is concluded that a symmetric response is obtained from the combination of EFG- and FE-methods including the algorithms for internal subdivisions of integration cells and the algorithms for the integration points in an integration cell.

6.2 Edge crack in mixed-mode loading situation

In this section the EFG-method and a combination of the method with the FE-method are applied to the problem of an edge crack in a mixed-mode loading situation, see Figure 6.1b. To
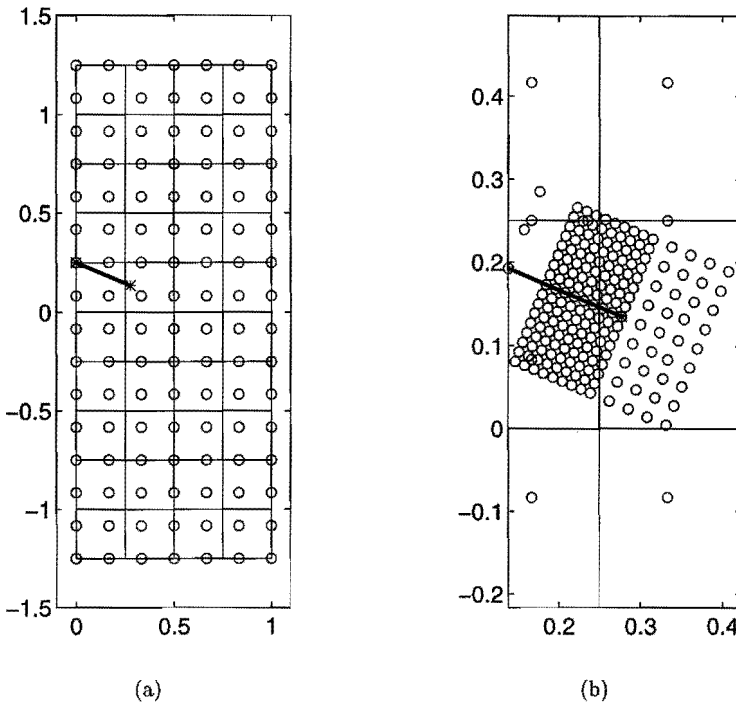
Figure 6.6: *Crack, integration cells and global distribution* (a), *and extra local distribution* (b) *of nodal points for EFG-analysis of edge crack in mixed-mode loading situation.*

this end, the dimensions of the cracked material domain in this figure are set equal to $b = h = 1$, the crack length is taken to be $a = 0.3b$ and for the angle of the crack with the vertical boundary we take $\beta = 3\pi/8$. In the analyses, again, the influences of the number of nodal points, the cell configuration, the set of basis functions and the combination of EFG-method and FE-method are investigated.

6.2.1   Results for EFG-method

For analyses of the problem by the EFG-method, two different nodal distributions are considered. The first one consists of 330 nodal points from which 112 arise from a global equidistant pattern and the remaining 208 nodes are extra nodes distributed along the initial crack path, see Figure 6.6. The second nodal distribution consists of 514 nodal points from which 231 nodes are from a global equidistant pattern. For the second nodal distribution, the local mesh sizes are 60% to 70% of the local mesh sizes for the first nodal distribution.

In the EFG-analyses of the problem, $\{1, x_1, x_2\}$ and $\{1, x_1, x_2, \sqrt{r}\}$ are used as sets of basis functions, where r is the distance to the crack tip. The sizes of the supports of the weight functions are given by (3.28). In this equation, $v = 2.0$ in the case of the linear basis, and $v = 2.5$ in the case of the basis extended with $\sqrt{r}$. Furthermore, divisions into 40 and 160 square

EFG-parameters	K_I^h/K_I	SD_I	K_{II}^h/K_{II}	SD_{II}
$\{1, x_1, x_2\}$, $\upsilon = 2.0$, 330 nodes, 40 cells	0.992	$1.63 \cdot 10^{-2}$	0.703	$4.83 \cdot 10^{-2}$
$\{1, x_1, x_2\}$, $\upsilon = 2.0$, 330 nodes, 160 cells	0.975	$1.10 \cdot 10^{-2}$	0.761	$1.24 \cdot 10^{-1}$
$\{1, x_1, x_2, \sqrt{r}\}, \upsilon = 2.5$, 330 nodes, 40 cells	1.003	$2.08 \cdot 10^{-2}$	1.039	$1.92 \cdot 10^{-2}$
$\{1, x_1, x_2, \sqrt{r}\}, \upsilon = 2.5$, 330 nodes, 160 cells	0.982	$7.49 \cdot 10^{-3}$	1.023	$1.95 \cdot 10^{-2}$
$\{1, x_1, x_2\}$, $\upsilon = 2.0$, 514 nodes, 160 cells	0.984	$1.01 \cdot 10^{-2}$	0.847	$3.04 \cdot 10^{-2}$
$\{1, x_1, x_2\}$, $\upsilon = 2.0$, 514 nodes, 640 cells	0.987	$1.18 \cdot 10^{-2}$	0.840	$3.32 \cdot 10^{-2}$
$\{1, x_1, x_2, \sqrt{r}\}, \upsilon = 2.5$, 514 nodes, 160 cells	0.995	$4.65 \cdot 10^{-3}$	1.001	$2.04 \cdot 10^{-2}$
$\{1, x_1, x_2, \sqrt{r}\}, \upsilon = 2.5$, 514 nodes, 640 cells	0.993	$7.76 \cdot 10^{-3}$	0.993	$1.75 \cdot 10^{-2}$

Table 6.3: *Mean values and standard deviations of K_I^h/K_I and K_{II}^h/K_{II} for EFG-analyses of edge crack in mixed-mode loading situation.*

integration cells are taken for the distribution of 330 nodes. The configuration of 40 cells is given in Figure 6.6. The domain is divided into 160 and 640 square cells for the distribution of 514 nodes. As in the previous example, the constant normal stress σ is prescribed at the horizontal boundaries, while the vertical boundaries are taken stress-free. Three displacements are prescribed to suppress the rigid body motions.

The stress intensity factors are computed from the components of **J**-vector, as described in Section 4.4. To investigate the path-independence of the values for **J**, several square curves γ are taken which are parallel to the vertical boundaries and which start at the lower crack surface at a distance $0.33a$ from the crack tip. The sizes s of these curves range from $0.67a$ to $1.33a$. The results obtained with the different EFG-analyses are given in Table 6.3. In the table, K_I^h and K_{II}^h are the computed stress intensity factors and $K_I = 1.43\sigma\sqrt{\pi a}$, $K_{II} = 0.342\sigma\sqrt{\pi a}$ are the exact values given in [61, Ch. 1]. In the columns of the table, mean values and standard deviations SD_I, SD_{II} are given for the obtained sets of values for K_I^h/K_I and K_{II}^h/K_{II}.

As in the previous example, the use of the basis extended with $\sqrt{r}$ results in more accurate stress intensity factors than when the linear basis is used. Since the values for the crack-surface integrals in (2.31) have a larger influence on K_{II}^h than on K_I^h, see (4.34) and (4.35), the difference in performance is seen very well from the obtained mode II stress intensity factors. Whereas these factors are within a few percents of the exact value in the case of the extended basis, relatively large errors are observed in the results for the linear basis. Therefore, it is concluded that, in comparison with the linear basis, the use of $\sqrt{r}$ leads to more accuracy in the displacements and stresses near the crack tip. The fact that the crack-surface integrals in the computation of **J** have a larger influence on K_{II}^h than on K_I^h, is also the reason for the fact that SD_{II} mostly exceeds SD_I.

As in the mode I example, it is observed that a refinement of the nodal distribution leads to more accuracy in the obtained stress intensity factors. Furthermore, the different cell configurations lead to small differences in the obtained results, especially for the nodal distribution of 514 nodes. The results given in Table 6.3 show that the computation of the **J**-vector by means of J-integration with a correction for the crack-surface integrals, as described in Section 4.4, gives reliable results. The stress intensity factors obtained from the components of **J** are within 2.5% of the exact values in the case of the use of $\sqrt{r}$ and 514 nodal points.
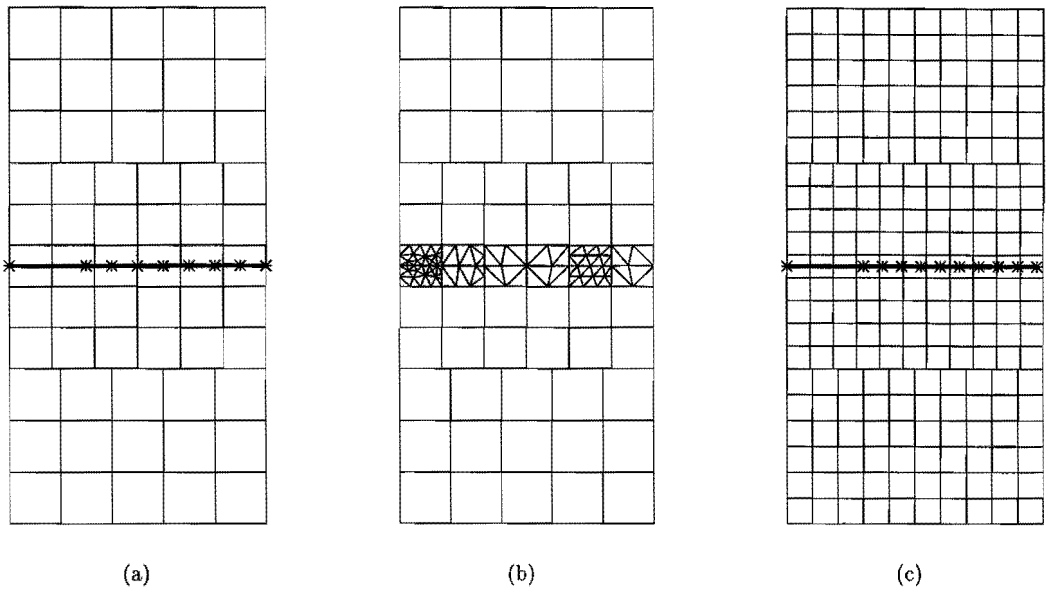
<table>
<tr><td>(a)</td><td>(b)</td></tr>
</table>
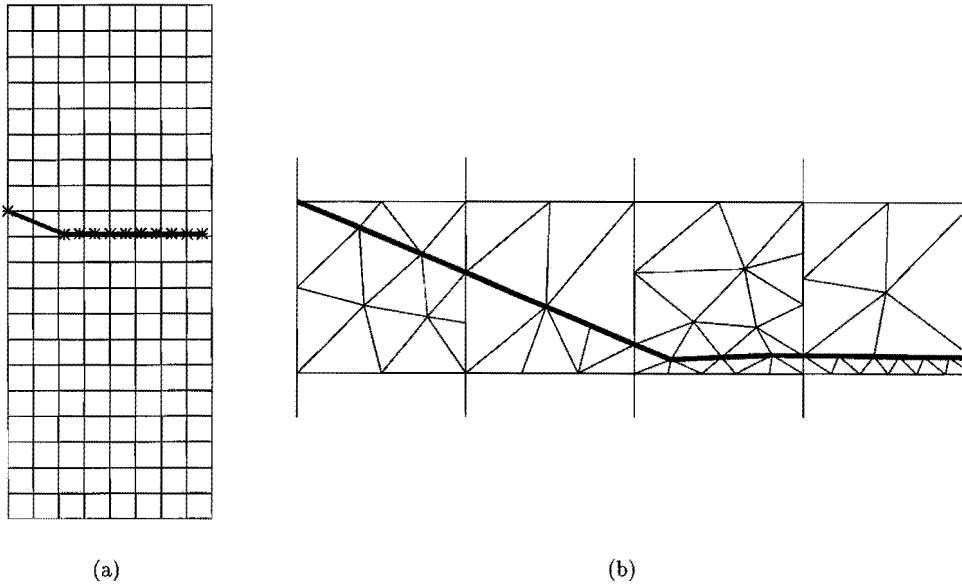
Figure 6.7: *Results of simulation of quasi-static crack propagation by EFG-method for edge crack in mixed-mode loading situation: (a) Crack path and initial cell configuration, and (b) part of final cell configuration for initial distribution of 330 nodal points. The cracks are indicated by thick solid lines and the subsequent positions of the crack tip are indicated by* ∗.

Quasi-static crack propagation is simulated for this mixed-mode loading situation with the distributions of 330 and 514 nodes in the initial step. In both cases $\{1, x_1, x_2, \sqrt{r}\}$ is taken as the set of basis functions and $v = 2.5$ is used for the values of the radii of the supports of the weight functions. The domain is divided into 160 square integration cells for the simulation with initial distribution of 330 nodal points, and into 640 square cells for the one with 514 nodal points. Given the piecewise linear crack $\{\mathbf{y}_b\}_{b=1,...,C}$, new crack segments are obtained, as described in the previous example, by (6.1) and (6.2), where we take $\Delta a = 0.075b$ for the step length. Larger values for Δa are not considered, since for such values it is observed that it is more likely to have fluctuations in the crack paths. Stress intensity factors are determined by J-integration with a correction for the crack surface integrals, see Section 4.4. To this end, a square curve γ is used, see Figure 4.10, parallel to the vertical boundaries with size $s = 3|\mathbf{y}_C - \mathbf{y}_{C-1}|$ and starting at $\mathbf{y}_{C-1}$. Again, during the simulations, the configuration of integration cells is kept fixed and is only changed due to subdivisions of some cells. The number of nodal points increases due to extra nodes placed around the new crack path. In the final step of the simulation starting with 330 nodes, 429 nodes are used and in the last step of the simulation which starts with 514 nodes, 615 nodes are used.

In Figure 6.7, the obtained crack path and the initial cell configuration are depicted for the simulation with initial distribution of 330 nodal points. A similar crack path has been obtained for the initial distribution of 514 nodal points. The computed crack paths are perpendicular to the direction of loading. The subsequent positions of the crack tip are within a horizontal zone

EFG+FE-parameters	K_I^h/K_I	SD_I	K_{II}^h/K_{II}	SD_{II}
$\{1, x_1, x_2, \sqrt{r}\}$, $v = 2.5$, 330 nodes, 70 cells	0.987	$1.94 \cdot 10^{-2}$	1.052	$3.47 \cdot 10^{-2}$
$\{1, x_1, x_2, \sqrt{r}\}$, $v = 2.5$, 330 nodes, 118 cells	0.984	$8.26 \cdot 10^{-3}$	1.011	$1.39 \cdot 10^{-2}$
$\{1, x_1, x_2, \sqrt{r}\}$, $v = 2.5$, 514 nodes, 214 cells	0.994	$4.98 \cdot 10^{-3}$	0.999	$2.10 \cdot 10^{-2}$
$\{1, x_1, x_2, \sqrt{r}\}$, $v = 2.5$, 514 nodes, 406 cells	0.993	$7.82 \cdot 10^{-3}$	0.992	$2.21 \cdot 10^{-2}$

Table 6.4: *Mean values and standard deviations of K_I^h/K_I and K_{II}^h/K_{II} for EFG+FE-analyses of edge crack in mixed-mode loading situation.*

of $0.005h$ and $0.003h$ width, respectively. The problem shows that, as described in [17, Ch. 4], during continued fracture the crack propagates mainly in mode I and that the mode II stress intensity factor becomes negligibly small.

A small part of the final cell configuration in the case of the initial number of 330 nodal points is given in Figure 6.7b. From this figure it is seen that the internal subdivisions of the cells into triangular integration cells match the crack path. From the obtained results we conclude that the local mesh sizes together with the step length $\Delta a = 0.075b$ result in smooth crack paths, since the fluctuations of the crack path in the vertical direction are very small. Therefore, this step length and nodal distributions with similar local mesh sizes are also used in the example presented in the next section.

6.2.2   Results for combination of EFG-method and FE-method

As in the previous section, the problem is also analyzed by means of the combination of the EFG-method and the FE-method with the help of interface elements. To this end, the nodal distributions of 330 and 514 nodes used in the EFG-analyses of the problem are also used for this combination. For the distribution of 330 nodes, six rows at the bottom and three rows at the top of the domain are regarded as coming from a FE-discretization of four-node quadrilaterals. The elements are coupled by four-node quadrilateral interface elements with the EFG-approach for the remaining part of the domain. For the distribution of 514 nodes, ten and five rows, respectively, are seen as emerging from a FE-discretization. For both nodal distributions, the EFG-method is applied on only 40% of the domain.

For numerical integration purposes, the EFG-part of the domain is divided into 16 and 64 rectangular integration cells in the case of the distribution of 330 nodal points, leading to a total number of 70 and 118 elements/cells, respectively. Divisions into 64 and 256 integration cells, resulting in 214 and 406 elements/cells, are taken for the distribution of 514 nodal points. In the EFG-part of the domain, the basis $\{1, x_1, x_2, \sqrt{r}\}$ is used. The radii for the weight functions are obtained with the help of (3.28), in which $v = 2.5$ is taken. Stress intensity factors are computed as for the EFG-analyses of the problem. Hence, the same curves γ are taken and these curves are entirely positioned in the EFG-part. In Table 6.4, results are found for several analyses of the problem. The mean values and standard deviations of the obtained values for K_I^h/K_I and K_{II}^h/K_{II} are given.

From the results shown in Table 6.4 it is seen that, as for the pure EFG-approach for the

<center>(a)   (b)</center>
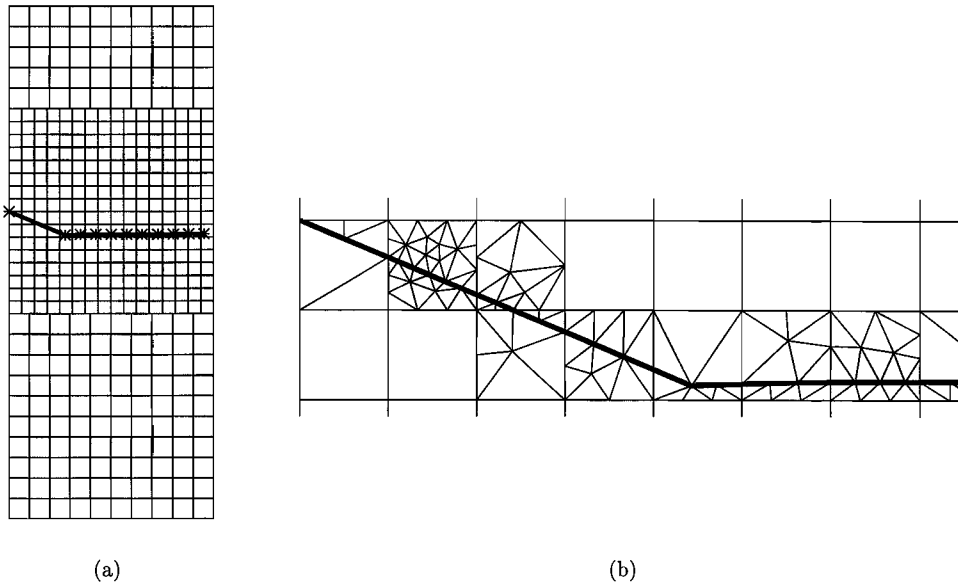
Figure 6.8: *Results of simulation of quasi-static crack propagation by combination of EFG- and FE-methods for edge crack in mixed-mode loading situation:* (a) *Crack path and* (b) *part of final element/cell configuration for initial distribution of 514 nodal points. The cracks are indicated by thick solid lines and the subsequent positions of the crack tip are indicated by* ∗.

problem, accurate values are found by the combined analyses. Again, the variation in K_{II}^h is larger than the variation in K_I^h, since the crack-surface integrals have more influence on K_{II}^h, see (2.31), (4.34) and (4.35). Some differences are seen in the results for the two cell configurations in the case of the distribution of 330 nodes. In the case of the distribution of 514 nodes, however, the mean values of the stress intensity factors for the two cell configurations for the EFG-part of the domain, are within 1% with a standard deviation of about 2%.

For the simulation of quasi-static crack propagation for this mixed-mode problem, the two nodal distributions are used in the initial step of a simulation. The set of basis functions is taken equal to $\{1, x_1, x_2, \sqrt{r}\}$ and the value of v is set equal to $v = 2.5$. The EFG-part of the domain is partitioned into 64 rectangular integration cells for the simulation with initial distribution of 330 nodal points, and into 256 rectangular integration cells for the distribution of 514 nodes. For the piecewise linear crack $\{\mathbf{y}_b\}_{1,\dots,C}$, new crack segments are obtained in the same manner as described before. Stress intensity factors necessary to determine the direction of crack propagation, are computed by means of the same curves γ as the ones used in the EFG-simulations. In the first step of the simulations by EFG+FE, however, a smaller size is taken for γ and its starting point is shifted towards the crack tip such that the curve is entirely positioned in the EFG-part of the domain.

In the simulations the configuration of elements/cells for the domain is kept fixed. Some integration cells in the EFG-part, however, can be subdivided into triangular integration cells. Many nodal points are also fixed. Only, extra nodes for the EFG-method are placed around the

new crack path. Hence, the number of nodal points increases during simulation. The simulation starting with 330 nodal points ends with 429 nodal points and the one starting with 514 nodes ends with 615 nodes.

The computed crack path, the initial configuration of elements/cells and a part of the final cell configuration for the simulation with initial distribution of 514 nodal points are given in Figure 6.8. For the simulation with initial distribution of 330 nodal points, the computed crack path is similar to the one given in the figure. After some steps, the crack paths propagate perpendicular to the direction of loading, as described in [17, Ch. 4]. This has also been observed in the EFG-approach for the problem. For the simulations, the subsequent positions of the crack tip are within a band of $0.005h$ width. Furthermore, for the computed crack paths for this problem given in this section, the end points are all within a distance of $0.01h$ from each other.

6.3   Single-edge notched beam under shear loading

As a final test we consider crack propagation under shear loading. The test proposed by Iosipescu [34] is studied. In this test a beam with a single-edge notch is loaded by compressive forces, see Figure 6.9. Following Feenstra [23, Ch. 5] and Schlangen [63, Ch. 3], we take $b = 1$ and $h = 2$ for the dimensions of the beam. As in Van Vroonhoven [72, Chs. 6, 8], initial crack lengths $a = 0.15b$ and $a = 0.25b$ are studied. The forces F_1 are applied at a distance $0.1h$ from the line of symmetry of the beam and the forces F_2 at a distance h from this line. Hence, we must take $F_2 = 0.1F_1$, because of equilibrium.

6.3.1   Results for EFG-method

For the simulation of quasi-static crack propagation by means of the EFG-method in the case of $a = 0.15b$, an initial distribution of 702 nodal points is used, from which 495 nodes arise from a global equidistant distribution. The local mesh size for the distribution equals $h_a = 0.1b$ at a remote distance from the crack. In the neighbourhood of the crack this size varies between $h_a = 0.04b$ at a certain distance from the crack tip and $h_a = 0.01b$ near the crack tip. For the initial crack length $a = 0.25b$, the global distribution of 495 nodes is also used. Then, 218 nodes are taken near the crack. The local mesh sizes for this nodal distribution are equal to those for the distribution of 702 nodal points

In each step of the simulation process, an EFG-analysis is performed with $\{1, x_1, x_2, \sqrt{r}\}$ as the set of basis functions. For the radii of the supports $\upsilon = 2.5$ is taken in equation (3.28). Numerical integration is performed by a division of the domain into 990 square integration cells, i.e., 15 cells in the vertical and 66 cells in the horizontal direction. The forces F_1 and F_2 are prescribed at the boundary and the rigid body motions are suppressed by setting three boundary displacements equal to zero.

Given the piecewise linear crack $\{\mathbf{y}_b\}_{b=1,...,C}$, new crack segments are obtained with (6.1) and (6.2), where $\Delta a = 0.075b$ is taken for the step length. The choice for Δa is based on the previous example. Stress intensity factors are obtained by J-integration with a correction for the crack-
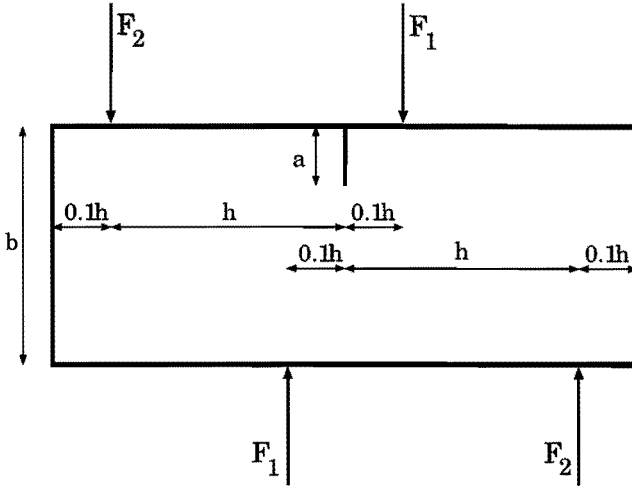
Figure 6.9: *Single-edge notched beam loaded by compressive forces.*

surface integrals, see Section 4.4. For J-integration a square curve γ is taken perpendicular to the last crack segment, with size $s = 3|\mathbf{y}_C - \mathbf{y}_{C-1}|$ and starting at the point $\mathbf{y}_{C-1}$. In the first two steps, however, the curve γ is taken smaller and its starting point is shifted towards the the crack tip, in order to avoid a negative influence of the stress concentrations near the crack due to the applied force F_1. The cell configurations are kept fixed during simulation and are only changed due to internal subdivisions of some cells. The number of nodal points increases during simulation. For the initial crack length $a = 0.15b$, 857 nodes are used in the last step of the simulation, while for $a = 0.25b$, 841 nodes are used in the last step. The computed crack paths are depicted in Figure 6.10. In this figure also a band is depicted taken from Schlangen [63, Ch. 4], in which crack paths were found experimentally in a relatively thick beam for an initial crack length of $a = 0.2b$. The used cell configuration is not given in the figure for reasons of presentation.

Due to the shear loading of the beam, crack propagation takes place along a curved path with its end point on the lower horizontal boundary to the left of the position where the force F_1 is applied, see Figure 6.10c and 6.10d. It is seen that the crack paths obtained with the EFG-method satisfy this requirement. In the final steps the crack propagates almost according to a straight line, which means that in these final steps crack propagation mainly takes place in mode I as described in [17, Ch. 4]. The initial steps of the simulations involve a pure shear loading of the crack, see [34]. The obtained mode I stress intensity factors in these steps, however, are not exactly zero, but are small and negative, which would imply closure of the crack. This has also been seen by Van Vroonhoven [71] in FE-analyses of this problem by means of the SEPRAN package [64]. After the first step, we have chosen to set the propagation angle equal to the propagation angle (2.27), postulated by the criterion based on the maximum circumferential stress, in which $K_I = 0$ and $K_{II} > 0$ is substituted, i.e. $\theta_p \approx -70.5$ degrees.

The problem of a single-edge notched beam has been widely studied, both experimentally and numerically, see [23, Ch. 5], Lubliner, Oliver, Oller and Oñate [50], Rots [62], [63, Chs. 4, 6],

(a)

(b)

(c)   (d)
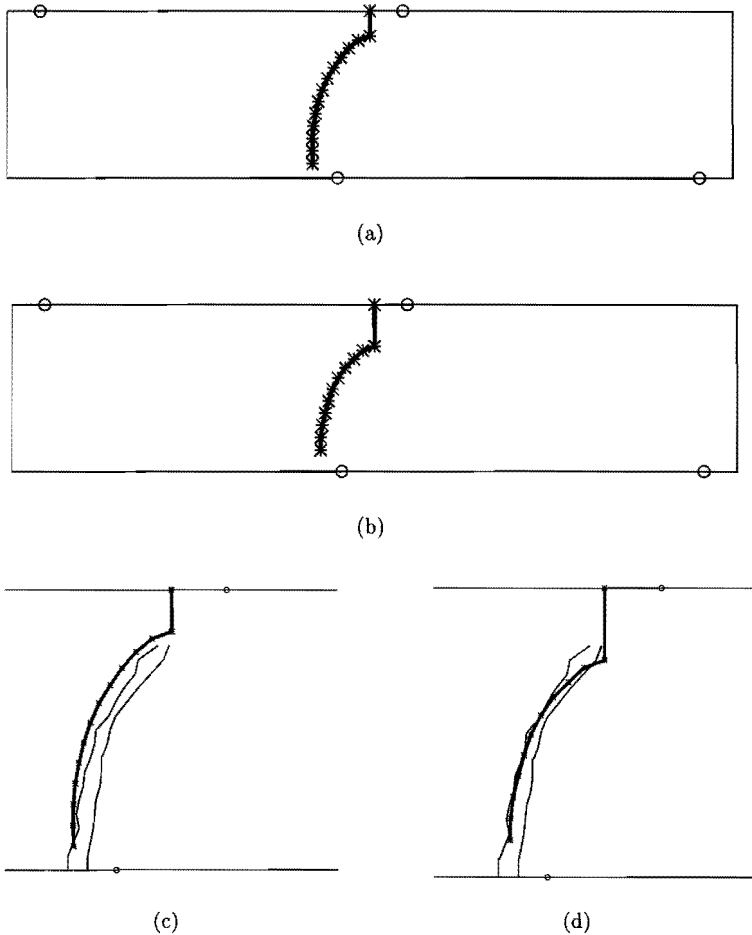
Figure 6.10: *Results of simulation of quasi-static crack propagation by EFG-method for single-edge notched beam under shear loading: Crack paths for* (a) $a = 0.15b$ *and* (b) $a = 0.25b$. *The positions where the forces are applied, are indicated by* ∘, *the subsequent positions of the crack tip by* ∗, *and the cracks by thick solid lines. In* (c) *and* (d) *the paths are depicted together with the experimentally determined band, indicated by thin solid lines, which is given by Schlangen.*

and [72, Chs. 6, 8]. From Figure 6.10c and 6.10d it is seen that the computed crack paths are in good agreement with the experimental results given in [63, Ch. 4] for the initial crack length $a = 0.2b$. The obtained crack paths agree also with the numerical results reported in [63, Ch. 6] and [72, Ch. 8], which all satisfy the requirement for the end point of the crack. Furthermore, the first steps of the simulation agree well with the crack paths in [72, Ch. 6] obtained with an uncoupled fracture approach, which gives only reliable results for the early stage of crack propagation for this problem. In [23] a straight crack path is obtained inclined at an angle of about 45 degrees with respect to the horizontal boundary. Beams of other dimensions are

considered in [50], where a plastic-damage model is used and in [62], where both smeared and discrete representations for a crack are used. The crack paths obtained in [23], [50] and [62] also satisfy the requirement for the end point of the crack.

6.3.2 Results for combination of EFG-method and FE-method

Simulation of quasi-static crack propagation for the problem is also performed by the combination of the EFG-method and the FE-method by means of interface elements. The distributions of 702 and 713 nodes used in the initial steps of the EFG-simulations are also used in the first steps of simulations by EFG+FE. Therefore, several rows of nodes next to the left and the right vertical boundaries of the beam are regarded as coming from FE-discretizations of four-node quadrilaterals. The elements are coupled with the EFG-part of the beam with the help of four-node quadrilateral interface elements. This EFG-part contains the crack and comprises less than 40% of the entire beam. Again, use is made of the basis $\{1, x_1, x_2, \sqrt{r}\}$ and the value of v is set to $v = 2.5$. For numerical integration purposes, the EFG-part is partitioned into 360 square integration cells. This leads to a total number of 640 elements/cells. Given the piecewise linear crack $\{\mathbf{y}_b\}_{b=1,\ldots,C}$, new crack segments are obtained in the same manner as in the previous analyses. The same curves γ used in the EFG-simulations, are taken in the current analyses for computation of the stress intensity factors. In the first two steps, however, the curve γ is taken smaller and its starting point is shifted towards the crack tip, in order to avoid a negative influence of the stress concentrations near the crack due to the applied force F_1. This has also the consequence that γ is entirely positioned in the EFG-part of the beam in each step. The element/cell configurations are kept fixed during the simulation and are only changed due to internal subdivisions of some cells. The number of nodal points increases during simulation. For both the initial crack length $a = 0.15b$ and $a = 0.25b$, 859 nodes are used in the last step of the simulation. Crack paths are given in Figure 6.11. The figure also shows the band taken from Schlangen [63, Ch. 4], in which crack paths were found experimentally in a relatively thick beam for an initial crack length of $a = 0.2b$. The used cell configuration for the EFG-part of the beam is not given in the figure for reasons of presentation.

As in the EFG-approach, Figure 6.11a and 6.11b show curved crack paths with the end points on the lower horizontal boundary to the left of the position where the force F_1 is applied. This has also been observed in experiments, see [63, Ch. 4]. Furthermore, in the final stage of crack propagation, the crack grows mainly in mode I as is expected, see [17, Ch. 4]. From Figure 6.11c and 6.11d, it is seen that the computed crack paths are in good agreement with the experimental results given in [63, Ch. 4] for the initial crack $a = 0.2b$. Again, in the initial step of the simulations, negative but small mode I stress intensity factors are obtained, which would imply closure of the crack. Therefore, we take the angle given by (2.27) with $K_I = 0$ and $K_{II} > 0$, as the crack propagation direction after the first step. The differences between the crack paths determined with the help of a pure EFG-approach and with the help of the combination of EFG and FE, are very small. The distances of the subsequent positions of the crack tip obtained with the two approaches, are within $0.007b$ and $0.006b$ for $a = 0.15b$ and $a = 0.25b$, respectively.

(a)
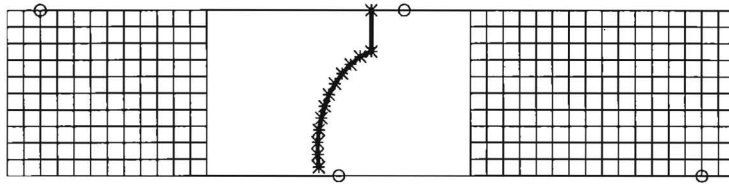
(b)

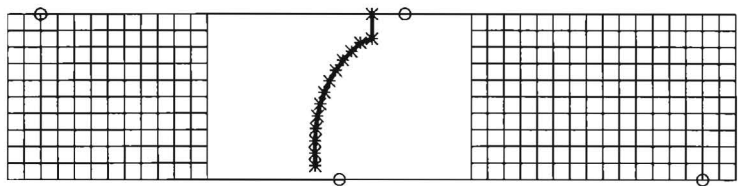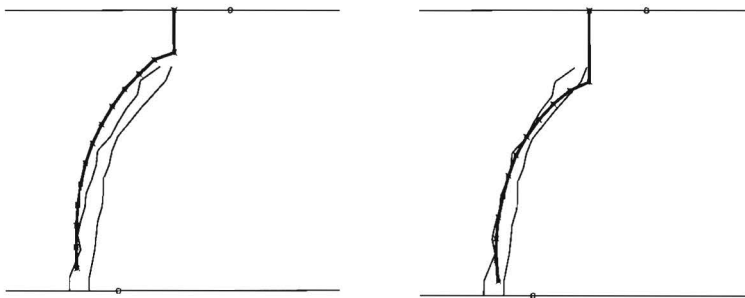(c)   (d)

Figure 6.11: *Results of simulation of quasi-static crack propagation by combination of EFG- and FE-methods for single-edge notched beam under shear loading: Crack paths for* (a) $a = 0.15b$ *and* (b) $a = 0.25b$. *The positions where the forces are applied, are indicated by* ∘, *the subsequent positions of the crack tip by* ∗, *and the cracks by thick solid lines. In* (c) *and* (d) *the paths are depicted together with the experimentally determined band, indicated by thin solid lines, which is given by Schlangen.*

6.4   Discussion and conclusions

In this chapter results have been reported for several (quasi-) static fracture mechanics problems in two dimensions. These results are obtained by application of the element-free Galerkin method and application of the combination of this method with the finite element method by

means of interface elements. Similar results for the application of the EFG-method have been reported in some of the papers mentioned in the introduction of this chapter. In [5], [7], [8] and [48] accurate stress intensity factors are given. To this end, use is made of a linear basis and a domain integral with a relatively large domain for computation of the J-vector. The crack is accounted for by symmetry considerations or by the application of the discontinuous crack model of Belytschko given in Section 3.2. Furthermore, in [5] and [8] progressive crack growth has been considered for a mixed-mode loading problem, which also shows that after some steps the crack propagates mainly in mode I.

In [6] stress intensity factors, which are accurate within a few percent of the exact values, are obtained for the application of the continuous crack model of Belytschko given in Section 3.2. Therefore, also a linear basis is used together with a domain integral with a relatively large domain for computation of the J-vector. In [25] and [58], results are reported for this crack model together with two different approaches to describe the singular stresses near the crack tip correctly. In the first approach, a linear basis is taken which is (locally) extended with four extra basis functions taken from the asymptotic expressions (2.21) for the displacements. In the second approach, the asymptotic expressions (2.21) are directly added to the shape functions obtained with the help of a linear basis. For the two approaches, the papers [25] and [58] report accurate stress intensity factors and accurate stress distributions for a mode I and a mixed-mode loading situation. The stress intensity factors in the papers are obtained with relatively small and relatively large domains for computation of the J-vector. Two mixed-mode problems in [25] show that crack propagation in the final stage takes place mainly in mode I. In contrast with the computations in this chapter, in the papers [5]-[8], [25], [48] and [58], no adaptation of the cell configuration takes place when a crack is in the interior of an integration cell.

The results presented in this chapter for the element-free Galerkin method and the combination of this method with the finite element method, lead to the following conclusions. Both approaches are able to determine accurate stress intensity factors for mode I and mixed-mode loading situations. The approaches are not very sensitive to variations in the cell configurations for numerical integration. Furthermore, an accurate performance of the method is obtained by the application of the combination of the methods, by the proposed way for determination of integration points for an integration cell, and by the way for determination of internal subdivisions of cells in the case of the presence of a crack. A study of the different sets of basis functions has shown that a linear basis extended with $\sqrt{r}$ should be preferred in a fracture mechanics problem to bases without this function. Surprisingly, a linear basis extended with a function which behaves like $\sqrt{r}$ near the crack tip and like a monomial for most of the remaining part of the material, leads to less accurate results than for a linear basis. This is attributed to the coupling of $\sqrt{r}$ with the monomial.

The application of the EFG-method and the application of a combination of the EFG- and FE-methods to quasi-static crack propagation problems, result in reliable crack paths. For a mode I loading problem straight crack paths have been obtained, while for a mixed-mode problem curved crack paths have been calculated. The problem of a single-edge notched beam has been investigated with the two approaches named above. The calculated crack paths agree with experimental and numerical results reported in the literature for this problem. In all problems it has been observed that the final cell configuration matches the obtained crack path. Therefore, it is concluded that a suitable method has been developed for the division of

integration cells in the case of the presence of a crack.

The differences in results obtained by the EFG-method and the EFG-FE combination are very small for all examples. Hence, we succeeded in the development of a combination of the EFG-method and the FE-method which is appropriate for application to fracture mechanics problems in two dimensions. In each example, the EFG-method has only been applied on approximately 40% of the material, leading to a reduction in computation time of 30 to 40%. The most expensive parts of the combined approaches are due to the refined EFG-discretizations near the crack. Larger reductions in computation time can be obtained by the application of the EFG-method on smaller parts of the domain.

Chapter 7

Concluding discussion

In this thesis a new formulation has been given of the element-free Galerkin (EFG) method in order to simulate crack propagation in brittle materials. Furthermore, combinations with the finite element (FE) method have been studied, leading to a reduction of computational effort. This chapter serves as a concluding discussion of the thesis. In the first section, conclusions are given of the presented work. In the second section, open ends of the study can be found together with recommendations for further research.

7.1 Conclusions

For the development of the EFG-method for the simulation of crack propagation, connectivity-free approximation techniques have been studied for the representation of the displacements in a weak form of the problem equations. The most convenient technique is moving least squares approximation (MLSA). Several models have been studied for a correct and accurate representation of the displacements and the stresses near a crack by means of MLSA (see Chapter 3). This resulted in the development of the so-called wedge model. Unless the fact that MLSA is not well-defined in the crack tip in the case of this model, it has been proven that the displacements can be correctly represented on the entire domain. Furthermore, two special basis functions have been introduced, in order to describe the singularity in the stresses at the crack tip. These functions both behave like the square root function in a neighbourhood of the crack tip.

In Chapter 4 the EFG-method has been studied. The discrete equations of the method obtained by the application of MLSA have been given. For computation of the entries in these equations, a numerical integration scheme is used which is based on a background configuration of integration cells. It is designed in such a way that it automatically accounts for the nodal distribution for MLSA, for the integration of quantities which are discontinuous over the crack, and for the integration of the singular derivatives of the special basis functions. The method has been tested by application to several two-dimensional elasto-static problems. From the results it is concluded that the method is convergent when the nodal distribution is refined, and that the rates of convergence exceed those for equivalent analyses by the FE-method. Furthermore, we can conclude that the EFG-method is not very sensitive to variations in the cell configurations.

Several ways have been studied for the computation of the stress intensity factors from analyses of fracture mechanics problems (see Chapter 4). We have chosen to compute the stress intensity factors from the so-called **J**-vector, which is obtained by means of contour integration. In addition to this type of integration, named J-integration, a correction is used to avoid integration over parts of the crack surfaces next to the crack tip. Hence, the errors in the approximation of the angular variation of the displacements near the crack tip have only a small influence on the computed values for the stress intensity factors.

Application of the EFG-method to several static fracture mechanics problems in two dimensions has shown that accurate values for the stress intensity factors are obtained (see Chapter 6). To this end, a special basis function, proposed in Chapter 3, has to be used within MLSA. This function equals the square root function on the entire domain. Surprisingly, the use of a special basis function which equals the square root function only in a close neighbourhood of the crack tip, results in inaccurate values for the stress intensity factors.

The EFG-method has also been used for the simulation of quasi-static crack propagation. In each step of such simulations, an analysis is performed of a cracked material domain. From the calculated stress intensity factors, the direction of crack propagation is determined and the crack is extended in this direction. The results show that the method calculates reliable crack paths, which are not very sensitive to variations in the cell configurations. From the results it is concluded that the proposed scheme for numerical integration leads to a robust and accurate numerical method, which is appropriate for the simulation of crack propagation.

Three possible ways for combination of the EFG-method and the FE-method have been considered (see Chapter 5): A combination by element-free coupling, a combination by a Lagrange multiplier, and a combination by interface elements. By the application of the combinations to several two-dimensional elasto-static problems, the performance has been studied. From the results it is concluded that the combinations are convergent when the nodal distribution is refined. However, the convergence rates generally do not exceed the rates for the applied FE-discretizations. Furthermore, it is concluded that the use of interface elements has to be preferred to the other two ways for combination.

The combination of the EFG-method and the FE-method by means of interface elements has been applied to fracture mechanics problems in two dimensions. The results show that accurate stress intensity factors are obtained and that reliable crack paths are calculated. The differences between the results obtained by the EFG-method and the combination are very small. Hence, it is concluded that we have succeeded in the development of a combination which is convenient for the application to crack propagation problems.

7.2 Open ends and further research

The added value of the study presented in this thesis is the new formulation of the element-free Galerkin method for the simulation of crack propagation. Detailed descriptions have been given of the several steps in the development of the method. Furthermore, the thesis presents a study on three possible ways for combination of the EFG-method with the FE-method. The developed numerical methods have been implemented in the MATLAB programming environment [51],

which is very suitable for the implementation of the FE-method and the EFG-method.

The disadvantage of the EFG-method is that the implementation requires a large amount of computation time for the simulation of crack propagation. This is partially due to MATLAB. A reduction of computation time has been obtained by the translation of several parts of the programs into machine code by the MATLAB compiler, which has become available recently. It is believed, however, that more significant reductions in computation time can be obtained by a translation of the programs to a compiler-based computer language such as the new Fortran 90 language, see Ellis, Philips and Lahey [21].

The large amount of computation time required for the simulation of crack propagation is also due to the EFG-method itself. The application of moving least squares approximation for the representation of the displacements, makes the method computationally expensive. In addition, since the displacements are not piecewise linear or piecewise quadratic (see Section 3.1), a large amount of integration points is necessary for an accurate and robust performance of the method. Therefore, an analysis for a material domain with the current formulation of the EFG-method requires approximately 10 times more computation time than an equivalent analysis by the FE-method. However, in the case of simulation of crack propagation with the EFG-method, no computation time is required for remeshing in between successive analysis steps, as is the case for the FE-method.

Some recommendations can be given for further research to come to a reduction of computation time for the method. First, it is recommended to study new and cheaper versions of the numerical integration scheme presented in Section 4.2, which are as accurate and robust as the current scheme. Secondly, it is necessary to reduce the number of nodal points which are used to model the crack surfaces. It is believed that one can do without the extra nodes used to model the "tail" of the crack, which has the consequence that one can simulate crack propagation with almost a fixed number of nodes.

As a third opportunity for reduction of computation time, a further study is recommended on the application of special basis functions in a local way. Here, one can think of basis functions which behave as the square root function in a small neighbourhood of the crack tip and as a fixed monomial on the remaining part of the material, similar to the one proposed in Section 3.2. Hence, during simulation of crack propagation, the entries in the linear system of equations can be obtained from the ones for the previous simulation step without much computational effort, since there is only a local change in the basis functions. This is in contrast with the current formulation, where in each simulation step the entire system of equations has to be computed, because of the global change in the set of basis functions. Such a basis function is also very interesting for the use in problems concerning multiple cracks. With the use of only one extra basis function in which the square root function for each crack tip is locally embedded, all the stress singularities can then be obtained.

Reduction of computation time can also be achieved by means of the developed combinations of the EFG-method and the FE-method. The computational effort of such combinations strongly depends on the part for the EFG-method. In the simulations by means of a combination of the methods presented in this thesis, the EFG-parts have been predefined, see Chapter 6. These relatively large parts of the domain are defined in such a way that it is likely that the crack path remains in these parts of the domain. For more advanced simulations of crack propagation

based on such a combination, the development of a numerical technique is recommended in which the EFG-parts are not predefined. In such a numerical technique, large parts of the domain are discretized by means of the FE-method and the EFG-parts only concern the direct environment of the crack. In the case of crack propagation into the FE-part, several elements have to be added to the EFG-parts of the domain. Such a numerical technique will lead to a large reduction in computation time and can be applied to more general crack propagation problems than those considered in this thesis.

Finally, a further development of the EFG-method is recommended. Here, we think of the development of the method for application to problems involving dynamic and/or three-dimensional effects, and problems concerning multiple cracks. Such a development will concern not only the study of special basis functions as described above, but also the study of basis functions in which a certain angular variation for the near-tip displacements is embedded. The further development will also have to deal with the extension of the wedge model and the numerical integration scheme to three dimensions and to problems involving multiple cracks.

The proposed development of the element-free Galerkin method, together with the speed up of the method, will make the method a more attractive alternative for the finite element method and for the boundary element method, concerning the simulation of quasi-static and dynamic crack propagation in two or three dimensions.

Appendix A

Angular variation of stresses and displacements

The variation in the polar angle of the stresses and displacements near a crack tip for linearly elastic material is given in this appendix.

In Section 2.2, it has been shown that the stresses in the neighbourhood of the crack tip are given by (2.18). The dependence on the polar angle θ is given by the functions f_{ij}^I and f_{ij}^{II}, $i, j = 1, 2$, which correspond to the opening mode and the sliding mode, respectively. The functions f_{ij}^I for the opening mode are given by

$$f_{11}^I(\theta) = \cos(\tfrac{1}{2}\theta)\left(1 - \sin(\tfrac{1}{2}\theta)\sin(\tfrac{3}{2}\theta)\right), \tag{A.1}$$

$$f_{22}^I(\theta) = \cos(\tfrac{1}{2}\theta)\left(1 + \sin(\tfrac{1}{2}\theta)\sin(\tfrac{3}{2}\theta)\right), \tag{A.2}$$

$$f_{12}^I(\theta) = \cos(\tfrac{1}{2}\theta)\sin(\tfrac{1}{2}\theta)\cos(\tfrac{3}{2}\theta). \tag{A.3}$$

The functions f_{ij}^{II} for the sliding mode are

$$f_{11}^{II}(\theta) = -\sin(\tfrac{1}{2}\theta)\left(2 + \cos(\tfrac{1}{2}\theta)\cos(\tfrac{3}{2}\theta)\right), \tag{A.4}$$

$$f_{22}^{II}(\theta) = \cos(\tfrac{1}{2}\theta)\sin(\tfrac{1}{2}\theta)\cos(\tfrac{3}{2}\theta), \tag{A.5}$$

$$f_{12}^{II}(\theta) = \cos(\tfrac{1}{2}\theta)\left(1 - \sin(\tfrac{1}{2}\theta)\sin(\tfrac{3}{2}\theta)\right). \tag{A.6}$$

The near-tip displacement field is given in Section 2.2 by equation (2.21). The angular variation of this field is given by the functions u_i^I and u_i^{II}, $i = 1, 2$, where

$$u_1^I(\theta) = \cos(\tfrac{1}{2}\theta)\left(\kappa - 1 + 2\sin^2(\tfrac{1}{2}\theta)\right), \tag{A.7}$$

$$u_2^I(\theta) = \sin(\tfrac{1}{2}\theta)\left(\kappa + 1 - 2\cos^2(\tfrac{1}{2}\theta)\right), \tag{A.8}$$

$$u_1^{II}(\theta) = \sin(\tfrac{1}{2}\theta)\left(\kappa + 1 + 2\cos^2(\tfrac{1}{2}\theta)\right), \tag{A.9}$$

$$u_2^{II}(\theta) = \cos(\tfrac{1}{2}\theta)\left(1 - \kappa + 2\sin^2(\tfrac{1}{2}\theta)\right). \tag{A.10}$$

In these equations, $\kappa = 3 - 4\nu$ in case of plane strain and $\kappa = (3 - \nu)/(1 + \nu)$ in case of plane stress.

Appendix B

Set-up for analyses by FE-method and EFG-method

In this appendix schematic set-ups are given for an analysis for a (cracked) material domain by means of the finite element method, the element-free Galerkin method or a combination of both methods. From the different steps in each set-up the similarity is seen between the different methods.

B.1 Set-up for FE-analysis

In general, a static analysis for a material domain Ω (containing a crack) by means of the FE-method consists of the following steps:

1. Divide Ω into elements Ω_e by means of connectivity of nodal points $\mathbf{x}_a$ such that the elements match or approximate the boundary $\partial\Omega$ and internal boundaries such as cracks;
2. Define volume force $\mathbf{f}^*$ in Ω, essential boundary conditions $\mathbf{u} = \mathbf{u}^*$ along Γ_u and natural boundary conditions $\sigma\mathbf{n} = \mathbf{p}^*$ along Γ_p;
3. For each element Ω_e compute the contribution to K and $\mathbf{f}$, see (2.50), by:
   a. Determine the matrix D which represents the constitutive equations in Ω_e;
   b. For each integration point $\bar{\mathbf{x}}_q$ in Ω_e:
      (i) Determine $\phi_a(\bar{\mathbf{x}}_q)$ and derivatives $\phi_{a,i}(\bar{\mathbf{x}}_q)$ for the nodal points $\mathbf{x}_a$ of Ω_e;
      (ii) Determine the matrices B_a, see (2.54);
      (iii) Compute integration point contribution to element integrals, e.g. see (2.56);
   c. Sum over integration point contributions to find element contributions;
4. Sum over element contributions to find stiffness matrix K and contribution to right-hand side vector $\mathbf{f}$;
5. For each element next to the boundary Γ_p determine contribution to $\mathbf{f}$ by:
   a. For each integration point $\bar{\mathbf{x}}_q$:
      (i) Determine $\phi_a(\bar{\mathbf{x}}_q)$ for the nodal points $\mathbf{x}_a$ of Ω_e on Γ_p;
      (ii) Compute integration point contribution to element integral for $\mathbf{f}$;
   b. Sum over integration point contributions to find the element contributions;
6. Sum over contributions of elements next to Γ_p to find right-hand side vector $\mathbf{f}$;

7. Reduce linear system (2.50) by substitution of $\mathbf{d}_a = \mathbf{u}^*(\mathbf{x}_a)$ for $\mathbf{x}_a$ on Γ_u;

8. Solve for reduced vector $\mathbf{d}$;

9. Compute by means of (2.49), differentiation and the constitutive equations, the displacements, strains and stresses in the domain;

10. Error estimates for the quantities can be determined when an exact solution is available;

11. Determine from the computed quantities the $\mathbf{J}$-vector and the stress intensity factors.

In a quasi-static analysis for a material domain by means of the FE-method, the above steps are repeated for a number of (time) steps.

B.2   Set-up for EFG-analysis

A static analysis for a material domain Ω (containing a crack) by means of the EFG-method generally consists of the following steps:

1. Define nodal points $\mathbf{x}_a$, weight functions w_a and basis functions p_c such that moving least squares approximation is well-defined for Ω;

2. Divide Ω into integration cells Δ_e such that the cells match or approximate the boundary $\partial\Omega$;

3. Divide the boundaries Γ_p and Γ_u into boundary integration cells;

4. Define volume force $\mathbf{f}^*$ in Ω, essential boundary conditions $\mathbf{u} = \mathbf{u}^*$ along Γ_u and natural boundary conditions $\sigma\mathbf{n} = \mathbf{p}^*$ along Γ_p;

5. For each integration cell Δ_e compute the contribution to K and $\mathbf{f}$, see (4.4), by:

   a. Determine the matrix D which represents the constitutive equations in Δ_e;

   b. Subdivide Δ_e into triangular subcells to match a crack in the cell;

   c. Determine integration points for Δ_e (by considering each triangular subcell);

   d. For each integration point $\bar{\mathbf{x}}_q$ in Δ_e:

      (i) Compute $\phi_a(\bar{\mathbf{x}}_q)$ and derivatives $\phi_{a,i}(\bar{\mathbf{x}}_q)$ for the nodal points $\mathbf{x}_a$ with non-zero weight function in $\bar{\mathbf{x}}_q$;

      (ii) Determine the matrices B_a, see (4.11);

      (iii) Compute integration point contribution to the cell integrals, e.g. see (4.14);

   e. Sum over integration point contributions to find the cell contributions;

6. Sum over cell contributions to find stiffness matrix K and contribution to right-hand side vector $\mathbf{f}$;

7. For each boundary integration cell in Γ_p determine the contribution to $\mathbf{f}$ by:

   a. Determine integration points for boundary integration cell;

   b. For each integration point $\bar{\mathbf{x}}_q$:

      (i) Determine $\phi_a(\bar{\mathbf{x}}_q)$ for the nodal points $\mathbf{x}_a$ with non-zero weight function in $\bar{\mathbf{x}}_q$;

      (ii) Compute integration point contribution to cell integral for $\mathbf{f}$;

   c. Sum over integration point contributions to find the cell contributions;

8. Sum over contributions of integration cells in Γ_p to find right-hand side vector $\mathbf{f}$;

9. For each boundary integration cell in Γ_u compute contribution to L and $\mathbf{r}$, see (4.4), by:

   a. Determine integration points for boundary integration cell;

   b. For each integration point $\bar{\mathbf{x}}_q$:

(i) Determine $\phi_a(\bar{\mathbf{x}}_q)$ for the nodal points $\mathbf{x}_a$ with non-zero weight function in $\bar{\mathbf{x}}_q$;

(ii) Compute integration point contribution to cell integrals for L and $\mathbf{r}$;

c. Sum over integration point contributions to find cell contributions;

10. Sum over contributions of integration cells in Γ_u to find matrix L and right-hand side vector $\mathbf{r}$;

11. Solve the linear system (4.4) for $\mathbf{d}$ and $\mathbf{l}$;

12. Compute by means of (4.1), differentiation and the constitutive equations, the displacements, strains and stresses in the domain;

13. Error estimates for the quantities can be determined when an exact solution is available;

14. Determine from the computed quantities the J-vector and the stress intensity factors.

In the case when the essential boundary conditions are prescribed at a set of discrete points, the steps **9** and **10** are replaced by a step which considers these discrete points.

In a quasi-static analysis for a material domain by means of the EFG-method, the above steps are repeated for a number of discrete (time) steps.

B.3   Set-up for EFG+FE-analysis

For a short description of a static analysis for a (cracked) material domain Ω by means of a combination of the EFG-method and the FE-method, the set-up is given for an analysis by the combination of the methods with the help of a Lagrange multiplier, see Section 5.2. Similar set-ups can be given for the combination of the EFG-method and the FE-method by means of element-free coupling, see Section 5.1, and the combination by means of interface elements, see Section 5.3. For the description in this section, Ω^1 is the subdomain where the FE-method is applied and Ω^2 the subdomain where the EFG-method is applied. Furthermore, Γ_1 and Γ_2 are the boundaries of Ω^1 and Ω^2, respectively.

An analysis by means of the combination of EFG and FE with the help of a Lagrange multiplier consists of a combination of steps given in the first two sections of this appendix. The subdomain Ω^1 is divided into finite elements according to step **1** in Section B.1. Parameters for moving least squares approximation (MLSA) on Ω^2, and a division of the subdomain and its boundaries $\Gamma_p \cap \Gamma_2$, $\Gamma_u \cap \Gamma_2$ and $\Gamma_1 \cap \Gamma_2$ into integration cells are chosen according to steps **1-3** in Section B.2. Volume force, essential and natural boundary conditions are defined afterwards. Then the linear system (5.7) is built up according to steps **3-7** in Section B.1 and steps **5-10** in Section B.2.

The combination between the subdomains Ω^1 and Ω^2 is accounted for by consideration of the integration cells for the internal boundary $\Gamma_1 \cap \Gamma_2$ similar to the steps **9-10** in Section B.2. For each integration point of a cell, the values of the FE-shape functions and MLSA-shape functions are obtained and the contribution to the matrices H_1 and H_2 are computed, see (5.7). Summing over the integration points and integration cells results in these matrices.

When the system (5.7) has been determined, it is solved for $\mathbf{d}^1$, $\mathbf{d}^2$, $\mathbf{l}^1$, $\mathbf{l}^2$ and $\mathbf{l}$. Similar to steps **9-11** in Section B.1 and **12-14** in Section B.2, with the help of $\mathbf{d}^1$ and $\mathbf{d}^2$ displacements, strains, stresses, error estimates and fracture mechanics parameters are obtained.

Appendix C

On MLSA for the wedge model

Concerning the wedge model presented in Section 3.2, moving least squares approximation (MLSA) is not well-defined for the crack tip. Nevertheless, it has been shown that values for the shape functions can be obtained. The shape functions are continuously differentiable, except for the crack tip. In this appendix a mathematical proof is given of the fact that the shape functions are continuous in the crack tip. In addition, it is proven that for continuously differentiable basis functions and weight functions, the shape functions are continuously differentiable except for the crack tip and that the derivatives of the shape functions are bounded in the vicinity of the crack tip.

It is assumed for MLSA on the domain Ω that:

[A1] A set of nodal points $\{\mathbf{x}_a\}_{a=1,\ldots,n}$ is given such that $\mathbf{x}_1 = \mathbf{0}$.

[A2] A set of basis functions $\{p_c(\mathbf{x})\}_{c=1,\ldots,m}$ is given with $p_1(\mathbf{x}) = 1$ for each $\mathbf{x} \in \Omega$, $p_c(\mathbf{0}) = 0$, $c > 1$, and such that each basis function is continuously differentiable for the entire domain Ω. Hence, a Taylor series expansion yields that $p_c(\mathbf{x}) = O(|\mathbf{x}|)$ for $\mathbf{x} \to \mathbf{0}$, $c > 1$.

[A3] A set of continuously differentiable weight functions $\{w_a(\mathbf{x})\}_{a=1,\ldots,n}$ is chosen such that

    − $w_1(\mathbf{0}) = 1$, $w_a(\mathbf{0}) = 0$, $a > 1$;

    − $|\nabla w_a(\mathbf{0})| = 0$, $a = 1, \ldots, n$;

    − w_1 has derivatives of any order in the interior of its support;

    − The origin $\mathbf{0}$ is not in the interior of the support of w_a, $a > 1$;

    − For $a > 1$, the weight function w_a has derivatives of any order in the interior of its support and all its derivatives are bounded in the neighbourhood of $\mathbf{0}$.

[A4] MLSA is well-defined for $\Omega \backslash \{\mathbf{0}\}$. Hence, for each $\mathbf{x} \in \Omega \backslash \{\mathbf{0}\}$ and each c with $1 < c \leq m$, a nodal point $\mathbf{x}_b$ with $2 \leq b \leq n$ can be found such that $w_b(\mathbf{x}) > 0$ and $p_c(\mathbf{x}_b) \neq 0$.

The notation $f(\mathbf{x}) = O(g(\mathbf{x}))$ for $\mathbf{x} \to \mathbf{0}$ means that there exists an $M > 0$ such that

$$|f(\mathbf{x})| \leq M |g(\mathbf{x})|, \qquad\qquad\qquad\qquad \text{(C.1)}$$

for $\mathbf{x}$ sufficiently close to $\mathbf{0}$.

The above assumptions hold true for the wedge model presented in Section 3.2, when the origin represents the crack tip and when a polynomial set of basis functions is used. In the remaining part of this appendix, the set of orthogonal basis functions $\{q_c(\mathbf{x}, \bar{\mathbf{x}})\}_{c=1,\dots,m}$, as given by (3.13) and (3.14), is used to prove that the shape functions are continuous and have bounded derivatives in the neighbourhood of the crack tip.

We shall prove that under the above assumptions we have for $c = 2, \dots, m$

$$\lim_{\bar{\mathbf{x}} \to \mathbf{0}} q_c(\mathbf{0}, \bar{\mathbf{x}}) = 0; \quad q_c(\mathbf{0}, \bar{\mathbf{x}}) = O\left(\sum_{a=2}^{n} \frac{w_a(\bar{\mathbf{x}})}{\sum_{b=1}^{n} w_b(\bar{\mathbf{x}})} \right) \quad \text{for } \bar{\mathbf{x}} \to \mathbf{0}, \tag{C.2}$$

$$|\nabla_{\bar{\mathbf{x}}} q_c(\mathbf{0}, \bar{\mathbf{x}})| = O(|\bar{\mathbf{x}}|) \quad \text{for } \bar{\mathbf{x}} \to \mathbf{0}. \tag{C.3}$$

For each $\mathbf{x} \in \Omega \backslash \{\mathbf{0}\}$ one has that

$$\lim_{\bar{\mathbf{x}} \to \mathbf{0}} q_c(\mathbf{x}, \bar{\mathbf{x}}) < +\infty, \quad c = 2, \dots, m, \tag{C.4}$$

and the limiting value equals a linear combination of $p_{c_1}(\mathbf{x})$, $1 \le c_1 \le c$. For each c, there exists an index $b > 1$ such that the limit (C.4) for $\mathbf{x} = \mathbf{x}_b$ is non-zero. Moreover, for $\mathbf{x} \in \Omega \backslash \{\mathbf{0}\}$

$$|\nabla_{\bar{\mathbf{x}}} q_c(\mathbf{x}, \bar{\mathbf{x}})| = O(|\bar{\mathbf{x}}|^{-1}) \quad \text{for } \bar{\mathbf{x}} \to \mathbf{0}, \quad c = 2, \dots, m, \tag{C.5}$$

$$\lim_{\bar{\mathbf{x}} \to \mathbf{0}} q_c(\bar{\mathbf{x}}, \bar{\mathbf{x}}) = 0; \quad q_c(\bar{\mathbf{x}}, \bar{\mathbf{x}}) = O(|\bar{\mathbf{x}}|) \quad \text{for } \bar{\mathbf{x}} \to \mathbf{0}, \quad c = 2, \dots, m, \tag{C.6}$$

$$|\nabla q_c(\bar{\mathbf{x}}, \bar{\mathbf{x}})| = O(1) \quad \text{for } \bar{\mathbf{x}} \to \mathbf{0}, \quad c = 2, \dots, m. \tag{C.7}$$

The notation $\lim_{\bar{\mathbf{x}} \to \mathbf{0}} f(\bar{\mathbf{x}}) < +\infty$ means that $f(\bar{\mathbf{x}})$ has a finite limiting value for $\bar{\mathbf{x}}$ approaching $\mathbf{0}$. The gradient in (C.7) should be understood in the following way,

$$\nabla q_c(\bar{\mathbf{x}}, \bar{\mathbf{x}}) = \nabla_{\mathbf{x}} q_c(\bar{\mathbf{x}}, \bar{\mathbf{x}}) + \nabla_{\bar{\mathbf{x}}} q_c(\bar{\mathbf{x}}, \bar{\mathbf{x}}), \quad c = 2, \dots, m. \tag{C.8}$$

Proof:
A proof of (C.2)-(C.7) will be given by means of induction on c.

I. For $c = 2$, equation (3.14) results with assumptions A1, A2 and A3 in

$$q_2(\mathbf{x}, \bar{\mathbf{x}}) = p_2(\mathbf{x}) - \frac{\sum_{a=2}^{n} w_a(\bar{\mathbf{x}}) p_2(\mathbf{x}_a)}{\sum_{a=1}^{n} w_a(\bar{\mathbf{x}})}. \tag{C.9}$$

Therefore,

$$q_2(\mathbf{0}, \bar{\mathbf{x}}) = -\frac{\sum_{a=2}^{n} w_a(\bar{\mathbf{x}}) p_2(\mathbf{x}_a)}{\sum_{a=1}^{n} w_a(\bar{\mathbf{x}})}, \tag{C.10}$$

from which (C.2) is obvious. From the assumption A3 for the weight functions it follows that (C.3) holds true.

From equations (C.9) and (C.10) it follows that for $\mathbf{x} \in \Omega \backslash \{\mathbf{0}\}$

$$\lim_{\bar{\mathbf{x}} \to \mathbf{0}} q_2(\mathbf{x}, \bar{\mathbf{x}}) = p_2(\mathbf{x}) - \lim_{\bar{\mathbf{x}} \to \mathbf{0}} q_2(\mathbf{0}, \bar{\mathbf{x}}) = p_2(\mathbf{x}), \tag{C.11}$$

because of (C.2). There can be found an index $b > 1$ such that the limiting value for $\mathbf{x} = \mathbf{x}_b$ is non-zero, otherwise assumption A4 is not valid. Hence, (C.4) holds true for $c = 2$. Equation (C.9) also shows that

$$\lim_{\bar{\mathbf{x}} \to \mathbf{0}} \nabla_{\bar{\mathbf{x}}} q_2(\mathbf{x}, \bar{\mathbf{x}}) = \lim_{\bar{\mathbf{x}} \to \mathbf{0}} \nabla_{\bar{\mathbf{x}}} q_2(\mathbf{0}, \bar{\mathbf{x}}). \tag{C.12}$$

Therefore, equation (C.5) for $c = 2$ follows directly from (C.3).

Equation (C.9) together with the assumptions for the basis and weight functions results in the fact that $q_2(\bar{\mathbf{x}}, \bar{\mathbf{x}}) = O(|\bar{\mathbf{x}}|)$ for $\bar{\mathbf{x}} \to \mathbf{0}$, which yields (C.6) for $c = 2$. Furthermore, one has that

$$\lim_{\bar{\mathbf{x}} \to \mathbf{0}} \nabla q_2(\bar{\mathbf{x}}, \bar{\mathbf{x}}) = \nabla p_2(\mathbf{0}) - \lim_{\bar{\mathbf{x}} \to \mathbf{0}} \nabla_{\bar{\mathbf{x}}} q_2(\mathbf{0}, \bar{\mathbf{x}}) = \nabla p_2(\mathbf{0}), \tag{C.13}$$

because of (C.3) and hence, (C.7) is valid for $c = 2$.

II. It is now assumed that (C.2)-(C.7) are valid for all c with $2 \le c \le c_1 - 1$, $c_1 \ge 3$. For $c = c_1$, the function $q_c(\mathbf{x}, \bar{\mathbf{x}})$ is given by

$$q_c(\mathbf{x}, \bar{\mathbf{x}}) = p_c(\mathbf{x}) - \sum_{d=1}^{c-1} \alpha_{cd}(\bar{\mathbf{x}}) q_d(\mathbf{x}, \bar{\mathbf{x}}), \tag{C.14}$$

see also (3.14), where because of assumption A2

$$\alpha_{cd}(\bar{\mathbf{x}}) = \frac{\sum_{a=2}^{n} w_a(\bar{\mathbf{x}}) p_c(\mathbf{x}_a) q_d(\mathbf{x}_a, \bar{\mathbf{x}})}{\sum_{a=1}^{n} w_a(\bar{\mathbf{x}}) q_d(\mathbf{x}_a, \bar{\mathbf{x}})^2}, \quad d = 1, \ldots, c-1. \tag{C.15}$$

For $d = 1$, one obtains

$$\alpha_{c1}(\bar{\mathbf{x}}) = \frac{\sum_{a=2}^{n} w_a(\bar{\mathbf{x}}) p_c(\mathbf{x}_a)}{\sum_{a=1}^{n} w_a(\bar{\mathbf{x}})} = O\left(\sum_{a=2}^{n} \frac{w_a(\bar{\mathbf{x}})}{\sum_{b=1}^{n} w_b(\bar{\mathbf{x}})} \right) \quad \text{for } \bar{\mathbf{x}} \to \mathbf{0}, \tag{C.16}$$

and for $d = 2, \ldots, c-1$ one obtains

$$\alpha_{cd}(\bar{\mathbf{x}}) = O(1) \quad \text{for } \bar{\mathbf{x}} \to \mathbf{0}, \tag{C.17}$$

since both the numerator and the denominator in (C.15) are of the same order, i.e., of the order $O(\sum_{a=2}^{n} w_a(\bar{\mathbf{x}}) / \sum_{b=1}^{n} w_b(\bar{\mathbf{x}}))$ for $\bar{\mathbf{x}} \to \mathbf{0}$, because of (C.2) and (C.4). Therefore,

$$\alpha_{cd}(\bar{\mathbf{x}}) q_d(\mathbf{0}, \bar{\mathbf{x}}) = O\left(\sum_{a=2}^{n} \frac{w_a(\bar{\mathbf{x}})}{\sum_{b=1}^{n} w_b(\bar{\mathbf{x}})} \right) \quad \text{for } \bar{\mathbf{x}} \to \mathbf{0}, \quad d = 2, \ldots, c-1, \tag{C.18}$$

which yields that (C.2) is valid for $c = c_1$.

Equation (C.16) together with assumption A3 shows that

$$|\nabla \alpha_{c1}(\bar{\mathbf{x}})| = O(|\bar{\mathbf{x}}|) \quad \text{for } \bar{\mathbf{x}} \to \mathbf{0}. \tag{C.19}$$

In addition, the gradient of $\alpha_{cd}(\bar{\mathbf{x}})$ for $d = 2, \ldots, c - 1$ is given by

$$
\begin{aligned}
\nabla \alpha_{cd}(\bar{\mathbf{x}}) \;=\;& \frac{\sum_{a=2}^{n} w_a(\bar{\mathbf{x}}) p_c(\mathbf{x}_a) \nabla_{\bar{\mathbf{x}}} q_d(\mathbf{x}_a, \bar{\mathbf{x}})}{\sum_{a=1}^{n} w_a(\bar{\mathbf{x}}) q_d(\mathbf{x}_a, \bar{\mathbf{x}})^2} \\[2mm]
& - \frac{\sum_{a=2}^{n} w_a(\bar{\mathbf{x}}) p_c(\mathbf{x}_a) q_d(\mathbf{x}_a, \bar{\mathbf{x}}) \sum_{b=1}^{n} 2 w_b(\bar{\mathbf{x}}) q_d(\mathbf{x}_b, \bar{\mathbf{x}}) \nabla_{\bar{\mathbf{x}}} q_d(\mathbf{x}_b, \bar{\mathbf{x}})}{(\sum_{a=1}^{n} w_a(\bar{\mathbf{x}}) q_d(\mathbf{x}_a, \bar{\mathbf{x}})^2)^2} \\[2mm]
& + \frac{\sum_{a=2}^{n} \sum_{b=1}^{n} [\nabla w_a(\bar{\mathbf{x}}) w_b(\bar{\mathbf{x}}) - w_a(\bar{\mathbf{x}}) \nabla w_b(\bar{\mathbf{x}})] p_c(\mathbf{x}_a) q_d(\mathbf{x}_a, \bar{\mathbf{x}}) q_d(\mathbf{x}_b, \bar{\mathbf{x}})^2}{(\sum_{a=1}^{n} w_a(\bar{\mathbf{x}}) q_d(\mathbf{x}_a, \bar{\mathbf{x}})^2)^2}.
\end{aligned}
\tag{C.20}
$$

Because of (C.2)-(C.5), the first two terms in (C.20) are $O(|\bar{\mathbf{x}}|^{-1})$ for $\bar{\mathbf{x}} \to \mathbf{0}$. The denominator of the last term is $O((\sum_{a=2}^{n} w_a(\bar{\mathbf{x}}) / \sum_{b=1}^{n} w_b(\bar{\mathbf{x}}))^2)$ for $\bar{\mathbf{x}} \to \mathbf{0}$. Hence, because of assumption A3, a Taylor series expansion shows that this denominator is of the order $O(|\bar{\mathbf{x}}|^4)$ for $\bar{\mathbf{x}} \to \mathbf{0}$. Furthermore, with assumption A3, it is seen from Taylor series expansions for $\nabla w_a(\bar{\mathbf{x}}) w_b(\bar{\mathbf{x}}) - w_a(\bar{\mathbf{x}}) \nabla w_b(\bar{\mathbf{x}})$, that the terms in the numerator of the last term in (C.20) for $a = 2, \ldots n$ and $b = 2, \ldots n$ are $O(|\bar{\mathbf{x}}|^3)$ for $\bar{\mathbf{x}} \to \mathbf{0}$. Because of (C.2) the terms in this numerator for $b = 1$ have order $O(|\bar{\mathbf{x}}|^5)$ for $\bar{\mathbf{x}} \to \mathbf{0}$. Therefore, the last term of (C.20) is also of order $O(|\bar{\mathbf{x}}|^{-1})$ for $\bar{\mathbf{x}} \to \mathbf{0}$ and we have

$$|\nabla \alpha_{cd}(\bar{\mathbf{x}})| = O(|\bar{\mathbf{x}}|^{-1}) \quad \text{for } \bar{\mathbf{x}} \to \mathbf{0}, \quad d = 2, \ldots, c - 1, \tag{C.21}$$

From (C.16), (C.17), (C.19), (C.21) and (C.2), (C.3) for $c < c_1$, it now follows that (C.3) holds true for $c = c_1$, since (C.2) yields that $q_c(\mathbf{0}, \bar{\mathbf{x}}) = O(|\bar{\mathbf{x}}|^2)$ for $\bar{\mathbf{x}} \to \mathbf{0}$.

Furthermore, from (C.16), (C.17), (C.19), (C.21) and (C.2)-(C.5) it follows that (C.4) and (C.5) are valid for $c = c_1$. For each c there exists indeed an index b such that the limit in (C.4) is non-zero, otherwise assumption A4 is not valid. With (C.6), (C.7) for $c < c_1$, and the assumptions for the basis functions it is seen that (C.6) and (C.7) hold true for $c = c_1$.

It has been proven that (C.2)-(C.7) hold true for $c = c_1$ and from the principle of mathematical induction one may conclude that (C.2)-(C.7) hold true for $c = 2, \ldots, m$.
End of proof

The shape functions $\phi_a(\mathbf{x})$, $a = 1, \ldots, n$, are given by (3.18). Because of assumptions A2 and A3, the expression (3.18) can be written as

$$\phi_a(\mathbf{x}) = \frac{w_a(\mathbf{x})}{\sum_{b=1}^{n} w_b(\mathbf{x})} + \sum_{c=2}^{m} \frac{w_a(\mathbf{x}) q_c(\mathbf{x}_a, \mathbf{x}) q_c(\mathbf{x}, \mathbf{x})}{\sum_{b=1}^{n} w_b(\mathbf{x}) q_c(\mathbf{x}_b, \mathbf{x})^2}, \quad a = 1, \ldots, n. \tag{C.22}$$

With the assumptions for the weight functions it is seen that the first term of (C.22) approaches

δ_{a1} for $\mathbf{x} \to \mathbf{0}$, i.e., approaches 1 for $a = 1$ and 0 for $a > 1$. Because of (C.2), (C.4) and (C.6), the second term in (C.22) is of the order $O(|\mathbf{x}|)$ for $\mathbf{x} \to \mathbf{0}$, which yields that

$$\lim_{\mathbf{x} \to \mathbf{0}} \phi_a(\mathbf{x}) = \delta_{a1}, \quad a = 1, \ldots, n. \tag{C.23}$$

From (C.23) it is concluded that the shape functions (C.22) are continuous. Moreover, the first term of (C.22) is continuously differentiable for the entire domain. The second term in (C.22) is continuously differentiable except for $\mathbf{x} = \mathbf{0}$. However, because of assumption A3 and (C.2)-(C.7), one has that the second term is $O(1)$ for $\mathbf{x} \to \mathbf{0}$. Hence, the derivatives of the shape functions are bounded near $\mathbf{0}$.

In general, the shape functions are not differentiable for $\mathbf{x} = \mathbf{0}$ as the following one-dimensional example shows. Consider the nodal points $x_1 = 0$ and $x_2 = 1$ and weight functions w_1 and w_2 such that $w_1(0) > 0$, $w_2(x) = 0$ for $x \leq 0$ and $w_2(x) > 0$ for $x > 0$. Let the set of basis functions be given by $\{1, x\}$. When the other weight functions vanish for $0 < x < \varepsilon$ with ε small, the shape function ϕ_2 for node x_2 is given by

$$\phi_2(x) = \begin{cases} 0, & x \leq 0, \\ x, & 0 < x < \varepsilon. \end{cases} \tag{C.24}$$

It can be seen easily that this shape function is not differentiable for $x = 0$.

Appendix D

On the subdivision of standard integration cells

In this appendix it is described in which way numerical integration is performed in a standard integration cell Δ_s, in order to obtain accurate values for the contribution of the integration cell Δ_e to the integrals in (4.7)-(4.10). The standard integration cell is divided into subcells and for each subcell Gaussian quadrature is used. The subdivision is based on the number of nodal points close to Δ_e, on the size of Δ_e, on the number of nodal points in Δ_e and on whether the integration cell is near the boundary, near the crack or near the crack tip.

D.1 Subdivision for quadrilateral integration cell Δ_e

Consider a quadrilateral cell Δ_e with the definition points $\mathbf{z}_1^e$, $\mathbf{z}_2^e$, $\mathbf{z}_3^e$ and $\mathbf{z}_4^e$ as its four vertices. The square $\{(\xi_1, \xi_2) \mid -1 \leq \xi_1 \leq 1, -1 \leq \xi_2 \leq 1\}$ is taken as standard integration cell Δ_s. In order to determine integration points for numerical integration in Δ_s, the next procedure is followed.

Let $\mathbf{x}_{a_1}$ be the nodal points such that $\mathbf{x}_{a_1} \in \Delta_e$ or such that one of the definition points is in the support of the weight function w_{a_1}. The nodal points $\mathbf{x}_{a_1}$ contribute to the cell integrals for K and $\mathbf{f}$. The central point of Δ_e is given by $\mathbf{z}_m^e$, i.e.

$$\mathbf{z}_m^e = \frac{1}{4} \sum_{\varrho=1}^{4} \mathbf{z}_\varrho^e. \tag{D.1}$$

Let r_m^e be the mean distance between the nodes $\mathbf{x}_{a_1}$ and the central point $\mathbf{z}_m^e$,

$$r_m^e = \frac{1}{M} \sum_{a_1} |\mathbf{x}_{a_1} - \mathbf{z}_m^e|, \tag{D.2}$$

which is a characteristic value for the density of the nodal points with respect to the size of Δ_e. In equation (D.2), M is the number of nodal points $\mathbf{x}_{a_1}$. Of course, M will be at most n,

the total number of nodal points. Furthermore, h_e is defined as the mean distance between the mid-side points of Δ_e and the central point $\mathbf{z}_m^e$,

$$h_e = \frac{1}{8} \sum_{\varrho=1}^{4} \left| \mathbf{z}_\varrho^e + \mathbf{z}_{\varrho+1}^e - 2\mathbf{z}_m^e \right|, \tag{D.3}$$

where $\mathbf{z}_5^e = \mathbf{z}_1^e$. The number of sides of Δ_e which are part of the boundary of the domain Ω or which are part of the crack, is denoted by s_e and the number of nodes $\mathbf{x}_{a_1}$ in Δ_e is denoted by M_e. Hence, $M_e \leq M$.

To obtain the contributions of Δ_e to K and $\mathbf{f}$, see (4.4), equation (4.14) is used. For numerical evaluation of the integrals over the standard cell, Δ_s is divided into $N_e \times N_e$ square subcells which all have the same size. Per subcell (4,4)-point Gaussian quadrature is performed. The value N_e is found from the following algorithm:

1. **if** $r_m^e < h_e\sqrt{2}$
    a. **if** $M_e + 2^{s_e}(M - M_e) < 7$
        $N_e = 1$
    b. **elseif** $M_e + 2^{s_e}(M - M_e) < 18$
        $N_e = 2$
    c. **elseif** $M_e + 2^{s_e}(M - M_e) < 36$
        $N_e = 3$
    d. **else**
        $N_e = 4$
    end
2. **elseif** $r_m^e < 2h_e\sqrt{2}$
    a. **if** $M_e + 2^{s_e}(M - M_e) < 18$
        $N_e = 1$
    b. **elseif** $M_e + 2^{s_e}(M - M_e) < 36$
        $N_e = 2$
    c. **else**
        $N_e = 3$
    end
3. **elseif** $r_m^e < (10/3)h_e\sqrt{2}$
    a. **if** $M_e + 2^{s_e}(M - M_e) < 36$
        $N_e = 1$
    b. **else**
        $N_e = 2$
    end
4. **else**
    $N_e = 1$
end
if $\min_{\varrho=1,\ldots,4,m} \left| \mathbf{z}_\varrho^e - \mathbf{y}_C \right| < 2h_a$
    $N_e := 2N_e$
end

This algorithm to determine N_e for Δ_s is just a choice. We are aware that other algorithms with similar properties can be designed. In the algorithm, $\mathbf{y}_C$ is the position of the crack tip and h_a is the local mesh size, see (3.27), for the nodal point $\mathbf{x}_a$ which is closest or equal to $\mathbf{y}_C$.

Four situations are distinguished in the algorithm. Situation **1** represents the case where the nodal points $\mathbf{x}_{a_1}$ are situated mostly inside Δ_e, since $h_e\sqrt{2}$ is the largest distance to the central point of the cell. In situation **2**, these nodes are situated mostly in Δ_e and its surrounding cells; $2h_e\sqrt{2}$ is the mean distance to $\mathbf{z}_m^e$ of points in Δ_e and its surrounding cells. Situation **3** represents the case when the nodes are situated mostly in Δ_e and two rows of its surrounding cells. In situation **4**, a significant part of the nodal points $\mathbf{x}_{a_1}$ is outside Δ_e and two rows of its surrounding cells.

By means of the subcases of **1**, **2**, **3** and **4**, we account for the density of the nodes $\mathbf{x}_{a_1}$ with respect to the size of Δ_e. We provide at least one fourth of a subcell per quadrilateral made up of nodal points. For instance, in the case of **2a**, the nodes are such that one subcell is sufficient whereas the case **2b** represents a situation where the density of the nodes is such that 4 subcells are necessary.

Since the shape functions can have large gradients near the crack tip, the number N_e is doubled in the last part of the algorithm, when the integration cell Δ_e is close to the crack tip.

D.2   Subdivision for triangular integration cell Δ_e

For a triangular integration cell Δ_e, its standard integration cell Δ_s is subdivided according to a similar procedure. Let the vertices of Δ_e be given by $\mathbf{z}_1^e$, $\mathbf{z}_2^e$ and $\mathbf{z}_3^e$. The standard cell is given by the triangle $\Delta_s = \{(\xi_1,\xi_2) \mid 0 \leq \xi_1 \leq 1, \, 0 \leq \xi_2 \leq 1, \, \xi_1 + \xi_2 \leq 1\}$. However, when the triangle has the crack tip as vertex, the standard cell is given by the square $\Delta_s = \{(\xi_1,\xi_2) \mid -1 \leq \xi_1 \leq 1, \, -1 \leq \xi_2 \leq 1\}$, see Section 4.2.

Let $\mathbf{x}_{a_1}$ be the nodal points such that $\mathbf{x}_{a_1} \in \Delta_e$ or such that one of the vertices is in the support of the weight function w_{a_1}. The central point of Δ_e is given by $\mathbf{z}_m^e$, i.e.

$$\mathbf{z}_m^e = \frac{1}{3} \sum_{\varrho=1}^{3} \mathbf{z}_\varrho^e. \tag{D.4}$$

Let r_m^e be the mean distance between the nodes $\mathbf{x}_{a_1}$ and the central point $\mathbf{z}_m^e$,

$$r_m^e = \frac{1}{M} \sum_{a_1} |\mathbf{x}_{a_1} - \mathbf{z}_m^e|, \tag{D.5}$$

where M is the number of nodal points $\mathbf{x}_{a_1}$. Furthermore, h_e is the mean distance between the vertices of the cell and the central point $\mathbf{z}_m^e$,

$$h_e = \frac{1}{3} \sum_{\varrho=1}^{3} \left| \mathbf{z}_\varrho^e - \mathbf{z}_m^e \right|. \tag{D.6}$$

The number of sides and additional vertices of Δ_e which are part of the boundary of Ω or which are part of the crack, is given by s_e and the number of nodes $\mathbf{x}_{a_1}$ in Δ_e is given by M_e. With an additional vertex is meant a vertex for which the sides where it is positioned on are not part of the boundary or part of the crack.

To obtain the contribution of Δ_e to K and $\mathbf{f}$, see (4.4), the standard integration cell Δ_s is subdivided. When Δ_s is a triangle, it is partitioned into N_e^2 triangular subcells, and when Δ_s is a square, it is partitioned into (N_e, N_e) square subcells. Per subcell then 13-point and (4,4)-point Gaussian quadrature, respectively, is performed. The value N_e is found from the following algorithm:

1. **if** $r_m^e < h_e$
       a. if $M_e + 2^{s_e}(M - M_e) < 7$
            $N_e = 1$
       b. elseif $M_e + 2^{s_e}(M - M_e) < 14$
            $N_e = 2$
       c. elseif $M_e + 2^{s_e}(M - M_e) < 29$
            $N_e = 3$
       d. else
            $N_e = 4$
       end
2. **elseif** $r_m^e < 2h_e$
       a. if $M_e + 2^{s_e}(M - M_e) < 14$
            $N_e = 1$
       b. elseif $M_e + 2^{s_e}(M - M_e) < 29$
            $N_e = 2$
       c. else
            $N_e = 3$
       end
3. **elseif** $r_m^e < 10h_e/3$
       a. if $M_e + 2^{s_e}(M - M_e) < 29$
            $N_e = 1$
       b. else
            $N_e = 2$
       end
4. **else**
       $N_e = 1$
end
if $\min_{\varrho=1,\dots,3,m} \left| \mathbf{z}_\varrho^e - \mathbf{y}_C \right| < 2h_a$
    $N_e := 2N_e$
end

In the algorithm, $\mathbf{y}_C$ is the position of the crack tip and h_a is the local mesh size, see (3.27), for the nodal point $\mathbf{x}_a$ which is closest or equal to $\mathbf{y}_C$.

Note the similarity of this algorithm with the algorithm for a quadrilateral integration cell Δ_e.

D.3   Subdivision for boundary integration cell Δ_e

Consider a boundary integration cell Δ_e with the interval $\{\xi \mid -1 \leq \xi \leq 1\}$ as standard integration cell Δ_s. This standard cell is also subdivided to obtain its contributions to the matrix L and the vectors $\mathbf{f}$ and $\mathbf{r}$, see (4.4). The vertices of Δ_e are given by $\mathbf{z}_1^e$ and $\mathbf{z}_2^e$.

Let $\mathbf{x}_{a_1}$ be the nodal points such that $\mathbf{z}_1^e$, $\mathbf{z}_2^e$ or the central point $\mathbf{z}_m^e$ of Δ_e are in the support of the weight function w_{a_1}. This central point $\mathbf{z}_m^e$ is given by

$$\mathbf{z}_m^e = \frac{1}{2}(\mathbf{z}_1^e + \mathbf{z}_2^e). \tag{D.7}$$

The mean distance r_m^e between the nodes $\mathbf{x}_{a_1}$ and the central point $\mathbf{z}_m^e$ is found from

$$r_m^e = \frac{1}{M} \sum_{a_1} |\mathbf{x}_{a_1} - \mathbf{z}_m^e|, \tag{D.8}$$

where M is the number of nodal points $\mathbf{x}_{a_1}$. Let h_e be given by

$$h_e = \frac{1}{2} |\mathbf{z}_2^e - \mathbf{z}_1^e|. \tag{D.9}$$

The integer s_e has the value 1 if one of the vertices of Δ_e is positioned on the crack or corner node of the domain under consideration. If this is not the case, s_e has the value 0.

Then, to obtain the contributions of cell Δ_e, its standard cell Δ_s is partitioned into N_e subcells (intervals) of the same size and 4-point Gaussian quadrature is performed for each subcell. The value N_e is found from the algorithm:

1. **if** $r_m^e < h_e$
    a. if $2^{s_e} M < 4$
        $N_e = 1$
    b. elseif $2^{s_e} M < 6$
        $N_e = 2$
    c. elseif $2^{s_e} M < 8$
        $N_e = 3$
    d. else
        $N_e = 4$
    end
2. **elseif** $r_m^e < 2h_e$
    a. if $2^{s_e} M < 8$
        $N_e = 1$
    b. elseif $2^{s_e} M < 14$
        $N_e = 2$
    c. else
        $N_e = 3$
    end

3. elseif $r_m^e < 10 h_e/3$
    a. if $2^{s_e} M < 12$
        $N_e = 1$
    b. else
        $N_e = 2$
    end
4. else
    $N_e = 1$
end

Since a boundary integration cell Δ_e is at a remote distance of the crack tip, no doubling of N_e has to be considered as in the previous algorithm.

Bibliography

[1] ATKIN, R.J., AND FOX, N. *An Introduction to the Theory of Elasticity.* Longman, London, 1980.

[2] ATKINSON, K.E. *An Introduction to Numerical Analysis.* John Wiley & Sons, New York, 1978.

[3] BARSOUM, R.S. On the use of Isoparametric Finite Elements in Linear Fracture Mechanics. *International Journal for Numerical Methods in Engineering* **10** (1976), 25–37.

[4] BELYTSCHKO, T., FISH, J., AND ENGELMANN, B.E. A Finite Element with Embedded Localization Zones. *Computer Methods in Applied Mechanics and Engineering* **70** (1988), 59–89.

[5] BELYTSCHKO, T., GU, L., AND LU, Y.Y. Fracture and Crack Growth by Element Free Galerkin Methods. *Modelling and Simulation in Material Science and Engineering* **2** (1994), 519–534.

[6] BELYTSCHKO, T., KRONGAUZ, Y., FLEMING, M., ORGAN, D., AND LIU, W.K. Smoothing and Accelerated Computations in the Element Free Galerkin Method. *Journal of Computational and Applied Mathematics* **74** (1996), 111–126.

[7] BELYTSCHKO, T., LU, Y.Y., AND GU, L. Element-free Galerkin Methods. *International Journal for Numerical Methods in Engineering* **37** (1994), 229–256.

[8] BELYTSCHKO, T., LU, Y.Y., AND GU, L. Crack Propagation by Element free Galerkin Methods. *Engineering Fracture Mechanics* **51** (1995), 295–315.

[9] BELYTSCHKO, T., LU, Y.Y., GU, L., AND TABBARA, M. Element-free Galerkin Methods for Static and Dynamic Fracture. *International Journal of Solids and Structures* **32** (1995), 2547–2570.

[10] BELYTSCHKO, T., ORGAN, D., AND KRONGAUZ, Y. A Coupled Finite Element-Element-free Galerkin Method. *Computational Mechanics* **17** (1995), 186–195.

[11] BELYTSCHKO, T., AND TABBARA, M. Dynamic Fracture using Element-free Galerkin Methods. *International Journal for Numerical Methods in Engineering* **39** (1996), 923–938.

[12] BREBBIA, C.A., AND DOMINGUEZ, J. *Boundary Elements, An Introductory Course.* Computational Mechanics Publications and McGraw-Hill, Southampton and New York, 1992.

[13] BROEK, D. *Elementary Engineering Fracture Mechanics.* Kluwer Academic Publishers, Dordrecht, 1986.

[14] CHABOCHE, J.L. Continuum Damage Mechanics: Part 1-General Concepts. *Transactions of ASME, Journal of Applied Mechanics* **55** (1988), 59–64.

[15] CHABOCHE, J.L. Continuum Damage Mechanics: Part 2-Damage Growth, Crack Initiation, and Crack Growth. *Transactions of ASME, Journal of Applied Mechanics* **55** (1988), 65–72.

[16] CHEN, G., AND ZHOU, J. *Boundary Element Methods.* Academic Press, London, 1992.

[17] CHEREPANOV, G.P. *Mechanics of Brittle Fracture.* McGraw-Hill, New York, 1979.

[18] CIARLET, P.G. *The Finite Element Method for Elliptical Problems.* North Holland Publishing Company, New York, 1978.

[19] COWPER, G.R. Gaussian Quadrature Formulas for Triangles. *International Journal for Numerical Methods in Engineering* **7** (1973), 405–408.

[20] EISCHEN, J.W. An Improved Method for Computing the J_2 Integral. *Engineering Fracture Mechanics* **26** (1987), 691–700.

[21] ELLIS, T.M.R., PHILIPS, I.R., AND LAHEY, T.M. *Fortran 90 Programming.* Addison-Wesley Publishing Company, Wokingham, 1994.

[22] ERDOGAN, F., AND SIH, G.C. On the Crack Extension in Plates Under Plane Loading and Transverse Shear. *Transactions of ASME, Journal of Basic Engineering* **85** (1963), 519–527.

[23] FEENSTRA, P.H. *Computational Aspects of Biaxial Stress in Plain and Reinforced Concrete.* PhD thesis, Delft University of Technology, 1993.

[24] FISH, J., AND BELYTSCHKO, T. Elements with Embedded Localization Zones for Large Deformation Problems. *Computer and Structures* **30** (1988), 247–256.

[25] FLEMING, M., CHU, Y.A., MORAN, B., AND BELYTSCHKO, T. Enriched Element-free Galerkin Methods for Crack Tip Fields. *International Journal for Numerical Methods in Engineering, to appear.*

[26] FRANKE, R. Scattered Data Interpolation: Tests of Some Methods. *Mathematics of Computation* **38**, 157 (1982), 181–200.

[27] FRANKE, R., AND NIELSON, G. Smooth Interpolation of Large Sets of Scattered Data. *International Journal for Numerical Methods in Engineering* **15** (1980), 1691–1704.

[28] GORDON, W.J., AND WIXOM, J.A. Shepard's Method of "Metric Interpolation" to Bivariate and Multivariate Interpolation. *Mathematics of Computation* **32**, 141 (1978), 253–264.

[29] HEGEN, D. Numerical Techniques for the Simulation of Crack Growth. *Eindhoven University of Technology* (1994). Final report of the postgraduate programme Mathematics for Industry.

[30] HEGEN, D. Element-free Galerkin Methods in combination with Finite Element approaches. *Computer Methods in Applied Mechanics and Engineering* **135** (1996), 143–166.

[31] HEGEN, D. A Numerical Model for Crack Growth in Brittle Materials based on the Element Free Galerkin Method. *Mechanisms and Mechanics of Damage and Failure of Engineering Materials and Structures II* (1996), 987–992. Proceedings of the 11th European Conference on Fracture, Poitiers-Futuroscope, France.

[32] HORSTEN, J.B.A.M., AND VAN VROONHOVEN, J.C.W. A Hybrid Fracture-Damage Crack Propagation Model. *Localized Damage III, Computer-Aided Assessment and Control* (1994), 367–374. Proceedings of the 3rd International Conference on Localized Damage, Udine, Italy.

[33] HUGHES, T.J.R. *The Finite Element Method.* Prentice-Hall, Englewood Cliffs NJ, 1987.

[34] IOSIPESCU, N. New Accurate Procedure for Single Shear Testing of Metals. *Journal of Materials* **2** (1967), 293–294.

[35] ISHIKAWA, H. A Finite Element Analysis of Stress Intensity Factors for Combined Tensile and Shear Loading by only a Virtual Crack Extension. *International Journal of Fracture* **16** (1980), R243–R247.

[36] JOHNSON, C. *Numerical Solution of Partial Differential Equations by the Finite Element Method.* Cambridge University Press, Cambridge, 1992.

[37] KANNINEN, M.F., AND POPELAR, C.H. *Advanced Fracture Mechanics.* Oxford Engineering Science Series, New York, 1985.

[38] KANSA, E.J. Multiquadratics-A Scattered Data Approximation Scheme with Application to Computational Fluid Dynamics-I. *Computers and Mathematics with Applications* **19**, 8/9 (1990), 127–145.

[39] KANSA, E.J. Multiquadratics-A Scattered Data Approximation Scheme with Application to Computational Fluid Dynamics-II. *Computers and Mathematics with Applications* **19**, 8/9 (1990), 147–161.

[40] KRONGAUZ, Y., AND BELYTSCHKO, T. Enforcement of Essential Boundary Conditions in Meshless Approximations using Finite Elements. *Computer Methods in Applied Mechanics and Engineering* **131** (1996), 133–145.

[41] KRYSL, P., AND BELYTSCHKO, T. Analysis of Thin Plates by the Element-free Galerkin Method. *Computational Mechanics* **16** (1996), 1–10.

[42] KRYSL, P., AND BELYTSCHKO, T. Analysis of Thin Shells by the Element-free Galerkin Method. *International Journal of Solids and Structures* **33** (1996), 3057–3080.

[43] LANCASTER, P., AND ŠALKAUSKAS, K. Surfaces Generated by Moving Least Squares Methods. *Mathematics of Computation* **37**, 155 (1981), 141–158.

[44] LANCASTER, P., AND ŠALKAUSKAS, K. *Curve and Surface Fitting, An Introduction.* Academic Press, London, 1986.

[45] LASRY, D., AND BELYTSCHKO, T. Localization Limiters in Transient Problems. *International Journal of Solids and Structures* **24** (1988), 581–597.

[46] LEMAITRE, J. Local Approach of Fracture. *Engineering Fracture Mechanics* **25** (1986), 523–537.

[47] LIM, I.L., JOHNSTON, I.W., AND CHOI, S.K. Application of Singular Quadratic Distorted Isoparametric Elements in Linear Fracture Mechanics. *International Journal for Numerical Methods in Engineering* **36** (1993), 2473–2499.

[48] LU, Y.Y., BELYTSCHKO, T., AND GU, L. A New Implementation of the Element Free Galerkin Method. *Computer Methods in Applied Mechanics and Engineering* **113** (1994), 397–414.

[49] LU, Y.Y., BELYTSCHKO, T., AND TABBARA, M. Element-free Galerkin Method for Wave Propagation and Dynamic Fracture. *Computer Methods in Applied Mechanics and Engineering* **126** (1995), 131–153.

[50] LUBLINER, J., OLIVER, J., OLLER, S., AND OÑATE, E. A Plastic-Damage Model for Concrete. *International Journal of Solids and Structures* **25** (1989), 299–326.

[51] MATLAB. *High-Performance Numeric Computation and Visualization Software. Reference Guide.* The MathWorks, Natick MA, 1992.

[52] MI, Y. *Three-Dimensional Analysis of Crack Growth.* Computational Mechanics Publications, Southampton, 1996.

[53] MONAGHAN, J.J. An Introduction to SPH. *Computer Physics Communications* **48** (1988), 89–96.

[54] MORAN, B., AND SHIH, C.F. A General Treatment of Crack Tip Contour Integrals. *International Journal of Fracture* **35** (1987), 295–310.

[55] MURAKAMI, S. Mechanical Modeling of Material Damage. *Transactions of ASME, Journal of Applied Mechanics* **55** (1988), 280–286.

[56] NAYROLES, B., TOUZOT, G., AND VILLON, P. Generalizing the Finite Element Method: Diffuse Approximation and Diffuse Elements. *Computational Mechanics* **10** (1992), 307–318.

[57] NISHIOKA, T., AND ATLURI, S.N. Numerical Modeling of Dynamic Crack Propagation in Finite Bodies, by Moving Singular Elements. *Transactions of ASME, Journal of Applied Mechanics* **47** (1980), 570–582.

[58] ORGAN, D., FLEMING, M., TERRY, T., AND BELYTSCHKO, T. Continuous Meshless Approximations for Nonconvex Bodies by Diffraction and Transparency. *Computational Mechanics* **18** (1996), 225–235.

[59] PARKS, D.M. A Stiffness Derivative Finite Element Technique for Determination of Crack Tip Stress Intensity Factors. *International Journal of Fracture* **10** (1974), 487–501.

[60] RICE, J. A Path Independent Integral and the Approximate Analysis of Strain Concentration by Notches and Cracks. *Transactions of ASME, Journal of Applied Mechanics* **35** (1968), 379–386.

[61] ROOKE, D.P., AND CARTWRIGHT, D.J. *Compendium of Stress Intensity Factors.* Her Majesty's Stationery Office, London, 1976.

[62] ROTS, J.G. Smeared and Discrete Representations of Localized Failure. *International Journal of Fracture* **51** (1991), 45–59.

[63] SCHLANGEN, E. *Experimental and Numerical Analysis of Fracture Processes in Concrete.* PhD thesis, Delft University of Technology, 1993.

[64] SEPRAN. *Sepra Analysis. Users Guide and Programmers Manual.* Ingenieursbureau Sepra, Leidschendam, The Netherlands, 1993.

[65] SLUYS, L.J. *Wave Propagation, Localisation and Dispersion in Softening Solids.* PhD thesis, Delft University of Technology, 1992.

[66] STERN, M. Families of Consistent Conforming Elements with Singular Derivative Fields. *International Journal for Numerical Methods in Engineering* **14** (1979), 409–421.

[67] STERN, M., AND BECKER, E.B. A Conforming Crack Tip Element with Quadratic Variation in the Singular Fields. *International Journal for Numerical Methods in Engineering* **12** (1978), 279–288.

[68] SUMI, Y. Computational Crack Path Prediction. *Theoretical and Applied Fracture Mechanics* **4** (1985), 149–156.

[69] TAYLOR, R.L., SIMO, J.C., ZIENKIEWICZ, O.C., AND CHAN, A.C.H. The Patch Test-A Condition for Assessing FEM Convergence. *International Journal for Numerical Methods in Engineering* **22** (1986), 39–62.

[70] TIMOSHENKO, S.P., AND GOODIER, J.N. *Theory of Elasticity.* McGraw-Hill, New York, 1970.

[71] VAN VROONHOVEN, J.C.W. Private communication (1996).

[72] VAN VROONHOVEN, J.C.W. *Dynamic Crack Propagation in Brittle Materials: Analyses Based on Fracture and Damage Mechanics.* PhD thesis, Eindhoven University of Technology, 1996.

[73] WASHIZU, K. *Variational Methods in Elasticity and Plasticity.* Pergamon Press, Oxford, 1968.

[74] XU, X.P., AND NEEDLEMAN, A. Numerical Simulations of Fast Crack Growth in Brittle Solids. *Journal of the Mechanics and Physics of Solids* **42** (1994), 1387–1434.

[75] ZIENKIEWICZ, O.C. *The Finite Element Method in Engineering Science.* McGraw-Hill, London, 1971.

List of symbols

This chapter contains an explanation of the symbols used in this thesis.

Roman symbols

a	index for discrete points and shape functions, radius of circular boundary, length of crack
a_1	index for discrete points
b	index for discrete points and shape functions, dimension of cracked material domain
c, c_1	index for basis functions
$\mathbf{d}$, $\mathbf{d}^1$, $\mathbf{d}^2$	vector containing nodal displacement vectors
$\mathbf{d}_a$, $\mathbf{d}_a^1$, $\mathbf{d}_a^2$	nodal displacement vector
d	index for basis functions, length of patch
d_a	modification function for presence of crack
d_1	modification function for nodal point at crack tip
d_a^1, d_a^2, d^3	functions for definition of modification function
$\mathbf{e}$, $\mathbf{e}_1$, $\mathbf{e}_2$, $\mathbf{e}_3$	unit vector
e	index for elements and integration cells
$\mathbf{f}$, $\mathbf{f}^1$, $\mathbf{f}^2$	right-hand side vector
$\mathbf{f}_a$	subvector of right-hand side vector
$\mathbf{f}^*$	volume force vector
f	general scalar function
f_i^*	entry of volume force vector
f_{ij}^I, f_{ij}^{II}	function for angular variation of elastic stresses near crack tip
g	general scalar function
g_C	function for position relative to crack
h	mesh size of distribution of nodes, dimension of cracked material domain
h_a	local mesh size of distribution of nodes
h_e	mean distance to central point of integration cell
h_1	local mesh size for nodal point at crack tip
h_a^i	local mesh size of distribution of nodes in quadrant
i	index for space dimensions
j	index for space dimensions
k	index for space dimensions, integer, number of shape functions

k_1, k_2	number of shape functions
$\mathbf{l}$, $\mathbf{l}^1$, $\mathbf{l}^2$	vector containing nodal vectors for representation of Lagrange multiplier
$\mathbf{l}_b$, $\mathbf{l}_b^1$, $\mathbf{l}_b^2$	nodal vector for representation of Lagrange multiplier
l	index for space dimensions, integer, length of patch
m	number of basis functions
$\mathbf{n}$	outward unit normal on boundary
n	number of nodal points
n_i, n_1, n_2	entry of outward unit normal on boundary, number of nodal points
$\mathbf{p}$	vector of basis functions
$\mathbf{p}^*$	prescribed boundary traction
p, p_c	basis function
p_i^*	entry of prescribed boundary traction
q_c	(orthogonal) basis function
$\mathbf{r}$, $\mathbf{r}^1$, $\mathbf{r}^2$	right-hand side vector
$\mathbf{r}_b$	subvector of right-hand side vector
r	distance to crack tip, polar coordinate
r_a	polar coordinate with respect to nodal point
r_m^e	mean distance of nodes
s	integer, size of square contour for computation of J-integral
s_a	scaling constant in weight function of Gaussian type
s_e	number of sides (and additional vertices) of integration cell contained in boundary or crack
$\mathbf{t}$	traction vector
t	time, interface function
t_a	non-negative function
$\mathbf{u}$, $\mathbf{u}^1$, $\mathbf{u}^2$	displacement vector, vector consisting of nodal values of u
$\mathbf{u}^*$	prescribed displacement
u	general function
u_a	nodal value of u
u_i, u_i^1, u_i^2	entry of displacement
u^h	approximant of u
u_i^0	elastic displacement of crack tip
u_i^*	entry of prescribed displacement vector
u_i^I, u_i^{II}	function for angular variation of elastic displacements near crack tip
$\mathbf{v}_1$, $\mathbf{v}_2$	unit vector for determination of local mesh size
$\mathbf{v}_1^a$, $\mathbf{v}_2^a$	unit vector for definition of modification function
$\mathbf{v}_1^b$, $\mathbf{v}_2^b$	unit vector for position relative to crack
w, w_a, w_a^{old}	weight function
w_1	weight function of nodal point at crack tip
w_a^{new}	modified weight function
$\mathbf{x}$, $\bar{\mathbf{x}}$	position vector of point in space
$\mathbf{x}_a$, $\mathbf{x}_a^1$, $\mathbf{x}_a^2$	position vector of nodal point
$\mathbf{x}_1$	position vector of nodal point at crack tip
$\bar{\mathbf{x}}_q$	position vector of integration point
x, x_i, x_1, x_2, x_3	Cartesian coordinate

$\mathbf{y}_b$	position vector of point of piecewise linear crack
$\mathbf{y}_C$	position vector of crack tip
$\mathbf{z}_a$	position vector of discrete point of Γ_u
$\mathbf{z}_m^e$	position vector of central point of integration cell
$\mathbf{z}_\varrho^e$	position vector of definition point for integration cell
A	matrix for computation of moving least squares approximant
B_a	matrix consisting of derivatives of shape functions
C	number of points which make up piecewise linear crack
$C^k(\Omega)$	space of k times continuously differentiable functions on Ω
D	matrix representing constitutive law of elastic material
E, E_1	Young's modulus of elasticity
E_d	Young's modulus of elasticity for damaged material
F, F_1, F_2	shear force
G	shear modulus
H_1, H_2	matrix for coupling of subdomains
$H^i(\Omega)$	Sobolev space of order i on Ω
H_a^i	set of distances between nodes
I	identity matrix
$\mathbf{J}$	vector obtained by J-integration
J_k	entry of $\mathbf{J}$-vector
K	stress intensity factor, stiffness matrix
K_{ab}	nodal submatrix of stiffness matrix
K_1, K_2	stiffness matrix
K_I, K_{II}	stress intensity factor
K_{I_C}	critical stress intensity factor
K_I^h, K_{II}^h	computed stress intensity factors
L, L_1, L_2	matrix for Lagrange multiplier
L_{ab}	nodal submatrix of matrix for Lagrange multiplier
$L^2(\Omega)$	set of square integrable functions on Ω
M	positive constant, number of nodal points
M_e	number of nodal points in integration cell
N	number of elements or number of integration cells
N_a	number of non-empty sets
N_e	number of subcells of standard integration cell
P	matrix consisting of nodal values of basis functions
P_{ca}	entry of matrix consisting of nodal values of basis functions
Q_a^i	quadrant with nodal point as vertex
R	convergence rate
R_a, R_a^{old}	radius of support of weight function
R_1	radius of support of weight function for nodal point at crack tip
R_a^{new}	modified radius of support of weight function
S	result of summation over nodal points
SD_I, SD_{II}	standard deviation
V_b	set for position relative to crack
W	diagonal matrix consisting of values of weight functions

W_{ab}	entry of diagonal matrix consisting of values of weight functions
$W_e,\ W_e^+,\ W_e^-$	elastic energy density

Greek and other symbols

α_{cd}	scalar for definition of orthogonal basis functions
β	crack angle
β_a	integer
$\gamma,\ \gamma_C^+,\ \gamma_C^-$	curve for definition of J-integral
$\gamma_C,\ \gamma_C^1,\ \gamma_C^2$	segment for computation of J-integral
δ	Dirac's delta function
δ_{ij}	Kronecker's delta
$\delta\mathbf{u},\ \delta\mathbf{u}^1,\ \delta\mathbf{u}^2$	test displacement vector
$\delta\boldsymbol{\lambda},\ \delta\boldsymbol{\lambda}^1,\ \delta\boldsymbol{\lambda}^2$	test Lagrange multiplier
$\delta u_i,\ \delta u_i^1,\ \delta u_i^2$	test displacement
$\delta\lambda_i,\ \delta\lambda_i^1,\ \delta\lambda_i^2$	entry of test Lagrange multiplier
ϵ	strain, Green Lagrange strain tensor
$\epsilon_{ij},\ \epsilon_{ij}^1,\ \epsilon_{ij}^2$	entry of Green Lagrange strain tensor in Cartesian coordinate system
$\varepsilon,\ \varepsilon_a,\ \varepsilon_1,\ \varepsilon_2$	(positive) real number
$\zeta,\ \zeta_a,\ \zeta_a^1,\ \zeta_a^2$	value of inner product
$\eta,\ \eta_1,\ \eta_2$	material constant for damage evolution
$\theta,\ \theta_a$	polar coordinate
θ_p	propagation angle of crack
θ_{C-1}	angle of direction of last segment of crack
κ	material parameter for planar deformation
$\boldsymbol{\lambda},\ \boldsymbol{\lambda}^a,\ \boldsymbol{\lambda}^1,\ \boldsymbol{\lambda}^2$	Lagrange multiplier
$\lambda_i,\ \lambda_i^1,\ \lambda_i^2$	entry of Lagrange multiplier
$\boldsymbol{\mu},\ \bar{\boldsymbol{\mu}}$	vector for linear combination of basis functions
μ_c	scalar for linear combination of basis functions
$\nu,\ \nu_1$	Poisson's contraction ratio
$\boldsymbol{\xi}$	position vector of point of standard element or standard integration cell
$\boldsymbol{\xi}_b$	position vector of local nodal point of standard element
$\boldsymbol{\xi}_\varsigma$	position vector of local definition point of standard integration cell
$\xi_i,\ \xi_1,\ \xi_2$	Cartesian coordinate in standard element
ρ	density of linearly elastic material
ϱ	index for definition points of integration cells
σ	stress, Cauchy stress tensor
$\sigma_{ij},\ \sigma_{ij}^1,\ \sigma_{ij}^2$	entry of Cauchy stress tensor in Cartesian coordinate system
σ_{ij}^0	finite elastic stress at crack tip
$\sigma_{\theta\theta}$	circumferential tensile stress
ς	index for local definition points of standard integration cell
τ	potential energy of elastic medium
υ	scalar for determination of sizes of supports of weight functions

$\phi_a,\ \phi_a^1,\ \phi_a^2$	global shape function
$\varphi_b,\ \varphi_\varsigma$	local shape function
χ	fourth-order tensor for constitutive equations
χ_{ijkl}	entry of fourth-order tensor for constitutive equations
$\psi_b,\ \psi_b^1,\ \psi_b^2$	function for representation of Lagrange multiplier
ω	wedge angle
$\Gamma_p,\ \Gamma_{p_i}$	boundary for prescribed traction
$\Gamma_u,\ \Gamma_{u_i}$	boundary for prescribed displacement
$\Gamma_1,\ \Gamma_2$	boundary of subdomain
Δa	step length for crack propagation
Δ_e	integration cell
Δ_s	standard integration cell
Ψ	angle
Ψ_a	angle of influence
Ω	undeformed configuration of elastic medium, domain
Ω_e	element
Ω_s	standard element
Ω^i	interface domain
$\Omega^1,\ \Omega^2$	subdomains
$\partial\Omega$	boundary of Ω
$\mathcal{B}$	linearly elastic medium
$\mathcal{D}$	damage variable
$\mathcal{G}$	energy release rate
$\mathcal{G}_C$	critical energy release rate
$\mathbf{0}$	vector containing only zeros
$I\!N$	set of natural numbers

Curriculum vitae

10 juni 1968   geboren te Exloo.

1980-1986   Gemeentelijke Scholengemeenschap te Emmen.
Diploma Atheneum B in juni 1986.

1986-1992   Rijksuniversiteit Groningen.
Studierichting Wiskunde.
Diplomering in augustus 1992 (cum laude).

Afgestudeerd in de functionaal en harmonische analyse. Titel afstudeerwerk: *Existence of a Fundamental Solution and a Definition of Hypoellipticy for Linear Partial Differential Difference Operators with constant coefficients.*

1992-1994   Technische Universiteit Eindhoven.
Postdoctorale ontwerpersopleiding Wiskunde voor de Industrie.
Diplomering in december 1994.

Eindopdracht in de continuümsmechanica uitgevoerd op het Philips Natuurkundig Laboratorium, Eindhoven. Titel eindrapport: *Numerical Techniques for the Simulation of Crack Growth.*

1994-1996   Technische Universiteit Eindhoven.
Assistent in Opleiding, faculteit Werktuigbouwkunde, vakgroep Fundamentele Werktuigkunde.

Promotie-onderzoek op het gebied van het elementvrij simuleren van scheurpropagatie in brosse materialen, uitgevoerd op het Philips Natuurkundig Laboratorium, Eindhoven.

The author of this thesis was born in 1968 in Exloo, The Netherlands. From 1980 to 1986 he received his secondary education at Gemeentelijke Scholengemeenschap in Emmen, where he graduated in June 1986.

During the years 1986-1992 he studied mathematics at the University of Groningen and specialized in pure analysis. In August 1992 he obtained the Master's degree in mathematics with honours. The subject of his Master's thesis was *Existence of a Fundamental Solution and a Definition of Hypoellipticy for Linear Partial Differential Difference Operators with constant coefficients.*

From 1992-1994 he followed the postgraduate programme Mathematics for Industry at Eindhoven University of Technology. In december 1994 he graduated on a final project in continuum mechanics carried out at the Philips Research Laboratories, Eindhoven. The subject of the final report was *Numerical Techniques for the Simulation of Crack Growth.*

During the years 1994-1996 the project at the Laboratories was continued as PhD research for the group Fundamentals of Mechanical Engineering at the Faculty of Mechanical Engineering of Eindhoven University of Technology. This PhD research focused on the element-free simulation of crack propagation in brittle materials.

Dankwoord

Ondanks het feit dat dit proefschrift één auteur kent, zou het niet tot stand zijn gekomen zonder de medewerking, de steun en de belangstelling, rechtstreeks of "vanaf de zijlijn", van vele mensen. Enkelen van hen wilde ik graag met name bedanken.

Allereerst bedank ik eerste promotor Frank Baaijens en Joost Horsten voor het initiëren van het promotie-onderzoek en hun steun in het beginstadium.

Jos van Vroonhoven heeft in het latere stadium de begeleiding op zich genomen en met zijn kritische kijk en gewillig oor me heel wat verbeteringen doen aanbrengen in de EFG-methode en het proefschrift, waarvoor mijn hartelijke dank.

Verder dank ik tweede promotor Rene de Borst en copromotor Piet Schreurs voor hun bijdrage tot de totstandkoming van dit proefschrift.

Ook ben ik Paul Tijink dank verschuldigd voor zijn commentaar op de hoofdstukken 2, 3 en 4.

Philips Natuurkundig Laboratorium diende drie jaar lang als basis voor het uitvoeren van het onderzoek. De groepsleiders Budi Sastra en Joseph Pankert dank ik voor het opnemen van mij in hun beider groepen, hun medewerking en het ter beschikking stellen van alle faciliteiten.

De (ex-)leden van hun groepen dank ik voor hun collegialiteit en, in vele gevallen, vriendschap, daarbij Wilbert van den Eijnde en Edwin Stierman in het bijzonder noemend.

Het onderzoek is uitgevoerd gedurende de drie jaar in de directe nabijheid van vier verschillende kamergenoten, te weten: Peter Rongen, Bas van Rens, Edwin van Dalm en Willem de Jonge. Hun dank ik allen voor hun behulpzaamheid, begrip en steun.

De computerondersteuningsgroep van het NatLab. verdient een speciaal woord van dank voor hun snelle en efficiënte oplossingen voor enkele problemen betreffende programmatuur en computers.

Naast het doen van onderzoek op het NatLab., is er ook fanatiek gevoetbald. Medespelers van WYbertjes, PSW'96 en de NatLab. selectie bedank ik hierbij voor vele sportieve uurtjes.

De muziekzender "Studio Brussel" heeft middels haar uitstekende programmering bijgedragen tot een goede sfeer voor het uitvoeren van het onderzoek.

Vrienden en familie ontvangen hierbij mijn uitdrukkelijke dank voor hun belangstelling en het opfrissen van me middels andere activiteiten.

Internet provided means to communicate with a lot of friends. Here I have to mention, especially, Nils Meland. The contact with him during my period at the NatLab. had a positive effect on my research.

Last but not least, dank ik Francis van der Velden voor haar liefde, steun, en begrip gedurende mijn laatste onderzoeksjaar.

Stellingen

behorende bij het proefschrift

An Element-free Galerkin Method for
Crack Propagation in Brittle Materials

van

Dries Hegen

1. Zowel de elementvrije Galerkin methode als een combinatie van deze methode met de eindige elementen methode bieden de mogelijkheid om scheurgroei te simuleren zonder het voortdurend wijzigen van een connectiviteit van knooppunten benodigd voor het benaderen van verplaatsingen en spanningen in het gescheurde materiaal.

   Dit proefschrift, hoofdstukken 3-6.

2. Een nauwkeurige benadering van het verplaatsingsveld in de directe omgeving van een scheur in twee-dimensionaal elastisch materiaal middels vormfuncties verkregen met behulp van de benaderingstechniek gebaseerd op "Moving Least Squares" is niet mogelijk als men blijft vasthouden aan de eis dat deze techniek goed gedefinieerd moet zijn in de scheurtip.

   Dit proefschrift, hoofdstuk 3.

3. Ondanks de toevoeging van het theoretische $\sqrt{r}$-gedrag in analyses van gescheurd elastisch materiaal middels de elementvrije Galerkin methode of de eindige elementen methode, zal het toepassen van vrij grove discretisaties in de θ-richting rondom de scheurtip niet leiden tot een heel nauwkeurig verplaatsingsveld nabij de scheurtip. Desalniettemin kunnen met behulp van een gecorrigeerde J-integraal nauwkeurige spanningsintensiteitsfactoren worden verkregen uit deze analyses.

   Dit proefschrift, hoofdstukken 4 en 6.
   J.W. Eischen, *Engineering Fracture Mechanics* **26** (1987), 691-700.

4. De eindige elementen techniek waarbij schade binnen een element beschreven kan worden met behulp van een localiseringszone, zoals voorgesteld door Belytschko, Fish en Engelmann, is niet toepasbaar op bros materiaalgedrag.

   T. Belytschko, J. Fish and B. Engelmann, *Computer Methods in Applied Mechanics and Engineering* **70** (1988), 59-89.
   D. Hegen, Eindrapport Ontwerpersopleiding Wiskunde voor de Industrie, Technische Universiteit Eindhoven (1994), 25-49.

5. Het bewijs zonder Fouriertransformatie van het bestaan van een fundamentele oplossing voor lineaire partiële differentiaal operatoren met constante coëfficiënten, zoals gegeven door Rosay, kan worden gegeneraliseerd tot lineaire partiële differentiaal differentie operatoren met constante coëfficiënten.

   J.P. Rosay, *The American Mathematical Monthly* **98** (1991), 518-523.
   D. Hegen, Afstudeerverslag, Rijksuniversiteit Groningen (1992).

6. De familienaam *Heegen* zoals die momenteel in Nederland voorkomt, is tot stand gekomen door een verschrijving van de familienaam *Hegen* bij de burgerlijke stand van de gemeente Zweeloo gedurende de periode 1865-1879.

   Geboorteregister gemeente Zweeloo, 12 juli 1865 t/m 30 september 1879.

7. Omdat in artikelen vaak niet precies wordt aangegeven hoe gerapporteerde numerieke resultaten zijn verkregen, verdient het aanbeveling om wanneer in een artikel resultaten van numerieke berekeningen worden gepresenteerd, deze vergezeld te doen gaan van de programmatuur waarmee de berekeningen zijn uitgevoerd.

8. Het feit dat elk jaar op 1 januari tijdens het traditionele Nieuwjaarsconcert muziek wordt gespeeld die in een ver verleden niet altijd even goed gewaardeerd werd, doet vermoeden dat over vele jaren louter hardrock en metal muziek ten gehore zal worden gebracht tijdens dit concert.

9. Ondanks het feit dat tegenwoordig middels allerlei geavanceerde computersoftware voor vele mechanische problemen zonder het gebruik van pen en papier oplossingen kunnen worden berekend, dient nog steeds *met verstand* gerekend te worden met deze software.

10. Gezien het grote maatschappelijke en economische belang van het voetbalspel, is er pas echt sprake van een Europese eenwording als er een Europese profvoetbalcompetitie is ingevoerd.

11. In een democratische staatsvorm zou een kiezer een veel actievere rol dienen te spelen dan eenmaal per zittingstermijn van het parlement zijn gang te maken naar de stembus.